Experimental Investigations of Sand-Water Coaxial and Swirling Jets in Stagnant Water

A thesis submitted to The Faculty of Graduate Studies

In partial fulfillment of the requirements for the degree of

Doctor of Philosophy

In

Civil Engineering

By

Fardin Sharif

Ph.D. Civil Engineering

Supervisor

Dr. Amir Azimi

Lakehead University

Thunder Bay, Ontario

July 2021

Author's Declaration Page

I hereby declare that I am the sole author of this thesis document. This is a true copy of this document, including any required revisions as accepted by my supervisor.

Abstract

Sand jets and particle clouds are found in many engineering applications, such as marine bed capping, dredging material disposal, and discharge of wastewater. A coaxial jet is composed of an inner jet surrounded by an annular jet and is often employed as an effective method to mix two different flow streams. Swirling jets form when an azimuthal velocity is added to the axial flow. Adding a swirling motion or carrier fluid can influence the hydrodynamics of flow and enhance mixing efficiency. Understanding the dynamics of sand particles and ambient water is important for proper design and optimizing coaxial and swirling jets in engineering systems. The coaxial sand-water or swirling impinging process can be used as an effective way to optimize the releasing condition and to enhance the placement of materials in ambient currents.

In the first part of this thesis, detailed laboratory experiments were conducted to study the dynamics of gravity-driven finite amount of sand particles (i.e., particle cloud) vertically released downward into stagnant water. The importance of nozzle diameter, sand particle mass, and particle size in spreading and mixing of particles in water was studied, and the main parameters controlling particle motion and mixing were identified by the aspect ratio and Stokes number. The axial and radial profiles of sand concentration and velocity were measured by an accurate and robust optical probe (PV6). Practical formulations to estimate the decay rate of sand concentration and velocity were developed to assist the analysis and design of dredge disposal. Parameters were calculated inside particle clouds to better understand the evolution of particle clouds in stagnant water.

The effects of velocity ratio of annular to core nozzle on particle dynamics of two-phase (sand-water) coaxial jets in stagnant water were also studied. Sand concentration and velocity measurements were formulated based on flow characteristics. The results demonstrated that the decay rate of sand axial velocity and concentration along the mixing zone, were independent of the velocity ratio. The axial velocity decay of sand-water coaxial jets indicated an inverse relationship with velocity ratio; velocity decay rates of sand particles decreased with increasing the velocity ratio. Experimental observations of sand-water coaxial jets showed that the spreading rate of coaxial jets decreased with increasing velocity ratio. The variations of drag coefficient and particle-particle collision parameter (i.e., Bagnold number) indicated that the particle grouping effect reduced the drag coefficient in sand-water coaxial jets with lower velocity ratios. Proper Orthogonal Decomposition (POD) and Spectral Proper Orthogonal

Decomposition (SPOD) image processing and image data analysis techniques were used to study the low-rank dynamic behavior of sand water coaxial jets. The flow parameters were decomposed into energy-ranked coherent structures by employing high-speed images and characterized by the Kelvin–Helmholtz (KH) type wave packet instabilities.

Finanlly, The effects of swirling motion on particle dynamics and mixing properties of sand-water swirling jets were studied. Prediction models were developed based on the measured data to estimate sand concentration and velocity of sand-water swirling jets with different initial flow configurations. It was found that aspect ratio and swirling number can significantly impact the variations of axial concentration and velocity decay rate in sand-water swirling jets. A strong decay rate of momentum flux was observed along the recirculation zone and it last at a distance equal to 20 times of nozzle diameter. In addition, the spreading rate of sand-water swirling jets increased with increasing swirling numbers.

Acknowledgments

I would like to express my sincere gratitude to my supervisor Dr. Amir Hossein Azimi for his guidance, patience, motivation, and enthusiasm. His guidance helped me throughout my research to overcome many obstacles. I would like to thank Dr. Baoqiang Liao, Dr. Jian Deng, and Dr. Muntasir Billah who kindly agreed to evaluate the quality of my research work as my committee members and gave me valuable suggestions and advice. I am also thankful to Mr. Morgan Ellis and Mr. Brandon Trepanier for their tremendous supports for my experimental setup and willingness to help.

Finally, I would like to particularly thank my family for their encouragement and being supportive of my endeavors.

Table of Contents

Abstract …… iii

List of Tables ix

List of Equations x

List of Figures xiii

Nomenclature xix

Chapter 1 General Introduction 1

1.1 Motivation and Background 1

1.2 Application of Sand jets and Particle Clouds 2

1.3 Overview of the thesis content and novelty of the study 5

Chapter 2 Particle Cloud Dynamical Properties in Stagnant Water 7

2.1 Introduction and litrature review 7

2.2 Material and methods. 10

2.2.1 Experimental setup 10

2.2.2 Signal processing 14

2.3 Results and Discussion 16

2.3.1 Evolution of particle clouds 16

2.3.2 Sand concentration 20

2.3.3 Sand velocity 25

2.3.4 Drag coefficient 28

2.3.5 Ambient entrainment 34

2.3.6 Energy transfer 37

2.3.7 Particle-particle interaction 38

2.4 Conclusion 40

Chapter 3 Effects of Velocity Ratio on Dynamics of Sand-Water Coaxial Jets 42

3.1 Introduction and litrature review 42

3.2 Material and methods. 47

3.2.1 Experimental setup 47
3.2.2 Signal processing 50
3.3 Results and Discussion 53
3.3.1 Mass and momentom flux 53
3.3.2 Spreading rate and mixing 57
3.3.3 Sand concentration 58
3.3.4 Sand velocity 60
3.3.5 Drag reduction of group particles 65
3.3.6 Particle-particle interactions 70
3.4 Conclusion 73
Chapter 4 Spectral and Proper Orthogonal Decomposition Analysis of Sand-Water Coaxial jets 75
4.1 Introduction and litrature review 75
4.2 Material and methods. 77
4.2.1 Experimental setup 77
4.2.2 Proper orthogonal decomposition of data (POD) 82
4.2.3 Spectral Proper orthogonal decomposition of data (SPOD). 82
4.3 Results and Discussion 84
4.3.1 Proper orthogonal decomposition of data (POD) 84
4.3.2 Spectral Proper orthogonal decomposition of data (SPOD) 88
4.4 Conclusion 91
Chapter 5 Experimental study of sand-water swirling jets in stagnantwater 93
5.1 Introduction and litrature review 93
5.2 Material and methods. 99
5.2.1 Experimental setup 99
5.2.2 Signal processing 104
5.3 Results and Discussion 107

5.3.1 Mass and momentom flux 107
5.3.2 Spreading rate and mixing 109
5.3.3 Swirling jets with unlimited sand mass 111
5.3.4 Swirling jets with limited sand mass 116
5.3.5 Drag coefficient 121
5.3.6 Power spectral analysis 124
5.4 Conclusion 126
Chapter 6 General Conclusions and Recommendations for Future Research 128
6.1 General Conclusion 128
6.2 Future research and studies. 133
Appendix 1: **Experimental study of Sand-Water Coaxial Jets with Low-Velocity Ratio** 139
Appendix 2: **A MATLAB® Signal Processing** 153
Appendix 3: **A MATLAB® Velocity Cross-Correlation**. 154
Appendix 4: **A MATLAB® Spectral and Proper Orthogonal Decomposition** 156
Refrences 157

List of Tables

Table 2.1 Experimental details and parameters of particle clouds in water.....12

Table 2.2 Coefficients of the proposed empirical correlations for predictions of the axial sand concentration c and the axial velocity *u* of particle clouds.....23

Table 3.1 List of two-phase coaxial jets investigations in the literature.....46

Table 3.2 Experimental parameters and non-dimensional parameters of the coaxial sand-water jet.....49

Table 4.1 Experimental details and parameters of sand-water coaxial jets in water with low and high-velocity ratio.....80

Table 5.1 List of two-phase swirling jets investigations in the literature.....98

Table 5.2 List of experiments and the related non-dimensional numbers in the present study of sand-water swirling jets in stagnant water.....102

List of Equations

Equation 2.1 Cloud number.....8

Equation 2.2 Sand mass flux of particle cloud.....18

Equation 2.3 Sand momentum flux of particle cloud.....18

Equation 2.4 Proposed model of centerline sand concentration along the cloud axis.....23

Equation 2.5 Non-linear functions of the aspect ratio.....23

Equation 2.6 Gaussian distribution model of radial sand concentration.....25

Equation 2.7 Coefficient of Gaussian distribution model of radial sand concentration.....25

Equation 2.8 Prediction of centerline sand velocity along the cloud axis.....26

Equation 2.9 Gaussian distribution model, radial variations of sand velocity.....28

Equation 2.10 Coefficient of Gaussian distribution model of radial sand velocity.....28

Equation 2.11 Momentum balance on a disc-shaped control volume.....29

Equation 2.12 Momentum flux of sand particles on a disc-shaped control volume.....29

Equation 2.13 Balance between the gravitational and buoyancy forces.....29

Equation 2.14 The drag force on individual sand particles 29

Equation 2.15 Average concentration on a disc-shaped control volume.....29

Equation 2.16 Drag coefficient of individual sand particles (Chien, 1994) 31

Equation 2.17 Correlation of the average drag coefficient particle and Reynolds number....31

Equation 2.18 Entrained volume of ambient water.....34

Equation 2.19 Sand-phase volume flux at each cross-section 34

Equation 2.20 Variations of sand volume flux in the radial direction.....34

Equation 2.21 The radial variations of the entrainment coefficient.....36

Equation 2.22 Bagnold number 39

Equation 2.23 Concentration of sand particles during flow propagation 39

Equation 2.24 Shear rate 39

Equation 3.1 Sand mass flux of coaxial jet.....54

Equation 3.2 Sand momentum flux of coaxial jet 54

Equation 3.3 Spreading rate of the sand-water coaxial jet 56

Equation 3.4 Proposed model of centerline sand concentration along the coaxial jet axis...59

Equation 3.5 Gaussian distribution function of the radial variations of sand concentration.60

Equation 3.6 Coefficient of Gaussian distribution model of radial sand concentration.....60

Equation 3.7 Proposed model of centerline velocity of sand-water coaxial jets…….....63

Equation 3.8 Gaussian distribution function of the radial variations of sand velocity.....64

Equation 3.9 Coefficient of Gaussian distribution model of radial sand velocity.....65

Equation 3.10 Momentum balance on a disc-shaped control volume.....65

Equation 3.11 Momentum flux of sand particles on a disc-shaped control volume.....65

Equation 3.12 Drag force acting on individual particles.....66

Equation 3.13 Estimated number of particles within the control volume.....66

Equation 3.14 Average concentration on a disc-shaped control volume.....66

Equation 3.15 The averaged drag force for a single sand particle was calculated.....66

Equation 3.16 Chien (1994) proposed a model for estimating the drag coefficient of individual sand particles based 66

Equation 3.17 Schiller & Neumann (Wörner, 2003) proposed of the drag coefficient of individual particles in stagnant water 66

Equation 3.18 Clift et al. (1974) the drag coefficient for non-spherical particles.....67

Equation 3.19 Drag coefficient of Engelund and Hansen (2010) 67

Equation 3.20 Proposed to predict the correlation between C_d and R_p.....70

Equation 3.21 Bagnold number.....70

Equation 2.22 Concentration of sand particles during flow propagation 70

Equation 3.23 Shear rate 71

Equation 4.1 POD matrix.....82

Equation 4.2 linear weighted sum of the modes 83

Equation 4.3 POD coefficient 84

Equation 5.1 Sand mass flux of swirling jet.....108

Equation 5.2 Sand momentum flux of swirling jet.....108

Equation 5.3 Spreading rate of the sand-water swirling jets 110

Equation 5.4 Proposed model of centerline sand concentration along the swirling jets axis.....112

Equation 5.5 Gaussian model of the radial variations of sand concentration of swirling jets.....112

Equation 5.6 Coefficient of Gaussian distribution model of radial sand concentration.....112

Equation 5.7 Proposed model of centerline velocity of sand-water swirling jets.....114

Equation 5.8 Gaussian distribution function of the radial variations of sand velocity.....116

Equation 5.9 Coefficient of Gaussian distribution model of radial sand velocity.....116

Equation 5.10 Buoyancy force of particles on a disc-shaped control volume.....121

Equation 5.11 Momentum balance on a disc-shaped control volume.....121

Equation 5.12 Momentum flux of sand particles on a disc-shaped control volume.....121

Equation 5.13 Individual drag force acting on a single particle.....121

Equation 5.14 Estimated number of particles within the control volume.....122

Equation 5.15 Average concentration on a disc-shaped control volume.....123

Equation 5.16 The averaged drag coefficient for a single sand particle 123

Equation 5.17 Proposed to predict the correlation between C_d and R_p.....123

List of Figures

Figure 1.1 Single oil-sand slurry flow disposed into tailing ponds.....2

Figure 1.2 A series of oil-sand slurry flow disposed into tailing ponds.....2

Figure 1.3 Palm Islands Construction.....3

Figure 1.4 Dredging ……..….....3

Figure 1.5 The three different phases of particle motion in particle-laden jets during open-water sediment disposal: convective descent, dynamic collapse, and passive diffusion (after Montgomery and Engler, 1986) 4

Figure 2.1 Schematics of the experimental setup and coordinate system: (a) experimental tank and position of nozzle; (b) detail images of PV6 probe; (c) position of PV6 probe for measuring at the cloud centerline at $r/d_o = 0$.....11

Figure 2.2 Time series of voltage signals detected by the optical probe at $x/d_o = 5$ and for different aspect ratios; a) $L_o/d_o = 19.6$, b) $L_o/d_o = 29.4$, c) $L_o/d_o = 39.2$.....14

Figure 2.3 Typical instantaneous sand velocity data extracted from voltage signals using different segment lengths L_s and segment overlapping ΔL_s for Test A3, $S_t = 0.52$ and $L_o/d_o = 39.2$ at $x/d_o = 6.25$; a) effect of segment length ($L_s = 512$, 1024, and 2048) on instantaneous sand velocity; b) effect of segment overlapping ($\Delta L_s = 0$, 25%, and 50%) on instantaneous sand velocity.....15

Figure 2.4 Evolution of particle cloud and segregation of sand particles for $S_t = 0.52$ and $L_o/d_o = 9.8$; a) $t^* = 1.2$, b) $t^* = 1.7$, c) $t^* = 2.2$, d) $t^* = 2.7$, e) $t^* = 3.3$, f) $t^* = 3.4$.....17

Figure 2.5 Variations of the normalized sand mass flux detected by the optical probe along the normalized axial direction for $S_t = 0.52$, b) Variations of the normalized momentum flux detected by the optical probe along the normalized axial direction for $S_t = 0.52$.{A1, A2, A3} 19

Figure 2.6 Effects of aspect ratio L_o/d_o and particle size on the normalized sand concentration c_m/c_o along the normalized axial direction; a) $S_t = 0.52$, $d_o = 8$ mm, b) $S_t = 0.74$, $d_o = 8$ mm, c) $S_t = 0.66$ and 0.93, $d_o = 10$ mm.....22

Figure 2.7 Effect of particle size on radial variations of normalized sand concentration c/cm with different normalized distances from the nozzle x/d_o; a) L_o/d_o = 39.2, S_t = 0.52, b) L_o/d_o = 39.2, S_t = 0.74.....24

Figure 2.8 Effect of L_o/d_o on variations of the normalized velocity u_m/u_o along the normalized axial distance from the nozzle x/d_o; a) S_t = 0.52, b) S_t = 0.74.....26

Figure 2.9 Variations of the normalized sand velocity u/u_m in transverse direction and for different normalized distances from the nozzle x/d_o for L_o/d_o = 39.2; a) S_t = 0.52, b) S_t = 0.74.....27

Figure 2.10 Schematic of particle cloud and the ambient flow; a) momentum balance, b) flow entrainment inside a particle cloud.....30

Figure 2.11 Variations of drag coefficient C_d of particle clouds with normalized transverse direction r/d_o and for different normalized axial distance from the nozzle x/d_o; a) S_t = 0.52, b) S_t = 0.74.....32

Figure 2.12 Effects of aspect ratio L_o/d_o on variations of drag coefficient C_d of particle clouds with particle Reynolds number Re_p along the vertical axis of the clouds x/d_o; a) S_t = 0.52, b) S_t = 0.74.....33

Figure 2.13 Effect of aspect ratio and depth progression on the radial variation of entrainment coefficient for S_t = 0.52; a) L_o/d_o = 39.2, b) L_o/d_o = 29.4, c) L_o/d_o = 19.6.....35

Figure 2.14 Entrainment coefficient of vertically downward particle cloud S_t = 0.74 and L_o/d_o=19.6.....37

Figure 2.15 Axial and radial variations of the power spectral density (PSD) of sand concentration for S_t = 0.52 and L_o/d_o =39.2; a) axial variation of PSD at the centerline, b) radial variation of PSD at x/d_o = 8.....38

Figure 2.16 Variations of the Bagnold number in transverse direction and at different normalized distances from the nozzle x/d_o; a) S_t = 0.52, b) S_t = 0.74.....40

Figure 3.1 Schematics of the experimental setup, instrumentations, and the adopted coordinate system.....48

Figure 3.2 Details of the coaxial nozzle arrangement and funnel-pipe assembly.....48

Figure 3.3 Typical instantaneous sand velocity data extracted from voltage signals and using different segment overlapping L_s = 0%, 25%, and 50% and segment lengths ΔL_s for Ru = 0.62 and x/d_o = 10: a) ΔL_s = 2048; b) ΔL_s = 1024; c) ΔL_s = 512.....52

Figure 3.4 Effects of velocity ratio on the time history of turbulent characteristics of sand-water coaxial jets at x/d_o = 24: a) time history of velocity fluctuations (u'); b) time history of turbulence intensity (u_{rms}/u_{ave}). 53

Figure 3.5 Variations of the integral quantities of sand-water coaxial jets with normalized distance from the nozzle for different velocity ratios, Ru = 0.62, 0.93, 1.24 and 1.86: a) variations of the normalized sand mass flux with normalized axial distance from the nozzle; b) variations of the normalized momentum flux with normalized axial distance from the nozzle……...…….55

Figure 3.6 Effects of velocity ratio on the spreading rate of sand-water coaxial jets: a) variation of the spreading rate with velocity ratio x/d_o; b) variation of the spreading rate with velocity ratio.....57

Figure 3.7 Images of sand-water coaxial jets for different velocity ratios: a) Ru = 1.86; b) Ru = 1.24; c) Ru = 0.93; d) Ru = 0.74; r) Ru = 0.62.....58

Figure 3.8 Effects of velocity ratio on variations of the normalized sand concentration c_m/c_o of sand-water coaxial jets with normalized axial distance from the nozzle x/d_o.....59

Figure 3.9 Effects of velocity ratio on the radial variations of normalized sand concentration c/c_m with normalized distance from the nozzle, x/d_o: a) Ru = 1.86; b) Ru = 0.93; c) Ru = 0.62……...……...61

Figure 3.10 Effects of velocity ratio on variations of the normalized sand velocity u_m/u_o of sand-water coaxial jets with normalized axial distance from the nozzle, x/d_o.....62

Figure 3.11 Effect of velocity ratio on the radial variations of normalized sand velocity u/u_m of sand-water coaxial jets with different normalized distances from the nozzle, x/d_o: a) Ru = 1.86; b) Ru = 0.93; c) Ru = 0.62.....64

Figure 3.12 Schematic of the momentum balance in a coaxial sand-water jet 67

Figure 3.13 Variations of the drag coefficient of sand particles C_d for sand-water coaxial jets with particle Reynolds number R_p for different normalized axial distance from the nozzle, x/d_o. 68

Figure 3.14 Variations of the drag coefficient of sand particles C_d for sand-water coaxial jets with particle Reynolds number R_p for different normalized axial distance from the nozzle x/d_o and for different velocity ratio ($0.62 \leq Ru \leq 1.86$) 69

Figure 3.15 Effect of velocity ratio on the radial variations of the Bagnold number with different normalized axial distance from the nozzle, x/d_o: a) $Ru = 1.86$; b) $Re = 0.93$ c) $Ru = 0.62$.....71

Figure 3.16 Effect of velocity ratio on the axial variations of the Bagnold number for sand-water coaxial jets.....72

Figure 4.1 A schematic view of the experimental setup, instrumentations, and the adopted coordinate system.....78

Figure 4.2 Details of the coaxial nozzle arrangement and funnel-pipe assembly.....79

Figure 4.3 Images of sand-water coaxial jets for different velocity ratios: a) $Ru = 0$; b) $Ru = 1.24$; c) $Ru = 0.93$: d) $Ru = 0.62$.....81

Figure 4.4 High-speed illumination images of sand-water coaxial jets for different velocity ratios with color tracer: a) $Ru = 0.35$; b) $Ru = 0.16$; c) $Ru = 0.12$; d) $Ru = 0.07$.....81

Figure 4.5 Proper Orthogonal Decomposition (POD) of a coaxial sand-water jet with $Ru = 1.86$: a) Mode 1; b) Mode 3; c) Mode 5; d) Mode 7; e) Mode 10.....84

Figure 4.6 Proper Orthogonal Decomposition (POD) of a coaxial sand-water jet $Ru = 0.74$: a) Mode 1; b) Mode 5; c) Mode 10; d) Mode 15; e) Mode 20.....85

Figure 4.7 Proper Orthogonal Decomposition (POD) of a coaxial sand-water jet $Ru = 0.37$: a) Mode 1; b) Mode 5; c) Mode 10; d) Mode 15; e) Mode 20.....86

Figure 4.8 Energy contribution of different Proper Orthogonal Decomposition (POD) modes for $0.06 \leq Ru \leq 1.24$.....87

Figure 4.9 Power Spectral Density (PSD) of different Proper Orthogonal Decomposition (POD) modes for a coaxial sand-water jet: a) $Re = 1.24$; b) $Re = 0.63$.....88

Figure 4.10 First two SPOD modes with the frequency of 1.95, 3.91 and 5.86 of sand-water coaxial jets for different velocity ratios $Ru = 0$.....89

Figure 4.11 First two SPOD modes with the frequency of 1.95, 3.91 and 5.86 of sand-water coaxial jets for different velocity ratios Ru = 1.24.....90

Figure 4.12 First two SPOD modes with the frequency of 1.95, 3.91 and 5.86 of sand-water coaxial jets for different velocity ratios Ru = 0.62.....90

Figure 4.13 The first three SPOD modes SPOD eigenvalue spectra with the frequency of sand-water coaxial jets for different velocity ratios Ru = 0, 0.62 and 1.24.....91

Figure 5.1 Schematics of the experimental setup, instrumentations, and the adopted coordinate system for swirling sand-water jets in stagnant water.....100

Figure 5.2 Detail schematic and three-dimensional print of the swirling cylinder and nozzle arrangement.....101

Figure 5.3 High speed images of sand-water swirling jets for different swirling numbers and $L_o/d_o \approx \infty$: a) Sw = 0; b) Sw = 0.45; c) Sw = 0.50; d) Sw = 0.55; e) Sw = 0.60.....103

Figure 5.4 Time series of voltage signals detected by the PV6 fiber optic probe at the centerline of the jet and at x/d_o = 10. Effect of swirling number on the raw voltage signals of a sand-water swirling jet with L_o/d_o = 20.9: a) Sw = 0.45; b) Sw = 0.60.....105

Figure 5.5 Time-history of the instantaneous sand velocity data extracted from voltage signals of the PV6 optical fiber probe. Effects of different segment overlapping, L_s = 0%, and 50% and segment lengths, ΔL_s on the centerline velocity of a swirling sand-water jet with Sw = 0.60 and $L_o/d_o \approx \infty$ at x/d_o = 10 with: a) ΔL_s = 2048; b) ΔL_s = 1024; c) ΔL_s = 512.....106

Figure 5.6 Effects of swirling number on the time history of turbulent characteristics of sand-water swirling jets with $L_o/d_o \approx \infty$. Velocity data were measured at the jet centerline and at x/d_o = 10: a) time history of velocity fluctuations, u'; b) time history of turbulence intensity, u_{rms}/u_{ave}.....107

Figure 5.7 Effects of swirling number on variations of the integral quantities of sand-water coaxial jets with normalized distance from the nozzle, x/d_o for sand-water swirling jets with $L_o/d_o \approx \infty$: a) variations of the normalized sand mass flux with x/d_o; b) variations of the normalized momentum flux with x/d_o.....109

Figure 5.8 Effects of swirling number on the spreading rate of sand-water swirling jets with $L_o/d_o \approx \infty$.....110

Figure 5.9 Effects of swirling number on variations of the normalized centerline sand concentration, c_m/c_o, with normalized axial distance from the nozzle, x/d_o, for sand-water swirling jets with $L_o/d_o \approx \infty$.....111

Figure 5.10 Effects of swirling number on the radial variations of normalized sand concentration, c/c_m, with normalized distance from the nozzle, x/d_o, for sand-water swirling jet with $L_o/d_o \approx \infty$: a) Sw = 0.45; b) Sw = 0.50; c) Sw = 0.55; d) Sw = 0.60.....113

Figure 5.11 Effects of swirling number on variations of the normalized centerline sand velocity, u_m/u_o, with normalized axial distance from the nozzle, x/d_o, for sand-water swirling jets with $L_o/d_o \approx \infty$.....114

Figure 5.12 Effects of swirling number on the radial variations of normalized centerline sand velocity, u/u_m, with normalized distance from the nozzle, x/d_o, for sand-water swirling jets with $L_o/d_o \approx \infty$: a) Sw = 0.45; b) Sw = 0.50; c) Sw = 0.55; d) Sw = 0.60.....115

Figure 5.13 Raw images of sand-water swilring jets with different swirling number and aspect ratio at the non-dimensional time of t^*=1.4: a) Sw = 0.45; b) Sw = 0.50; c) Sw = 0.55; d) Sw = 0.6.....118

Figure 5.14 Effects of swirling number, Sw, and aspect ratio, L_o/d_o, on variations of normalized centerline sand concentration, c_m/c_o, with normalized axial distance from the nozzle, x/d_o: a) Sw = 0.45; b) Sw = 0.50; c) Sw = 0.55; d) Sw = 0.60.....119

Figure 5.15 Effects of swirling number on the radial variations of normalized sand velocity, u/u_m, with normalized distance from the nozzle, x/d_o for sand-water swirling jets with $L_o/d_o \approx \infty$: a) Sw = 0.45; b) Sw = 0.50; c) Sw = 0.55; d) Sw = 0.60.....120

Figure 5.16 Schematic of the momentum balance in sand-water swirling jets.....122

Figure 5.17 Variations of the drag coefficient of sand particles, C_d, for sand-water swirling jets with particle Reynolds number, R_p, for different normalized axial distance from the nozzle, x/d_o, and $L_o/d_o \approx \infty$.....124

Figure 5.18 Power Spectral Density (PSD) analysis of sand concentration for sand-water swirling jets with $L_o/d_o \approx \infty$ and swirling numbers of 0.45 and 0.60: a) x/d_o = 20, r/d_o = 2.5; b) x/d_o = 30, r/d_o = 2.5.....125

Figure 6.1 Schematic of the hemispherical bucket release mechanism.....134

Figure 6.2 Schematic of the coaxial sand jet surrounded by annular water jet.....136

Figure 6.3 Schematic of the swirling coaxial without initial premix mechanism.....138

Nomenclature

A_s surface area of the cloud, m^2

A_p projected frontal area of individual particle, m^2

B buoyancy, m^4/s^2

Ba Bagnold number

b half-width of the jet, cm

b_c half-width of the jet concentration profile where $c/c_o = 80\%$, cm

b_u half-width of the jet velocity profile where $u/u_m = 50\%$, cm

c concentration, %

c_{ave} average sand volumetric concentration of particle cloud, %

$\overline{c}$ average sand volumetric concentration of a jet, %

c_o initial concentration at the nozzle, %

c_m sand volumetric concentration at the centerline of jet, %

$c*$ concentration of the material during flow propagation, %

C_d drag coefficient

d_a annular nozzle diameter size, mm

d_o central nozzle diameter size, mm

D_{50} diameter of particles in which 50% are finer, mm

Ec energy contribution of each mode

f_D individual particle drag force, N

F_B buoyancy force, N

F_D drag force, N

F_g gravitational force, N

Fr Froude number

g acceleration due to gravity, m/s^2

g' reduced gravity, m/s^2

L_o length of sand occupied in nozzle, mm

L_s size of signal overlapping

m sand mass, g

$\dot{m}$ sand mass flux, kg/s

m_o initial sand mass at the nozzle, g

$\dot{m}_o$ initial sand mass flux at the nozzle, kg/s

$\dot{M}$ momentum flux of the coaxial jet, kg.m^4 /s^2

$\dot{M}_o$ initial momentum flux at the nozzle, kg.m^4 /s^2

M_p number of single snapshots pixels

N_b number of snapshots blocks

Nc cloud number

N_f the length of SPOD segmentation

N_t number of snapshots

N_p number of particles

N_o number of overlap snapshots

Q volume flux, m^3/s

Q_p time-dependent intensity coefficients

r horizontal distance from the jet axis, m

r_o bulk radius of the particle cloud, m

Ru velocity ratio of annular to core stream

Re Reynolds number

R_p particle Reynolds number

S matrix of singular values

S_t Stokes number

Sw Swirling number

x_a temporal variables of POD

t^* non-dimensional time scale

U spatial matrix

u particle velocity, m/s

u_{ave} particle average velocity, m/s

u_c circulation velocity, m/s

u_e entrainment velocity, m/s

u_m sand velocity at the centerline of the jet, m/s

u_o initial sand velocity at the nozzle, m/s

u_{ow} initial water velocity at the nozzle, m/s

u_{rms} root-mean-square of particles velocities, m/s

u_∞ terminal settling velocity, m/s

u' velocity fluctuations, m/s^2

P single data matrix of SPOD snapshots

P_B single data matrix of SPOD snapshots in each block

V volume of particle cloud, m^3

V_{disc} disc shaped control volume, m^3

V_o initial volume of sand jet in tube, m^3

V_n matrix of proper orthogonal modes

x distance from the nozzle, m

x_a special variables of POD

X matrix of sequence images

μ dynamic viscosity, m^2/s

ρ_s densities of sand particles, kg/m^3

ρ_w densities of water, kg/m^3

β_{ij} temporal coefficients

τ_p particle relaxation time, s

τ_f time scale of the flow, s

φ sphericity ratio

φ_j orthogonal eigenvectors or spatial modes

γ shear rate, 1/s

w estimated cloud width, m

w_j estimated jet width, m

α_e entrainment coefficient

α_{ij} POD coefficient

ΔL_s signal segment size

ΔQ_e entrainment flow rate, m^3/s

λ eigen values

Chapter 1

General Introduction

1.1 Motivation and Background

Canada has the third-largest proven oil reserve in the world with an estimation of 174 billion barrels of oil deposited in form of Oil-sand in the Northern Alberta (Alberta Energy and Utilizes Board, 2005). Alberta's oil sand operation is one of the world's largest industrial projects. Oil sand is a mixture of sand, clay, water and bitumen. The crude oil can extract during the refinery process from bitumen. Oil sand tailings are the results of bitumen refinery which consist of a mixture of water, sand, clay, and residual bitumen. It is mostly the by-product of hot water treatment process used to separate the oil from sand and clay in oil sand mining operations. Tailings are stored in large engineered dam and dyke facilities to form a tailings pond. The top water layer segregates from sand, clay, and bitumen and reuses in bitumen extraction. Water is continuously recycled from tailings ponds and is pumped back into the extraction process, resulting in significant reduction of freshwater intake. Managing the volume of tailings in oil-sand tailing ponds was found to be one of the most challenging environmental problem in mining industries.

Many techniques are employed to enhance the reclamation processes in tailing pond operation such as capping fine residuals by a uniform layer of sand. Another effective method of tailing pond recovery is to discharge by-product slurries inform of sand-laden turbulent jets into tailing ponds (Figure 1.1 and 1.2) to accelerate the settling process of fine particles. In this method, very small suspended particles coagulate and form larger particles due to turbulent shear layer and intense mixing generates by sand-laden turbulent jets. This process results in significant reduction in volume of fine tailings and enhances the water recovery rate. Therefore, it is important to be able to control physical mixing by understanding the dynamics of sediments induced by turbulent jets. The mechanism involved in the settlement of sand particles in stagnant ambient water (i.e., tailing ponds) is correlated with many parameters.

This present research study focuses on understanding the effects of controlling factors on the behavior of sand-water turbulent jets in ambient water. The initial configurations in particle-laden jets such as particle size, sand mass, nozzle diameter, etc., influence the concentration, velocity, mixing strength, and turbulent properties of particle-laden jets.

Therefore, to minimize sediment losses to the ambient environment and improve the release mechanism, it is necessary to understand the flow characteristics with different initial flow conditions for efficient design and optimizing the systems. In addition, detailed laboratory experiments are required to understand the nature of sand motions in such a complex fluid domain and develop practical models for the different flow conditions.

Figure 1.1: Single nozzle oil-sand slurry jet disposes slurry into tailing ponds.
https://www.thestar.com/opinion/editorialopinion/2012/01/30/covering_the_oilsands.html

Figure 1.2: A series of oil-sand slurry pipes dispose slurries into tailing ponds.
http://priceofoil.org/2014/02/24/tar-sands-tailing-ponds-leaking/

1.2 Application of Sand jets and Particle Clouds

Particle-laden jets with high initial momentum and particle concentration are commonly known as sand/slurry jets (Hall et al., 2010; Azimi et al., 2012a, 2012b). Further, gravity-driven sand jets with limited sand mass are known as particle clouds in the literature. Sand jets and particle clouds can be found in many engineering applications such as marine bed capping, artificial island formation, dredged material disposal, and discharge of slurry flow into a tailing storage facility. (Buhler and Papantoniou, 1991; Bush et al., 2003; Azimi et al.,

2011; Azimi et al., 2012a, 2012b; Manzouri and Azimi, 2019a, 2019b). Moreover, there is great interest in understanding the mixing processes in particle-laden jets and particle clouds for environmental engineering applications (Mohammadidinani et al., 2017; Moghadaripour et al., 2017a, 2017b). In artificial island construction, sand is continuously discharged and pumped through a pipe from barges into desired marine environments to develop an island foundation. In most cases, sediments are discharged obliquely through a pipe with angle respect to the vertical axis (Figure 1.3).

Figure 1.3: Palm Islands construction by oblique discharge of slurry jet.

https://www.aboutcivil.org/palm-island-dubai-megastructure.html

Dredging is the act of removing sediments and debris from the bottom of lakes, rivers, and other water bodies. It is a routine necessity on maintaining or increasing the depth of navigation channels and ship's waterways around the world. Dredging is also used as a method to replenish sand on some public beaches and to reduce the exposure of wildlife, and people from contamination and prevent the spread of contaminants to other areas of the water body (Figure 1.4).

Figure 1.4: Dredging sediment from the bottom of a lake.

http://www.theindependentbd.com/arcprint/details/134426/2018-01-26

The schematic of the general mechanism in spreading and settlement of dredged material disposal at the open water is shown in Figure1.5. The dredged material is disposed and descended through the water column as a jet. The behavior of dredged material can be divided into three different types of transport stages based on the dominant physical forces. These stages are convective descent, dynamic collapse, and diffusion. At the descent phase, large volumes of open water flow entrainment occur in the jet. Therefore, some materials concentrate in the upper part of the entrained water due to turbulent shear stress. In the collapse phase, the natural level of buoyancy balance and conversion of vertical momentum to horizontal momentum leads to a higher spreading rate and ambient water entrainment of dredged material. In the final phase of convective descent, diffusive processes dominate the jet flow due to higher energy dissipation. Therefore, mixing of the remaining portion of materials with the lower water column accelerates and leads to material enter to settlement process (Truitt, 1988; Gensheimer, 2010). Each phase in open-water sediment disposal can impact the long-term stabilities of dredged materials since the concentration and size of dredging material in two-phase sand jet varies with operation time. Therefore, the effects of controlling parameters on mixing and turbulent properties of sand-water jets are studied by laboratory experiments. The research presented will focus entirely on the first and second phases of particle-laden jets.

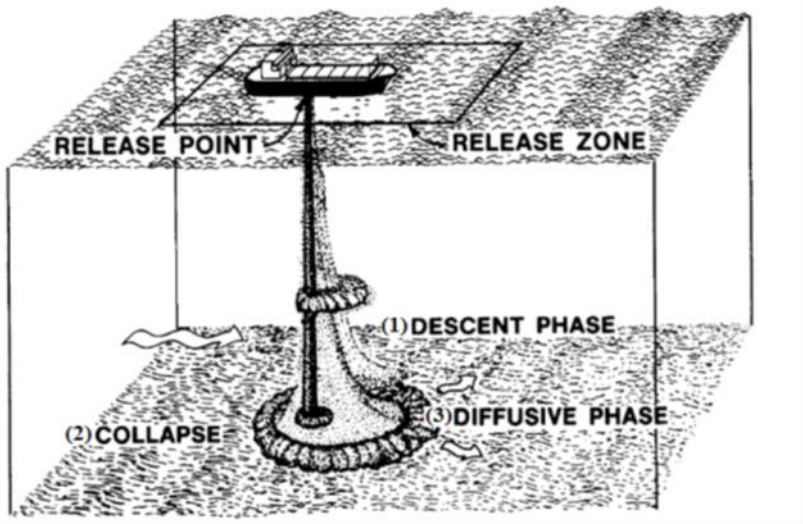

Figure 1.5: The three different phases of particle motion in particle-laden jets during open-water sediment disposal: convective descent, dynamic collapse, and passive diffusion (after Montgomery and Engler, 1986).

1.3 Overview of the thesis content and novelty of the Study

This thesis is composed of four detailed series of experimental investigations including the general conclusion and topics for future fundamental and applied research. Each contribution is presented in a separate chapter and the following is a brief introduction to each chapter.

1.3.1 *Particle cloud dynamics*

Chapter 2 describes a detailed laboratory study on particle cloud dynamics in stagnant water. Most recent research studies on evolution of particle clouds in water used Lagrangian method to measure and predict cloud size and its entrainment with the ambient fluid over time. In addition, particle velocity and concentration are often averaged over the entire volume of cloud, while less attention is paid to investigate sand velocity and concentration distributions inside the particle cloud. Therefore, the main objective of Chapter 2 was to understand the energy transfer and entrainment inside particle clouds by measuring the instantaneous particle velocity and concentration in axial and transverse directions using a light refractive particle velocimetry technique. Using particle velocity and concentration inside the cloud, the effects of particle size and aspect ratio on the energy transfer and entrainment inside particle clouds were evaluated. The second objective of this chapter was to develop practical formulations for the prediction of sand velocity and concentration in both axial and transverse directions by employing dimensional analysis and multi-variable regression analysis. The core region of particle clouds, where particle-particle interaction is dominant, was defined by calculating particle collision stress using sand velocity and concentration distribution.

1.3.2 *Sand-water coaxial jets*

In Chapter 3, a series of detailed laboratory studies were carried out to understand the dynamics of sand-water coaxial jets in stagnant water. Most of previous studies have focused on the dynamics of two-phase coaxial jets with relatively low mass loading ratios and small particle sizes by injecting particles in either the inner or outer nozzles of single-phase coaxial jets. Here, we introduced a new injection mechanism and conducted a series of experiments on particle-laden coaxial jets. The tests were designed by setting the core water jet surrounded by the outer sand jet to study the mixing of sand particles for a wide range of velocity ratios. The composition of the inner water flow and the outer sand flow with high mass loading ratios and water discharges were used to investigate the mixing capacity of new design. The main objective of this chapter was to examine the effects of velocity ratio on variations in jet characteristics such as spreading rate, sand velocity and concentration profiles, as well as

studying interparticle collisions by observing the variations of drag coefficients and Bagnold numbers in both axial and radial directions. The secondary objective of this chapter was to develop prediction models that estimate sand velocity and concentration in both axial and transverse directions for designing sand-water coaxial jets and optimization.

In Chapter 4, spectral and proper orthogonal decomposition (SPOD and POD) methods were employed to study the low-rank dynamic and turbulent kinetic energy of sand water coaxial jets from high-speed imaging. The main objective of Chapter 4 was to study the dynamic behavior, energy contribution of high, and low-ranked coherent flow configuration of coaxial sand-water jets by the resolvent analysis ability of the Proper Orthogonal Decomposition (POD) technique. Secondly, Spectral Proper Orthogonal Decomposition (SPOD) is derived from a space-time POD data for statistically stationary flows and resolved the modes (low-rank dynamics) that each oscillates at a single frequency. In addition, the energy contribution of low-rank modes was also studied.

1.3.3 *Experimental study of sand-water swirling jets in stagnant water*

The dynamics of swirling sand jets in stagnant water were studied in Chapter 5. Most of the previous studies have focused on the dynamics of gas-solid swirling jets and less attention has been paid to study the effects of swirl intensity on the dynamics of sand-water swirling jets. A series of laboratory experiments on particle-laden swirling jets was conducted to study the effects of swirl intensity and the availability of sand mass on the motion of particles. The main objective of this chapter is to examine the effects of swirling number and particle aspect ratio on the flow characteristics such as spreading rate, sand velocity, and sand concentration profiles. The effects of swirl intensity and aspect ratio on the inter-scale particle dynamics such as particle-particle collision and drag coefficients were investigated. The second objective was to develop models for estimation of sand velocity and concentration in both axial and transverse directions to be used for design and optimization of the performance of sand-water swirling jets.

Chapter 2

Particle cloud dynamical properties in stagnant water

2.1 Introduction and literature review

Particle clouds can be formed by the instantaneous releasing a finite mass of sand particles into the ambient fluid. Particle motion in the water is inherently a two-phase interactive process with three different phases of motion (Rahimipour and Wilkinson, 1992). Once particles are released into water, they form a particle cloud which starts to accelerate due to the density difference between sand particles and water. This stage of evolution is called the acceleration or ballistic phase. The particle cloud then forms a circulating cloud front and a rotating fluid vortex ring in the thermal or self-preserved phase, during which time momentum is transferred from the particle cloud to the ambient fluid. Finally, in the dispersive regime, individual particles slow down with a settling velocity of u_∞. Many research studies have investigated the dynamics of a particle cloud in the acceleration, thermal, and swarm regimes (Noh and Fernando, 1993; Bush et al., 2003; Lai et al., 2013; Wang et al., 2014; Moghadaripour et al., 2017a, 2017b). For example, the normalized buoyancy $B/x^2u_\infty^2$ was used to classify particle clouds into thermal and swarm regimes where buoyancy was defined as $B = mg/\rho_s = (\pi d_o^2/4)L_o c_o g$, and x was the distance from the nozzle, m was the sand mass, ρ_s was the sand density, g was the acceleration due to gravity, L_o was the length of the occupied sand particle in a pipe with an inner diameter d_o, and c_o was the initial sand concentration with a value of 0.6 vol/vol for loosely packed and uniform sand particles. It was found that for a normalized buoyancy higher than 0.1, particle clouds are in the thermal regime, while for $B/x^2u_\infty^2 \leq 0.1$, particles descend as a swarm of individual particles (Bush et al., 2003; Azimi et al., 2012a).

More recently, the effect of sand mass and nozzle size showed a considerable impact on the motion of particle clouds. For gravity-driven particle clouds, the initial aspect ratio of L_o/d_o was found to be an important parameter to estimate cloud penetration length, width, and velocity. For relatively small aspect ratios, $0.125 \leq L_o/d_o \leq 4$, and low initial density differences between 1% and 10%, the spreading rates were found to be greatly affected by the initial aspect ratio (Lai et al., 2015). It was also found that particle size affects the depth progression for particle clouds with a relatively small aspect ratio of $0.6 \leq L_o/d_o \leq 7.5$ (Wang et al., 2014).

A paper based on the content of this chapter has been published in the *International Journal of Multiphase Flow* as Sharif, F., Azimi, A. H., 2020. Particle cloud dynamics in stagnant water. 125, 101–119.

It has also been shown that the effects of particle size on the dynamics of sand jets and particle clouds can be described by the relationship between particle relaxation time, $\tau_p = \rho_s D_{50}^2/18\mu$, and the time scale of the flow, $\tau_f = d_o/u_o$, where u_o is the initial sand velocity at the nozzle, D_{50} is the mean particle size, and μ is the dynamic viscosity of the ambient fluid. The particle relaxation time characterizes the energy transfer between particles and ambient water (Gore and Crowe, 1989). This relationship can be expressed by the Stokes number, $S_t = \tau_p/\tau_f$, and spreading of particle clouds and particle-laden jets were found to be correlated with the Stokes number (Buhler and Papantoniou, 2001; Azimi et al., 2012a; Moghadaripour et al., 2017b). Further, larger particles with $S_t >> 1$ were insensitive to vortex motions and turbulent eddies and can even break the flow eddies and cause smaller jet spreading. Three particle classifications were therefore developed based on the Stokes number by Moghadaripour et al. (2017a): small particle ($0 < S_t \leq 0.1$), medium particle ($0.1 < S_t < 0.33$), and large particle ($0.33 \leq S_t < 1$). In practice, the individual settling of particles with the settling velocity of u_∞ doesn't occur due to wake effects; in order to physically define a boundary between thermal and swarm regimes, a threshold velocity of $1.4u_\infty$ was defined for particle clouds with $S_t > 1$, below which particle clouds behave like a swarm of individual particles (Moghadaripour et al., 2017b). For particle clouds with smaller particles (i.e., $0.10 < S_t < 0.33$) the threshold cloud velocity was found to be $5u_\infty$ (Azimi et al., 2012a).

The cloud number Nc is also important in analyzing particle dynamics and can be defined as a ratio of the settling velocity of individual particles u_∞ to the characteristic circulation velocity u_c within the particle thermal as $Nc = u_\infty/u_c$, where $u_c = B^{1/2}/r_o$ and r_o is the bulk radius of the particle cloud (Rahimipour and Wilkinson, 1992). Moghadaripour et al. (2017b) also showed that in particle clouds, the cloud number simultaneously describes the effects of particle size and aspect ratio as:

$$Nc = \left[\frac{\frac{1}{2}}{\frac{\pi}{4} c_0^{1/2} c_1 \left(\frac{\Delta\rho}{\rho} \right)^{1/2}} \right] \left(\frac{L_o}{d_o} \right)^{-1/2} S_t \tag{2.1}$$

where c_1 is a coefficient to correlate the initial velocity to the nozzle size as $u_o = c_1(gd_o)^{1/2}$. In this study, the constant value in the bracket was 7/8.

In addition, the mean velocity and sand concentration in solid-liquid (sand/slurry) jets and particle clouds are necessary to understand the anatomy of sand jets and particle clouds, as they evolve in the ambient and help explain ambient entrainment and mixing. Variations of sand concentration along the main axis of sand jets with Stoke numbers of 0.42 and 0.7 were found to be similar to single-phase jets (Hall et al., 2010). However, the results obtained on sand jets with no initial water-phase momentum and with different particle sizes (i.e., $S_t = 0.46$, 0.70, 1.46) indicated that particle size significantly changes the mean centerline axial velocity (Azimi et al., 2011). Overall, the centerline velocity of solid-liquid jets decayed with a lower rate in comparison with single-phase water jets (Azimi et al., 2011; 2012b). For slurry jets, with an initial water-phase momentum and a wide range of particle sizes ($0.07 \leq S_t \leq 11.37$), slurry jets with smaller particle sizes decayed at a slightly faster rate (Azimi et al., 2012b). As a result, smaller entrainments were observed for solid-liquid jets and an adverse relationship was found between sand concentration and entrainment capacity.

The particle grouping effects on drag coefficient C_d have likewise been studied by many researchers (Azimi et al., 2012b; Moghadaripour et al., 2017a; Mohammadidinani et al., 2017; Azimi, 2019; Manzouri and Azimi, 2019b). Azimi et al. (2012b) found the shape of sand jet fronts is directly related to the particle Reynolds number R_p, where $R_p = \rho_w u D_{50}/\mu$, ρ_w is water density, and u is particle velocity for slurry jets. They predicted the wake effects of the leading particles by calculating the average drag coefficient C_d using the momentum equation in steady-state conditions. The overall shape and grouping effect of particles reduced the drag coefficient of sand jet fronts by almost 50% for $0.26 \leq S_t \leq 11.37$. Moghadaripour et al. (2017a) found that the computed average drag coefficients of particle clouds were significantly smaller than the individual spherical sand particles of the same size for $R_p > 120$. Recently, the drag reduction of particle clouds in viscous ambient (Azimi, 2019) and in water with a layer of oil (Manzouri and Azimi, 2019b) indicated that drag reductions are significantly correlated with particle size and mass to nozzle aspect ratio. For particle clouds in viscous ambient, the prediction model for non-spherical particles provided a more accurate estimation of drag coefficient.

With regards to ambient entrainment, it is quantified by the entrainment coefficient α_e and defined as a ratio of entrainment velocity to centerline velocity u_m (Morton et al., 1956). For single-phase jets, the entrainment coefficient is constant along the jet axis with a theoretical value of $\alpha_e = 0.13$ (Morton et al., 1956). The entrainment coefficient of a single-phase plume has been found to be almost 50% larger than a single-phase water jet (Papanicolaou and List,

1988). The concept of absolute entrainment coefficient was later introduced to show that solid-liquid jets are more efficient in mixing than single-phase jets based on higher values of absolute entrainment coefficients (Azimi et al., 2012b). For particle clouds, the entrainment coefficient varies with particle size and aspect ratio. However, for particle clouds with small aspect ratios ($L_o/d_o \leq 0.11$), a weak correlation was found between particle size and entrainment coefficient α_e (Bush et al., 2003). In contrast, for particle clouds with relatively larger aspect ratios ($0.8 \leq L_o/d_o \leq 40.1$), particle size played an important role on variations of α_e with time (Moghadaripour et al., 2017); they showed that entrainment linearly decreased with L_o/d_o from $\alpha_e = 0.3$ for $L_o/d_o \approx 0.1$ to around 0.05 for $L_o/d_o \approx 100$.

Chapter 2 is aimed at investigating the effect of nozzle diameter and particle size in the form of aspect ratio and Stokes number on axial and radial sand velocity and concentration inside the particle cloud using a light refractive particle velocimetry technique. Consequently, practical formulations for the prediction of sand velocity and concentration in both axial and transverse directions can be developed based on aspect ratio and Stokes number by implementing the measurements data. The drag coefficient, particle-particle interaction energy transfer and entrainment inside particle clouds can be evaluated with special emphasis on the effects of nozzle diameter and particle size and their effect on the hydrodynamics of the particle clouds. Comparing developed equations with the classical experimental studies with less complexity (i.e., the single-phase jet and particle-laden turbulent jets) and validate them with recent Lagrangian approaches on the evolution of particle clouds in water can address the effects of each controlling parameter on the characteristics of the particle cloud.

The chapter is organized as follows: material and method including the experimental setup and signal processing techniques are described in section 2.2. In section 2.3, experimental results including the study of the evolution of the particle cloud, axial and radial concentration and velocity measurements are presented. Besides, drag coefficient and grouping effect, ambient entrainment, energy transfer and particle-particle interaction are also described in this chapter. Finally, a summary and conclusions of this study are presented in section 2.4.

2.2 Material and Methods

2.2.1 *Experimental setup*

Laboratory experiments were carried out in the Multiphase Research Flow Laboratory (MRFL) at Lakehead University to study the dynamics of particle clouds in stagnant water.

Sand particles were released through circular nozzles with the inner diameters of d_o = 8 mm and 10 mm into a rectangular glass tank of 1.65 m long, 0.85 m wide, and 0.85 m deep. The tank was filled with tap water and the ambient temperature was kept constant over time with a value of 20°C ± 1°C. The schematic of the experimental setup and the adopted coordinate system are shown in Figure 2.1.

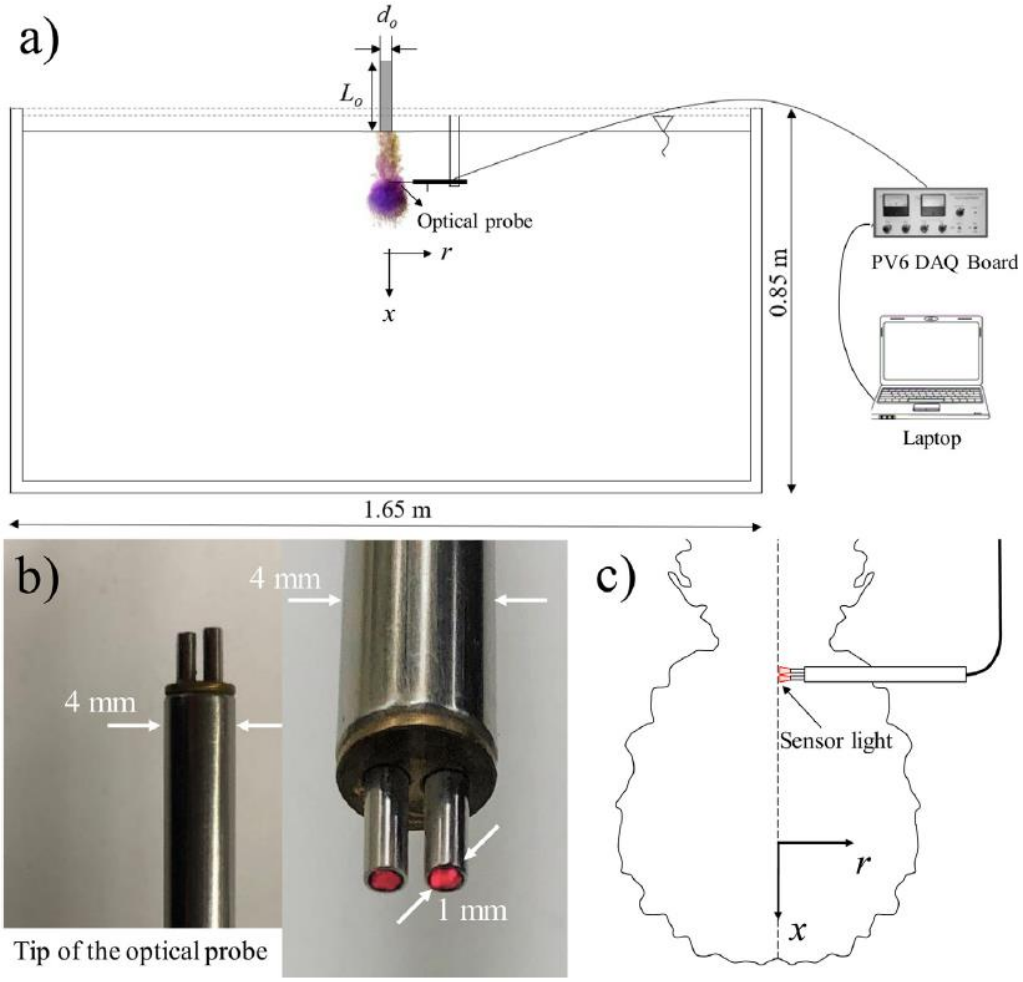

Figure 2.1: Schematics of the experimental setup and coordinate system: (a) experimental tank and position of nozzle; (b) detail images of PV6 probe; (c) position of PV6 probe for measuring at the cloud centerline at $r/d_o = 0$.

The clouds were formed by releasing particles vertically through a circular nozzle and into the water surface. In order to avoid nozzle blockage due to saturation of sand particles with water, a 3 mm distance was kept between the nozzle and the water surface. Different masses of dry sand particles (i.e., m = 6 g, 12 g, 18 g, and 24 g) were selected to form the correlation between sand mass and nozzle diameter with a relatively wide range of aspect ratios of $9.5 \leq L_o/d_o \leq 39.2$. Two particle sizes with a median diameter of D_{50} = 0.507 mm and 0.718 mm with

a density of 2,540 kg/m^3 were implemented to produce the Stokes numbers of S_t = 0.52, 0.66, 0.74, and 0.93. Experimental details and non-dimensional parameters are shown in Table 2.1. Particle size, nozzle dimeter and mass are the controlling parameters in growth and motion of particle clouds in water. The range of parameters was selected to correspond to those seen in nature, consistency and capability of measurements. Values of S_t in this study indicate that all follow the eddy motions (i.e., 0.33< S_t < 1). In addition, when Nc < 1, the sediment cloud is in the thermal regime (Lai., et al 2013).

Table 2.1: Experimental details and parameters of particle clouds in water.

Test No.	D_{50} (mm)	m (g)	d_o (mm)	u_∞ (m/s)	L_o/d_o	Re_p	S_t	Nc
A0	507	6	8	0.075	9.80	37.6	0.52	0.062
A1	507	12	8	0.075	19.6	37.6	0.52	0.066
A2	507	18	8	0.075	29.4	37.6	0.52	0.074
A3	507	24	8	0.075	39.2	37.6	0.52	0.087
A4	718	12	8	0.089	19.6	48	0.74	0.104
A5	718	18	8	0.089	29.4	48	0.74	0.112
A6	718	24	8	0.089	39.2	48	0.74	0.124
B1	507	18	10	0.075	9.50	37.6	0.66	0.058
B2	507	24	10	0.075	12.7	37.6	0.66	0.048
B3	718	24	10	0.089	12.7	48	0.93	0.074

A high-speed camera (Prosilica GT 1910c CCD, Germany) with a speed of 20 frames per second was employed at a perpendicular distance of 1.4 m from the tank to take images of particle clouds and segregation of sand particles. The camera was fitted with either a 90-mm Kowa F 1.8 (Kowa, Japan) or a 18–55 mm AF-Sinkkor, 13.5–5.6 GII (Nikon, Japan) lens. In order to visualize the entrained flow and the motion of particles in water, a dye tracing method was used by implementing Thiamin tracing particles (Jamieson Laboratories, Windsor, Canada). A small quantity of tracing particles was used to ensure that the densities of the water and the solution were similar. An 18-inch-long dimmable LED blacklight (WOWTOU, China) containing nine three-watt bulbs was implemented for flow visualization.

A light-refractive fiber optic probe with a signal amplification and processing unit (PV6) was used to measure instantaneous time-series sand velocities and concentrations (Institute of Processing Engineering, Chinese Academy of Science, China). A high-resolution data acquisition board (National Instrument, Austin, U.S.) was utilized to convert the analog

voltage signals from a PV6 processing unit to digital signals. The fiber optic probe and the signal processing (PV6) unit have been successfully used in other fluidized bed studies (Liu et al., 2003a, 2003b), sand/slurry jets (Hall et al., 2010; Azimi et al., 2015) and can be used in viscoplastic sand mixtures (Azimi, 2015; 2016; 2017). The probe tip had a diameter of 4 mm and contained two light sources and two light-refracting optical sensors with a diameter of 1 mm each. The two-fiber optics were set 2.14 mm apart and they received the emitted light from the two light sources in the sensor tip (see Figure 2.1). The optical probe measures the light-refractive signals from sand particles in a 3 mm distance from the tip of the probe and it was positioned perpendicular to the main flow direction in order to detect correct voltage signals. As sand particles passed through the tip of the sensors, two voltage signals with a time lag were generated as a result of light refraction by the sand particles. The time-series voltage signals were generated with a time shift due to the time required for particles to pass through the two optical sensors. Both sand concentration and velocity were measured for half of the particle cloud assuming complete symmetry. To minimize the intrusive impact of the probe on concentration and velocity measurements, probe measurements commenced from the edge of the cloud and progressed towards the centerline (see Figure 2.1c).

The larger the number of sand particles refracting light from the light sources, the higher the voltage generated by the optical sensors. Therefore, the time-averaged voltage signals from each probe was proportional to the sand concentration passing by the tip of the probes. Time-averaged voltage can be converted to sand concentration using a calibration curve. The time delay between the time-series voltage signals from each sensor were therefore calculated using a signal cross-correlation technique. The signal processing was implemented by the MATLAB signal processing toolbox (The MathWorks Inc., Natick, U.S.). The full MATLAB® m-file code and an example is included in Appendix 2 and 3. The instantaneous velocity data was calculated by dividing the constant distance between the two probes Δx (i.e., 2.14 mm) by the time lag between the two signals Δt. The time lag between the two voltage signals was then calculated at each instant by implementing the cross-correlation technique. The optical probe was placed at different locations along the axis of particle clouds (x-axis) and in different transverse directions (r-axis). Velocity and concentration measurements were taken for different cross-sections ranging from $x/d_o = 10$ to 40 and for different radial directions of $-5 < r/d_o < 5$. For $x/d_o > 40$ and $r/d_o > 5$, voltage signals were less reliable due to an insufficient number of sand particles which resulted in insufficient signal strength.

2.2.2 *Signal processing*

The quality of voltage signals was improved by reducing signal noises and overshooting spikes using the wavelet transform toolbox in the MATLAB software package (The MathWorks Inc., Natick, U.S.). Wavelet transformation leads to a sparse representation of many time-series signals by transforming the concentrated signal features into a few large-magnitude wavelet coefficients. Small wavelet coefficients are considered noise and they are removed without affecting the signal quality (Weeks, 2010) and this noise removal technique has been successfully employed in turbulent wall jets (Shojaeizadeh et al., 2018). In order to attain high quality velocity data, a voltage sampling rate of 61,440 Hz was selected. The sampling time of experiments ranged between 1.5 seconds and 4 seconds resulting in the voltage data ranging from 92,160 to 245,760 data points. Figure 2.2 shows the time series for voltage signals of particle clouds for one optical sensor at $x/d_o = 5$ and for $L_o/d_o = 19.6$, 29.4, and 39.2. As can be seen, the high-strength voltage signals are attributed to high concentration indicating that the optical probe can clearly detect the beginning and the end of particle clouds. Similar voltage signals with different time lags were recorded by the second sensor and used to calculate instantaneous velocity data.

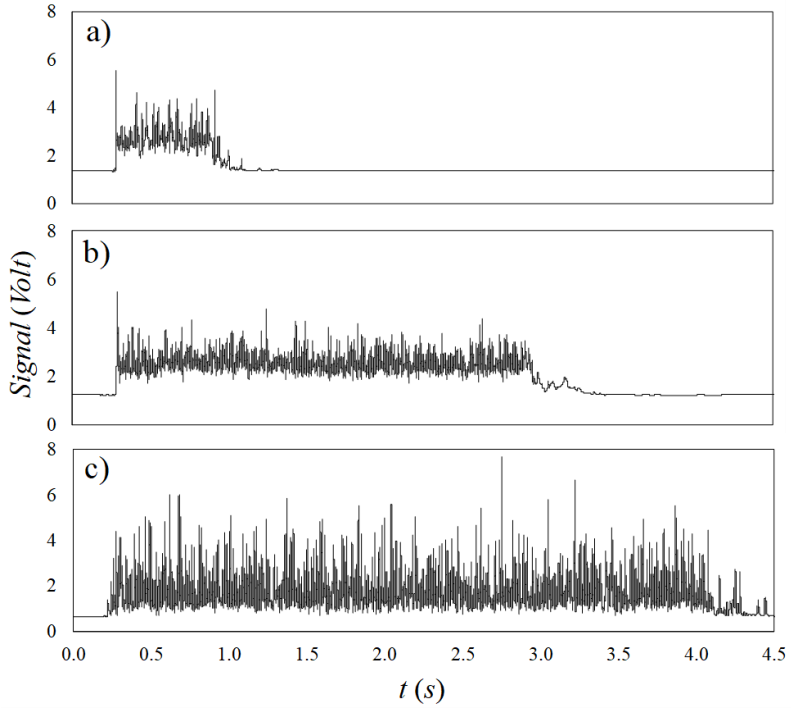

Figure 2.2: Time series of voltage signals detected by the optical probe at $x/d_o = 5$ and for different aspect ratios; a) $L_o/d_o = 19.6$, b) $L_o/d_o = 29.4$, c) $L_o/d_o = 39.2$.

The frequency of time-series velocity data is determined by selecting a segment of voltage signals. In order to employ signal cross-correlations, the segment length should be 2^n where n is a positive number. A frequency of 30 Hz for time-series velocity data can be obtained by selecting a segment size of $L_s = 2^{11} = 2{,}048$ (i.e., 30 x $2^{11} = 61{,}440$). Higher frequencies for velocity can be attained by reducing the segment lengths to $2^9 = 512$ and $2^{10} = 1024$. It should be noted that the cross-correlation of voltage signals with small segment lengths increases the probability of over/undershoots and reduces the quality of turbulent velocity data. To investigate the effect of segment length on the accuracy and consistency of velocity data, voltage signal time series were divided into different segment lengths containing 512, 1,024, and 2,048 data points. The sampling frequency of velocity data increased by reducing the segment lengths from 30 Hz for $L_s = 2{,}048$ to 60 Hz and 120 Hz for $L_s = 1{,}024$ and 512. Figure 2.3a shows the effect of segment length on the instantaneous sand velocity data with a constant overlapping of ΔL_s = 50%. The time-averaged sand velocity for this test was 0.5 m/s and reducing the segment length from 2,048 to 512 increased the cross-correlated mean velocity by 9%. The turbulent intensity for 2,048 data in each segment was 20.5% and it also increased to 24.4% when segment length was reduced to 512 data points.

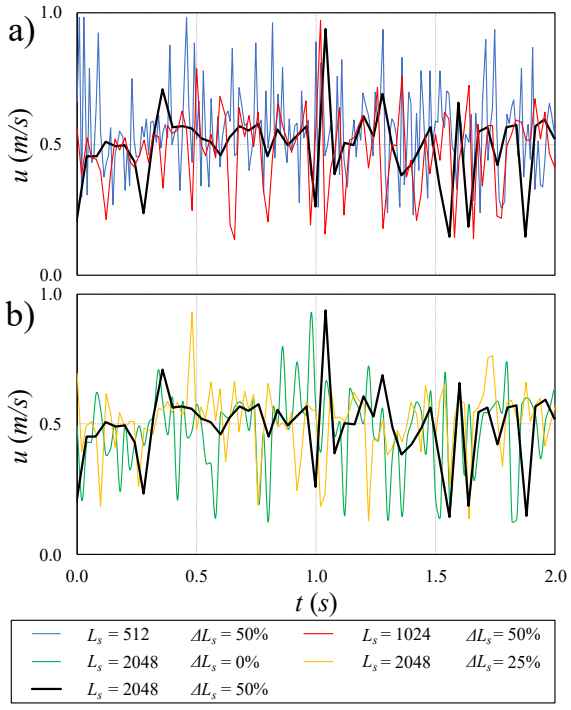

Figure 2.3: Typical instantaneous sand velocity data extracted from voltage signals using different segment lengths L_s and segment overlapping ΔL_s for Test A3, $S_t = 0.52$ and $L_o/d_o = 39.2$ at $x/d_o = 6.25$; a) effect of segment length (L_s = 512, 1024, and 2048) on instantaneous

sand velocity; b) effect of segment overlapping ($\Delta L_s = 0$, 25%, and 50%) on instantaneous sand velocity.

Lastly, raw signal segment overlapping has been successfully employed in the past to achieve a smooth transition between each of the two segments and to stabilize cross-correlated data (Willer and Gharib, 1991; Adrian, 1986a; Azimi et al., 2012a). In segment overlapping, a percentage of previously processed signals is used in cross-correlation to the next signal segment. In order to investigate the effect of signal overlapping on velocity data, voltage signals with a segment length L_s in 2,048 voltage data points were overlapped by $\Delta L_s = 10\%$, 25%, and 50%. Figure. 2.3 shows the typical time-series of centerline sand velocity data obtained from cross-correlation of voltage signals for $S_t = 0.52$, $L_o/d_o = 39.2$, and $x/d_o = 6.25$. Figure. 2.3b shows the effect of segment overlapping on the instantaneous centerline velocity for the same test and the same position (i.e., $x/d_o = 6.25$). It was found that the data uncertainty for overlapping average velocities was ±3% corresponding to ±15 mm/s. Furthermore, the data uncertainty for turbulence intensity of segment overlapping was ±13% and a turbulent intensity of 20.5% was achieved when 50% segment overlapping was used. According to the results of signal analysis and suitability of a sampling rate of 30 Hz for this study, a segment length of L_s = 2,048 with 50% overlapping was selected for all data.

2.3 Results and Discussion

2.3.1 *Evolution of particle clouds*

Figure 2.4 shows images of both solid and fluid phases of particle clouds and the effect of flow entrainment on the growth rate of particle clouds for $L_o/d_o = 9.8$ and $S_t = 0.52$. A non-dimensional time scale t^* was used, where for t^*=1 all particles were in water (Moghadaripour et al., 2017b; Manzouri and Azimi, 2019b). Figure 2.4a shows a particle cloud in the initial (i.e., Ballistic) phase as the flow entrainment is just established. As can be seen, both particles and the entrained fluid are mixed and phase separation has not started. Figure 2.4b and 2.4c show particle clouds in the thermal regime. As can be seen, sand particles are still in the cloud and ambient fluid entrains as the cloud descends like a coherent mass. A buoyant frontal head and shear layer lobes around the boundary of the tail are due to the relatively large density difference and they are evident in this regime. Figure 2.4d shows the onset of phase separation where the particle cloud separates from the water-phase thermal due to density difference and reduced ambient entrainment of the solid phase. Figure 2.4f shows the onset of the swarm regime occurring at $t^* = 3.4$ for this test with $L_o/d_o = 9.8$ and $S_t = 0.52$. The two phases separated

when the fluid velocity decreased due to ambient entrainment and the particle cloud moved faster due to wake effects between particles and the buoyancy caused by the density difference. After phase separation, the swarm of particles descended at a rate approximately 1.3 times that of the settling velocity of the individual particles (Moghadaripour et al., 2017 b) while the entrained fluid phase descended as a single-phase puff. Figure 2.4 clearly shows the variations of the widths of both phases in different stages of evolution. The widths of both phases were approximately the same as in the initial and thermal regimes. However, in swarm regime (see Figure. 2.4f), the cloud width in the water phase continuously increased while the solid-phase cloud width became constant.

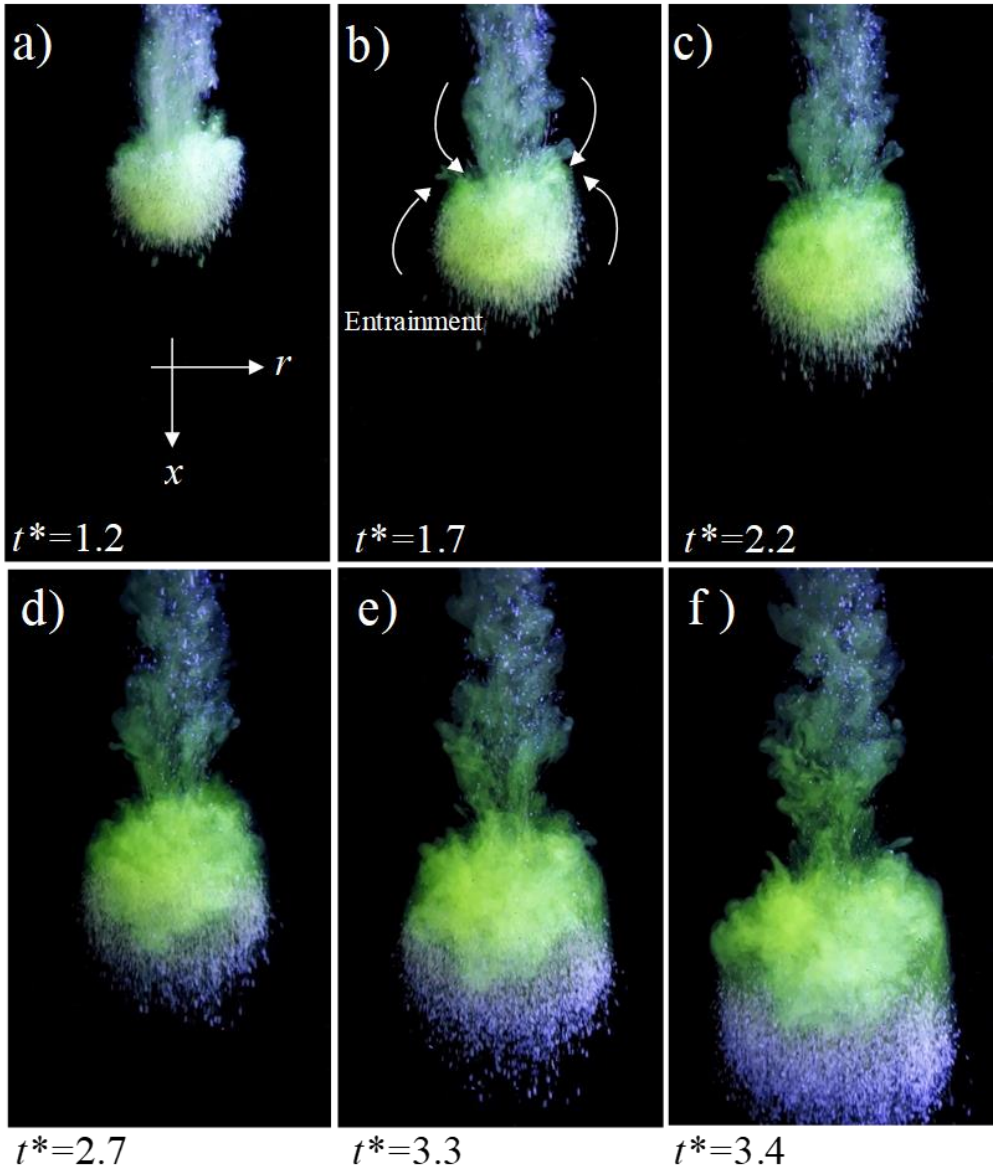

Figure 2.4: Evolution of particle cloud and segregation of sand particles for $S_t = 0.52$ and $L_o/d_o = 9.8$; a) $t^* = 1.2$, b) $t^* = 1.7$, c) $t^* = 2.2$, d) $t^* = 2.7$, e) $t^* = 3.3$, f) $t^* = 3.4$.

We also show that integral quantities, such as sand mass and momentum fluxes in different cross-sections, can be used as an indicator to evaluate the operational range of the optical probe. These integral quantities can also be used to validate the accuracy of calibration curves and the cross-correlation method for converting voltage signals to sand concentrations and time-averaged sand velocities. Sand mass flux in each cross-section can be calculated by integrating the product of sand concentration and velocity over each cross-section as:

$$\dot{m} = \frac{dm}{dt} = 2\pi\rho_s \int_0^r cu\, r dr \tag{2.2}$$

The sand momentum flux was therefore calculated in each cross-section by integrating the product of sand concentration and velocity as:

$$\dot{M} = \frac{dM}{dt} = 2\pi\rho_s \int_0^r cu^2 r dr \tag{2.3}$$

Figure 2.5 shows the variations of the defined integral quantities along the main axis of particle clouds to evaluate the performance and operational range of the optical probe. The ratio of the integrated to the initial sand mass flux at the nozzle $\dot{m}_o = \rho_s(\pi d_o^2/4)u_o c_o$ was calculated in each cross-section and variations were plotted with x/d_o in Figure 2.5a. Theoretically, sand mass flux should be preserved in the axial direction as particle clouds descend. However, due to the limitation of the optical probe to detect very low sand concentrations far from the cloud centerline, the calculated mass flux based on probe measurements decreased with distance from the nozzle. As can be seen in Figure 2.5a, the integrated sand mass flux was above 90% of the initial sand mass flux for $x/d_o < 5$ and the optical probe captured more than 75% of the initial sand mass flux at $x/d_o = 40$ by measuring sand concentration and velocity within $-5 \leq r/d_o \leq 5$. Figure 2.5a also shows the variation of normalized sand mass flux calculated by proposed formulations for sand concentration and velocity in transverse direction for $-5 \leq r/d_o \leq 5$. As can be seen, sand mass flux is preserved up to $x/d_o = 15$ and decreased to 75% of the initial sand mass flux at $x/d_o = 40$.

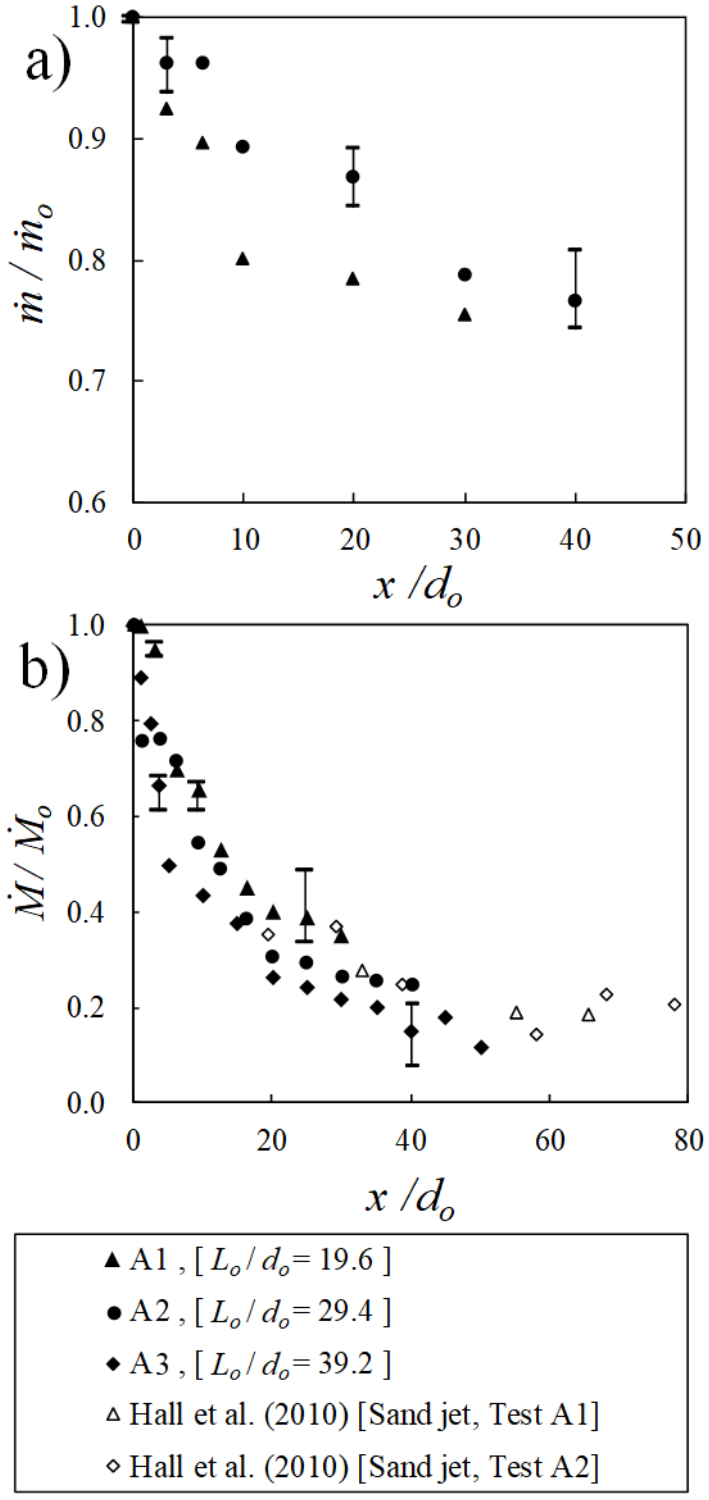

Figure 2.5: a) Variations of the normalized sand mass flux detected by the optical probe along the normalized axial direction for S_t = 0.52, b) Variations of the normalized momentum flux detected by the optical probe along the normalized axial direction for S_t = 0.52.{A1, A2, A3}

It has been shown that as particle clouds descend further, sand concentration over the entire volume and especially at the edges, decreases due to ambient flow entrainment. Therefore, signal strength reduces at the edges of the cloud and the probe is not able to

accurately measure sand concentration. In addition, due to turbulent entrainment and formation of turbulent eddies in the shear layer between particle cloud and ambient fluid, the reliability of signal cross-correlation decreases with an insufficient number of sand particles and significant particle scattering which contaminates voltage signals (Azimi et al., 2015). In this present study, high-quality voltage signals were obtained from the centerline up to $r/d_o = 5$.

The momentum flux in sand jets (i.e., $L_o/d_o \approx \infty$) also decreases with distance from the nozzle (Hall et al., 2010; Azimi et al. 2012b). Figure 2.5b shows the variations of sand momentum flux with x/d_o for particle clouds with L_o/d_o = 19.6, 29.4, and 39.6. The sand momentum flux was normalized with the initial momentum flux at the nozzle $\dot{M}_o = \rho_s(\pi d_o^2/4)u_o^2 c_o$. The sand momentum fluxes were calculated based on sand velocity and concentration was measured with a similar probe for sand jets with a sand particle diameter of D_{50} = 0.206 mm that were added for comparison (Hall et al., 2010). As can be seen, sand momentum flux continuously decreased from the nozzle ($x/d_o = 0$) to x/d_o = 40 and became constant for $x/d_o > 40$ indicating the formation of a swarm regime where the cloud width and settling velocity are approximately independent of distance from the nozzle. At this stage, the buoyancy force of sand particles becomes comparable with the total drag force acting on sand particles.

2.3.2 *Sand concentration*

The effects of aspect ratio and particle size on variations of sand concentration with distance are described in this section. Variations of centerline concentration in single-phase buoyant jets (i.e., sodium-chloride-water solution) and sand jets (i.e., $L_o/d_o \approx \infty$) indicated that the centerline concentration decreases non-linearly with distance from the nozzle. The centerline concentration c_m was normalized with the initial sand concentration c_o, and the distance from the nozzle x was normalized with the nozzle diameter d_o. Figure 2.6 shows the correlation between the normalized sand concentration c_m/c_o and x/d_o for $19.6 \leq L_o/d_o \leq 39.6$ and for large particle sizes (i.e., $0.33 \leq S_t \leq 1$) in a log-log scale. The overbars in sand concentration data indicate the uncertainty of concentration measurements in this study. The zone of jet development (i.e., $c_m/c_o \approx 1$) is six times the nozzle diameter size for single-phase jets (Rajaratnam, 1976) and between $5.42d_o$ and $6d_o$ for sand jets (Hall et al., 2010). The zone of jet development decreased between $2d_o$ and $4d_o$ in gravity-driven particle clouds due to smaller initial momentum.

As can be seen from Figure 2.6, the centerline concentration in particle clouds decreased with a slower rate in comparison with single-phase buoyant and sand jets. Figure 2.6a shows the correlations of the normalized centerline concentration with x/d_o for $S_t = 0.52$ and different aspect ratios. As shown, the decay rate in centerline concentration for $L_o/d_o = 19.6$ and 29.4 were slower than sand jets. However, for the higher aspect ratio of $L_o/d_o = 39.2$, the decay rate of sand concentration in particle clouds became similar to sand jets for $5 \leq x/d_o \leq 25$. For $x/d_o > 25$, the effect of high-aspect ratio diminished, and the decay rate became similar to particle clouds with small aspect ratios (see Figure 2.6a). The constant centerline concentration in large x/d_o indicated that particle clouds were in swarm regime. For particle clouds with medium particle size, constant concentration occurred at $x/d_o \approx 20$. According to a regime classification based on buoyancy B, the onset of swarm regime occurs at $x/d_o = 14$, indicating that the optical probe successfully detected the small variations of sand concentration along the jet axis in thermal regime and showed nearly constant concentration once particle clouds entered the swarm regime. Figure 2.6b shows the variations of normalized sand concentration with x/d_o for $S_t = 0.74$. It was found that sand concentrations decayed at a slower rate than the decay rate of sand jets. The region of constant centerline concentration for $L_o/d_o = 19.6$ and 39.2 occurred at $x/d_o = 37.5$ and 43.75. The effect of particle size on variations of sand centerline concentration with x/d_o for $L_o/d_o = 12.7$ and different Stokes numbers of 0.66 and 0.93 are shown in Figure 6c. For relatively low aspect ratios, the region of jet development reduces to two times that of nozzle diameter. As can be seen, particle size has a minor effect on the decay rate of sand concentration and the decay rate was higher in particle clouds with smaller aspect ratios.

The aspect ratio L_o/d_o can be increased either by increasing the mass of sand particles m or by reducing the nozzle diameter d_o. Increasing sand mass results in an increase in buoyancy as $B = mg/\rho_s$ and the excess buoyancy force increases the momentum and consequently the frontal velocity of particle clouds. Therefore, higher depth progression of particle clouds can be expected for tests with higher L_o/d_o and higher Stokes numbers as observed by Moghadaripour et al. (2017b). In other words, the higher buoyancy reduces the cloud expansion rate and the swarm regime occurs at higher x/d_o. Furthermore, particle clouds with lower aspect ratios tend to follow eddies and the motion of particles in the cloud is entrained by the fluid phase which results in a constant decay rate.

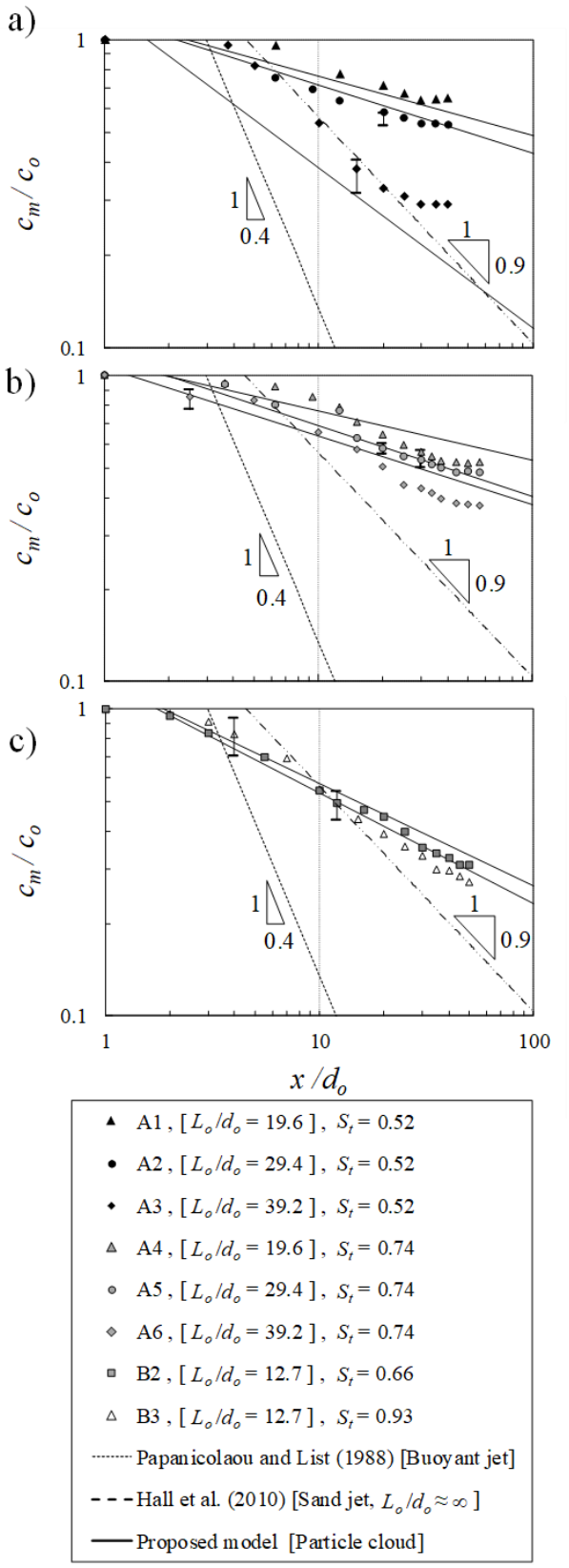

Figure 2.6: Effects of aspect ratio L_o/d_o and particle size on the normalized sand concentration c_m/c_o along the normalized axial direction; a) S_t = 0.52, d_o = 8 mm, b) S_t = 0.74, d_o = 8 mm, c) S_t = 0.66 and 0.93, d_o = 10 mm.

Semi-empirical formulations were also proposed in order to predict the motion of particle clouds in water and estimate sand concentration and velocity at different points in the ambient. A power law correlation was developed for prediction of centerline sand concentration along the cloud axis as:

$$\frac{c_m}{c_o} = a\left(\frac{x}{d_o}\right)^{-b} \tag{2.4}$$

where a and b were found to be non-linear functions of the aspect ratio as:

$$a,b = A\left(\frac{L_o}{d_o}\right)^2 + B\left(\frac{L_o}{d_o}\right) + C \tag{2.5}$$

The coefficients of *A*, *B*, and *C* for different sand particle sizes are listed in Table 2.2 The proposed formula for prediction of sand concentration is applicable for large particle sizes (i.e., $0.33 \leq S_t \leq 1$) and aspect ratios in the range of $19.6 \leq L_o/d_o \leq 39.6$. Solid curves in Figure 2.6 show the predictions of the normalized sand centerline concentration along the normalized axis with a maximum prediction uncertainty of 5.4% and 6.3% for S_t = 0.52 and 0.74 respectively. Refering to the variability in prediction due to plausible alternative input values.

Table 2.2: Coefficients of the proposed empirical correlations for predictions of the axial sand concentration *c* and the axial velocity *u* of particle clouds.

S_t			A	B	C	R^2
c	0.52	*a*	0.0004	-0.0191	1.4059	0.87
		b	-0.0014	0.0656	-0.9396	
	0.74	*a*	0.0001	-0.0111	1.3778	0.88
		b	-0.0007	0.0415	-0.7757	
u	0.52	*a*	-0.0004	0.0214	1.0216	0.92
		b	0.0007	-0.0430	0.2750	
	0.74	*a*	-0.0018	0.1027	-0.0191	0.86
		b	0.0008	-0.0509	0.4560	

Variations of sand concentration in transverse direction were measured in four sections. Figure 2.7 shows the transverse profiles of normalized sand concentration c/c_m for large particle sizes (i.e., $0.33 \leq S_t \leq 1$) and $L_o/d_o = 39.2$. Because sand concentrations were above $0.5c_m$, it was not possible to use $0.5c_m$ as a classic length scale and the radial distance from the nozzle r was normalized with nozzle diameter d_o. As can be seen in Figure 2.7, a Gaussian distribution describes the radial variations of sand concentration. Figure 2.7a shows the radial concentration profile for $S_t = 0.52$ and the results indicate that particle clouds with smaller particle sizes spread more than particle clouds with larger particle sizes. Relatively low superficial velocity between the ambient water and particles in the clouds provides enough time for particles to follow water eddies which caused particle dispersion from the centerline (Azimi et al., 2012a).

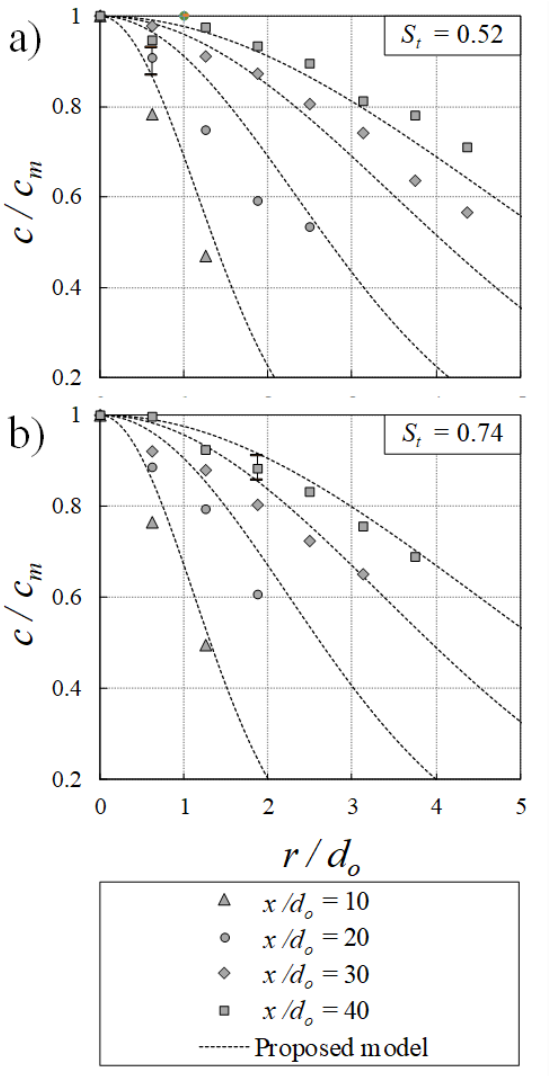

Figure 2.7: Effect of particle size on radial variations of normalized sand concentration c/cm with different normalized distances from the nozzle x/d_o; a) $L_o/d_o = 39.2$, $S_t = 0.52$, b) $L_o/d_o = 39.2$, $S_t = 0.74$.

Using the Gaussian distribution model, radial variations of sand concentration in particle clouds is formulated as:

$$\frac{c}{c_m} = \exp\left[-0.693\psi\left(\frac{r}{d_o}\right)^2\right] \tag{2.6}$$

The coefficient of determination R^2 of Eq. (2.6) is 0.90 indicating the accuracy of our data and the suitability of the selected distribution model for sand concentration. The parameter ψ was found to be correlated with x/d_o and S_t as:

$$\psi = 62\left(\frac{x}{d_o}\right)^{-2} S_t^{1/5} \tag{2.7}$$

The dotted curves in Figure 2.7 show the performance of the proposed model for the prediction of sand concentration in the radial direction.

2.3.3 *Sand velocity*

Effects of particle size and aspect ratio on variations of the sand centerline velocity in particle clouds along with x/d_o were plotted in log-log scale (Figure 2.8). The centerline sand velocity u_m was normalized with the initial velocity of particles at the nozzle u_o. The prediction curves for sand centerline velocity of sand jets (i.e., $L_o/d_o \approx \infty$) and with a small particle size range of $0 < S_t \leq 0.1$ and centerline velocity of water in single-phase turbulent jets were included for comparison. The maximum uncertainty for sand centerline velocity for $S_t = 0.52$ and 0.74 were 3.6% and 5.5% respectively. To investigate the effect of particle size on the centerline sand velocity, data points for $S_t = 0.52$ and 0.74 were added as shown in Figure 2.8a and 2.8b respectively. The sand centerline velocities decreased with increasing L_o/d_o for both sand sizes. Sand particles in clouds with small particle sizes (i.e., S_t = 0.52) mixed well with the surrounding water, and as a result, sand velocity decayed with a faster rate. Recent observations on sand and slurry jets indicate that the grouping effect in particle clouds becomes less significant for $0.33 \leq S_t < 1$. Therefore, particles tend to fall downward and reach cloud-settling velocity at a relatively short distance from the nozzle in comparison with particle clouds with small particle sizes (Azimi et al., 2012a, 2012b). The effect of particle size in velocity decay also becomes more pronounced for $L_o/d_o \geq 5.8$ (Moghadaripour et al., 2017b).

Therefore, an empirical formula was developed to predict the sand centerline velocity in the initial and thermal phases with a coefficient of determination of $R^2 = 0.88$ as:

$$\frac{u_m}{u_o} = a\left(\frac{x}{d_o}\right)^{-b}$$

(2.8)

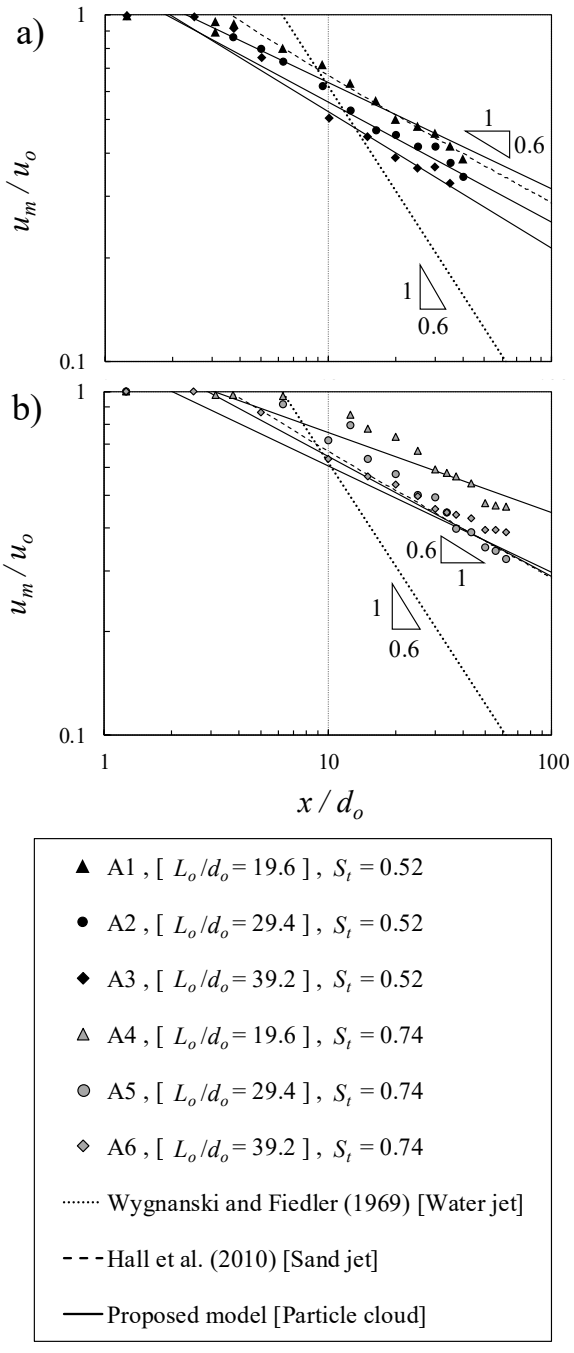

Figure 2.8: Effect of L_o/d_o on variations of the normalized velocity u_m/u_o along the normalized axial distance from the nozzle x/d_o; a) $S_t = 0.52$, b) $S_t = 0.74$.

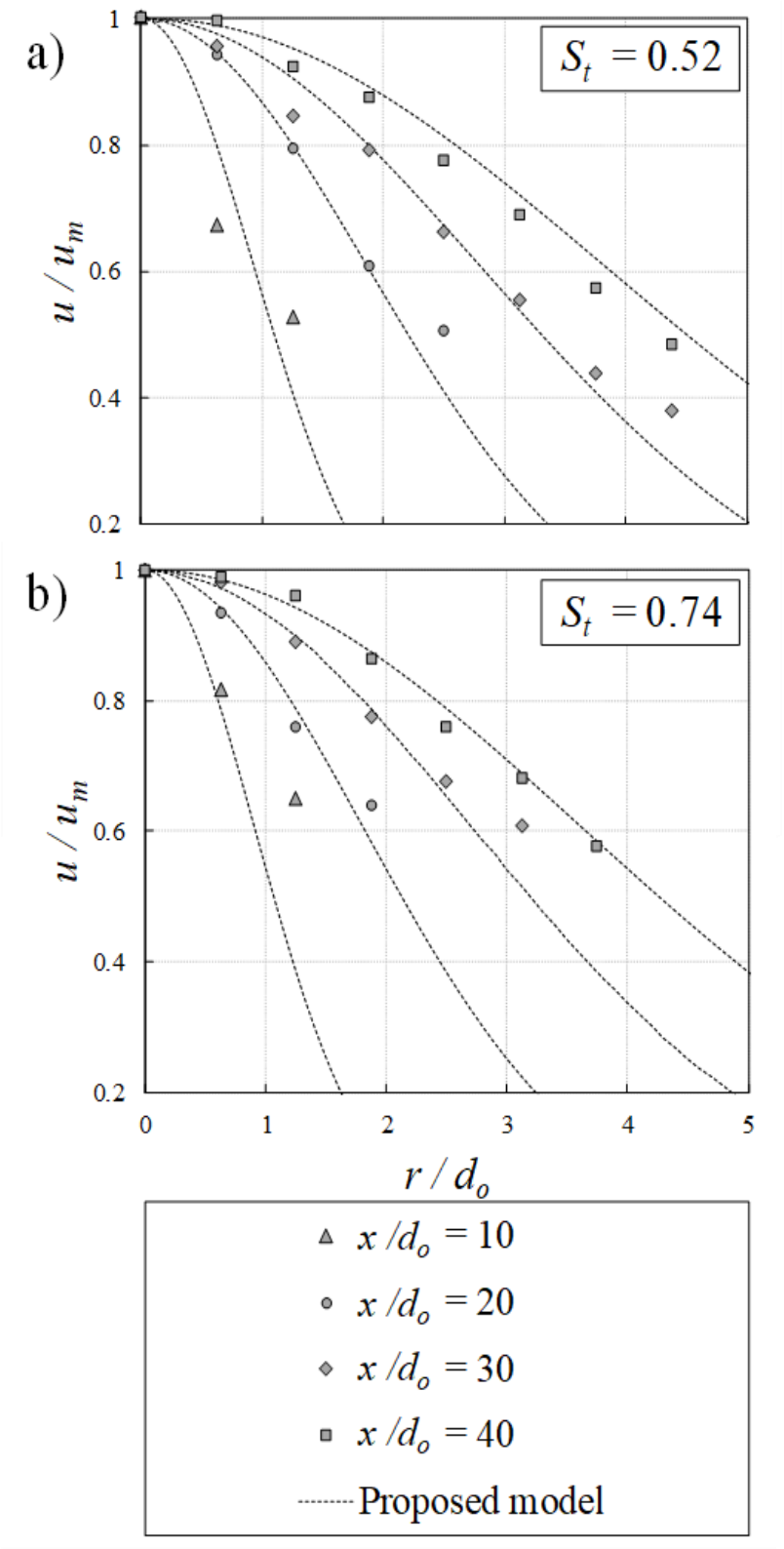

Figure 2.9: Variations of the normalized sand velocity u/u_m in transverse direction and for different normalized distances from the nozzle x/d_o for $L_o/d_o = 39.2$; a) $S_t = 0.52$, b) $S_t = 0.74$.

The variations of sand axial velocity in radial direction for particle clouds with different Stokes numbers are shown in Figure 2.9. The axial velocity u was normalized with the centerline velocity u_m and the radial distance from the centerline r was normalized with the nozzle diameter d_o.

Similar to sand concentration, a Gaussian model was selected to predict the radial variations of the sand axial velocity for $10 \leq x/d_o \leq 40$ with a coefficient of determination of $R^2 = 0.91$ as:

$$\frac{u}{u_m} = \exp\left[-0.693\xi\left(\frac{r}{d_o}\right)^2\right] \tag{2.9}$$

It was found that ξ has a power-law correlation with x/d_o and S_t that can be described as:

$$\xi = 96\left(\frac{x}{d_o}\right)^{-2} S_t^{1/5} \tag{2.10}$$

The proposed formula for prediction of sand velocity is applicable for large particle sizes (i.e., $0.33 \leq S_t \leq 1$) and aspect ratios in the range of $19.6 \leq L_o/d_o \leq 39.6$.

2.3.4 *Drag coefficient*

In order to evaluate the mixing performance of particle clouds and to predict the motion of particle clouds in water, force imbalance was written in momentum equation and a drag coefficient was calculated. The drag coefficient in particle clouds is correlated with particle size and shape, level of turbulence, particle-particle interactions, and ambient flow characteristics (Crowe et al., 1998). The effect of wake formation behind particle clouds in sand jet front was quantified by calculating the averaged drag coefficient C_d of a group of particles in steady-state condition (Azimi et al., 2012b). And, using average frontal velocity, Moghadaripour et al. (2017b) calculated C_d for gravity-driven particle clouds for a wide range of aspect ratios. The buoyancy force of particles F_B can also be calculated for each set of experiments and remains constant during the evolution of particles for $t^* > 1$ (Moghadaripour et al., 2017a). Thus, the average drag force F_D can be computed by balancing the rate of change

of momentum flux $M(x)$ with the gravitational F_g and buoyancy F_B forces on a disc-shaped control volume (see Figure 2.10b) as:

$$M(x+\Delta x)-M(x)=F_g\left(x+\frac{\Delta x}{2}\right)-F_B\left(x+\frac{\Delta x}{2}\right)-F_D\left(x+\frac{\Delta x}{2}\right)$$

(2.11)

The momentum flux of sand particles $M(x)$ at each cross-section can be calculated by integrating the product of sand concentration and velocity in radial direction as:

$$M(x)=2\pi\rho_s\int_0^{r(x)}c(x)u(x)^2r(x)dr$$

(2.12)

The balance between the gravitational and buoyancy forces at $(x + \Delta x/2)$ can be calculated as:

$$\pi(\rho_s-\rho_w)g\Delta x\left(\int_0^{r(x)}c(x)r(x)dr+\int_0^{r(x+\Delta x)}c(x+\Delta x)r(x+\Delta x)dr\right)=\sum F$$

(2.13)

The drag force on individual sand particles f_D can then be calculated by dividing the total drag force $F_D(x+\Delta x/2)$ obtained from momentum equation (Eq. (2.11)) by the total number of particles in the disc-shape control volume N_p as:

$$f_D=\frac{F_D}{N_P}=\left(\frac{\pi D_{50}^3}{6c_{ave}V_{disc}}\right)F_D$$

(2.14)

where $c_{ave}V_{disc}$ can be calculated in each adjacent section as:

$$c_{ave}V_{disc}=\frac{\pi}{2}\left(c(x)+c(x+\Delta x)\right)\left(\int_0^{r(x)}r(x)dr+\int_0^{r(x+\Delta x)}r(x+\Delta x)dr\right)\Delta x$$

(2.15)

Using the classical formulation for drag force (i.e., $f_D = 0.5C_d\rho_sA_P[(u(x)+u(x+\Delta x))/2]^2$) where A_p is the projected area of individual sand particles $A_p = N_p(\pi D_{50}^2/4)$, the average drag coefficient of sand particles over a small volume of $(\sim\Delta x(\Delta r)^2)$ can be calculated for particle clouds with different aspect ratios and sand sizes.

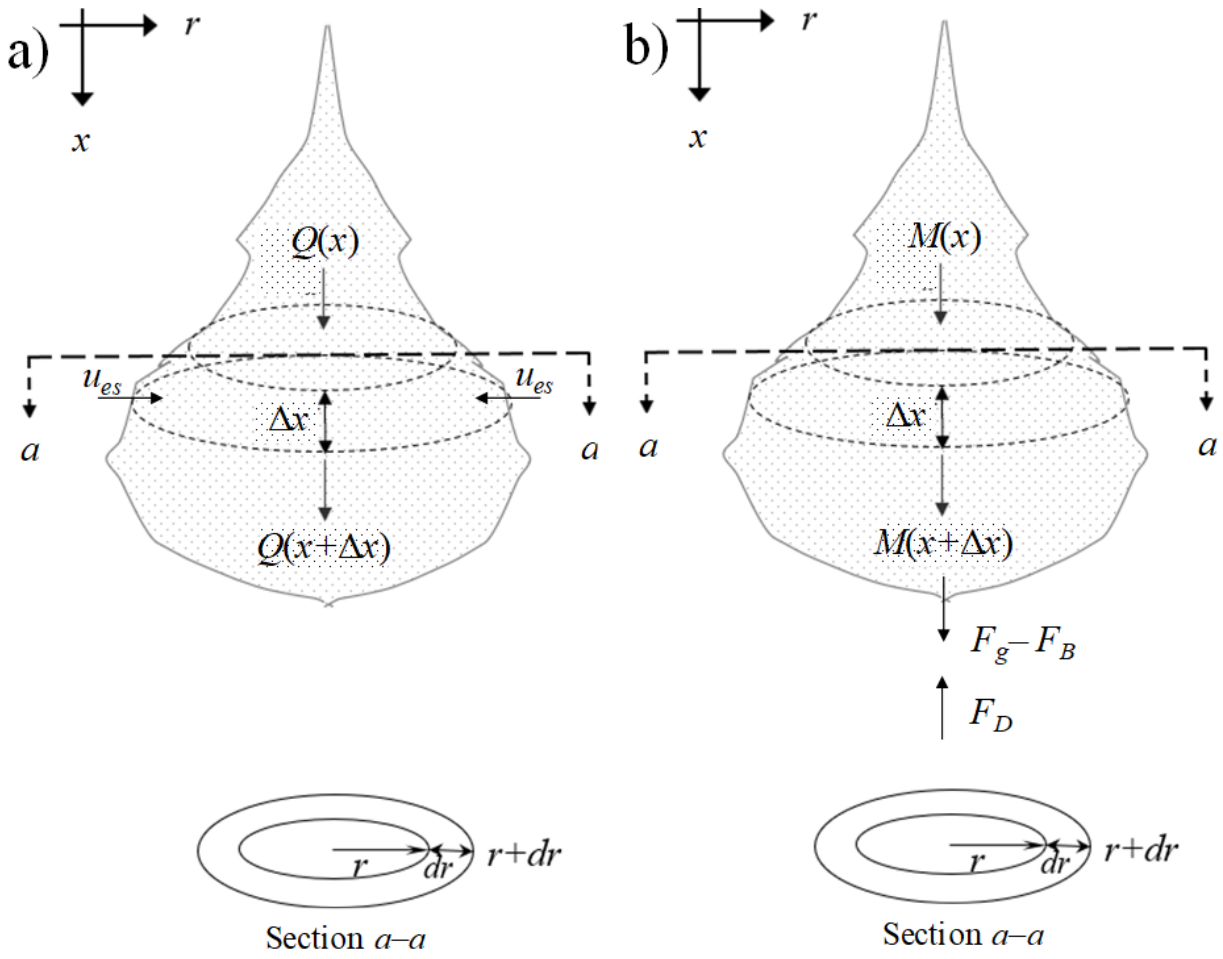

Figure 2.10: Schematic of particle cloud and the ambient flow; a) momentum balance, b) flow entrainment inside a particle cloud.

Figure 2.11 shows the effects of aspect ratio and particle size on variations of the average drag coefficient of sand particles C_d in normalized radial direction r/d_o for $S_t = 0.52$ and 0.74. The uncertainty in the estimation of drag coefficients that carried over from the uncertainty of sand concentration and velocity measurements were also added as overbars in Figure 2.11. As illustrated, the drag coefficients were increased in the radial direction from a value of less than 0.1 in the centerline to slightly above 0.4 at $r/d_o = 4$. This indicates that the grouping effect in the cloud centerline reduced the drag coefficient by four times. Figure 2.11a shows the effects of aspect ratio on variations of the drag coefficient for $S_t = 0.52$. It was found that C_d is almost independent of the axial distance for relatively high aspect ratios, whereas for $L_o/d_o = 19.6$, the drag coefficient increased as the particle cloud descended. The variations of C_d with r/d_o for larger particle sizes are shown in Figure 2.11b where the averaged drag coefficient C_d decreased as particle size increased. This indicates that large particles generate stronger wakes behind them and that consequently, and with similar rates of momentum change, particles move faster due to drag reduction. Similar phenomena have been previously

reported on the effect of particle size on the axial velocity of sand jets (Azimi et al., 2011). Variations of the average drag coefficient with particle Reynolds number Re_p for S_t = 0.52 and 0.74 are shown in Figure 2.12.

Proposed formulations of drag coefficients for a sphere with a diameter of D_{50} (Wörner, 2003) and of individual sand particles (Chien, 1994) are also added in Figure 2.12 by including the effect of sphericity of particles for low Reynolds numbers (R_p < 5000). The sphericity of a particle is a ratio of the surface of a sphere having the same volume as the particle and the actual surface area of the particle. The drag coefficient of individual sand particles with a sphericity ratio in the range of $0.2 \leq \varphi \leq 1$ is expressed as (Chien, 1994):

$$C_d = \frac{30}{R_p} + 67.3\exp(-5\varphi) \tag{2.16}$$

As can be seen in Figure 2.12, the average drag coefficients in particle clouds were smaller than the individual sand particles due to grouping effect and wake formation behind individual sand particles. A formula describing the correlation between the average drag coefficient and particle Reynolds number was developed for particle cloud using curve fitting as:

$$C_d = \psi_d S_t \, e^{(-0.008 R_p)} \tag{2.17}$$

where the values of ψ_d for S_t = 0.52 and 0.74 are 1.35 and 2.75 respectively. The coefficient of determination R^2 of Eq. (2.17) for S_t = 0.52 and 0.74 were 0.95 and 0.98 respectively.

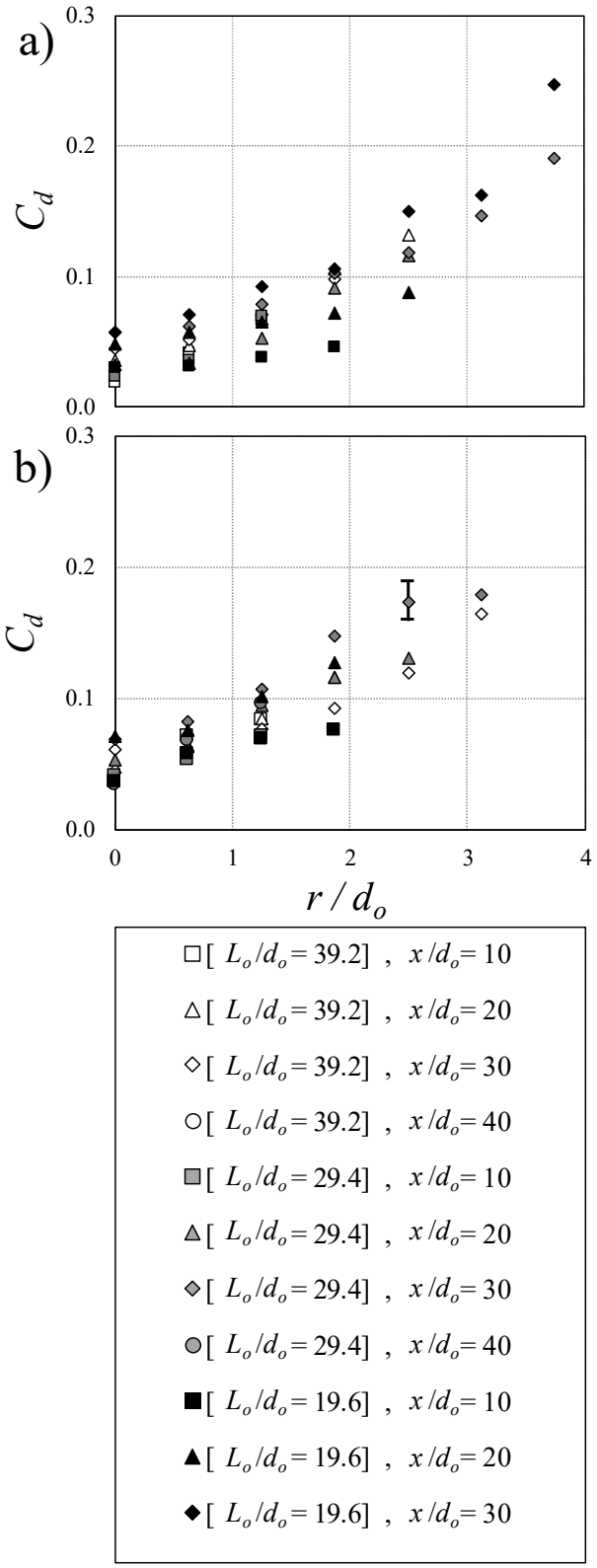

Figure 2.11: Variations of drag coefficient C_d of particle clouds with normalized transverse direction r/d_o and for different normalized axial distance from the nozzle x/d_o; a) S_t = 0.52, b) S_t = 0.74.

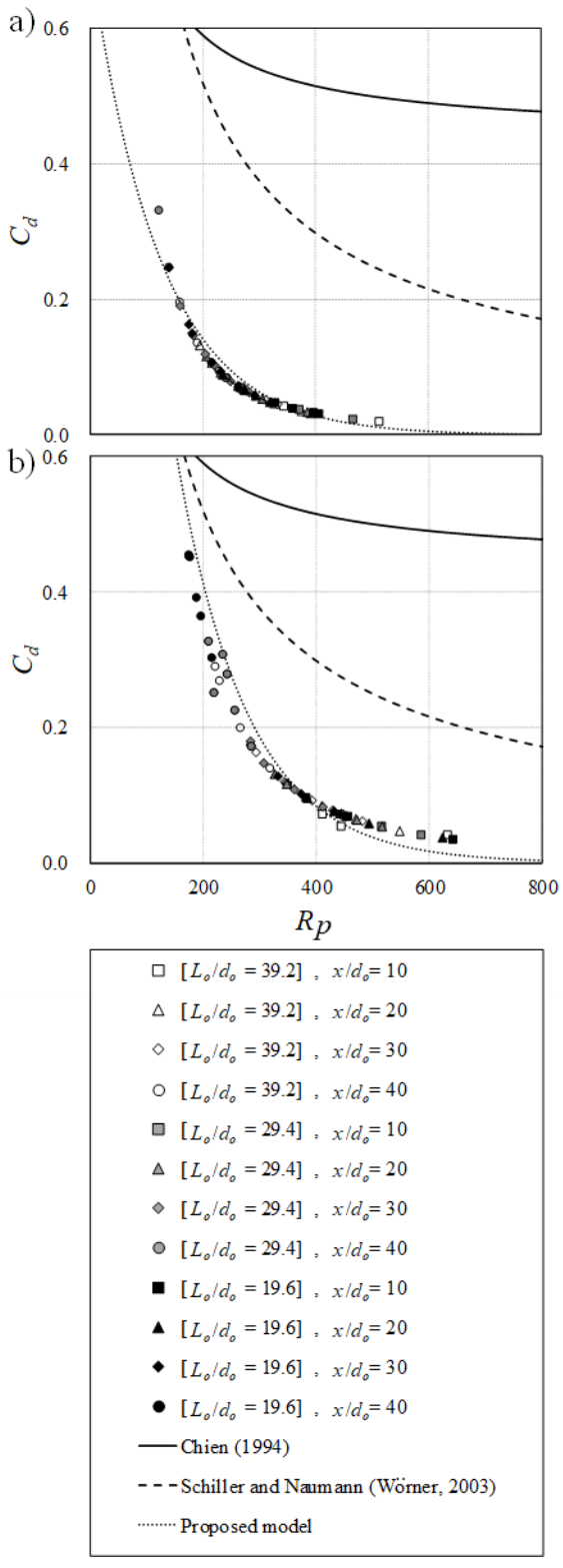

Figure 2.12: Effects of aspect ratio L_o/d_o on variations of drag coefficient C_d of particle clouds with particle Reynolds number R_p along the vertical axis of the clouds x/d_o; a) S_t = 0.52, b) S_t = 0.74.

2.3.5 *Ambient entrainment*

The entrainment coefficient α_e is one of the key parameters describing the mixing efficiency of particle clouds with ambient water. After the initial regime, the total buoyancy of particles induces a descending buoyant thermal and the fluid entrained into the buoyant thermal is referred to as the fluid phase of particle clouds. The sand particles in the periphery of a particle cloud typically set the surrounding ambient fluid into motion. The ambient fluid entrains into particle clouds due to turbulent entrainment, and as a result, changes the concentration and velocity of the clouds as they descend.

Batchelor (1954) defined the entrainment coefficient α_e as a parameter to link the entrainment velocity to the centerline axial velocity of buoyant plumes. The entrained volume of ambient water into a particle cloud of a radius r (see Figure 2.10a) can be equated to the rate of change of the cloud volume with time as:

$$\frac{dV}{dt} = A_s u_e = \Delta Q_e \tag{2.18}$$

where ΔQ_e is the entrained volume flux inside a particle cloud, A_s is the surface area of the inner cloud, and u_e is the entrainment velocity. Using the proposed formula for prediction of sand velocity in radial direction (Eq. (2.9)), the sand-phase volume flux at each cross-section can be calculated as:

$$Q\,(x) = 2\pi \int_0^{w/2} (1-c) u_m(x) \exp\left[-0.693 \xi \left(\frac{r(x)}{d_o} \right)^2 \right] r(x) dr \tag{2.19}$$

Assuming the boundary conditions as $r = w/2$, $u \rightarrow 0$, where w is the estimated cloud width for $c = 0.01 c_m$ and as $x_o/d_o > 40$ then $u_m \rightarrow 0$.

Variations of sand volume flux in the radial direction can be expressed as:

$$\Delta Q_e = \frac{dQ(x)}{dx} = \frac{Q(x+\Delta x) - Q(x)}{\Delta x} = 2\pi \alpha_e u r dr \tag{2.20}$$

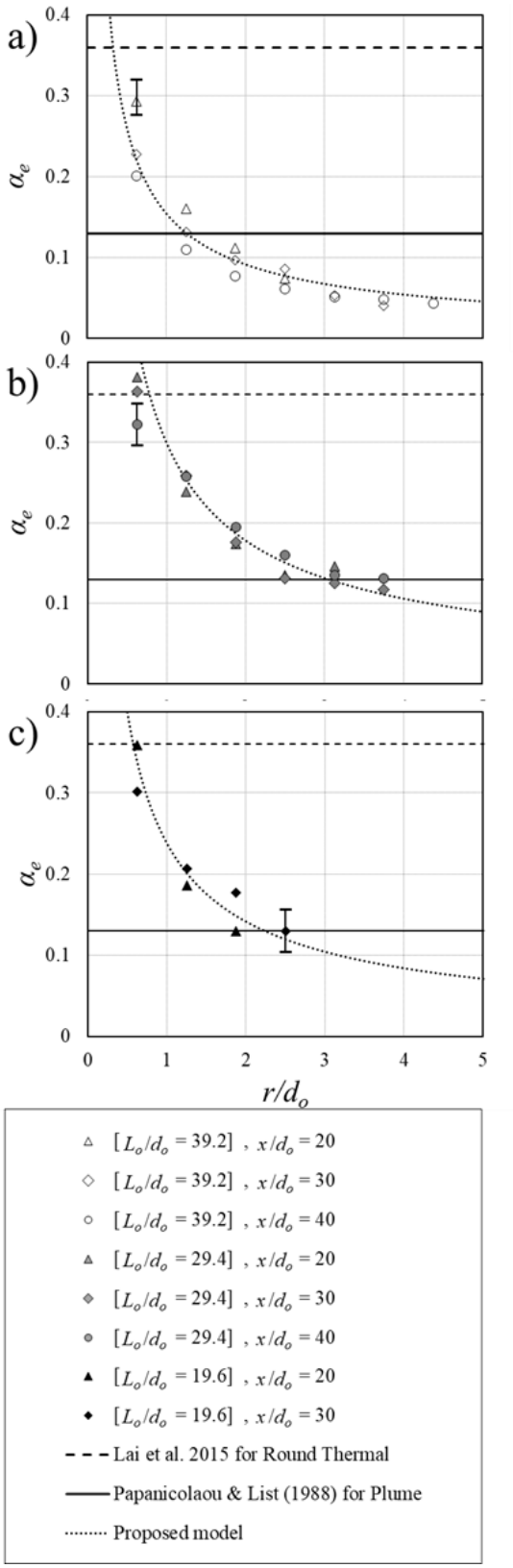

Figure 2.13: Effect of aspect ratio and depth progression on the radial variation of entrainment coefficient for $S_t = 0.52$; a) $L_o/d_o = 39.2$, b) $L_o/d_o = 29.4$, c) $L_o/d_o = 19.6$.

The entrainment coefficient for single-phase water jets have varied from 0.065 to 0.08 and for single-phase plumes between 0.1 and 0.16, and they are constant with time (Fischer et al., 1979; Papanicolaou & List, 1988). Zhao (2012) investigated the effect of release height on the entrainment coefficient of particle clouds and found α_e = 0.234. For three-dimensional sediment thermals, the entrainment coefficient was reported in a range of 0.1–0.3 and was constant with time (Wen and Nacamuli, 1996). Figure 2.13 shows the radial distribution of the entrainment coefficient for different aspect ratios ($19.6 \leq L_o/d_o \leq 39.6$) and medium particle sizes with S_t = 0.52.

The prediction curves of Papanicolaou & List (1988) for single-phase jets and plumes and round thermals with L_o/d_o = 0.44 by Lai et al. (2015) were also added for comparison. As shown, the entrainment coefficients were not constant inside the cloud and they decreased as the inter-particle spacing increased within particle clouds in the radial direction. The minimum entrainment coefficients at r/d_o = 5 for particle clouds with L_o/d_o = 19.6, 29.4, and 39.2 were 0.13, 0.12, and 0.04, respectively. Therefore, higher depth progression and spreading rates of particle clouds can be expected for tests with higher L_o/d_o. Figure 2.14 shows the effect of distance from the nozzle x/d_o on the entrainment coefficient of a particle cloud with a larger particle size S_t = 0.74 and L_o/d_o = 19.6. In this case, the radial variations of entrainment coefficients of particle clouds with relatively larger particles were similar to particle clouds with smaller particles, but the values of entrainment coefficients were smaller. For example, α_e at r/d_o = 1.25 was around 0.2 ± 0.01 for S_t = 0.52 whereas α_e reduced to 0.18 ± 0.02 for S_t = 0.74.

The radial variations of the entrainment coefficient with respect to particle size S_t and aspect ratio L_o/d_o were also modeled with a power-law formulation with a coefficient of determination of R^2 = 0.93 as:

$$\alpha_e = \psi_e \, S_t^{1/3} \left(\frac{r}{d_o}\right)^{-3/4} \left(\frac{L}{d_o}\right)^{1/5} \tag{2.21}$$

where the values of ψ_e for S_t = 0.52 and 0.74 are 0.09 and 0.12 respectively.

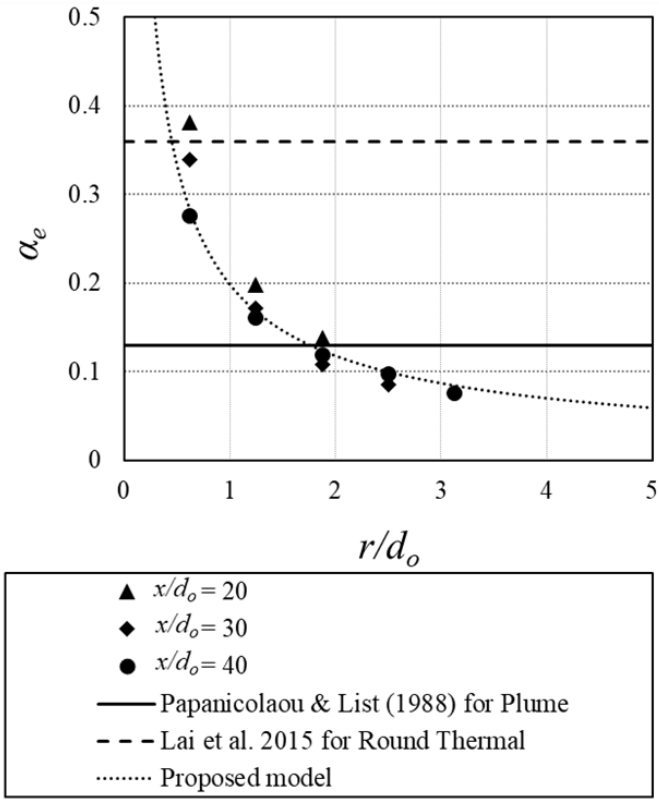

Figure 2.14: Entrainment coefficient of vertically downward particle cloud S_t = 0.74 and L_o/d_o=19.6.

2.3.6 *Energy transfer*

The energy of particles in particle clouds is transferred from the mean flow to a cascade of vortices. The energy transfer within particles is described by the power spectral density (PSD) of time-series velocity data.

Figure 2.15 shows the variations of an energy cascade in the axial and radial directions for L_o/d_o = 39.2 and S_t = 0.52. The dominant frequency of eddies is shown by the first peak in the power spectrum plot with a value of 1.5 Hz for sand velocity in the axial direction (Figure 2.15a). As can be seen, the maximum energy contribution was within small frequencies of less than 10 Hz. The spectral energy decreased in the frequency range between 0.1 Hz and 10 Hz by almost three orders of magnitude and the flow of energy transfer was well characterized by the Kolmogorov −5/3 scaling law. A similar frequency range was also found in buoyant thermals, indicating that the minimum sampling rate should be greater than 20 Hz (Papanicolaou and List, 1988). Furthermore, by attributing the signal strength to concentration, the power spectrum of the signal decreased by increasing x/d_o because sand concentration decreased by x/d_o as well. The energy level of sand particles also decreased in the transverse

direction. Figure 2.15b shows the power spectral density of sand particles in the transverse direction: the power spectrum of sand concentration was consistent with a Kolmogorov −5/3 scaling law and the dominant frequency was around 0.7 Hz, slightly far from the axis of the cloud at $r/d_o = 1.25$.

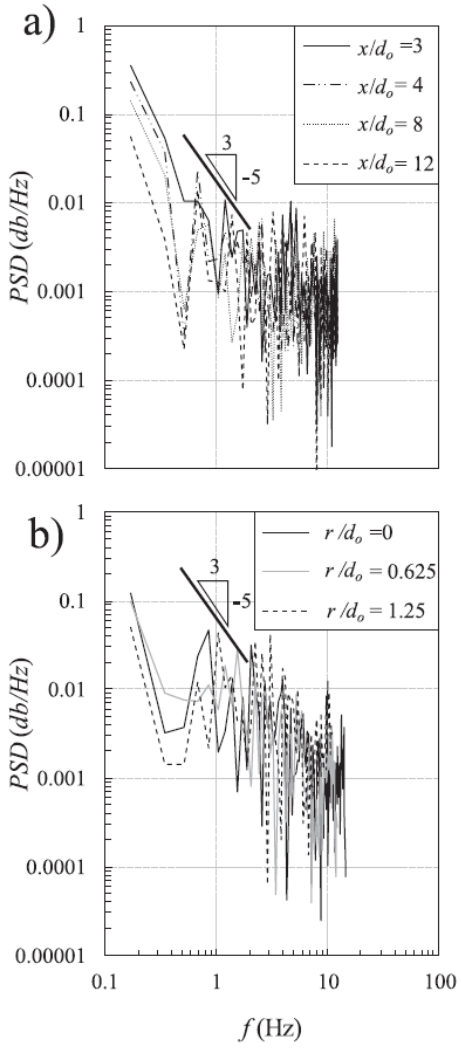

Figure 2.15: Axial and radial variations of the power spectral density (PSD) of sand concentration for $S_t = 0.52$ and $L_o/d_o = 39.2$; a) axial variation of PSD at the centerline, b) radial variation of PSD at $x/d_o = 8$.

2.3.7 *Particle-particle interaction*

The Bagnold number has been proposed as an indicator to study the movement of highly concentrated sediments in water (Bagnold, 1954). This number is a ratio of grain collision stresses to the viscous fluid stresses defined by:

$$Ba = c^* \frac{\rho_s D_{50}^2}{\mu}\left(\frac{du}{dr}\right)$$

(2.22)

where du/dr is the shear rate and c^* is the concentration of sand particles during flow propagation as defined by:

$$c^* = \left[\frac{c^{1/3}}{c_o^{1/3} - c^{1/3}}\right]^{1/2}$$

(2.23)

Using the proposed formula for prediction of sand velocity in the radial direction (Eq. (2.9)), the shear rate can then be defined as:

$$\frac{du}{dr} = 1.39\left(\frac{\xi}{d_o}\right)^2 \exp\left[-0.693\,\xi\left(\frac{r}{d_o}\right)^2\right]$$

(2.24)

By assuming the boundary conditions as $u = 0$, $r/d_o \rightarrow w/2$, where w is the estimated cloud width for $u = 0.01u_m$ and as $x_o/d_o > 40$ then $u_m \rightarrow 0$. Bagnold (1954) also classified the motion of sediments in water into three types of regimes: viscous, transitional, and gain-inertia. For $Ba < 40$, the flow dominates by the viscous fluid stresses. However, for Ba between 40 and 450, the flow is in transition regime. For $Ba > 450$, the stress is primarily transmitted by particle collision and typically indicates significant inter-particle collision. The radial variations of Bagnold numbers for particle clouds with different particle sizes and axial distances from the nozzle were calculated based on the proposed formulations for sand concentration and velocity to define the region of high inter-particle collision. Figure 2.16 shows the radial variations of calculated Bagnold numbers for $S_t = 0.52$ and 0.74. As can be seen, the Bagnold number had the maximum value at the infinitesimal distance from the centerline and decreased in the radial direction. It was also found that for $S_t = 0.74$, the Bagnold number was slightly greater than 450 for $x/d_o = 10$. This indicates that the inter-particle collision dominates the flow for higher stokes numbers and for $x/d_o < 10$. The value of the Bagnold number in the same location decreased from 450 to 141 for $S_t = 0.52$. The values of the Bagnold number were smaller than 45 for $x/d_o \geq 20$, indicating that the micro-viscose regime controls the flow.

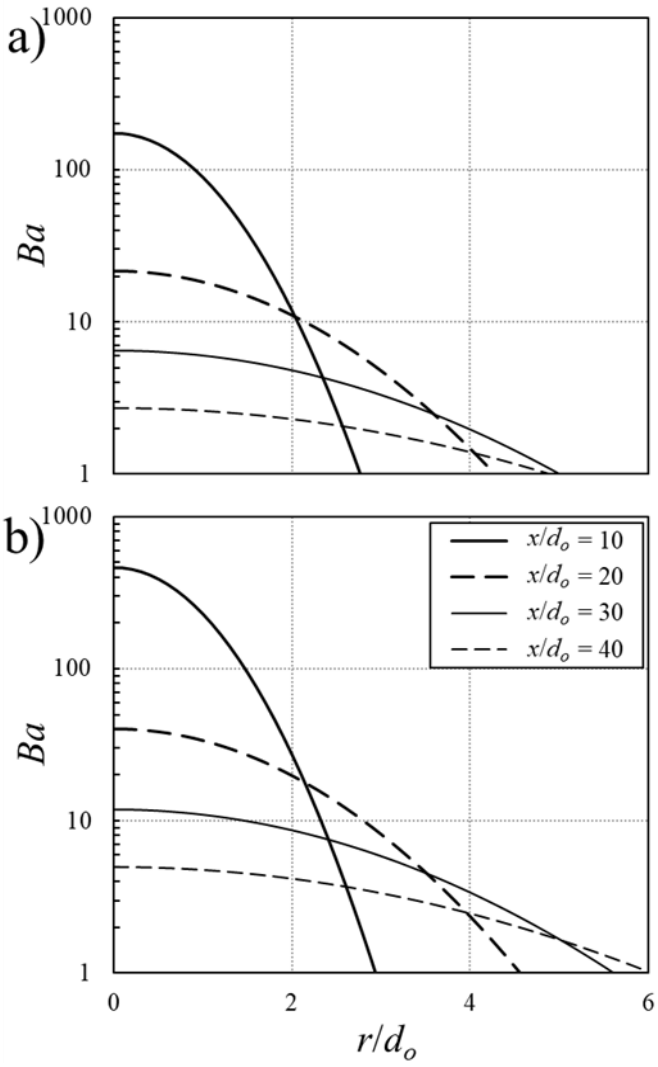

Figure 2.16: Variations of the Bagnold number in transverse direction and at different normalized distances from the nozzle x/d_o; a) $S_t = 0.52$, b) $S_t = 0.74$.

2.4 Conclusions

A series of laboratory experiments were conducted to investigate the effects of initial aspect ratio L_o/d_o and particle size on the dynamics of particle clouds in stagnant water. An accurate and robust optical probe (PV6) was utilized to measure sand concentration and velocity of particle clouds in both axial and transverse directions. The performance of the optical probe was verified with integral quantities of particle clouds such as sand-phase mass and momentum fluxes. The axial sand velocities and concentrations were measured for medium sand particles with Stokes numbers ranging from 0.52 to 0.93 and for aspect ratios ranging from 19.6 to 39.2.

The zone of jet development was found to be between two and four times that of nozzle diameter for particle clouds that were smaller than the zone of jet development in both water and sand jets. It was found that for particle clouds with S_t = 0.52, the centerline sand concentration in particle clouds decreased with a slower rate than single-phase buoyant and sand jets. For the same particle size, sand concentration was found to be constant at $x/d_o > 20$, whereas for larger sand size, $S_t = 0.74$, constant sand concentration was observed at $x/d_o > 45$. It was also found that the decay rate of sand concentration was higher in particle clouds with smaller aspect ratios. A power law formula was proposed for predicting centerline sand concentration.

Using the axial and radial distributions of sand concentration and velocity, drag coefficients of particle clouds were calculated inside particle clouds. It was found that the drag coefficients were increased in the radial direction from a value of less than 0.1 in the centerline to slightly above 0.4 at $r/d_o = 4$, indicating the grouping effect in the core region of particle clouds. The drag coefficients were approximately independent of the axial distance from the nozzle for relatively high aspect ratios, whereas for $L_o/d_o = 19.6$, the drag coefficient increased as particle cloud descended.

Additionally, the entrainment coefficients of vertically downward particle clouds were computed at different cross-sections. The variations of entrainment coefficients in radial direction were calculated from measurements to find the inner cross-sectional distribution of ambient entrainment of particle clouds. It was found that the entrainment coefficient non-linearly decreased as the inter-particle spacing increased in the transverse direction. As well, the radial variations of entrainment coefficients of particle clouds with relatively larger particles were similar to particle clouds with smaller particles, but the values of the entrainment coefficients were smaller.

Finally, the inter-particle energy transfer inside particle clouds was observed by the power spectral density (PSD) and the results showed that the dominant frequency of velocity data was 1.5 Hz and the energy cascade followed the Kolmogorov −5/3 scaling law. The inter-particle collision of particle clouds was evaluated by calculating the Bagnold number in both axial and radial directions. It was found that the inter-particle collision occurred for $x/d_o \leq 10$ for $S_t = 0.74$ and $S_t = 0.52$ and that the values of Bagnold numbers were smaller than 45 for $x/d_o \geq 20$, indicating that the micro-viscose regime controls the flow.

Chapter 3

Effects of velocity ratio on dynamics of sand-water coaxial jets

3.1 Introduction and literature review

Turbulent jets are flows generated by an initial source of momentum and have many engineering applications in various mixing and combustion processes. A single-phase jet is a fluid moving through a pipe or a nozzle which enters a quiescent ambient of the same fluid. A shear flow is formed between the entering and ambient fluids, causing strong shear layer mixing and turbulence between the two fluids (Abramovich, 1963; Rajaratnam, 1976; Fischer et al., 1979; Lee and Chu, 2003). A coaxial jet is composed of an inner jet surrounded by an annular jet and is often employed as an effective method to mix two different fluid streams such as those found in combustion chambers, industrial burners, and air blast atomizers (Balarac and Métais, 2005; Balarac et al., 2007; Safer and Beghidja, 2019).

Particle-laden turbulent jets consist of solid particles moving through an ambient fluid (e.g., gas or water) with a high initial momentum. Two-phase, solid-liquid turbulent jets are commonly known as sand/slurry jets in the field of engineering and have many applications in marine bed capping, hydro-transport systems, and wastewater disposal (Balarac et al., 2007; Azimi 2012a, b; Canton et al., 2017; Zhang et al., 2018). Several research studies have been performed to understand the dynamics of particles in two-phase solid-liquid turbulent jets (Brush, 1962; Fan et al., 1990; Mazurek et al., 2002; Tamburello and Amitay, 2008; Virdung and Rasmuson, 2007; Casciola et al., 2010; Hall et al., 2010; Azimi et al., 2011, 2012a, b; Lau and Nathan, 2014). The addition of a discrete phase (e.g., sand particles) to a continuous fluid phase (e.g., water) increases the number of controlling parameters such as initial particle concentration c_o, nozzle diameter d_o, and mean particle size D_{50} which is defined as a diameter of particles in which 50% are finer. These controlling parameters, in addition to the relative sand and water mass fluxes, significantly affect time-averaged properties of jets such as axial and radial velocities of the continuous phase, particle dynamics (i.e., concentration and velocity of particles), jet spreading rate, turbulence level, and mixing capability.

A paper based on the content of this chapter has been published in the *International Journal of Multiphase Flow* as Sharif, F., Azimi, A. H., 2021. Effects of velocity ratio on dynamics of sand-water coaxial jets. 140, 103643.

The Stokes number, S_t, is the ratio of the particle relaxation time, $\tau_p = \rho_s D_{50}^2/18\mu$, and the time scale of the flow, $\tau_f = d_o/u_o$, where ρ_s is the particle density, μ is the dynamic viscosity of the ambient fluid, and u_o is the jet initial velocity. The Stokes number has been used to classify the motion of particles in ambient fluids and determine the mixing characteristics of sand/slurry jets (Gore and Crowe, 1989; Moghadaripour et al., 2017a, b). In particular, the importance of S_t on particle dispersion in shear flow indicated that for $S_t << 1$, the particles follow the water flow patterns and adopt the same mixing and spreading rate as of the water phase. For $S_t \approx 1$, particles are entrained by the vortices of the water phase and spin around the fluid mixing zone. For $S_t >> 1$however, particles are not engaged by the vortices in the flow field (Crowe et al., 1985). Moghadaripour et al. (2017a) later used the Stokes number for classifying sand particle sizes as: small particles ($0 < S_t \leq 0.1$), medium particles ($0.1 < S_t < 0.33$), and large particles ($0.33 \leq S_t < 1$). Some mixing indices, such as the spreading rate in particle clouds and particle-laden jets, have also been found to be correlated with the Stokes number (Bühler and Papantoniou, 2001; Azimi et al., 2012a; Moghadaripour et al., 2017b).

Dynamics of two-phase turbulent jets have been studied by measuring the variations of axial and radial velocities and sand concentrations. The variations of sand concentration along the vertical axis of sand jets with Stokes numbers of 0.42 and 0.7 were found to be similar to single-phase water jets (Hall et al., 2010). However, the results of sand jets for $S_t = 0.46$, 0.70, 1.46 indicated that the particle size significantly changes the mean centerline axial velocity (Azimi et al., 2011).

Overall, the centerline velocity of solid-liquid jets decayes with a lower rate than single-phase water jets (Azimi et al., 2011; 2012b). Experimental results of slurry jets with a wide range of Stokes numbers (i.e., $0.07 \leq S_t \leq 11.37$) indicated a higher velocity decay in slurry jets with small Stokes numbers (Azimi et al., 2012b). Similarly, Lau and Nathan, (2014) found that velocity decay increased with decreasing Stokes number ($0.3 \leq S_t \leq 11.2$) and the length of the potential core, the region in which the axial velocity is constant and equal to the initial velocity at the nozzle (Akaike and Nemoto, 1988), decreased with S_t. The centerline sand velocity in slurry wall jets increased with increasing S_t as high as 15%, and sand concentration decreased linearly for $x/d_o > 5$ (Azimi et al., 2015). Jiang et al. (2005) indicated that the centerline sand velocity in slurry jets with small particles ($0 < S_t \leq 0.1$) was higher than the water-phase velocity and can be formulated as the sum of the water-phase velocity and particle settling velocity.

Inter-scale parameters in particle-laden jets, such as particle-particle interaction and grouping effects are quantified by the cross-sectional average drag coefficient, C_d (Azimi et

al., 2012b; Moghadaripour et al., 2017a, b; Mohammadidinani et al., 2017; Azimi, 2019; Manzouri and Azimi, 2019; Sharif and Azimi, 2020). Employing the steady-state momentum equation, Azimi et al. (2012b) found that the average drag coefficient in slurry jets is similar to the C_d of an individual particle whereas far from the jet, the average drag coefficient became smaller than the C_d of individual particles. They further showed that the particle grouping effect decreased the drag coefficient by approximately 50% in sand jet fronts with $0.26 \leq S_t \leq 11.37$. Then, based on laboratory experimental results, Moghadaripour et al. (2017b) formulated the axial variations of drag coefficients of particle clouds with large particle sizes (i.e., $0.33 \leq S_t < 1$). They found that the grouping effect caused a dramatic reduction of C_d in comparison with individual sand particles for particle Reynolds number $R_p > 120$ where $R_p = \rho_w u D_{50}/\mu$, u is the particle velocity, and ρ_w is the water density. Recently, Sharif and Azimi (2020) conducted a series of experiments on the dynamics of particle clouds and found that the drag coefficients of particle clouds increased in the radial direction, C_d ranged between 0.1 and 0.4, and the lower values of particle drag coefficients were linked with the particle grouping effect.

Many other research studies have investigated the mixing process of single-phase coaxial jets as an effective method for environmental engineering systems and combustion chambers. Such systems improve mixing efficiency and reduce environmental pollutant emissions (Crow and Champagne, 1971; Dahm et al., 1992; Wicker and Eaton, 1994; Villermaux and Rehab, 2000; Balarac and Métais, 2005; Balarac et al., 2007; Safer and Beghidja, 2019). The nature of flow in single-phase coaxial jets has been classified into three different regions: the initial merging zone starting from the nozzle exit to the length where the annular flow has disappeared; the intermediate merging zone in which the core and the annular section merge; and the fully developed zone (Ko and Kwan, 1976). Coaxial jets contribute to the mixing process by creating two distinct shear layers. The first shear layer is formed between the surrounded fluid and the annular jet and the second shear layer is formed between the annular and the core jet (Balarac et al., 2007). The boundary between the annular and core streams increases with the fluctuation of the outer shear layer.

The large-scale rotating vortices in shear layer boundaries play an important role in turbulent transfer within a coaxial jet (Crow and Champagne, 1971). Using experimental results, Buresti et al. (1998) extracted two strings of rotating vortices with a well-defined harmony close to the nozzle. The vorticity thickness enhancement of the annular shear layer was found to be another mechanism of mixing in coaxial jets in which the vorticity thickness increases when the outer flow velocity is larger than the core velocity (Dahm et al., 1992;

Wicker and Eaton, 1994; Villermaux and Rehab, 2000). When the inner vortices are trapped in the free space between the two consecutive outer vortices, the evolution of the inner vortices is dictated by the motion of the outer vortices. In the vortex dynamics of coaxial jets, this phenomenon is called the locking effect and was introduced by Balarac and Métais (2007). Streamwise vortices have also shown a significant impact on the mixing of coaxial jets due to formation of counter-rotating pairs as the streamwise vortices elongated between consecutive vortex rings through annular and core shear layers (Balarac et al., 2007).

In addition, the effects of velocity ratio of annular to central streams, *Ru*, on fluid dynamics of single-phase coaxial jets have been investigated in the literature (Ko and Kwan, 1976; Park and Chen, 1989; Wicker and Eaton, 1994; Buresti et al., 1998; Warda et al.1999; Sadr and Klewicki, 2003; Canton et al., 2017). Champagne and Wygnanski (1971) indicated the importance of velocity ratio in mixing and flow properties of the potential core and found distinct initial potential cores in the near field of single-phase coaxial jet separated by an annular mixing region. Dahm et al. (1992) found an axisymmetric instability in single-phase coaxial jets with $Ru > 0.71$ and moderate Reynolds numbers (i.e., $1{,}333 \leq Re \leq 10{,}668$) where $Re = \rho_w u_{ow} d_o/\mu$ and u_{ow} is the initial water velocity at the nozzle.Wicker and Eaton (1994) indicated that the initial vortex development in the shear layer occurred independently in single-phase coaxial jets with $Ru > 1$. However, for this velocity ratio, a strong annular layer dominated the core flow and the annular potential core became independent of the velocity ratio for a distance approximately three times that of the annular nozzle diameter. It was also reported that the wake effects between central and annular shear layers caused by constant nozzle annular gap thickness continues up to $x/d_o < 5$. Other experimental studies have shown that the length of the inner potential core in single-phase coaxial jets is correlated with *Ru*, while the length of the annular shear layer is independent of *Ru* (Warda et al., 1999). It was also found that the length of the annular potential core was linearly correlated with velocity ratio for $Re = 41{,}000$ (Sadr and Klewicki, 2003). In addition, it was shown that the turbulence level in single-phase coaxial jets was influenced by *Ru* and the absolute velocity of the annular jet.

For particle-laden coaxial jets with $Ru = 1.5$ and $Re = 8400$, the potential core was found to be symmetric with a pine-tree shape for $x/d_o \leq 4$; far from the nozzle ($x/d_o > 4$), sand particles adopted an oscillatory motion and the potential core became axisymmetric (Pedel et al., 2014). The oscillatory motion of particle-laden coaxial jets was attributed to the interactions between particles and large eddies in the inner shear layer. The radial dispersion of particles was

enhanced significantly for $x/d_o > 6$ (Pedel et al., 2014). Further, the effect of sand particles and mass loading showed a considerable impact on the dynamics of particle-laden coaxial jets (Mostafa et al., 1990; Fan et al., 1996; Sadr and Klewicki, 2005; Kannaiyan and Sadr, 2013). Mostafa et al. (1990) investigated the formation of potential core in particle-laden coaxial jets with glass beads with a mean diameter of 0.105 mm and compared their results with single-phase coaxial jets and found a uniform mean particle velocity across the jet cross-section. The presence of discrete particles in coaxial jets reduced the turbulence intensity and enhanced the anisotropy level leading to an increase in energy dissipation rate.

The velocity ratio and mass loading in particle-laden coaxial jets were found to have an inverse effect on the spreading rate of coaxial jets (Fan et al., 1996, 1997). Sadr and Klewicki (2005) indicated that the addition of particles in two-phase coaxial jets had no effect on the mean flow velocity profile of the initial region. The results also demonstrated a small and moderate enhancement in axial turbulent intensity from 0.4% to 0.8% and radial gradients of velocity fluctuations, respectively. The degree of turbulence enhancement was found to be directly correlated with particle volume fraction. Kannaiyan and Sadr (2013) found the decay of mean flow velocity in axial direction was similar in both single-phase and two-phase coaxial jets with a mass loading of 22% and a velocity ratio of Ru = 1.11. Close to the nozzle, the existence of particles reduced turbulent intensity; further downstream, turbulent intensities were similar to the corresponding single-phase coaxial jet.

Table 3.1: List of two-phase coaxial jets investigations in the literature.

Experimental study	Jet type	D_{50} (mm)	Ru (-)	d_o (mm)	d_a (mm)	ρ_s (kg/m^3)	c_o (%)
Fan et al. (1997)	Solid-Gas	0.05-0.2	1.5 - 3	40	68	1250	0.5 - 1.5
Mostafa et al. (1990)	Solid-Gas	0.11	0.87, 1.4	24.1	29	2500	0.2
Sadr and Klewicki (2005)	Solid-Liquid	0.24	0.11 - 1.15	30	75	2450	0.03 - 0.09
Kumaran and Sadr (2013)	Solid-Liquid	0.24	0.18, 1.11	30	75	2450	0.074, 0.22
This Study	Solid-Liquid	0.57	0.62-1.86	12	22	2450	60

In Chapter 3 the results of detailed laboratory experiments of sand-water coaxial jets issuing horizontally into stagnant water are presented. Most of the previous studies have focused on the dynamics of two-phase coaxial jets with relatively low mass loading ratios and small particle sizes by injecting particles in either the inner or outer nozzles of single-phase coaxial jets (see Table 3.1). A set of the coaxial nozzle without initial premixing was designed

to study the effect of the annular to core nozzle velocity ratio used to investigate the mixing capability of the new configuration. The effects of velocity ratio on variations of spreading rate, sand velocity and concentration profiles, also inter-scale properties such as interparticle collisions and drag coefficients are presented in this chapter. Furthermore, prediction models as a function of velocity ratio were developed to estimate sand velocity and concentration in both axial and transverse directions for designing sand-water coaxial jets and optimization.

This chapter is organized as follows: material and method including the experimental setup and signal processing techniques are described in section 3.2. In section 3.3, experimental results including the study of mass and momentum flux, spreading rate and mixing, axial and radial concentration and velocity measurements are presented. Besides, drag reduction of group particles and particle-particle interaction is also described in this chapter. Finally, the conclusions of this study are presented in section 3.4.

3.2 Material and methods

3.2.1 *Experimental setup*

Detailed laboratory experiments were conducted in the Multiphase Flow Research Laboratory (MFRL) at Lakehead University to study the dynamics of sand-water coaxial jets. All experiments were carried out in a rectangular tank of 1.65 m long, 0.85 m wide, and 0.85 m. The tank was filled with tap water and the ambient temperature was kept constant over time with a value of 20°C ± 1°C. The schematic of the experimental setup, instrumentations, and the adopted coordinate system are shown in Figure 3.1. A discharge assembly consisting of a funnel and two concentric pipes at the outlet was designed to model the coaxial jets. The central nozzle diameter of the funnel and the coaxial annular diameter were d_o = 12 mm and d_a = 22 mm, respectively. This design provided a constant annular gap thickness of 2.5 mm. The schematics of the coaxial nozzle arrangement and funnel-pipe assembly are shown in Figure 3.2. The water was injected through the central pipe, while dry sand particles were discharged through the funnel and flowed through the annular gap of the coaxial nozzle. The pre-mixing of sand and water did not occur in the annular pipe and all sand particles were mixed with the central jet once they discharged into the ambient water. An accurate flow meter (LZT M-15, UXCEL, China) was used to generate different flow rates ranging between 0.5 L/min and 18 L/min which provided velocity ratios in the range of $0 \leq Ru \leq 1.86$. Sand particles with a median diameter of D_{50} = 0.507 mm and a density of ρ_s = 2540 kg/m^3 were used in this study.

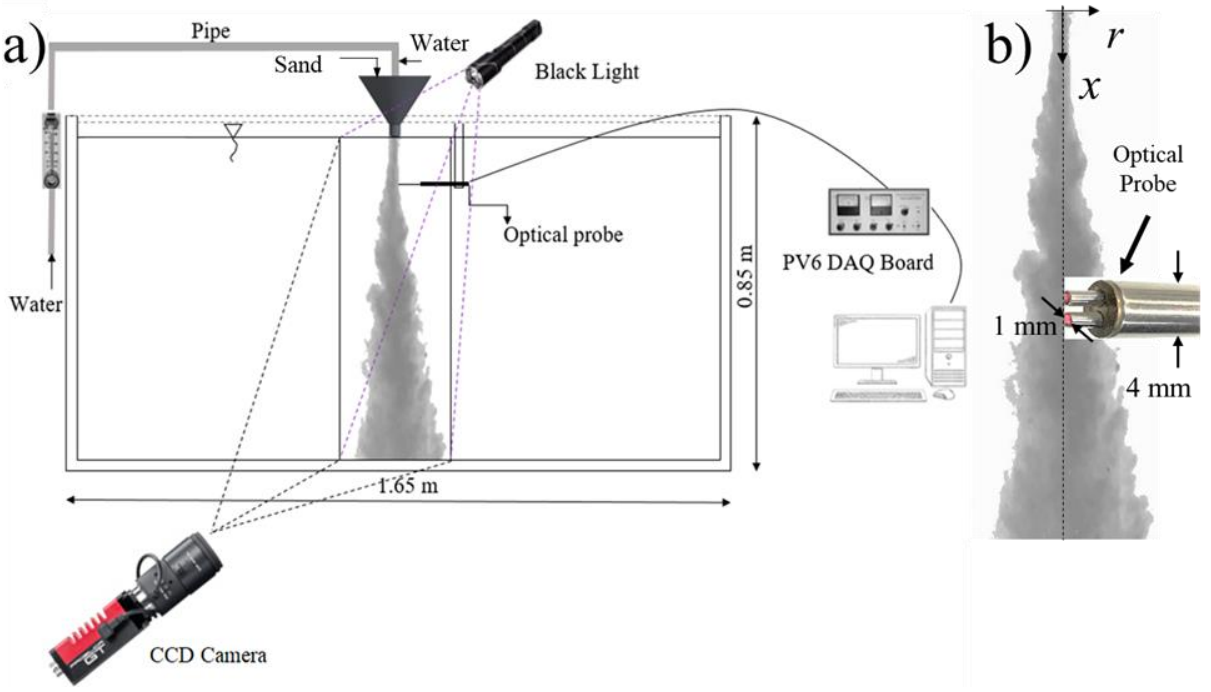

Figure 3.1: Schematics of the experimental setup, instrumentations, and the adopted coordinate system.

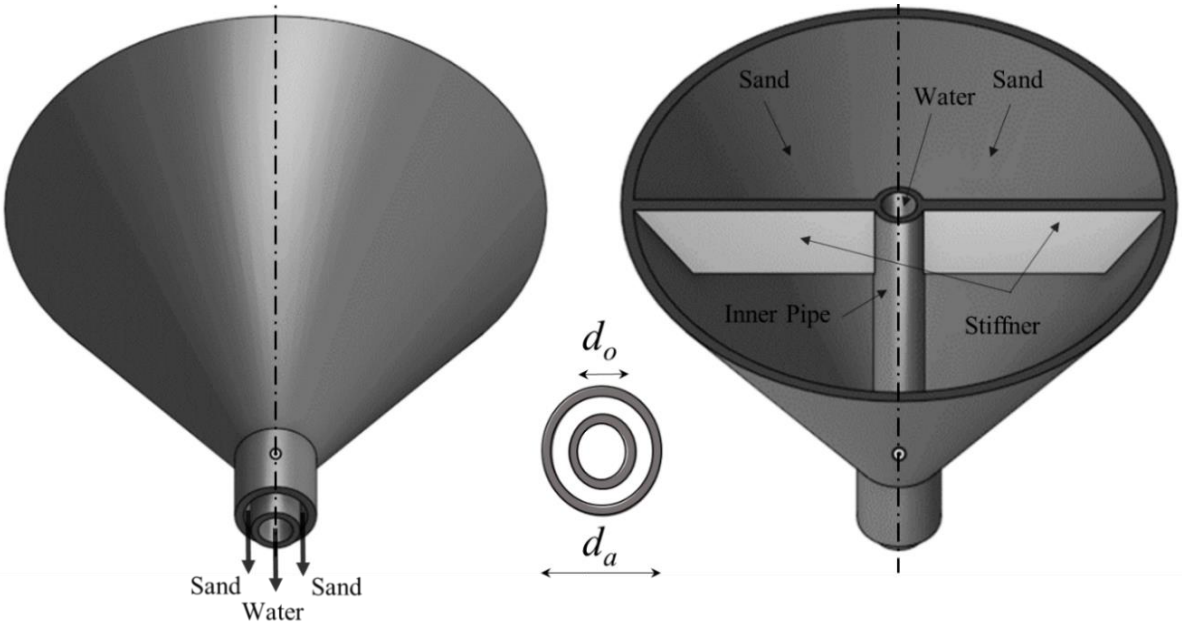

Figure 3.2: Details of the coaxial nozzle arrangement and funnel-pipe assembly.

The uniformity of particle sizes was evaluated by fitting the sand particle size distribution data with the lognormal probability curves. In addition, particle size was chosen based on probe measurement capability and $S_t \approx 1$ for this experiment. The sand mass flux was $\dot{m}_o = 27$ g/s with a loosely packed initial sand concentration of approximately 60%. Overall, six experiments were tested in this study to investigate particle dynamics of sand-water coaxial

jets. The experimental variables and important non-dimensional parameters are listed in Table 3.2. full MATLAB® m-file code is included in Appendix 4. In order to avoid nozzle blockage due to saturation of sand particles with water, a 3 mm distance was kept between the annular nozzle exit and water surface. The annular nozzle diameter of d_o = 12 mm with particle size of D_{50} = 0.507 mm gave a Stokes number value of 0.57. The range of Stokes numbers in this study (i.e., $0.33 \leq S_t < 1$) indicated that the sand particles used could be classified as large particles (Moghadaripour et al., 2017a). The experimental results of $0 \leq Ru \leq 0.33$ and $S_t = 0.7$ is included in Appendix 1.

A light illumination method was performed for better visualization and improving the quality of the images of the sand-water mixture. To serve this purpose, 18 dimmable Light Emitting Diodes (LED) with a power of three watts were employed (Black light, WOWTOU, China). A high-speed camera (Prosilica GT 1910c CCD, Germany) with two lenses, a 90-mm lens with a focal length of 1.8 m (Kowa-F-1.8, Nagoya, Japan) and a variable lens (18–55 mm, AF-Sinkkor, 13.5–5.6 GII, Nikon, Tokyo, Japan), were used for flow visualization. Images were recorded at a speed of 60 frames per second.

Table 3.2: Experimental parameters and non-dimensional parameters of the coaxial sand-water jet.

No.	Test	D_{50} (mm)	d_o (mm)	d_a (mm)	$\dot{m}_o$ (g/s)	u_{ow} (m/s)	*Re*	*Ru*	*Fr*
1	B1	0.507	12	22	27	0	0	0	0
2	B2	0.507	12	22	27	0.59	7063	1.86	0.09
3	B3	0.507	12	22	27	0.88	10595	1.24	0.13
5	B4	0.507	12	22	27	1.18	14126	0.93	0.17
5	B5	0.507	12	22	27	1.47	17658	0.74	0.21
6	B6	0.507	12	22	27	1.77	21189	0.62	0.26

The images were used to study sand and water motions and flow entrainment in sand-water coaxial jets. A light-refractive optic probe equipped with a quartz cover to reduce the effect of blind spots with signal amplification and a processing unit (PV6, Institute of Processing Engineering, Chinese Academy of Science, China) was implemented with a capability of measuring a simultaneous time series of sand concentration and velocity. The probe tip diameter was 4 mm and contained two light sources and two light-refracting optical

sensors with a diameter of 1 mm each (see Figure 3.1b). The fiber optics were 2.14 mm apart and they received the emitted light from the two light sources in the sensor's tip. A high-resolution data acquisition board (National Instrument, Austin, U.S.) was used for analog-to-digital voltage conversion by taking raw signals from the PV6 processing unit. The fiber optic probe and the PV6 signal processing unit have been successfully utilized in many other multi-phase flow tests such as gas and solid fluidization systems, sand/slurry jets, and particle cloud studies and provided high-accuracy measurements (Hall et al., 2010; Azimi et al., 2015; Taofeeq et al., 2018; Sharif and Azimi, 2020).

A voltage sampling rate of 61,440 Hz was selected to attain high-quality data. The sampling time of the experiments was 20 s resulting in 1,228,800 data samples for each measurement point. The signal processing was implemented by the MATLAB signal processing toolbox (The MathWorks Inc., Natick, U.S.). The full MATLAB® m-file code and an example is included in Appendix 2 and 3. The optical probe was placed perpendicularly at different locations along the axis of the coaxial jet (x-axis) and in different transverse directions (r-axis). The sand velocity and concentration were measured at different cross-sections ranging from $1 < x/d_o < 40$ and at different radial directions of $-5 < r/d_o < 5$. The numbers of sand particles were insufficient to provide strong signals for $x/d_o > 40$ and $r/d_o > 5$.

3.2.2 *Signal processing*

The wavelet transform technique was utilized to minimize the signal noise based on finding the differences between the wavelet spectrum of the noise and the true signal at different scales (Mallat and Hwang, 1992). The reconstructed signal (i.e, without a noise) was then compiled using the wavelet transform reconstruction algorithm (The MathWorks Inc., Natick, U.S.). Traditional de-noising techniques require users to set a frequency band for noises, whereas the wavelet transform technique does not require any prior knowledge of the signal and it better preserves the information on the primary signals (Wu et al., 2001). The wavelet noise removal technique has also been successfully employed in other studies on turbulent wall jets and particle clouds (Shojaeizadeh et al., 2018; Sharif and Azimi, 2020). In order to convert voltage signals to velocity data, a segment of the time-series of voltages from each sensor was required for cross-correlation. The segment size and overlap between each segment can significantly improve the quality of velocity data, therefore, the effect of voltage data partitioning (i.e., selection of window size) and overlap of voltage segments on variations of velocity and turbulence properties of sand particles were investigated. This analysis was

performed by partitioning the time series of voltage signals into different segment lengths and overlapping a percentage of processed data's time series. The window length was considered an important parameter in both determining the frequency resolution and calculating the average values (Lim et al., 2020). A 50% overlap of the time-series segments was first employed to investigate the velocity variance for estimation of power spectra with the fast Fourier transform algorithm (Welch, 1967). Recently, segment overlapping was employed to high-frequency time-series data (Azimi et al., 2012a; Schmidt et al., 2017; Sharif and Azimi, 2020; Lim et al., 2020) and this study indicated the importance of segment length and overlapping.

A frequency of 30 Hz for the time series of velocity data was selected with a base segment size of $\Delta L_s = 2^{11} = 2{,}048$ voltage signals. For an extensive investigation of segment length efficiency on the accuracy and consistency of velocity data, the time series of voltage signals were divided into different segment lengths of 512, 1,024, and 2,048 data points. Higher-frequency velocity data was attained by reducing the segment lengths to $\Delta L_s = 2^9 = 512$ and $2^{10} = 1{,}024$. In doing so, the sampling frequency of velocity data was increased by reducing the segment lengths to L_s = 60 Hz and 120 Hz for L_s = 1,024 and 512, respectively. Figure 3.3 shows the cross-correlations of voltage signals with different segment sizes of 512, 1,024, and 2,048 and different overlap of 25% and 50%. As can be seen, reducing the segment size increased the calculated velocity fluctuations of sand particles. It was also found that data uncertainty due to segment overlapping for sand velocity was ±6% which was equal to ±7 mm/s. Furthermore, the data uncertainty for turbulence intensity of segment overlap (i.e., ΔL_s = 2,048) was ±16% and a turbulent intensity of ±56% was obtained when 50% segment overlapping was used. Also, the turbulence intensity increased by ±37% and ±41% when the segment length was reduced to ΔL_s = 512, and 1,024, respectively. The smaller window sizes and overlapping resulted in higher signal fluctuations and noisy data. Therefore, a segment length of ΔL_s = 2,048 with no overlapping (L_s = 0%) was selected for data preparation and analysis.

The effect of velocity ratio on turbulence characteristics of sand-water coaxial jets was also investigated and the time-series of turbulent characteristics are shown in Figure 3.4. The time histories of particle velocity fluctuations, u' at x/d_o = 24 and for sand-water coaxial jets with different velocity ratios (i.e., $0 \leq Ru \leq 1.86$) are plotted in Figure 3.4a

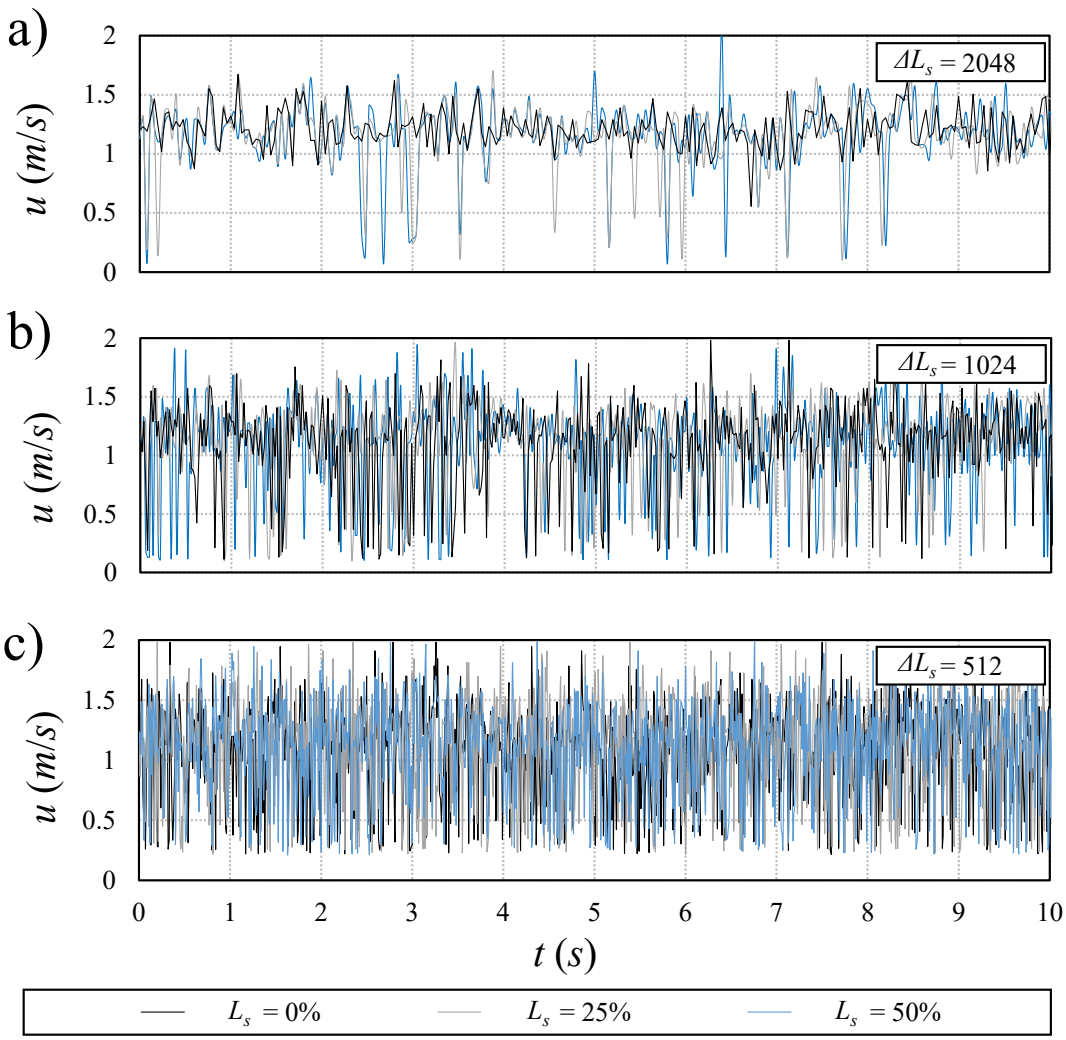

Figure 3.3: Typical instantaneous sand velocity data extracted from voltage signals and using different segment overlapping L_s = 0%, 25%, and 50% and segment lengths ΔL_s for Ru = 0.62 and x/d_o = 10: a) ΔL_s = 2048; b) ΔL_s = 1024; c) ΔL_s = 512.

The time series of velocity fluctuations indicated that the water flow in the inner jet of sand-water coaxial jets has a noticeable impact on the uncertainties of velocity fluctuations in comparison with a single sand jet with no water discharge (i.e., Ru = 0). It was found that data uncertainties for Ru = 0, 0.74, and 1.86 were ± 3.5%, ± 0.61%, and ± 0.67%, respectively. The time history data indicated an inverse correlation between velocity fluctuations and velocity ratio and velocity fluctuations decreased as Ru increased. Figure 3.4b shows the effect of velocity ratio on the time history of turbulence intensity. The turbulence intensity was calculated based on the ratio of the root-mean-square of particle velocity, u_{rms}, to the time-averaged particle velocity, u_{ave}. It was found that the turbulence intensities of Ru = 0.74 and 1.86 were below the turbulence intensity of the single-phase by 7% and 3%, respectively.

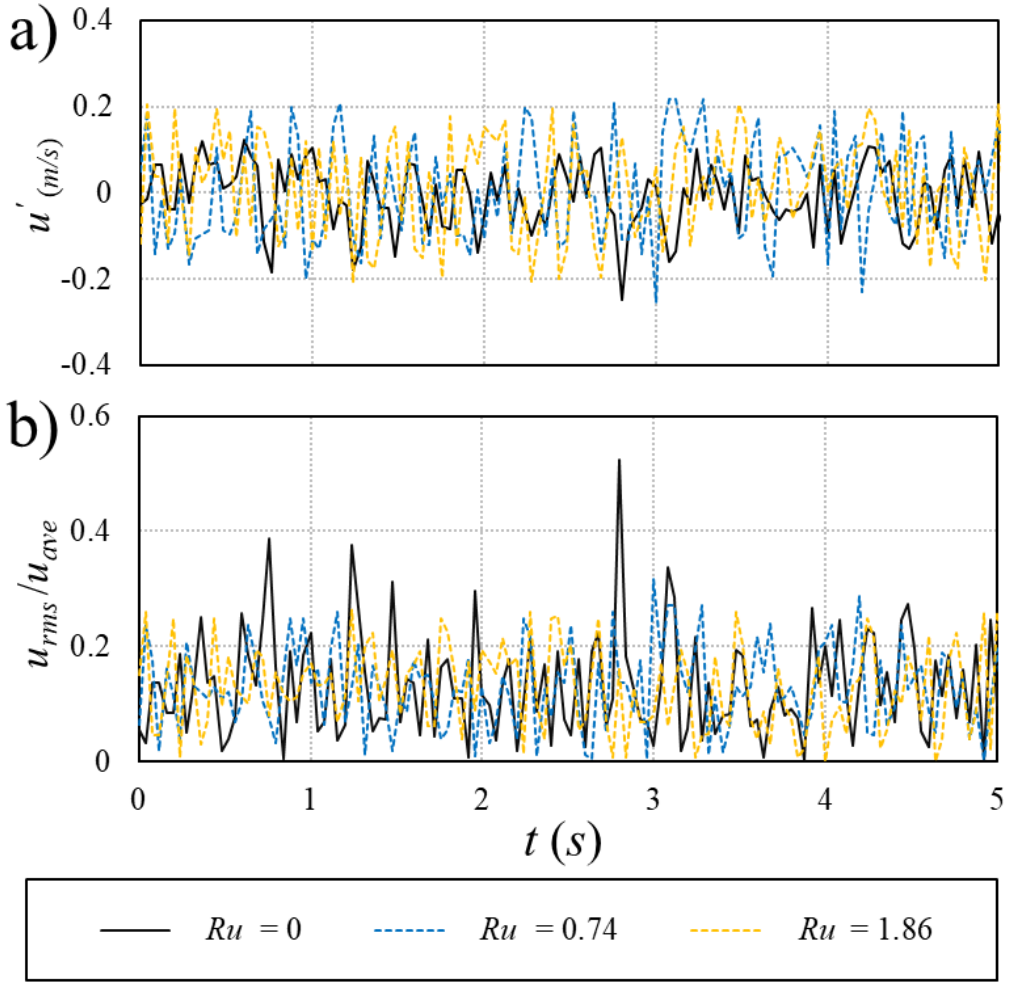

Figure 3.4: Effects of velocity ratio on the time history of turbulent characteristics of sand-water coaxial jets at $x/d_o = 24$: a) time history of velocity fluctuations (u'); b) time history of turbulence intensity (u_{rms}/u_{ave}).

3.3 Results and discussion

3.3.1 *Mass and momentum fluxes*

To assess the accuracy of optical probe measurements and signal processing techniques, integral quantities such as sand mass and momentum fluxes were calculated in different cross sections along the vertical axis. The total number of sand particles that pass certain cross section (i.e., a volume with a thickness of unity) in a sand-water coaxial jet can be calculated by integrating the product of sand velocity and concentration over a known cross section as:

$$\dot{m} = \frac{dm}{dt} = 2\pi\rho_s \int_0^r c(x,r)u(x,r)\, r dr$$

(3.1)

Similarly, the sand-phase momentum flux can be calculated in each cross section as:

$$\dot{M} = \frac{dM}{dt} = 2\pi\rho_s \int_0^r c(x,r)u(x,r)^2 r dr$$

(3.2)

Figure 3.5 shows the variations of the defined integral quantities with x/d_o for sand-water coaxial jets with different velocity ratios of Ru = 0.62, 0.93, 1.24, and 1.86. The ratio of the integrated mass flux in each cross-section was normalized with the initial sand mass flux at the nozzle $\dot{m}_o = \rho_s[\pi(d_a^2 - d_o^2)/4]u_o c_o$ where c_o is the initial sand concentration. Figure 3.5a shows the variations of sand mass flux with x/d_o for sand-water coaxial jets and slurry jets with a sand particle diameter of D_{50} = 0.206 mm (Hall et al., 2010); the overbars indicate the uncertainty of measurement in this study. The calculated sand mass flux in some points were above unity indicating that the initial sand mass flux was underestimated due to uncertainty in estimation of c_o = 0.6 and neglecting the effects of sand particle size distribution. As can be seen in Figure 5a, the integrated sand mass flux was more than 90% of the initial sand mass flux for $x/d_o < 12$, and it reduced to 80% for $x/d_o < 40$. It is worth noting that the calculated sand mass and momentum fluxes were based on sand velocity and concentration measurement within $-5 \le r/d_o \le 5$. Therefore, all particles left beyond the measurement region were not included in calculations. A lower sand mass flux was consistently detected in previous tests as the sensitivity of light refracting probes and the quality of voltage signals decrease once sand concentration decreases far from the jet's centerline (Hall et al., 2010; Sharif and Azimi, 2020). For example, mass flux measurements by Hall et al. (2010) scattered around the unity with a maximum fluctuation range of ±23%. Figure 3.5b in our study shows the variations of sand momentum flux with x/d_o for sand-water coaxial jets with different velocity ratios. The sand momentum flux was normalized with the initial sand momentum flux at the nozzle, $\dot{M}_o = \rho_s[\pi(d_a^2 - d_o^2)/4]u_o^2 c_o$. The measured sand momentum fluxes for slurry jets in Hall et al. (2010) were also plotted for comparison. As can be seen, sand momentum flux continuously decreased from the nozzle (i.e., $x/d_o = 0$) and became constant for $x/d_o > 20$. This indicates a uniform sand velocity and concentration distribution beyond this region. At this region, the coaxial jet flow is very weak and sand particles reached their settling velocities. The maximum uncertainty level of sand mass flux was ±6.9% for $x/d_o < 20$. However, further downstream at $x/d_o > 30$,

the maximum uncertainty level increased to ±9.3% due to lower sand concentration and probe sensitivity.

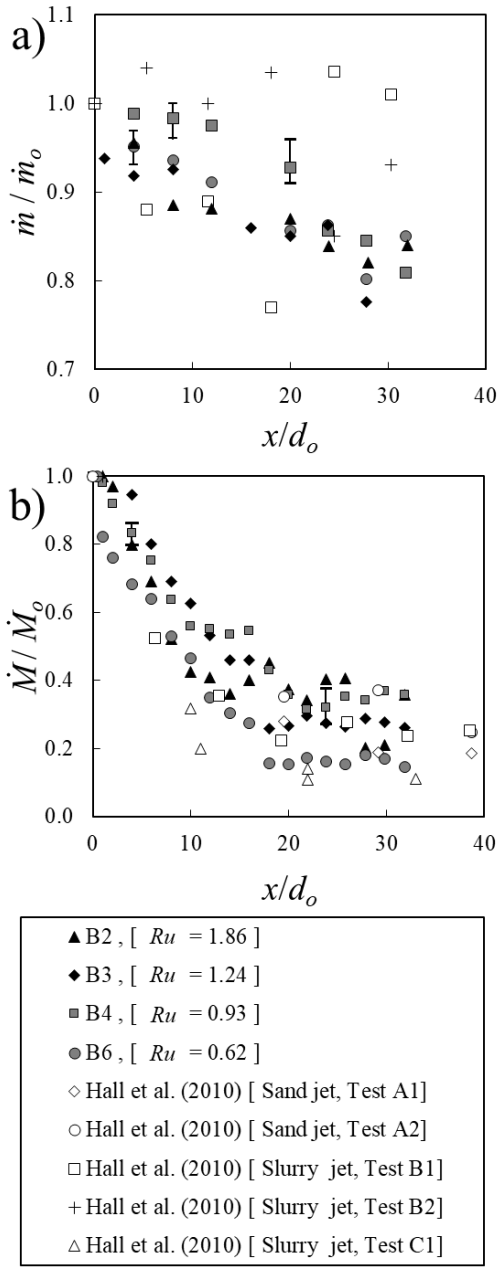

Figure 3.5: Variations of the integral quantities of sand-water coaxial jets with normalized distance from the nozzle for different velocity ratios, Ru = 0.62, 0.93, 1.24 and 1.86: a) variations of the normalized sand mass flux with normalized axial distance from the nozzle; b) variations of the normalized momentum flux with normalized axial distance from the nozzle.

3.3.2 *Spreading rate and mixing*

The spreading rate in jets is defined as $db(x)/dx$ where $b(x)$ is the half-width of the jet at a point where the velocity is 50% of the centerline velocity (Kotsovinos, 1976; Rajaratnam,

1976). Many experimental studies in the literature have used the definition of half-width to normalize velocity and concentration data (Fischer et al., 1979; Lee and Chu, 2003; Azimi et al., 2012b). The spreading rate in single-phase water jets has ranged between 0.104 and 0.115 (Wang and Law, 2002) and the spreading rate of slurry jets has been found to be correlated with sand initial concentration, $c_o^{-3/2}$ (Azimi et al., 2012b). In particle-laden jets and plumes, the normalized sand concentration c/c_m does not reach the 50% value, and as a result, higher concentration and velocity have been used as a scaling factor for prediction of the spreading rate (Azimi et al., 2012a; Moghadaripour et al., 2017a; Sharif and Azimi, 2020). The reference velocity and concentration for prediction of spreading rate was chosen based on c/c_m = 80%.

Figure 3.6 shows the variations of the normalized half-width, based on concentration profile b_c, with the normalized distance from the nozzle for sand-water coaxial jets with different velocity ratios (i.e., $0.62 \leq Ru \leq 1.86$). The spreading rates of single-phase water jets (i.e., $db(x)/dx = 0.114$), as recommended by Wygnanski and Fiedler (1969), and slurry jets was also added for comparison (Azimi et al., 2012b). Fan et al. (1996) indicated that the spreading rate of single-phase coaxial jets was higher than solid-gas coaxial jets. Mazurek et al., (2002) further showed that the sand jet spreading rate increases with the Froude number where $Fr = u_o/d_o g[(\rho_s - \rho_w)/\rho_w]$ and g is the acceleration due to gravity. The virtual origin of jets, which is the intersection of the half-width of spreading rate and the jet axis, was reported between $0.9d_a$ and d_a (Flora and Goldschmidt, 1969). Figure 3.6 shows the effects of the velocity ratio on the spreading rate of sand-water coaxial jets in this study, and the spreading rate of sand-water coaxial jets for all velocity ratios were lower than the spreading rate of single-phase jets and higher than slurry jets (Figure 3.6a). As can be seen in Figure 3.6b the spreading rate of sand-water coaxial jets decreased by increasing Ru. It was found that spreading of the sand-water coaxial jet linearly correlated with Ru as:

$$b_c/d_o = -0.033Ru + 0.11 \quad (3.3)$$

The coefficient of determination was $R^2 = 0.98$ indicating a strong correlation between spreading rate and Ru. Figure 3.7 shows the luminescent visualization of sand-water coaxial jets for a wide range of velocity ratios. The green areas show the region of high tracer intensity which indicates high mixing and entrainment (see Figure 3.7a). The higher intensity of green tracer can be found at the outer edges of the coaxial jets as well (see Figures. 3.7b-3.7d).

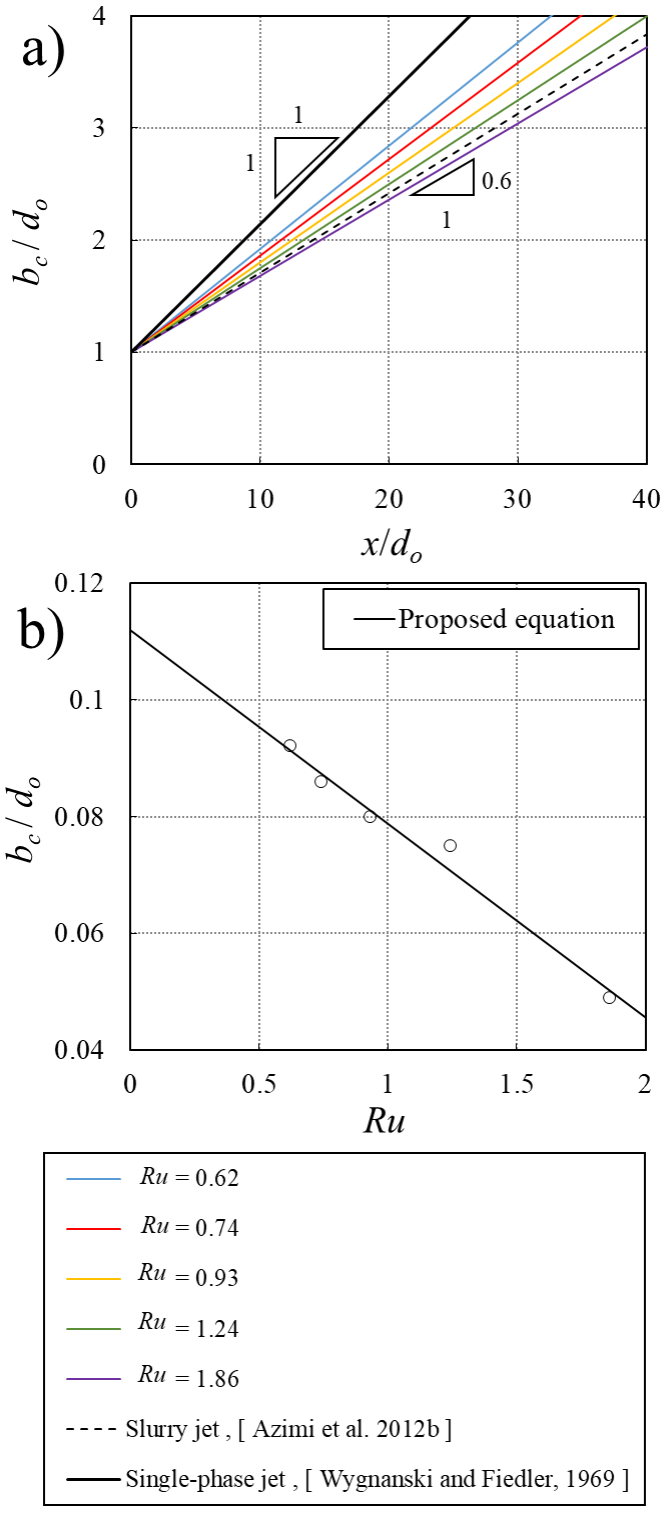

Figure 3.6: Effects of velocity ratio on the spreading rate of sand-water coaxial jets: a) variation of the spreading rate with velocity ratio x/d_o; b) variation of the spreading rate with velocity ratio.

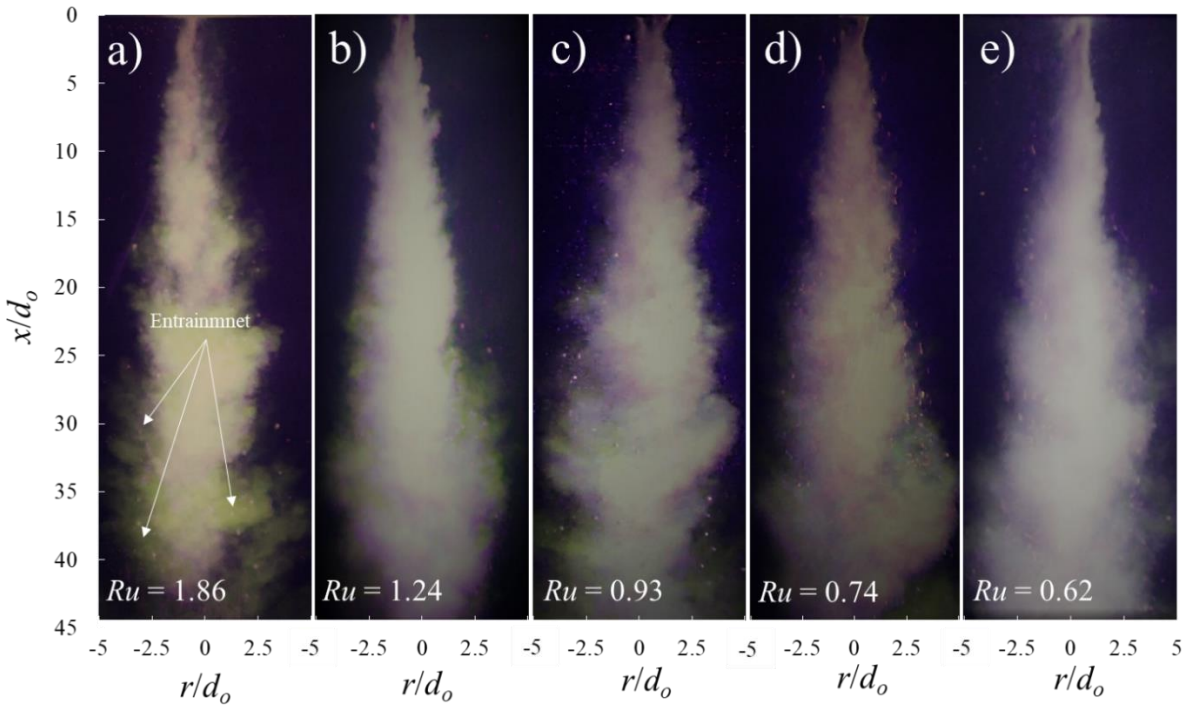

Figure 3.7: Images of sand-water coaxial jets for different velocity ratios: a) Ru = 1.86; b) Ru = 1.24; c) Ru = 0.93; d) Ru = 0.74; r) Ru = 0.62.

3.3.3 *Sand concentration*

The effects of velocity ratio on variations of the centerline concentration of sand particles with distance from the nozzle for sand-water coaxial jets is shown in Figure 3.8. The centerline concentration c_m was normalized with the initial sand concentration c_o, the distance from the nozzle x was normalized with the inner nozzle diameter d_o, and all data points were plotted in log-log scale. The overbar in the sand concentration data indicates the uncertainty of concentration measurements. The variations of sand centerline concentration for sand and slurry jets were also included in Figure 3.8. As can be seen, the normalized sand concentration c_m/c_o varied non-linearly with x/d_o and the slope of correlations linked with Ru. As can be seen in Figure 3.8, all cases exhibited a similar decay rate for sand concentration within the mixing zone of a length approximately six times that of the nozzle diameter. The zone of jet development (i.e., $c_m/c_o \approx 1$) is six times that of the nozzle diameter for single-phase jets and between $3.7d_o$ and $5.8d_o$ for slurry jets (Hall et al., 2010). Sadr and Klewicki (2003) found that the zone of flow development for single-phase coaxial jets with $Ru > 1$ is three times more than the nozzle diameter. Beyond the initial region (i.e., $x/d_o > 6$), the decay rates of sand concentration in sand-water coaxial jets were faster than the mixing region. The decay rates of sand concentration in sand-water coaxial jets were lower than the decay rate of sand

concentration in slurry jets, except for Ru =1.86, and higher than the particle clouds with S_t = 0.52 (Sharif and Azimi, 2020). A power law correlation was developed for predicting the centerline sand concentration along the jet axis as (R^2 = 0.98):

$$\frac{c_m}{c_o} = \frac{1}{2}[Ru+1]\left(\frac{x}{d_o}\right)^{-\frac{Ru}{3}} \tag{3.4}$$

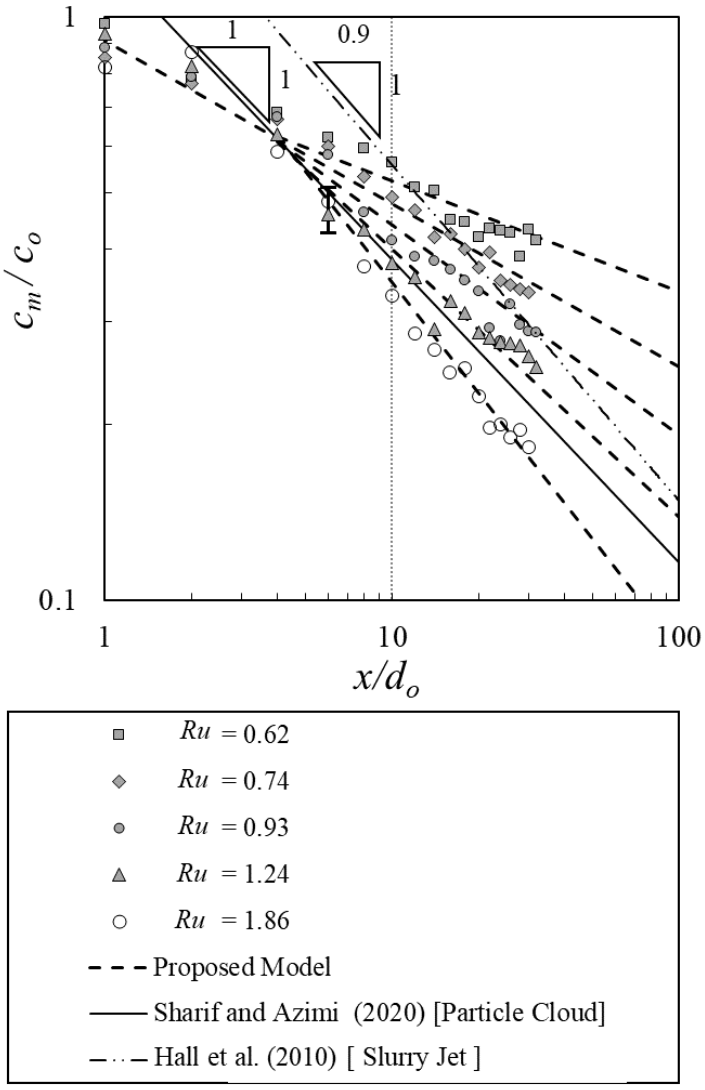

Figure 3.8: Effects of velocity ratio on variations of the normalized sand concentration c_m/c_o of sand-water coaxial jets with normalized axial distance from the nozzle x/d_o.

Figure 3.9 shows the transverse profiles of the normalized sand concentration c/c_m with the normalized transverse distance from the nozzle r/d_o for sand-water coaxial jets with a wide range of velocity ratios (i.e., $0.62 \leq Ru \leq 1.86$). As sand concentrations were above $0.5c_m$, it

was not possible to use $0.5c_m$ as a classic scale to normalize the radial distance from the nozzle r, therefore, the radial distance from the jet axis was normalized with the nozzle diameter d_o. The radial concentration variation of single-phase water jets by Lee and Chu (2003) was also added to Figure 3.9 for comparison. A Gaussian distribution was then used to describe the radial variations of sand concentration similar to the radial distribution of single-phase jets. The radial distribution of sand concentration indicates that the spreading rate of sand-water coaxial jets increased by decreasing Ru. The relatively high spreading rate allowed sand particles to disperse and mix with the ambient water. For $x/d_o > 28$ and $r/d_o > 3$, particles tended to follow the shear layer eddies and a discrepancy occurred between the coaxial jet measurements and the radial distribution of concentration in single-phase water jets.

Using a Gaussian distribution function, the radial variations of sand concentration in sand-water coaxial jets can be described as:

$$\frac{c}{c_m} = \exp\left[-0.693\,\psi_c\left(\frac{r}{d_o}\right)^{1.4}\right] \tag{3.5}$$

with a coefficient of determination $R^2 = 0.94$. The parameter ψ_c was correlated with both x/d_o and Ru and can be described as:

$$\psi_c = \alpha_c\, Ru^{1/2}\left(\frac{x}{d_o}\right)^{-5/4} \tag{3.6}$$

where α_c is a coefficient with a value of 4.18 for velocity ratios ranging between 0.62 to 1.86.

3.3.4 *Sand velocity*

Variations of normalized sand centerline velocity with x/d_o for sand-water coaxial jets are plotted in Figure 3.10. The centerline sand velocity u_m was normalized with the initial velocity of sand particles at the nozzle u_o and the correlations of normalized velocity with distance were plotted in log-log scale. The predictions of sand centerline velocity of slurry jets with a small particle size range of $0 < S_t \leq 0.1$ (Hall et al., 2010) and the centerline velocity of water in single-phase buoyant jets (Papanicolaou and List, 1988) were included in Figure 3.10 for comparison.

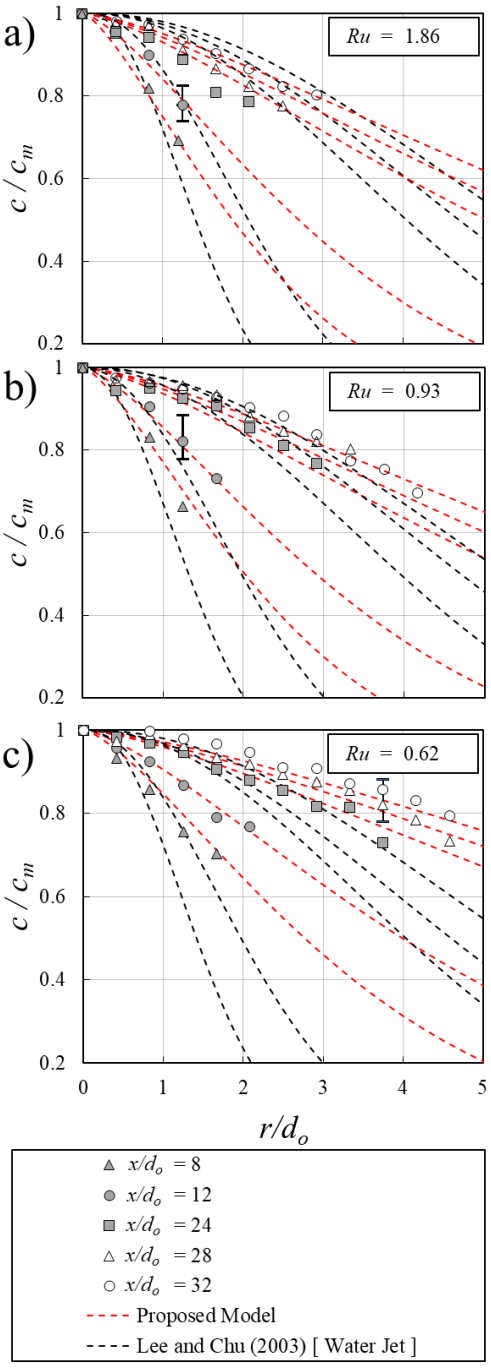

Figure 3.9: Effects of velocity ratio on the radial variations of normalized sand concentration c/c_m with normalized distance from the nozzle, x/d_o: a) $Ru = 1.86$; b) $Ru = 0.93$; c) $Ru = 0.62$.

The prediction equation for centerline velocity variations of sand particles in particle clouds with $S_t = 0.52$ (Sharif and Azimi, 2020) was also included in Figure 3.10. The maximum uncertainty of sand velocity measurements is shown as an overbar indicating a variation of ±7.1%. As can be seen, the decay rate of sand velocity at the jet centerline was independent of the velocity ratio for $x/d_o \leq 6$ (i.e., initial mixing zone). However, for $x/d_o > 6$ the decay rate of sand velocity was correlated with velocity ratio and it increased with decreasing Ru. The decay

rate of sand velocity was similar to slurry jets for sand-water coaxial jets with small velocity ratios (i.e., Ru = 0.62). However, the decay rate of velocity in sand-water coaxial jets was higher than the decay rate of particle clouds (Sharif and Azimi, 2020) and lower than the decay rate of single-phase buoyant jets (Papanicolaou and List, 1988). The wide variation in sand centreline velocity clearly emphasizes the importance of velocity ratio as a controlling parameter in particle mixing by two-phase sand-water coaxial jets.

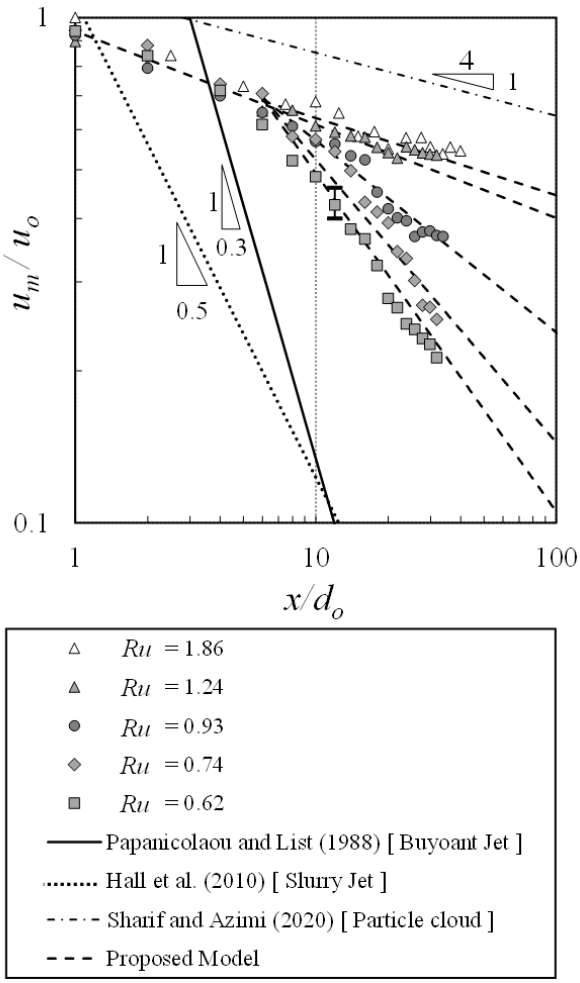

Figure 3.10: Effects of velocity ratio on variations of the normalized sand velocity u_m/u_o of sand-water coaxial jets with normalized axial distance from the nozzle, x/d_o.

Moreover, due to the covering effect in the potential core of annular jets (i.e., $x/d_o \leq 6$), the outer region of coaxial jets (i.e., sand jet) was less affected by the inner water jet. Consequently, all jets with different velocity ratios experience the same flow characteristics in this region (Chan and Ko, 1978). On the other hand, in the zone of developed flow (i.e., $x/d_o >$ 6), the jet characteristics such as the decay rate of velocity and concentration varied significantly with velocity ratio. In the zone of developed flow, the momentum of the water

phase was transferred to the sand inner jet and sand velocity became comparable to water jet velocity indicating a one-way coupling between sand particles and water. In other words, the excess potential energy and momentum contributed by the high-water velocity caused an increase in the mean velocity of the sand-phase and decreased the decay rate in comparison for $x/d_o > 6$. An empirical formula was developed to predict the sand-phase centerline velocity of sand-water coaxial jets in flow development zone**:**

$$\frac{u_m}{u_o} = a\left(\frac{x}{d_o}\right)^{-b} \tag{3.7}$$

where a and b are exponential functions of velocity ratio and they are defined as $a = 7/5Ru^{-9/10}$ and $b = 1/3Ru^{-3/2}$ with $R^2 = 0.9$ and 0.94, respectively.The effect of velocity ratio on the radial distribution of sand axial velocity in sand-water coaxial jets are shown in Figure 3.11. The axial velocities at different radial positions u were normalized with the centerline axial velocity u_m and the radial distance from the centerline r was normalized with the nozzle diameter d_o. The radial distribution of water velocity for single-phase water jets was also added for comparison (Lee and Chu, 2003). The results of this study show that at $x/d_o = 8$ and 12 the radial distributions of sand axial velocity were similar to the radial distribution of single-phase jets. However, for $x/d_o > 12$, the radial distributions of sand axial velocity were much wider than the prediction curves for single-phase water jets. As depicted in Figure 3.11a, less radial discrepancy was found between the radial velocity distribution of sand-water coaxial jet with $Ru = 1.86$ and single-phase water jets, whereas the discrepancy between the radial distribution of sand axial velocity for sand-water coaxial jets and the prediction curves of single-phase water jet is noticeable at $x/d_o = 32$ (see Figure 3.11b). For coaxial jets with smaller velocity ratios (i.e., $Ru = 0.62$), the deviation between the axial velocity measurements and single-phase jet began at $x/d_o = 24$ (see Figure 3.11c). In coaxial jets with a high-velocity ratio, the zone of fully developed jets was established much further from the nozzle at $x/d_o \geq 32$ and as velocity ratio decreased, the zone of fully developed jets was formed closer to the nozzle at $x/d_o \geq 24$.

In the zone of fully developed jets, the rate of momentum transfer from the water phase was very high, such that for relatively small particle sizes, sand particles followed the shear layer vortices of the outer jet and the radial distribution of sand axial velocity became wider than the corresponding single-phase jet.

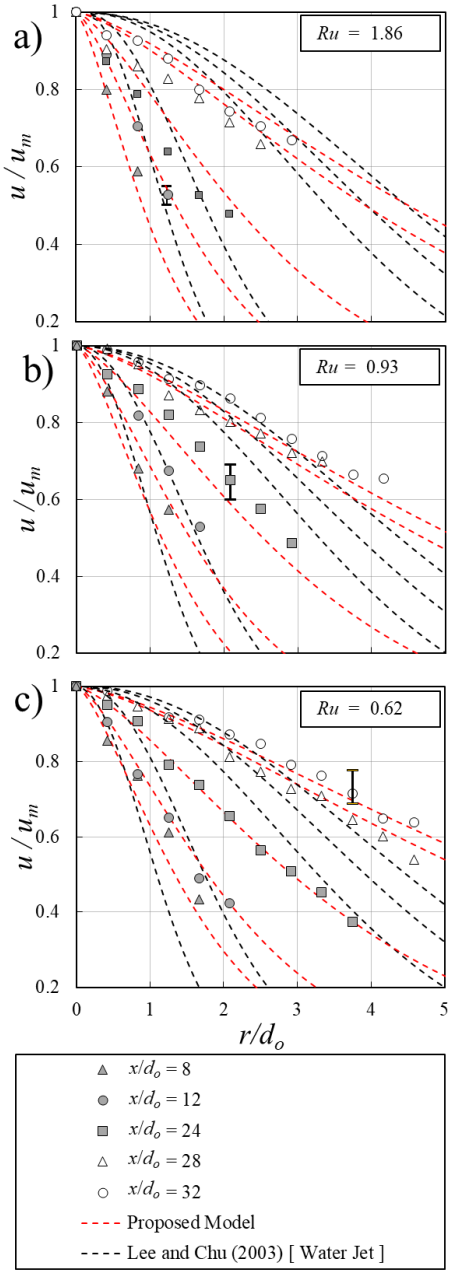

Figure 3.11: Effect of velocity ratio on the radial variations of normalized sand velocity u/u_m of sand-water coaxial jets with different normalized distances from the nozzle, x/d_o: a) Ru = 1.86; b) Ru = 0.93; c) Ru = 0.62.

A Gaussian distribution model was selected to develop a prediction model for radial distribution of sand axial velocity for $8 \leq x/d_o \leq 32$ as (R^2= 0.98):

$$\frac{u}{u_m} = \exp\left[-0.693\,\psi_u \left(\frac{r}{d_o}\right)^{1.4}\right] \tag{3.8}$$

The parameter ψ_u was found to be correlated with x/d_o and Ru as:

$$\psi_u = \alpha_u Ru^{1/2}\left(\frac{x}{d_o}\right)^{-1} \tag{3.9}$$

and the values of the coefficient α_u were 6.78 and 3.32 for $8 \leq x/d_o < 24$ and $x/d_o > 24$, respectively.

3.3.5 *Drag reduction of group particles*

To investigate the particle motion and particle-particle interactions in sand-water coaxial jets, the cross-sectional average of drag coefficients at different distances from the nozzle were calculated and the results were compared with the drag coefficient of individual sand particles of the same size. The average drag force F_D over a cross-section in sand-water coaxial jets was computed by balancing the rate of change of momentum of the sand-phase in a disk-shaped control volume (see Figure 12). The momentum flux of the sand phase was also calculated using the radial distributions of the axial sand velocity and concentration (Azimi et al., 2012b). The buoyancy force of particles $F_B = mg\rho_w/\rho_s$ can be estimated knowing the mass of sand particles, m, in a disk-shaped control volume. Thus by balancing the rate of change of momentum $M_{(x)}$ with the gravitational F_g and buoyancy F_B forces on a disc-shaped control volume, the average drag force F_D can be computed as:

$$M_{(x+\Delta x)} - M_{(x)} = F_{g_{(x+\frac{\Delta x}{2})}} - F_{B(x+\frac{\Delta x}{2})} - F_{D(x+\frac{\Delta x}{2})} \tag{3.10}$$

The momentum flux of sand particles $M_{(x)}$ at each cross-section can be calculated by integrating the product of sand concentration and velocity in radial direction as:

$$M_{(x+\Delta x)} - M_{(x)} = 2\pi\rho_s \left(\int_0^{r_{(x+\Delta x)}} c_{(x+\Delta x)} u_{(x+\Delta x)}{}^2 r_{(x+\Delta x)} dr - \int_0^{r_{(x)}} c_{(x)} u_{(x)}{}^2 r_{(x)} dr \right) \tag{3.11}$$

To calculate the drag coefficient acting on individual particles in a disk-shaped control volume, the computed drag force was divided by the estimated number of particles within the control volume as:

$$f_D = F_D / N_p$$

(3.12)

and the number of particles N_p can be calculated as:

$$N_p = \frac{6\bar{c}\, V_{disc}}{\pi D_{50}^3}$$

(3.13)

where $\bar{c}$ is the average volume of sand particles occupying in the disk-shaped control volume V_{disc} and this product was calculated for each cross-section as:

$$\bar{c} V_{disc} = \frac{1}{2} 2\pi \left(\int_0^{r_{(x)}} c_{(x)} r_{(x)} dr + \int_0^{r_{(x+\Delta x)}} c_{(x+\Delta x)} r_{(x+\Delta x)} dr \right) \Delta x$$

(3.14)

Using Eqs. (3.7-3.9), the averaged drag force for a single sand particle was calculated as:

$$f_D = \frac{1}{8} C_d \rho_w \frac{\pi D_{50}^{\ 2}}{4} (u_{(x)} + u_{(x+\Delta x)})^2$$

(3.15)

Chien (1994) proposed a model for estimating the drag coefficient of individual sand particles based on the sphericity ratio in the range of $0.2 \leq \varphi \leq 1$ (where $\varphi = 1$ is a sphere shape) and for $R_p \leq 5000$ as:

$$C_d = \frac{30}{R_p} + 67.3 \exp(-5\varphi)$$

(3.16)

Schiller & Neumann (Wörner, 2003) proposed an equation to calculate the drag coefficient of individual particles in stagnant water for $0.1 \leq R_p \leq 800$ as:

$$C_d = \frac{24}{R_p} + (1 + 0.15 R_p^{\ 0.687})$$

(3.17)

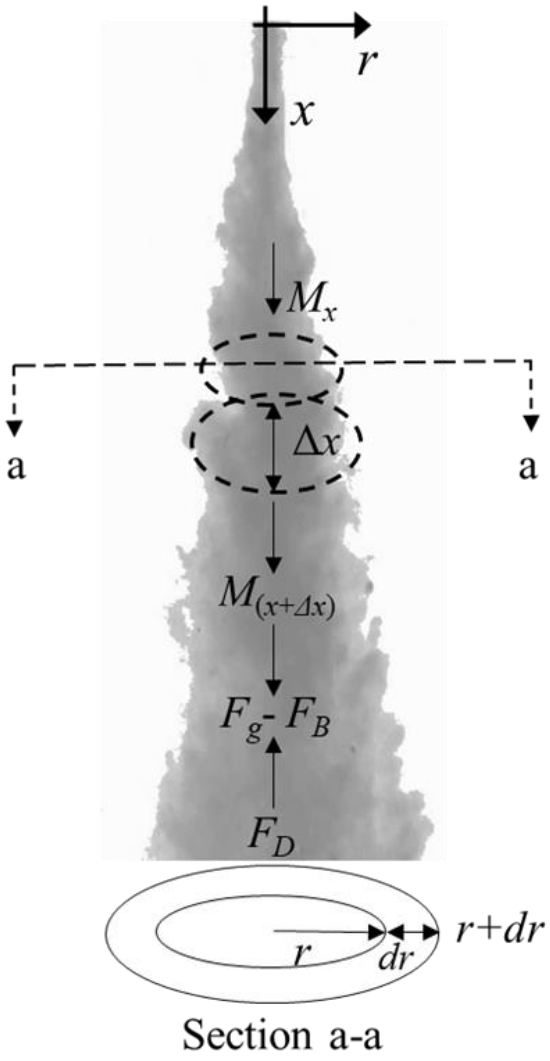

Figure 3.12: Schematic of the momentum balance in a coaxial sand-water jet.

Clift et al. (1978) formulated the drag coefficient for non-spherical particles for $40 \leq R_p \leq 400$ as:

$$C_d = 9.69\, R_p^{-0.78}(1 + 0.08 R_p^{0.82})$$

(3.18)

For sand and gravel, the drag coefficient was formulated by Engelund and Hansen (1967) as:

$$C_d = \frac{24}{R_p} + 1.5$$

(3.19)

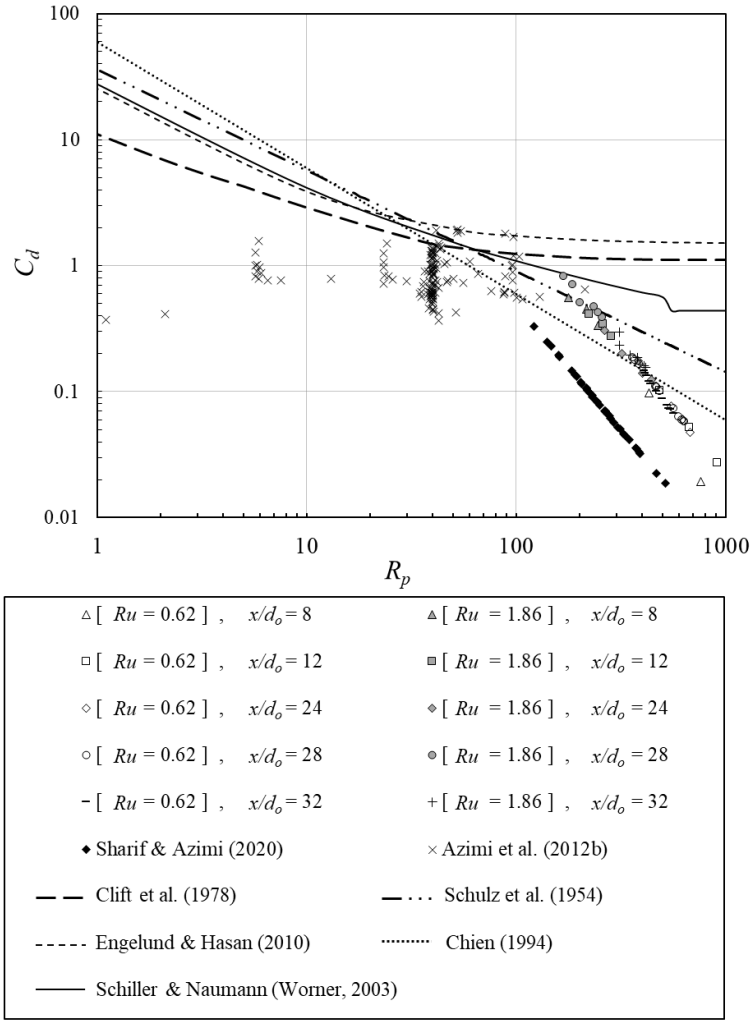

Figure 3.13: Variations of the drag coefficient of sand particles C_d for sand-water coaxial jets with particle Reynolds number R_p for different normalized axial distance from the nozzle, x/d_o.

Figure 3.13 shows the variations in the cross-sectional average drag coefficients of sand-water coaxial jets with particle Reynolds number R_p in the range of $100 < R_p < 700$. The estimated average drag coefficient of slurry jets (Azimi et al., 2012), particle clusters (Azimi, 2019), and particle clouds (Sharif and Azimi, 2020) were added for comparison (see chapter 2). Different prediction models for estimating of drag coefficients of individual spheres and sand particles were also added to Figure 3.13. As can be seen, the variations of drag coefficients in sand-water coaxial jets had a similar trend with the proposed equations of Schultz et al. (1954) and Chien (1994) based on sphericity ratio assumptions. However, the average drag coefficients of sand-water coaxial jets were smaller than the predictions: for higher particle Reynolds numbers (i.e., $R_p > 100$), the grouping effect significantly reduced the average drag coefficient of particle groups (Azimi et al., 2012b). Similar grouping effects were found in sand-water coaxial jets: the drag coefficients of sand-water coaxial jets with higher velocity

ratios became higher than C_d of the coaxial jets with low-velocity ratios. Furthermore, the drag coefficients of coaxial jets were slightly higher than the C_d of particle clouds and close to the C_d of slurry jets. The relatively lower values of particle Reynolds numbers in particle clouds and sand jets in comparison with coaxial sand-water jets was due to lower sand particle velocity in particle clouds and sand jets.

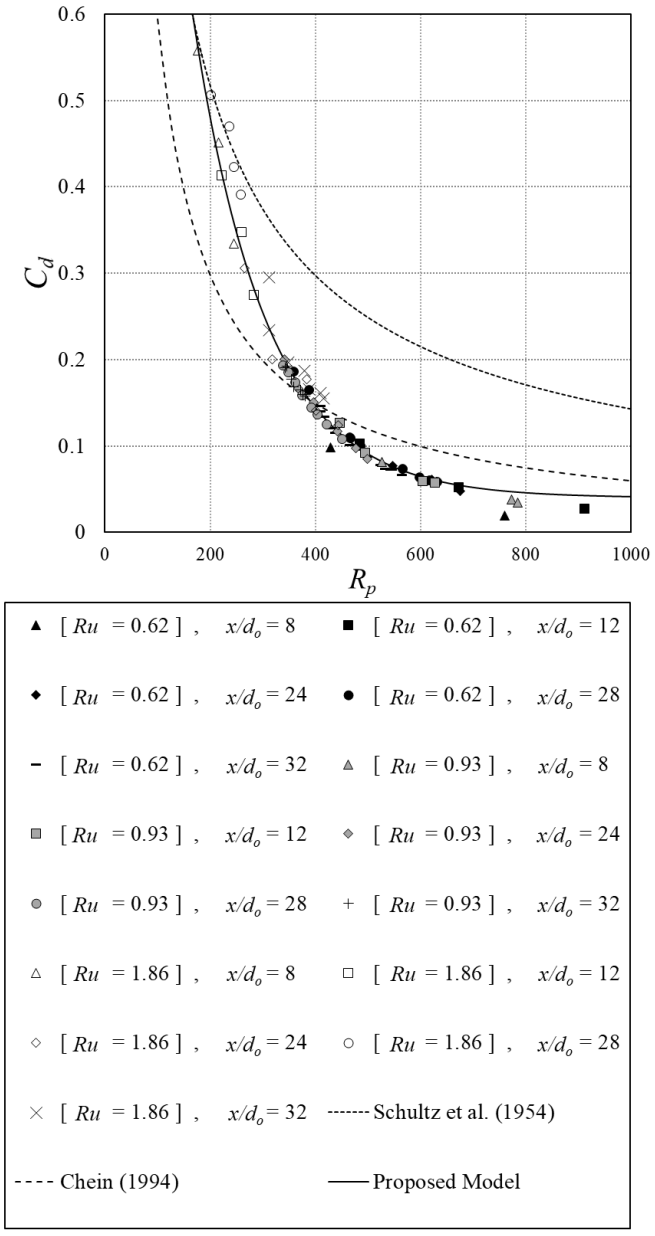

Figure 3.14: Variations of the drag coefficient of sand particles C_d for sand-water coaxial jets with particle Reynolds number R_p for different normalized axial distance from the nozzle x/d_o and for different velocity ratio ($0.62 \leq Ru \leq 1.86$).

Figure 3.14 shows the effects of velocity ratio (i.e., $0.62 \leq Ru \leq 1.86$) on variations of the average drag coefficient of sand particles C_d with particle Reynolds number R_p. The drag coefficient prediction models for none-spherical particles (Schultz et al., 1954) and individual sand particles (Chien, 1994) with a sphericity ratio of 0.75 were also added for comparison. As shown, the drag coefficients for Ru = 1.86 were higher than the C_d of individual particles, whereas for Ru = 0.93 and 0.62, the drag coefficient reduced by almost two times compared to the C_d for coaxial jets with Ru = 1.86 and became less than the C_d of individual particles. This indicates that the higher decay rate of sand concentration associated with sand-water coaxial jets with higher velocity ratios decreased the grouping effect and as a result, increased the averaged drag coefficient. Therefore, C_d increased significantly, and the grouping effect became less significant as particles descended far from the nozzle. A formula was thus proposed to predict the correlation between C_d and R_p for sand-water coaxial jets ($R^2 = 0.92$):

$$C_d = 0.04 + 2\, e^{(-0.007 R_p)} \tag{3.20}$$

3.3.6 *Particle-particle interactions*

The effect of particle-particle interactions in shear flows and multi-phase turbulent jets can be studied by investigating the variations of the Bagnold number in both axial and radial directions. Sharif and Azimi (2020) evaluated the interparticle collision of particle clouds by calculating the Bagnold number and found that the interparticle collision occurred for $x/d_o \leq 10$, while for $x/d_o \geq 20$, the micro-viscous regime dominated the flow. The Bagnold number is a ratio of collisional stress to fluid shear stress (Bagnold, 1954) and expressed as:

$$Ba = c^* \frac{\rho_s \gamma\, D_{50}{}^2}{\mu} \tag{3.21}$$

where $\gamma = du/dr$ is the shear rate and c^* is the concentration of particles during flow spreading. Concentration can be expressed as:

$$c^* = \left[\frac{c^{1/3}}{c_o{}^{1/3} - c^{1/3}}\right]^{1/2} \tag{3.22}$$

The shear rate along the radial direction can be calculated using the proposed model for predicting axial velocity (Eq. (3.5)), as:

$$\frac{du}{dr} = 0.97\psi_u u_m \frac{r^{0.4}}{d_o^{1.4}} \exp\left[-0.693\psi_u \left(\frac{r}{d_o}\right)^{1.4}\right] \tag{3.23}$$

By assuming the boundary conditions as $u = 0$, $r/d_o \rightarrow w_j/2$, where w_j is the estimated jet width for $u = 0.01u_m$ and as $x_o/d_o > 32$ then $u_m \rightarrow 0$. The effect of velocity ratio on the radial variation of Bagnold numbers for $8 \leq x/d_o \leq 32$ is shown in Figure 3.15. The boundary of the transition regime ($Ba = 40$) and interparticle regimes ($Ba = 450$) were also included in Figure 3.15 and it can be seen that the Bagnold number at each cross-section has a peak value close to the axis of the jet and decreases far from the axis.

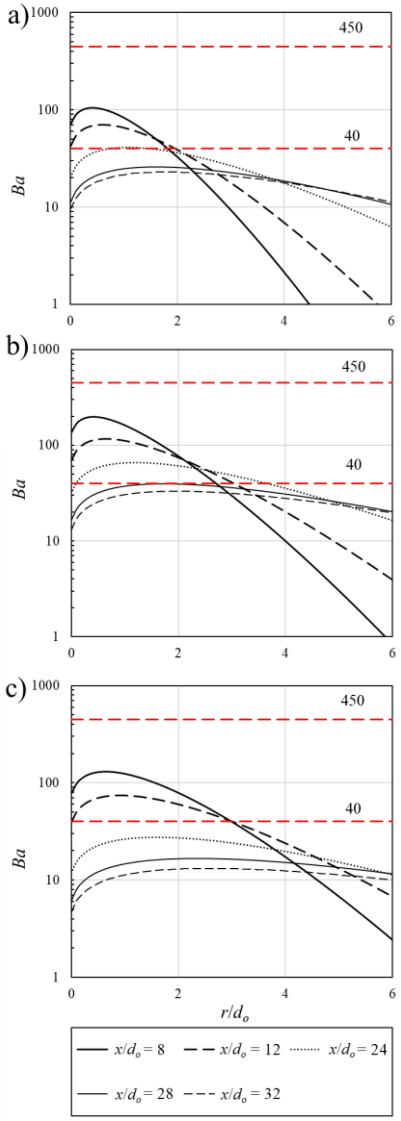

Figure 3.15: Effect of velocity ratio on the radial variations of the Bagnold number with different normalized axial distance from the nozzle, x/d_o: a) $Ru = 1.86$; b) $Re = 0.93$ c) $Ru = 0.62$

Figure 15a further shows the variations of the Bagnold number for sand-water coaxial jets with a velocity ratio of Ru = 1.86: all values of Bagnold numbers were in the transitional regime for $8 \leq x/d_o \leq 12$ and $r/d_o < 2$. For $x/d_o > 12$, the micro-viscous regime dominated the flow. For moderate velocity ratios (Ru = 0.93), the transitional regime occurred at $8 \leq x/d_o \leq 24$ and $r/d_o < 3$ (see Figure 3.15b). Furthermore, as depicted in Figure 3.15c coaxial jets with Ru = 0.62 experienced higher picks at $8 \leq x/d_o \leq 12$ and $r/d_o < 3$ indicating particle-particle interactions within the defined range of axial and radial distances from the nozzle.

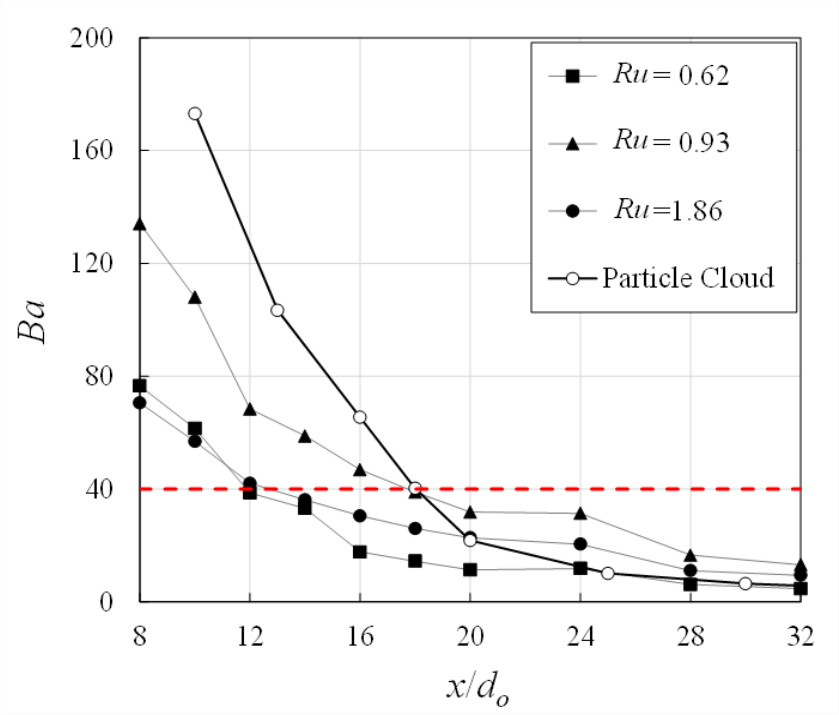

Figure 3.16: Effect of velocity ratio on the axial variations of the Bagnold number for sand-water coaxial jets.

Finally, the axial variation of Bagnold numbers in sand-water coaxial jets with different velocity ratios is shown in Figure 3.16. The axial variations of Bagnold numbers for particle clouds (Sharif and Azimi, 2020) were also included in Figure 3.16 for comparison. As can be seen, the sand-water coaxial jets with Ru = 0.93 experienced more interparticle interaction due to higher Bagnold numbers. As a result, sand particles in these coaxial jets reached the micro viscous regime for $x/d_o \leq 18$. For coaxial jets with Ru = 0.62 and 1.86, the Bagnold numbers decreased by approximately 50% and reached the micro viscous regime for $x/d_o \leq 12$. This indicates that the higher spreading rate for Ru = 0.62 and the higher concentration decay rate for Ru = 1.86 reduced the interparticle interactions. It was also found that all sand-water coaxial jets had smaller Bagnold numbers than the particle clouds.

3.4 Conclusions

Detailed laboratory experiments were carried out to study the effects of velocity ratio on dynamics of sand-water coaxial jets in stagnant water. The sand concentration and velocity of sand-water coaxial jets in both axial and transverse directions were measured by the light refractive optical probe (PV6). Integral quantities such as mass and momentum flux were computed to evaluate the performance of the optical probe and the accuracy of measurements. Experimental observations for sand-water coaxial jets indicated that the inner water jet can reduce the turbulent intensity of coaxial jets in the range of 3% to 7%. The effect of velocity ratio, Ru, on the spreading rate of sand-water coaxial jets was examined and it was found that the spreading rate increased by decreasing velocity ratio and can be correlated with a linear function. For moderate velocity ratios (i.e., $0.62 \leq Ru \leq 0.93$), the spreading rate was higher than the spreading rate of slurry jets and lower than the spreading rate of single-phase jets. For $Ru \geq 1.24$, the spreading rate of sand-water coaxial jets was similar to the spreading rate of slurry jets.

The mixing zone in sand-water coaxial jets was found to be six times that of the inner nozzle diameter. Far from the initial region (i.e., $x/d_o > 6$), the particle velocity and concentration decay rate were slightly higher than the mixing region and had a direct relationship with velocity ratio. It was found the centerline sand concentration decreased at a smaller rate than single-phase buoyant jets and slurry jets for $0.62 \leq Ru \leq 1.24$ and at a higher rate than particle clouds for $0.62 \leq Ru \leq 1.86$. Furthermore, the centerline sand velocity ratio for $Ru = 1.24$ had approximately similar decay rates as slurry jets as the velocity ratio of slurry jets was close to unity (i.e., $Ru \approx 1$). Therefore, as velocity ratios increased significantly (i.e., Ru =1.86) the concentration decay rate increased as well. The radial variations of concentration and the velocity of sand-water coaxial jets were also investigated. It was shown that radial concentration can be correlated and described by Gaussian distribution while the radial distribution of sand concentration indicates that the spreading rate of sand-water coaxial jets increased by decreasing velocity ratio. Furthermore, less radial discrepancy was found between the radial velocity distribution of the sand-water coaxial jets with higher Ru and single-phase water jets. For sand-water coaxial jets with high-velocity ratios, the zone of the fully developed jet was established much further from the nozzle at $x/d_o \geq 32$, and as the velocity ratio decreased, the zone of the fully developed jet formed closer to the nozzle for $x/d_o \geq 24$.

The average drag coefficient of sand particles over different cross-sections of sand-water coaxial jets were calculated by using the axial and radial sand concentration and velocity data. It was found that the grouping effect decreased the average drag coefficient in comparison to the drag coefficient of individual particles with smaller velocity ratios. Due to higher rates of concentration decay in sand-water coaxial jets with high-velocity ratios, the grouping effect became less significant and caused higher drag coefficients in coaxial jets compared to the drag coefficient of individual particles. Lastly, the impact of the inner water jet on the radial interparticle collision in sand-water coaxial jets was studied by evaluating the variation in Bagnold numbers at different cross-sections along the jet axis. It was found that for all velocity ratios, the mixed jets were in the transitional regime at the beginning of the jet (i.e., $x/d_o \leq 12$) and far from the nozzle, sand particles entrained by the vortex structures and micro viscous fluid stresses controlled the flow.

Chapter 4

Spectral and Proper Orthogonal Decomposition analysis of sand-water coaxial jets

4.1 Introduction

Turbulent jets have many engineering applications particularly in mixing enhancement and water quality improvement. Formation of large-scale coherent shear layer between the jet's shear flow and ambient are responsible for mixing and entraining processes of turbulent jets (Zang et al., 2015). These structures provide insight into physical behavior of the flow field formed by the jets subjected to spatial or temporal oscillation (Arote et al., 2020).

The study of the coherent shear layer structures with flow-visualization techniques has been great research interest for many decades (Morel, 1975, 1977; Sirovich, 1987; Holmes et al., 1996; Wegener, 2014; Sieber et al., 2016; Schmidt., 2017; Wang and Yang, 2018; Kadu et al., 2020; Zhang et al., 2021). Coherent structures are spatially and temporally orthogonal and play an important role in the dynamics of turbulent jets (Hingam, 2017; Schmidt et al 2017). Increasing the initial Reynolds number intensified vortex formation in the near-field shear layers (Becker and Massaro, 1968). Grinstein and Devore (1996) showed that coherent structures are closely related to the main attributes of the jet flow and enhanced the entrainment and mixing of jet shear flow with the ambient fluid. A coaxial jet is a two-channel concentric nozzle coaxial nozzles consist of a core nozzle surrounded by an annular nozzle. Adding a second phase (i.e., fluid, sand particles) influence the flow configuration and dynamics of the jets. The initial development of shear layer boundaries between the two phases of coaxial jets can impact the growth, the dispersion of two phases and vortex-pairing further downstream of the jet. (Michalke, 1965; Winant and Browand, 1974; Gutmark and Ho, 1983; Crow and Champagne, 1971). Therefore, investigation of the high and low-ranked coherent structures is important for understanding the development of coaxial jets. Several statistical methods have been examined to capture the influence of particles on the mixing and inter-scale coherent structures in turbulent flow fields. The most widely used statistical method to resolve turbulent data is the Proper Orthogonal Decomposition (POD) technique (Lumley, 1967). POD became a viable method to capture optimal status functions by recognizing the formations with the largest mean square prediction such as Karhunen–Loève Decomposition (Loève, 1945; Karhunen, 1946) and Singular Value Decomposition (SVD).

A paper based on the content of this chapter is currently being prepared for submission to the *Journal of Hydraulic Research* as Sharif, F., Azimi, A. H., 2021. Spectral and proper orthogonal decomposition analysis of Sand-water coaxial jets.

The POD method was first implemented by Lumley (1967) to distinguish the coherent structures of turbulent flows. The POD technique decomposes the time-history data into its lower-ranked special components modes and the frequency-ranked dynamic modes.

The Proper Orthogonal Decomposition (POD) technique has been extensively used to identify the most persistent structures in the flow fields (Butcher and Spencer, 2019). The identification of large-scale coherent structures by detecting wave packets plays an important role in understanding the dynamics of turbulent jets (Schmidt et al., 2018).

The Proper Orthogonal Decomposition (POD) technique is appropriate for detecting individual features in the flow morphology by decomposing the time-history data into its lower-ranked components (Charalampous et al., 2019). This method was proposed by Pearson (1901) to study multidimensional data series by reducing the number of dimensions and has been utilized in turbulent flow to extract structural velocity components from turbulent jets (Berkooz et al., 1993; Arienty et al., 2009; Charalanpous et al., 2014). The snapshot method is often applied to perform the Proper Orthogonal Decomposition (POD) (Holmes et al., 1996; Sirovich, 1987). The flexibility and capability of the POD technique are highly recognized in the study of turbulent flows (Berkooz et al., 1993). The shear-coaxial jet flow oscillation was identified by extracting the lower-ranked POD modes from a series of high-speed images (Teshome et al., 2012). Hua et al. (2016) characterized several different dynamic modes of coaxial jets. They found that the modulations of the density field that impacted each of these modes were at least an order of magnitude smaller than the spatial variations in the time-averaged flow. The time-resolved POD image analysis of confined coaxial flow indicated that the large-scale oscillations depend on the fastest stream either annular or central nozzle (Charalampous et al., 2014). POD analysis for turbulent jets revealed that the large-scale oscillations have the most energetic spatial structures with a low-frequency peak (Semeraro et al., 2012). The two distinct peak frequencies associated with vortex formation in the outer and inner shear layers were observed by Zang et al. (2018).

Most recently, Schmidt et al. (2017) characterized the spatial properties of flow oscillations using the Spectral Proper Orthogonal Decomposition (SPOD) on the time-resolved flow field data. Thus, SPOD is an accurate method for characterizing narrowband oscillations in comparison to the traditional proper orthogonal decomposition. SPOD can identify not only the special properties of coherent motions but also, can extract frequencies and energy levels simultaneously. However, the traditional POD is only capable of obtaining special structures.

The temporal coefficients of the orthogonal modes of turbulent jets were found to be linked to Kelvin-Helmholtz (KH) type wave packet instabilities (Schmidt et al., 2017). Kadu et al. (2020) observed that a pairs of counter-rotating vortical structures in the first two modes in the inner mixing layer of coaxial jets by employing SPOD technique. Spectral proper orthogonal decomposition analysis of rotating round jets revealed the flow oscillation amplitudes vary linearly with flow initial configuration such as velocity, and flows rotation intensity. The detected orthogonal modes and their frequencies were linked to the coherent structures in the near-field region of turbulent jets by Zhang et al. (2021).

The above studies and many others have expanded the knowledge to further analyze the coherent structures in free jet flows and single-phase coaxial jets. The role of coherent structure dynamics and topology in the mixing and entrainment properties of sand water coaxial jet is needed to be investigated. The present chapter is an attempt to identify and characterize the coherent structures formed in sand-water coaxial jets and study the effect velocity ratio on these structures. This understanding is significant for optimizing and designing flow initial configuration for oscillating jets in view of their diverse industrial applications. The Spectral and Proper Orthogonal Decomposition can be utilized to study the low-rank dynamic and energy contribution of sand-water coaxial jets with high and low-velocity ratios. As the first objective of Chapter 4, the dynamic behavior, energy contribution of high, and low-ranked coherent flow configuration of coaxial sand-water jets were investigated by the Proper Orthogonal Decomposition (POD) technique. Secondly, Spectral Proper Orthogonal Decomposition (SPOD) technique provides insight into the time scale associated with the spatial modes and dynamics of the particle motions in sand-water coaxial jet.

This chapter is organized as follows: material and method including the experimental setup and the description of Spectral and Proper Orthogonal Decomposition techniques processing section in section 4.2. In section 4.3, The experimental data analysis of POD and SPOD is discussed. Finally, a summary and conclusions of this study are presented in section 4.4.

4.2 Material and methods

4.2.1 *Experimental setup*

Detailed laboratory experiments were conducted in the Multiphase Flow Research Laboratory (MFRL) at Lakehead University to study the lowe-rank dynamics of sand-water coaxial jets. All experiments were carried out in a rectangular tank of 1.65 m long, 0.85 m

wide, and 0.85 m deep. The tank was filled with tap water and the ambient temperature was kept constant over time with a value of 20°C ± 1°C. The schematic of the experimental setup, instrumentations and the adopted coordinate system are shown in Figure 4.1. A discharge assembly consisting of a funnel and two concentric pipes at the outlet was designed to model the coaxial jets. Two different funnel sets consisted of two concentric nozzles at their outlet were designed.

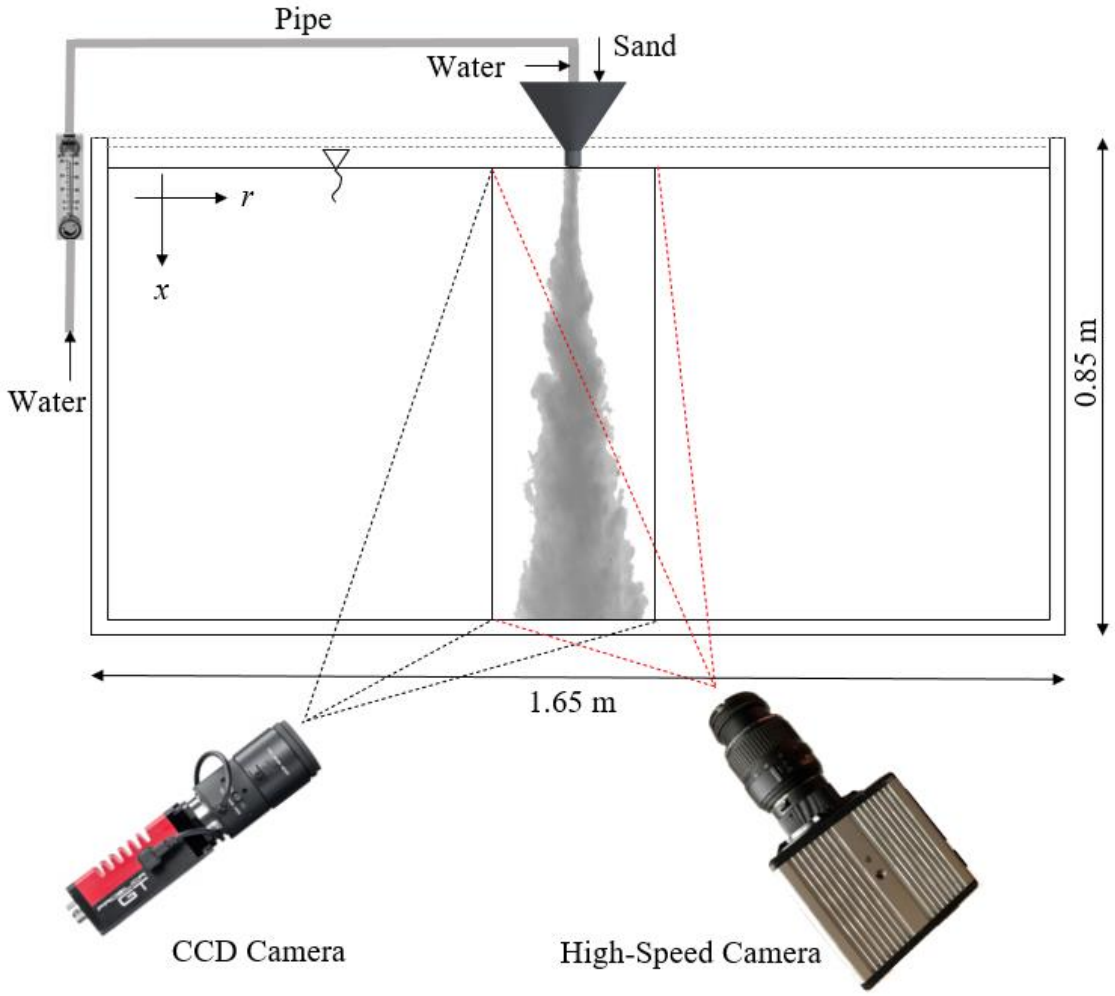

Figure 4.1: A schematic view of the experimental setup, instrumentations, and the adopted coordinate system.

The central nozzle diameter of the primary funnel and the coaxial annular diameter were d_o = 8 mm and d_a = 18 mm with the Stokes number, S_t, of 0.4, respectively. The second coaxial nozzle had the inner and annular diameters of 12 mm and 22 mm (i.e., S_t = 0.57), respectively. Stokes number, S_t, can be used to link particle relaxation time, $\tau_p = \rho_s D_{50}^2/18\mu$ to the energy transfer between particles and ambient water. Where, ρ_s is the density of the particles, D_{50} is the mean particle size, and μ is the dynamic viscosity of the ambient fluid. It

describes as the ratio of particle relaxation time and the time scale of the flow, $\tau_f = d_o/u_o$, where u_o is the initial sand velocity at the nozzle (Gore and Crowe, 1989). This design provided an annular gap of 2.5 mm for both type of funnels. The schematics of the coaxial nozzle arrangement and funnel-pipe assembly are shown in Figure. 4.2.

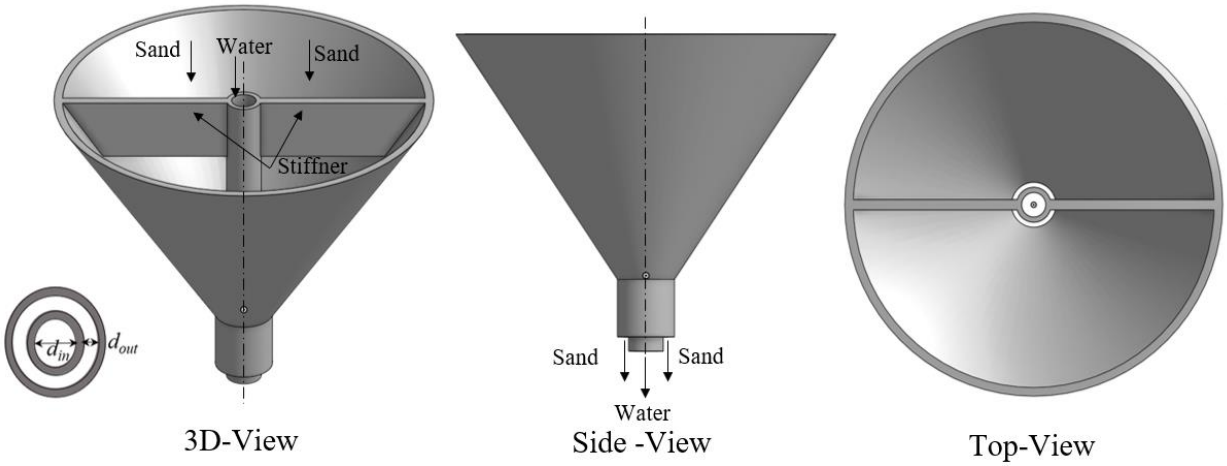

Figure 4.2: Details of the coaxial nozzle arrangement and funnel-pipe assembly.

A system of valves and an accurate flow meter (LZT M-15, UXCEL, China) were implemented to control and measure different flow rates ranging between 0.5 L/min and 18 L/min which provided velocity ratios in the range of $0 \leq Ru \leq 1.86$ and Reynolds numbers between 6,622 and 21,189. Sand particles with a median diameter of D_{50} = 0.507 mm and a density of ρ_s = 2540 kg/m^3 were used in this study. The mass flux of the annular sand phase was set to 18 g/s and 27 g/s for annular diameters of 12 mm and 22 mm, respectively. The sand particles in the funnel were loosely packed and the initial sand concentration was approximately 60% by volume. Overall, 12 experiments were tested in this study to investigate particle dynamics of sand-water coaxial jets (see Table 4.1). In addition, light illumination technique with the Thiamine tracer (Jamieson Laboratories, Windsor, Canada) under the black light was used to perform POD analysis and extract particle motion. An 18-inch-long dimmable LED blacklight (WOWTOU, China) with nine three-watt bulbs was utilized for flow visualization. Particle oscillations were studied by capturing time series of images with a high-speed camera (Photron-FASTCAM, 1024PCI-100KC) and with a resolution of 1024×1024 pixels. Previous research studies indicated that the selected image resolution and speed are suitable for the SPOD analysis (Schmidt et al., 2017). The camera was equipped with a 15-55 mm AF-S Nikkor, 1:3.5-5.6 GII lens (Nikon, Japan) to capture images and periodic motions of sand particles. Raw images were captured with a frame rate of 250 to 500 frames per second and a shutter speed of 0.004 sec. The full MATLAB® m-file code is included in Appendix 4.

Figure 4.3 shows the instantaneous snapshot images of sand-water coaxial jets with different velocity ratios. As can be seen, sand particles are more symmetrical in coaxial sand-water jets in comparison to the single-phase jets (Ru = 0) due to the existence of carrier fluid. The luminescent visualization of sand-water coaxial jets for $Ru \leq 0.35$ is also shown in Figure 4.4.

Table. 4.1: Experimental details and parameters of sand-water coaxial jets in water with low and high-velocity ratio.

No.	Test No.	D_{50} (mm)	d_o (mm)	d_a (mm)	$\dot{m}_o$ (kg/s)	u_{wo} (m/s)	Re	Ru	S_t
1	A1	0.507	6	12	10	0	0	0	0.4
2	A2	0.507	6	12	10	0.75	6622	0.35	0.4
3	A3	0.507	6	12	10	1.16	9270	0.18	0.4
4	A4	0.507	6	12	10	1.49	11919	0.16	0.4
5	A5	0.507	6	12	10	1.99	15892	0.12	0.4
6	A6	0.507	6	12	10	3.32	26486	0.07	0.4
7	B1	0.507	12	22	27	0	0	0	0.57
8	B2	0.507	12	22	27	0.59	7063	1.86	0.57
9	B3	0.507	12	22	27	0.88	10595	1.24	0.57
10	B4	0.507	12	22	27	1.18	14126	0.93	0.57
11	B5	0.507	12	22	27	1.47	17658	0.74	0.57
12	B6	0.507	12	22	27	1.77	21189	0.62	0.57

As can be seen in Figures 4.4a and 4.4b the green color intensity pattern as a tracer indicates a high degree of turbulent mixing between the ambient fluid and the outer part of the coaxial jet. For smaller velocity ratios (i.e., Ru = 0.12 and 0.07), the jet spreading can be

deduced by the elongated dyed pattern and spreads less strongly into the ambient fluid (see in Figures 4.4c and 4.4d).

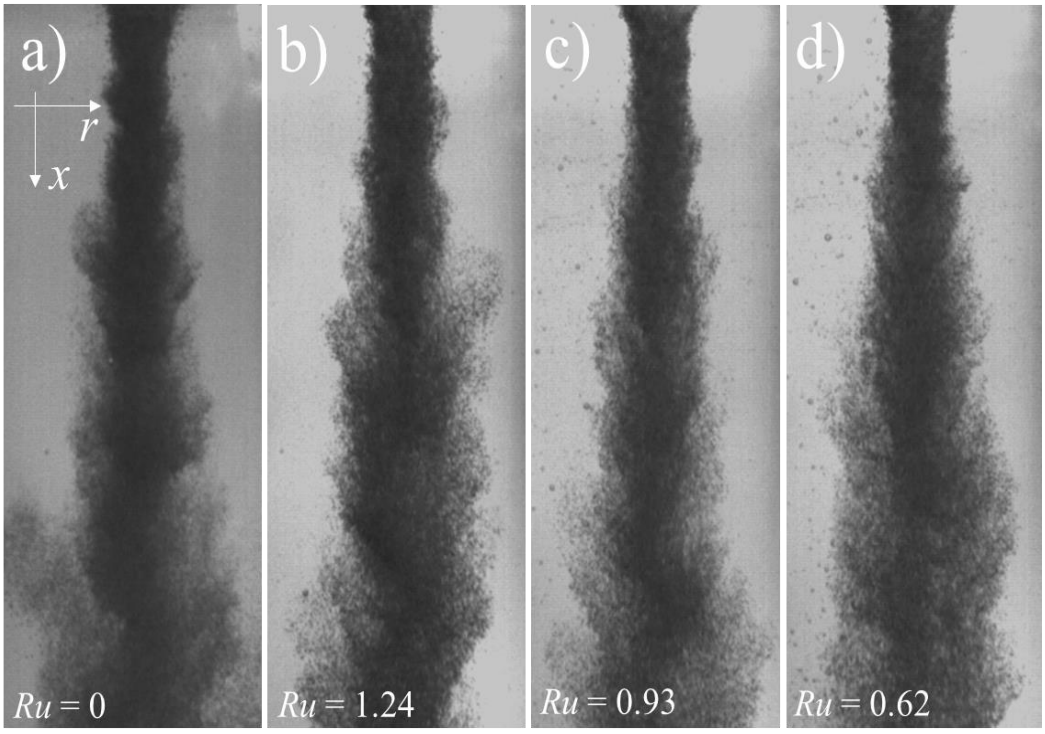

Figure 4.3: High speed images of sand-water coaxial jets for different velocity ratios: a) *Ru* = 0; b) *Ru* = 1.24; c) *Ru* = 0.93; d) *Ru* = 0.62.

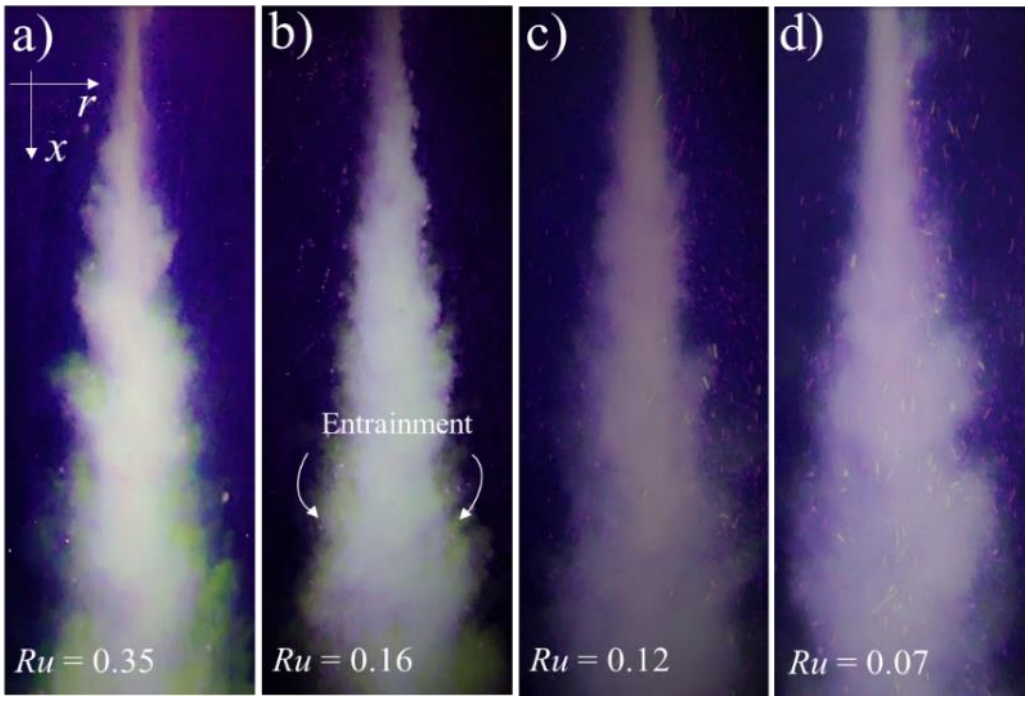

Figure 4.4: High speed illumination images of sand-water coaxial jets for different velocity ratios with color tracer: a) *Ru* = 0.35; b) *Ru* = 0.16; c) *Ru* = 0.12; d) *Ru* = 0.07.

4.2.2 *Proper Orthogonal Decomposition*

The initial step in analysis of coherent structure in sand-water coaxial jets is to investigate the POD results based on the original set of high-speed snapshots (Siegel et al., 2006). Therefore, a series of snapshots was adjusted to construct a single data matrix X using N_t snapshots and M_p pixels. Each row of the X matrix was formed by conditioning consecutive rows from the top row of pixels to the bottom row of pixels. To isolate the periodic fluctuations of the coherent structures, the mean value in matrix X needs to be subtracted. A POD can be obtained by decomposing the data in matrix X as:

$$X = USV_n^T \tag{4.1}$$

where U is an $N_t \times N_t$ orthogonal matrix stands for the spatial structure of each mode and the matrix N is the number of the decomposed modes, S is an $N_t \times M_p$ diagonal matrix of singular values. The matrix V_n^T in Eq. (4.1) is a transposed $M_p \times M_p$ orthogonal matrix consist of the coefficients corresponds to the time progression of the modes. The time-dependent intensity coefficients, Q_p, can be defined as $Q_p = US$. Each column of Q_p is a vector of time-dependent proportional coefficients, while the columns of V_n are the proper orthogonal modes and are called the eigenvectors.

The first mode containing the temporal properties and the highest variance contribution can be referred to the first column of the matrix Q_p. On the other hand, the first column of the V_p matrix holds the spatial fluctuations of the first mode, and so on, for subsequent columns of the Q_p and V_p matrices (Wegener, 2014). As stated, each POD mode is spatially orthogonal and may sustain multiple convoluted structures; therefore, a Fourier spectrum analysis of each Q_p matrix can pinpoint the peak frequencies linked to the convoluted periodicities (Higham et al., 2018).

4.2.3 *Spectral Proper Orthogonal Decomposition*

The Spectral POD method theoretically considers as a variant of the POD method. The fundamental algorithm of SPOD is stemmed from Welch's decomposition method (Schmidt et al., 2017, 2020). The coherent structure and flow oscillation can be characterized based on the different scales of special, frequencies, and energy intensities. In addition, special and flow fluctuation in different frequencies are linked together particularly in turbulent flows.

Conventional post-processing techniques such as Proper Orthogonal Decomposition (POD) and Dynamic Mode Decomposition (DMD) are not capable of obtaining coherent structures in both space-frequency simultaneously. DMD is a promising method in decomposing time series of data into frequency ordered, while POD outperforms in selecting the orthogonal set of basis vectors that conserves energy the most to represent the system (Shen et al., 2020). However, SPOD can extract the energy content and frequency by combining POD and DMD capabilities and extract both special and time-related properties. Due to the particles' motion complexity in the coaxial turbulent jets flow, the coherent structures carrying the most turbulent kinetic energies (TKEs) that dominate the dynamics are of great interest to investigate. Thus, SPOD is employed in this study to reveal the dynamic (dominant features) of the flow through a set of statistical proportions (Sirovich, 1987). There are different variants of SPOD analysis, for this study proposed algorithm by Schmidt and Colonius, 2020 has been employed. The employed model is based on Welch (1967) averaging technique to extracted the frequency domain properties of the time history data set knows as the Power Spectrum Density (PSD). Therefore, the orthogonal modes matrix can be obtained as an increasing frequency spectrum. The SPOD is applied on ensembles of 1500 to 2500 snapshots to construct a single data matrix P using N_t snapshots and M_p pixels. To increase the date accuracy and to reduce the windowing effect the matrix P was fragmented into N_b blocks that overlap by N_o snapshots. Different the length of segmentation (i.e., 64, 128, 256…) has been examined to find the most suitable fragment. However, larger block sizes and overlap led to the larger data. The size of the N_b block can be described as $N_b=(N_t-N_o)/(N_f-N_o)$ where N_f is the length of segmentation (i.e., 64, 128, 256…) corresponding to an overlap of 50%.

To arrange each block of snapshots the Welch periodogram technique was employed to form each block in frequency order of the temporal Fourier transform of the data. Finally, reordered frequency-based blocks were decomposed by the POD to obtain the spatial modes of each block as a linear weighted sum of the modes and can be described by (Sirovich, 1987):

$$P_{B_i}(x_a,t_a)=\sum_{j=1}^{r_p}\alpha_{ij}\varphi_j(x) \tag{4.2}$$

where x_a and t_a are the independent variables corresponding to special and temporal properties of data sets, respectively, $i = 1$ to N_b, $j = 1$ to $r_p < N_b$. The orthogonal eigenvectors called spatial modes $\varphi_j(x)$, corresponding spatial features data matrix. Furthermore, the coefficient $\alpha_{ij}(t)$ can be defined as:

$$\alpha_{ij}(t) = \beta_{ij}(t)\ \lambda_j^{0.5} \tag{4.3}$$

where β_{ij} is the temporal coefficients and λ_j is the eigenvalue. The matrix of eigenvalues are arranged in orthogonal order (i.e., $\lambda_1 \geq \lambda_2 \geq \ldots \geq \lambda_n \geq 0$)leads to the SPOD of each snapshots block. Therefore, SPOD modes are the eigenvectors of a cross-spectral density tensor at each frequency as combinations of a subset of the modes carrying the dominant energy.

4.3 Results and Discussion

4.3.1 *Proper orthogonal decomposition of data*

Different experiments were studied to find the connection between the POD modes and to a certain flow property in coaxial sand-water jets. POD modes (i.e., 1, 3, 5, 7 and 10) with Ru = 1.86 and Ec is the energy contribution of each mode compare to the total energy of modes (i.e., $\lambda_i/\Sigma\lambda_i$) are shown in Figure 4.5.

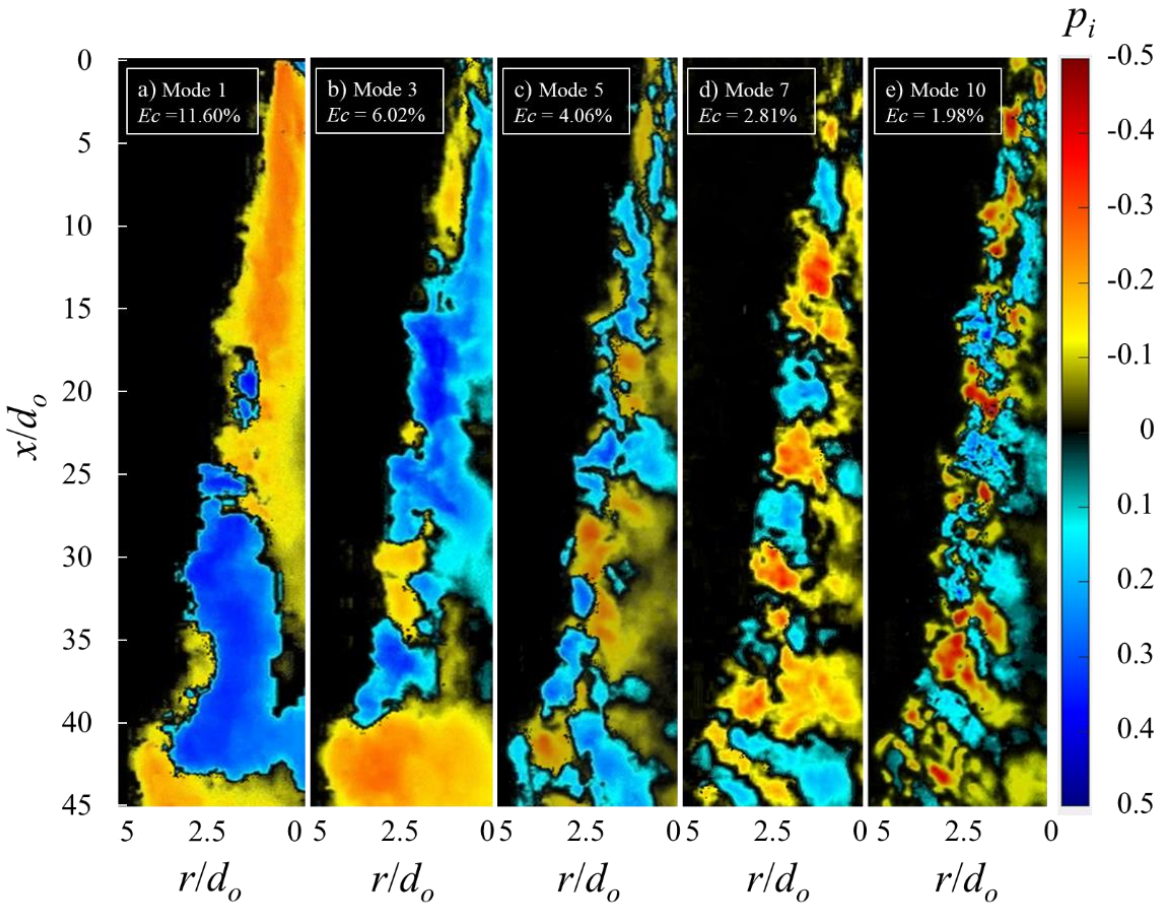

Figure 4.5: Proper Orthogonal Decomposition (POD) of a coaxial sand-water jet with Ru = 1.86: a) Mode 1; b) Mode 3; c) Mode 5; d) Mode 7; e) Mode 10.

As can be seen in Figure 4.5a, mode 1 has the largest consistent and energetic structure in the initial zone of the jet (i.e., $x/d_o < 25$). In Figure 4.5b the blue paired mode dominated the flow structure. However, the energy contribution of the second mode decreased by almost two times. The first two modes can be attributed to the major configuration, coherent structure, and flapping motion of the jet (Charalampous et al., 2019). The more disturbing patterns can be readily noticed in modes 5, 7, 10 (see Figures 4.5c, 4.5d, and 4.5e). Direct examination of the modes confirmed the existence of harmonic and low energy motions. The POD modes (i.e., 1, 5, 10, 15 and 20) for $Ru = 0.74$ also depicted in Figure 4.6. Mode 1 is the most energetic mode indicating the flapping side of the liquid jet elongated across the centerline (i.e., $x/d_o < 22$, see Figure 4.6a). The blue color area represented the flow alternate pattern which increased further downstream due to flow deflection patterns. (Charalampous et al., 2019). Modes 5 and mode 10 are disorganized and could be linked to vorticial motion with different frequencies (Figures 4.6b and 4.6c). Mode 15 and 20 has more scattered and noisy related to lower-ranked motion structures (Figures 4.6d and 4.6e) (Arienti et al., 2009).

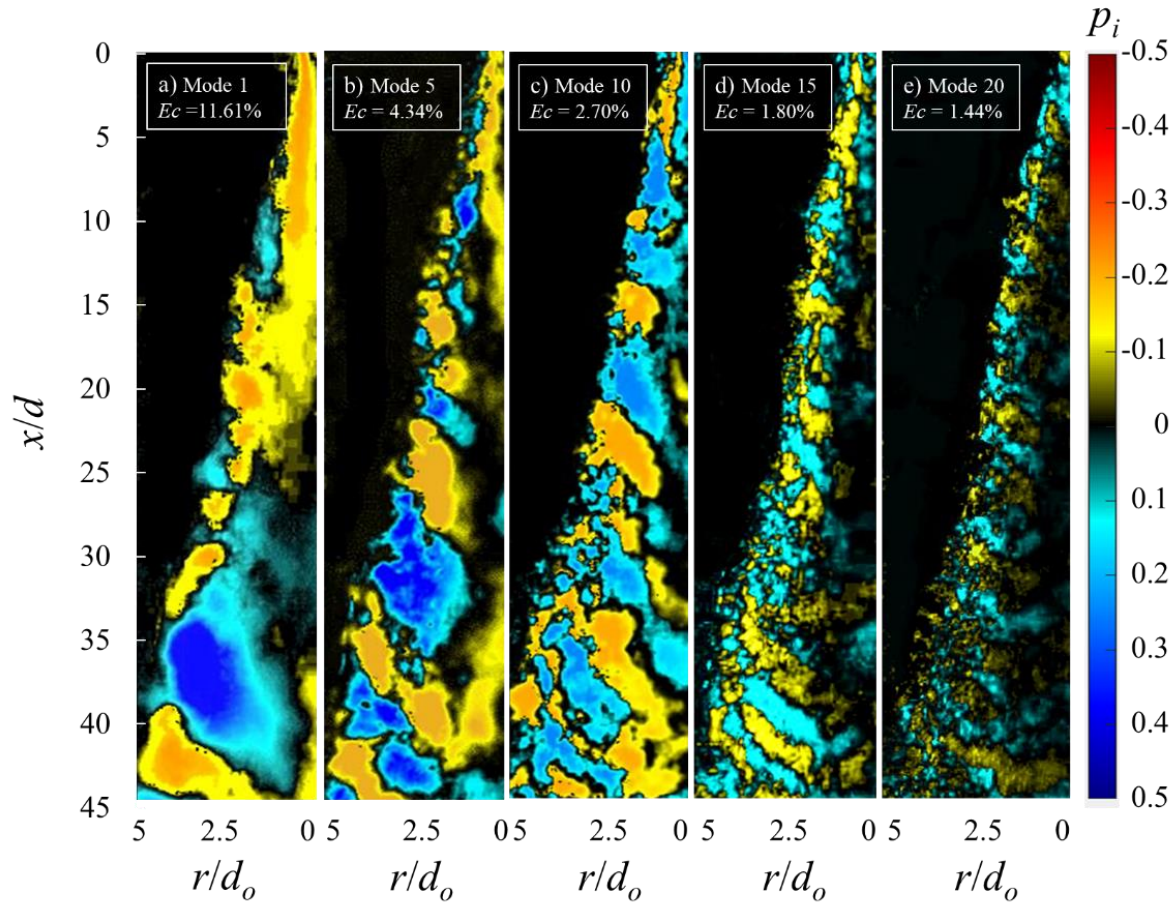

Figure 4.6: Proper Orthogonal Decomposition (POD) of a coaxial sand-water jet $Ru = 0.74$: a) Mode 1; b) Mode 5; c) Mode 10; d) Mode 15; e) Mode 20.

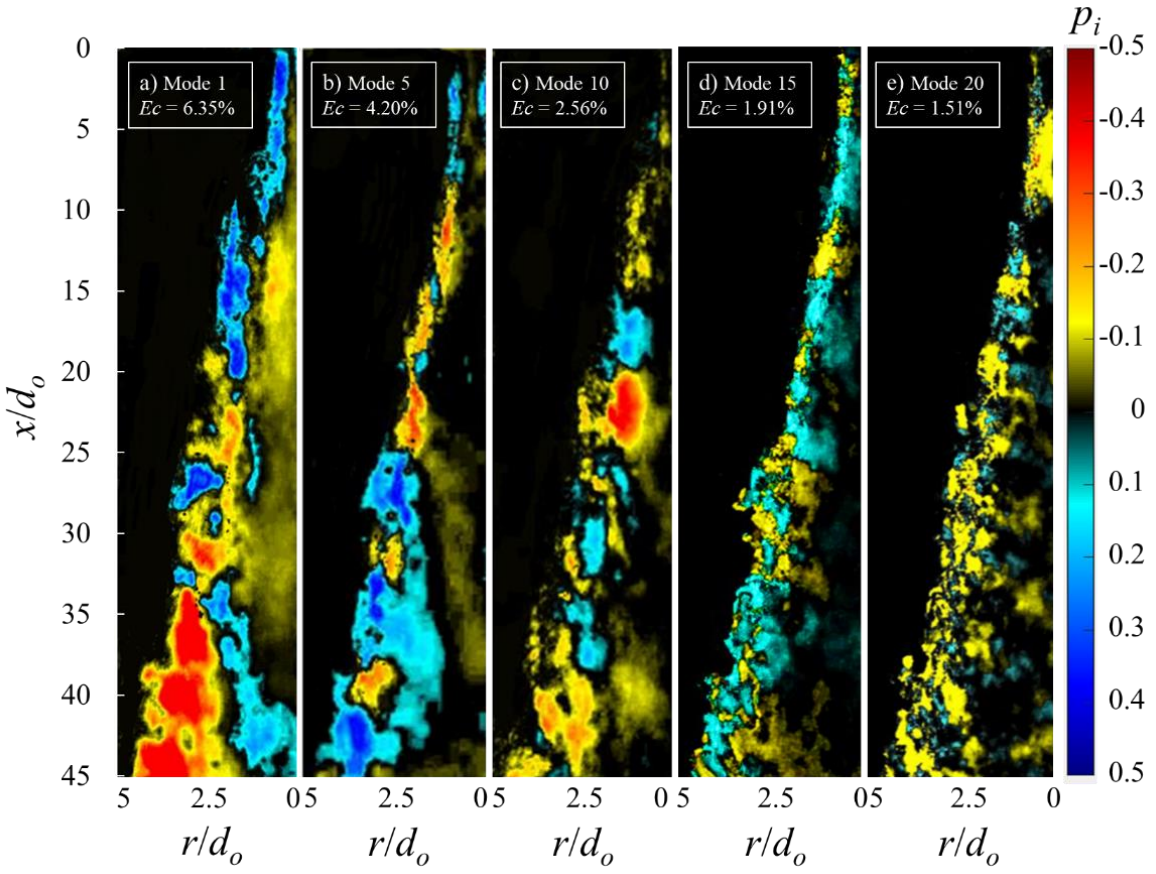

Figure 4.7: Proper Orthogonal Decomposition (POD) of a coaxial sand-water jet $Ru = 0.35$: a) Mode 1; b) Mode 5; c) Mode 10; d) Mode 15; e) Mode 20.

The effect of small velocity (i.e., $Ru = 0.35$) on the POD modes was shown in Figure 4.7. As can be seen from Figure 4.7a, the energy level of the first mode is 6.35% which is almost twice smaller than the coaxial jet with $Ru = 0.74$. The coaxial jet with smaller velocity ratio has more distributed patterns for modes 1 to 20.

The eigenvalue contribution, $E_c = \lambda_i / \Sigma\lambda_i$, in each flapping mode with respect to Ru is shown in Figure 4.8. It was observed that for higher velocity ratios, $Ru \geq 0.62$, the energy contribution of each mode was almost doubled in comparison to low-velocity ratios. The power spectral density of temporal coefficients for $Ru = 1.24$, 0.62 were shown in Figure 4.9. The POD modes of $Ru = 1.24$ demonstrated that a maximum frequency exists in the first two modes which indicates a coherent structure of dominant modes at approximately 0.28 Hz. A minor maximum in the frequency peaks (i.e., 0.75Hz to 1.43Hz) was also present in the PSD of modes 3, 5, 7 and 10 (see Figure 4.9a). However, for $Ru = 0.62$, frequencies correspond to the peak of each mode were between 0.68Hz and 4Hz (Figure 4.9b). These peaks show compound

compositions and strong hydrodynamic oscillations occur in the shear layer of the jet in a particular mode that corresponds to these dominant frequencies (Karami and Soria, 2018).

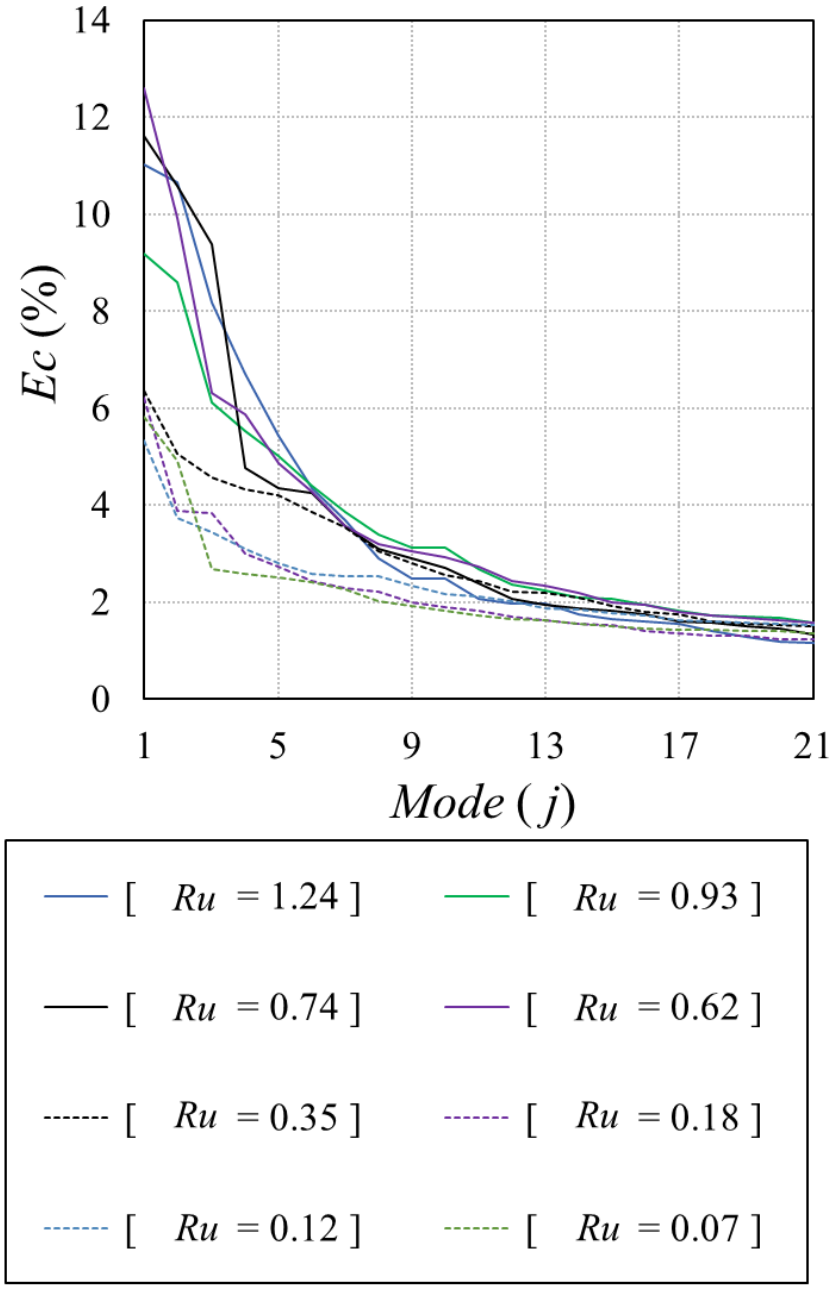

Figure 4.8: Energy contribution of different Proper Orthogonal Decomposition (POD) modes for $0.07 \leq Ru \leq 1.24$.

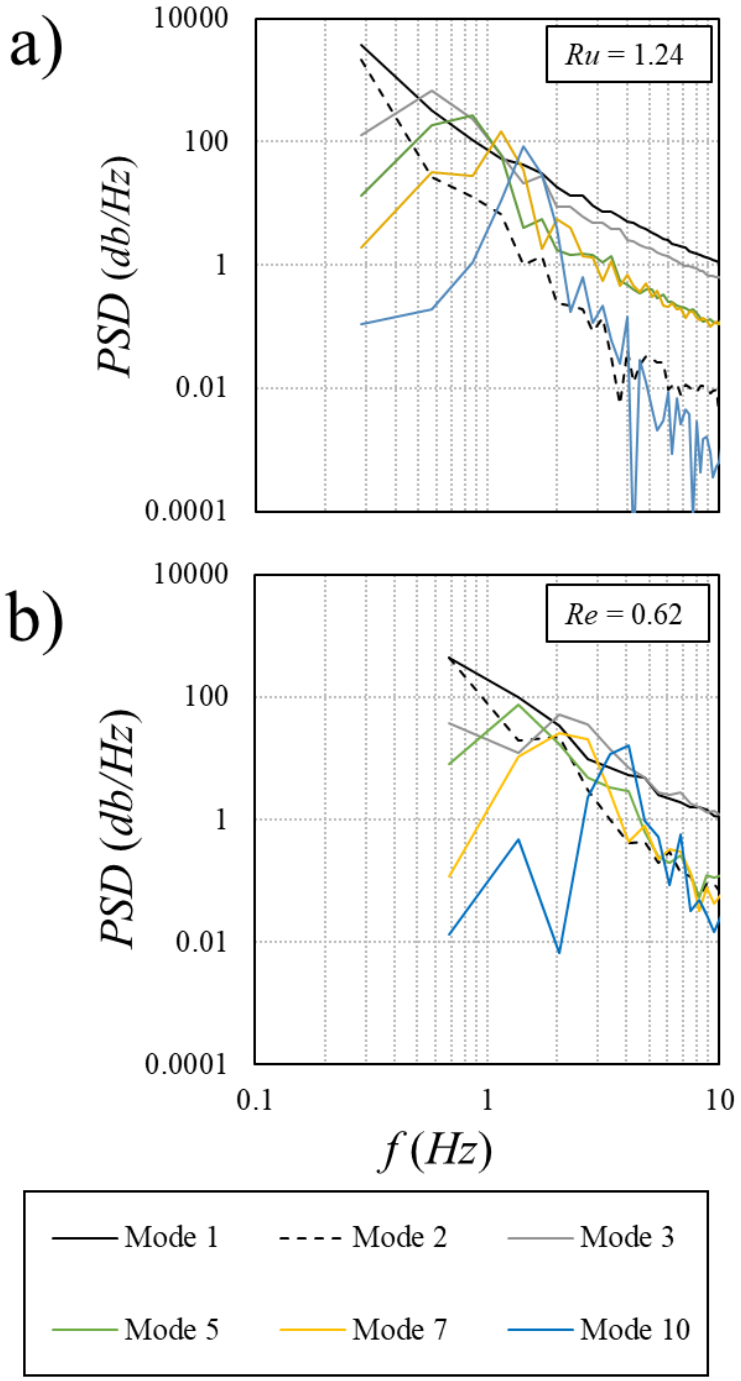

Figure 4.9: Power Spectral Density (PSD) of different Proper Orthogonal Decomposition (POD) modes for a coaxial sand-water jet: a) *Re* = 1.24; b) *Re* = 0.63.

4.3.2 *Spectral proper orthogonal decomposition of data*

The SPOD analysis was performed for a series of 1500 high-speed snapshots to investigate the low-rank dynamic of particles and flow properties. The block size was chosen as 256 data with a 50% overlap. The first two SPOD mode visualization for the velocity ratio

of *Ru* = 0, 1.24, and 0.62 were shown in Figures 4.10 - 4.12. As can be seen, Kelvin–Helmholtz (KH) type wave packets can be easily seen in all velocity ratios, *Ru.* The first two SPOD mode visualization for the frequencies of 1.95 Hz, 3.91 Hz, and 5.86 Hz for *Ru* = 0 are shown in Figure 4.10. The Kelvin–Helmholtz (KH) type wave packs can be distinguished in all exhibited modes. The large size in wave packs with a frequency of 1.95 Hz can be distinguished further downstream indicating particle oscillation and shedding (see Figures 4.10a and 4.10d) which were already shown in instantaneous high-speed images (See Figure 4.3a). As the frequency increased, the size of wave packs decreased accordingly (Figure 4.10a-c, 4.10e, and 4.10f). However, by adding a carrier fluid as the second phase (i.e., *Ru* = 1.24) wave packs turned to an axially elongated shape (See Figure 4.11).

A comparison of the modal shape with high-speed images demonstrated an almost uniform flow and particle pattern along the jet axis (see Figure 4.3b). In addition, decreasing the velocity ratio to 0.62 led to higher water phase velocity in the core stream therefore, particles adopted the water phase properties and have a more uniform pattern as shown in Figure 4.3d. Therefore, the intensity of wave packs corresponds to flow vortex shedding and oscillation decreased (Figure 4.12). The first three SPOD modes eigenvalue spectra correspond to turbulent kinetic energy for different velocity ratios of *Ru* = 0, 0.62 and 1.24 were also shown in Figure 4.13. As can be seen, for *Ru* = 0 experiencing a high turbulent kinetic energy level.

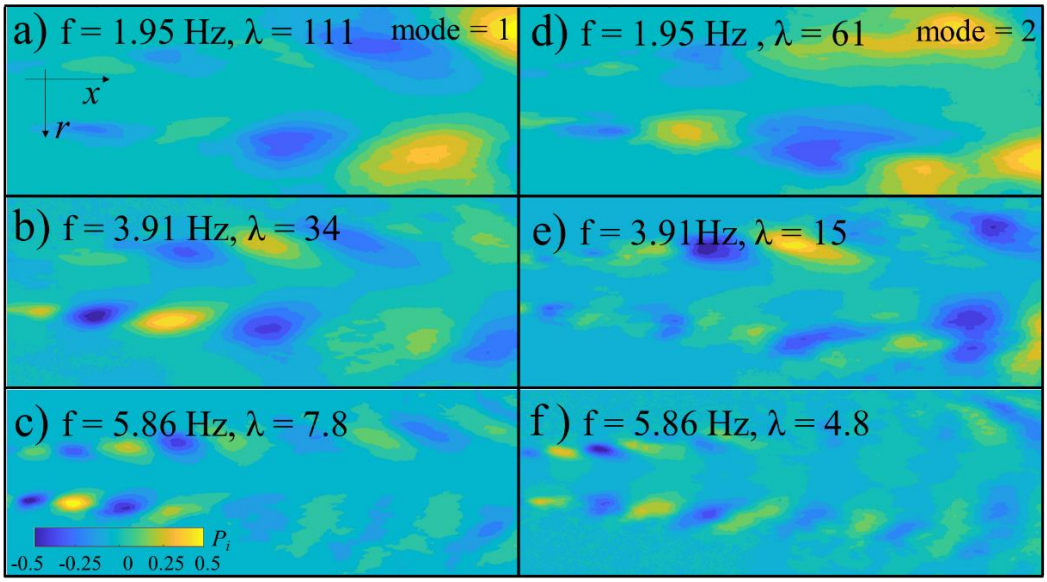

Figure 4.10: First two SPOD modes with the frequency of 1.95, 3.91 and 5.86 of sand-water coaxial jets for different velocity ratios *Ru* = 0.

However, adding up the second face of water led to a great reduction of energy level due to less flow oscillation and shedding. In addition, a large gap between the first two modes *Ru*= 0 and 1.24 represents that the higher energy portion was stored in mode one and can be linked to high vortex shedding.

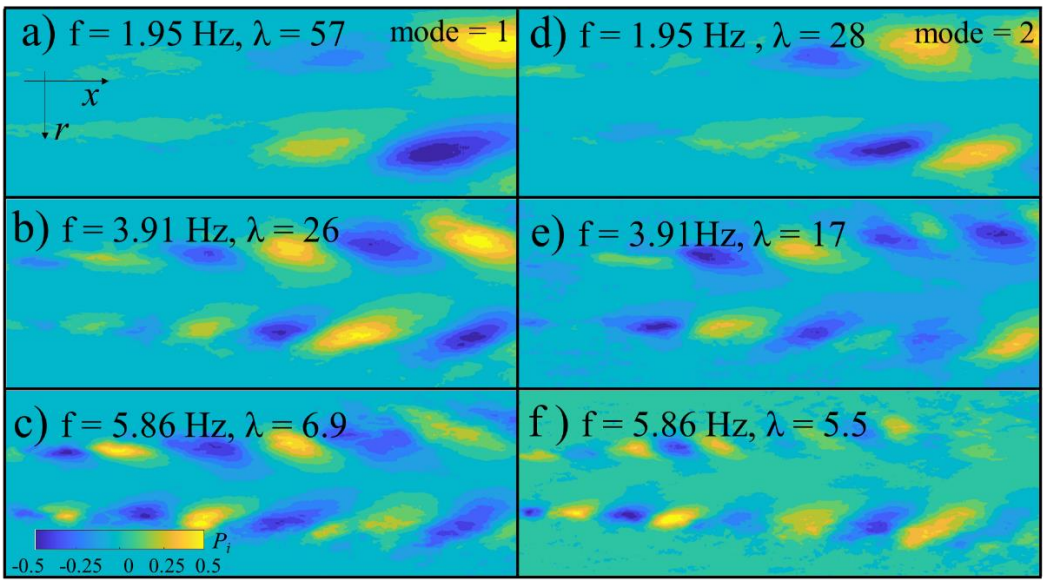

Figure 4.11: First two SPOD modes with the frequency of 1.95, 3.91 and 5.86 of sand-water coaxial jets for different velocity ratios *Ru* = 1.24.

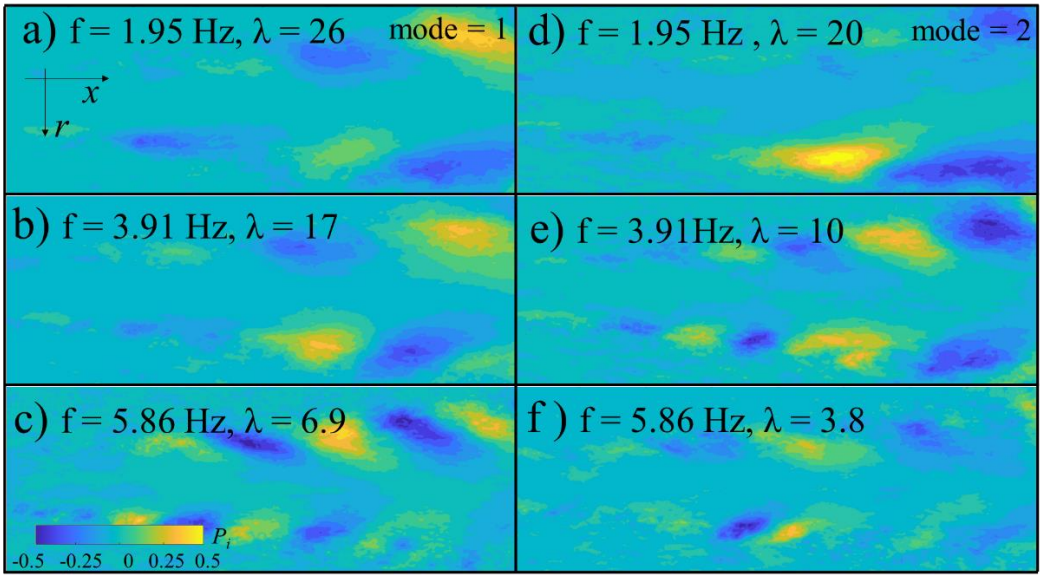

Figure 4.12: First two SPOD modes with the frequency of 1.95, 3.91 and 5.86 of sand-water coaxial jets for different velocity ratios *Ru* = 0.62.

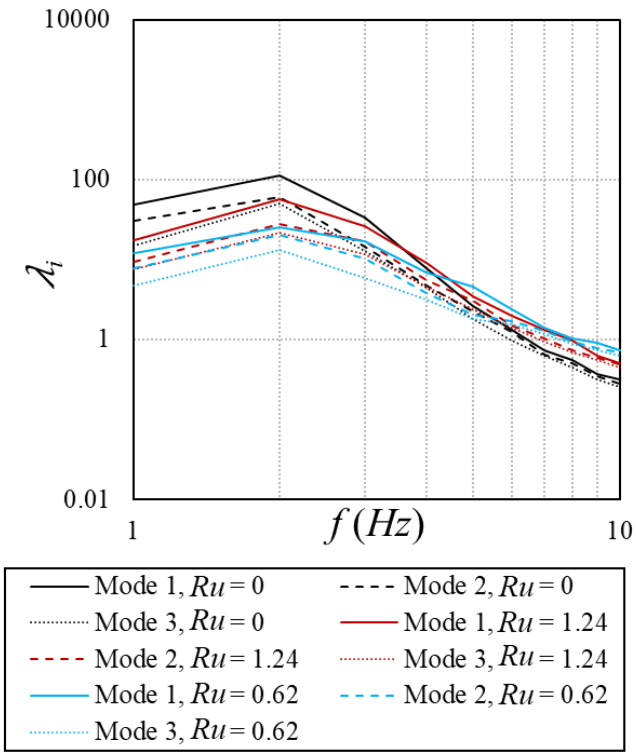

Figure 4.13: The first three SPOD modes SPOD eigenvalue spectra with the frequency of 1.95 sand-water coaxial jets for different velocity ratios Ru = 0, 0.62 and 1.24.

4.4 Conclusions

Detailed laboratory experiments were carried out to study the effects of initial water-phase Reynolds number $0 \leq Ru \leq 26{,}486$ and velocity ratio $0 \leq Ru \leq 1.86$ on the low-rank dynamics of the coaxial sand-water jet in stagnant water. The Spectral and Proper Orthogonal Decomposition method of snapshot images were used to investigate the water and sand phase mixing and interaction properties, dominant modes structures, and energy spectra by decomposing them into different energy-ranked modes. The POD results indicated that the influence of the velocity ratio and given Reynolds number plays a significant role in modal analysis and it could reduce the energy contribution of each mode by almost two times for a smaller velocity ratio (i.e., $Ru \leq 0.35$). The Power Spectrum Density (PSD) of the POD eigenvalue demonstrated that the first ten-mode dominants frequency spans from 0.28 Hz to 4 Hz. The SPOD analysis was performed for a series of highspeed snapshot images to study the low-rank dynamic of particles and flow configurations. The Kelvin–Helmholtz (KH) type wave packets were observed in low frequencies and the first three modes associated with the annular nozzle. It was found that decreasing the velocity ratio led to lower vortex shedding and particle fluctuation due to high velocity of the water phase. In addition, the gap between the first and

second eigenspectra curves of SPOD modes indicated that a significant portion of the turbulence kinetic energy and flow vortex shedding is stored in low-frequency modes of coaxial sand-water jets with a higher velocity ratio (i.e., Ru = 1.24).

Chapter 5

Experimental study of sand-water swirling jets in stagnant water

5.1 Introduction

A single-phase turbulent jet is a moving fluid that enters from a nozzle to a quiescent body of the same fluid causing a velocity shear between the entering and the ambient fluids. Turbulent jets have many engineering applications such as energy dissipator and mixer (Fischer et al., 1979; Lee and Chu, 2003). The initial momentum and the strong shear layer generate strong turbulence and enhance mixing between two fluids (Abramovich, 1963; Rajaratnam, 1976). Swirling jets can be formed by adding a spiral motion to the jet leading to more ambient fluid entrainment and hence mixing improvement. Swirling jets have been utilized in many industrial applications such as combustion devices and jet pumps in the past (Gupta, 1984; Schetz, 1980; Wicker and Eaton, 2001; Liu et al., 2020). Increasing the swirl motion along the jet axis forms a recirculation zone and causes the vortex core breakdown (Billant et al., 1998; Loiseleux and Chomaz, 2003; Liang and Maxworthy, 2005; Oberleithner et al., 2012; García-Villalba et al., 2006). The vortex core breakdown is a sudden change in the structure of a vortex core with a corresponding divergence of the stream surfaces near the axis (Benjamin, 1962). Lambourne and Bryer (1961) characterized two predominant vortex breakdowns known as the bubble and the spiral type. In the case of bubble, asymmetric vortex breakdown occurred along the jet axis. On the other hand, for the spiral type, a deformed oscillatory flow motion was observed along the centerline of the jet beyond the stagnation point. By including an unlimited mass of sand particles as the second phase in water jets, solid-liquid, particle-laden, or slurry jets are formed. Whereas particle clouds can be formed by the instantaneous release of a finite mass of sand particles into the ambient fluid.

Particle-laden turbulent jets have many engineering applications such as marine bed capping, hydro-transport systems, and wastewater disposal (Balarac et al., 2007; Azimi et al., 2012a, b; Canton et al., 2017; Zhang et al., 2018). Several research studies have been performed to understand the dynamics of particles and flow configuration in solid-liquid turbulent jets (Brush, 1962; Fan et al., 1990; Rahimipour and Wilkinson, 1992; Mazurek et al., 2002; Tamburello and Amitay, 2008; Virdung and Rasmuson, 2007; Casciola et al., 2010; Hall et al., 2010; Azimi et al., 2011, 2012a, b; Janati and Azimi, 2021).

A paper based on the content of this chapter is currently being prepared for submission to the *International Journal of Multiphase flow* as Sharif, F., Azimi, A. H., 2021. Experimental study of sand-water swirling jets in stagnant water.

The particle dynamics and particle-particle interactions in particle-laden turbulent jets are correlated with the initial inlet configurations such as particle size, D_{50}, initial particle concentration, c_o, nozzle diameter, d_o, and the initial velocity of particles, u_o. Many laboratory experiments were conducted to study the evolution, mixing properties, turbulence attenuation/augmentation, and spreading rates of two-phase turbulent jets (Huai et al., 2013; Jiang et al, 2005; Virdung and Rasmuson, 2007; Hall et al, 2010, Azimi et al., 2012a, b).

The spreading rate of single-phase jet was found to be between 0.125 and 0.2 (Gutmark and Ho, 1983). Weisbrot et al. (1982) indicated that the spreading rate is a function of velocity, u, and it can be scaled with $u^{-3/2}$. The spreading rate in water jets has ranged between 0.104 and 0.115 and for slurry jets ranged between 0.08 and 0.11. (Wang and Law, 2002; Hall et al., 2010). Azimi et al. (2012b) indicated that the spreading rate of slurry jets can be correlated with sand initial concentration as $c_o^{-3/2}$. The effect of particle size on the spreading of dilute slurry jets was found to be equal to the jet's half-width whereas this value for jets with large particles can be as low as 0.3 of the jet's half-width (Azimi et al., 2012b). Jufar et al. (2020) studied the effect of swirling motion on the spreading rate of single-phase turbulent jets. They found that the spreading rate between 0.167 and 0.191. Murugan et al. (2020) observed that jet spreading width increased abruptly in the downstream region of the recirculation region.

Nozzle size and the mass of released particles can be expressed as an aspect ratio, L_o/d_o, where L_o is a length of sand particles filled in a pipe with a diameter of d_o. The aspect ratio has been used to estimate the spreading rate and propagation of forced single-phase thermals (Bond and Johari, 2005). The studies of the sand jets' motion with relatively small aspect ratios (i.e., $0.125 \leq L_o/d_o \leq 4$) revealed that the aspect ratio altered the spreading rate of sand jets. It was found that increasing the aspect ratio from 0.125 to 2 led to an approximately 40% reduction (i.e., 0.31 to 0.13) in the spreading rate (Lai et al., 2015). Wang et al. (2014) indicated that particle size impacts the depth progression for particle clouds with a small aspect ratio of $0.6 \leq L_o/d_o \leq 7.5$. The spreading rate of particle cloud with a large particle size range (i.e., $0.33 \leq S_t < 1$) and aspect ratio of $0.8 \leq L_o/d_o \leq 40.1$ indicated that the aspect ratio became less significant on the cloud spreading rate for $L_o/d_o \geq 5.8$ (Moghadaripour et al., 2017a). The zone of the flow development of particles in particle clouds with a relatively higher aspect ratio (i.e., $19.6 \leq L_o/d_o \leq 39.2$) was found to be between 2 to 4 times of initial nozzle diameter (Sharif and Azimi, 2020). The zone of flow development in particle clouds was smaller than the zone of jet development in both water and sand jets. In addition, a higher depth progression and

spreading rates of particle clouds for tests with a higher aspect ratio (i.e., L_o/d_o =39.2) was observed (Sharif and Azimi, 2020).

The Stokes number, S_t, characterizes the behavior of particles evolving within the ambient fluids and it can be defined as the ratio of the particle relaxation time, $\tau_p = \rho_s D_{50}^2/18\mu$, and the time scale of flow, $\tau_f = d_o/u_o$, where ρ_s is the particle density and μ is the dynamic viscosity of ambient fluid (Gore and Crowe, 1989; Moghadaripour et al., 2017a, b; Gai et al., 2020). The spreading rate of particle clouds and particle-laden jets has been scaled by the Stokes number (Bühler and Papantoniou, 2001; Azimi et al., 2012a; Moghadaripour et al., 2017b). For Stokes number close to unity, particles are entrained by the fluid vortex core (Crowe et al., 1985). For particle-laden jets with $S_t << 1$, particles follow the fluid motion while for $S_t >> 1$, the ambient fluid has less impact on the particle motion. Moghadaripour et al. (2017a) classified sand particle sizes based on Stokes number as: small particles ($0 < S_t \leq 0.1$), medium particles ($0.1 < S_t < 0.33$), and large particles ($0.33 \leq S_t < 1$).

The dynamics of two-phase turbulent jets have been studied by measuring the variations of axial and radial velocities and sand concentrations. Parthasarathy and Faeth (1987) studied the structure of solid-liquid jets in ambient water and dilute particle concentrations with particle volume fractions of smaller than 5% was used. They found small velocity variation along the jet axis for $x/d_o < 3$. However, for $x/d_o \geq 3$, the velocity decay rate correlated with x^{-1} and that was similar to the velocity decay rate of single-phase circular jets. Jiang et al. (2005) indicated that the centerline sand velocity in slurry jets with small particles (i.e., $0 < S_t \leq 0.1$) was higher than the water-phase velocity. The variations of the centerline sand velocity was formulated as the sum of the water-phase velocity and the particle settling velocity. The decay rate of particle velocity in the axial direction was found to be less than that of the water velocity owing to the settling velocity of particles (Huai et al., 2013). In general, the centerline velocity of solid-liquid jets decayed at a slower rate than the single-phase water jets (Azimi et al., 2011; 2012b). The variations of sand concentration along the vertical axis of sand jets with Stokes numbers of 0.42 and 0.7 were found to be similar to single-phase water jets (Hall et al., 2010). Hall et al. (2010) indicated the variation of axial sand concentration and velocity with distance from the nozzle as power correlation of –5/3 and –1/3, respectively. The experimental results of slurry jets with a wide range of Stokes numbers (i.e., $0.07 \leq S_t \leq 11.37$) indicated a higher velocity decay rate varied between –1 and –1/3 (Azimi et al., 2012b). Lau and Nathan (2014) also indicated that the velocity decay rate, beyond the potential core of length 4 to 5 pipe diameters, is a function of Stokes number for $0.3 \leq S_t \leq 11.2$ and can be scale by x^{-1}.

Many research studies have investigated the mixing process of single-phase swirling jets as an effective method due to the existence of the recirculation zone (Davies et al., 1971; Gupta et al., 1984; Billant et al., 1998; Loiseleux and Chomaz 2003; Liang and Maxworthy 2005; García-Villalba et al., 2006; Oberleithner et al., 2012; García-Villalba et al., 2020). The recirculation zone can be categorized into transitional and established flow zones (Davies et al., 1971). The most dominant coherent structures in swirling flows are the Precessing Vortex Cores (PVC) oriented at a low angle with respect to the axis of rotation (Gupta et al., 1984). At the PVC, the reverse flow region propels around the axis with a distinct frequency and with a single-helical structure pattern (Syred, 2006; Oberleithner et al., 2012). Martinelli et al. (2007) found that the precessing frequency is a linear correlation of Reynolds number, *Re*, at a given swirl intensity. Reynolds number defined as $Re = \rho_w u_{ow} d_o/\mu$, where ρ_w = water density and u_{ow} is the initial water velocity at the nozzle. The intensity of swirling motion can significantly impact the coherent structure and it was characterized by the swirling number, *Sw*. It is defined as the ratio of the axial flux of tangential momentum to the axial flux of axial momentum and jet radius (Ceglia et al., 2013 and Ogus et al., 2016). Mcllwain and Pollard (2002) found that the swirling effect enhances the vortex ring breakdown mechanism by increasing the number of streamwise cords. Meliga et al. (2012a) showed that axisymmetric breakdown depends on the swirl number and Vanierschot and Ogus (2019) found that increasing the swirling number up to 0.57 reduces the processing frequency of the spiral vortex core. Crow and Champange (1971) indicated that the roll-up of vortex rings can be occurred due to Kelvin-Helmholtz instability. Park et al. (1998) found that the vortex structure and momentum coupling have a significant impact on the location and size of the central recirculation zone.

Introducing particles to the swirling jet can impact dynamic characteristics of swirling flow such as velocity fluctuation, spreading rate, and overall vortex structure (Eaton and Fessler, 1994; Wicker and Eaton, 1999, 2001; Gomes and Vincent, 2002; George et al., 2009; Gui, et al., 2010; Liu et al., 2010; Kazemi et al., 2018; Liu et al., 2020). Eaton and Fessler (1994) found that in solid-gas swirling jets with $1 \leq S_t \leq 10$, vortex formation caused particles to migrate from vortex core to outer regions leading to more organized particle concentration beyond the vortex core known as preferential concentration. Gomez and Vincent (2002) showed that the centrifugal inertial effect is responsible for concentrating particles in the Processing Vortex Core (PVC) and keeping the central zone clear of particles. Gui et al. (2010) observed the choke-like behavior in the main and radial stream particles with a large momentum. Wicker and Eaton (1999) indicated that the axial vorticity reduced particle

dispersion in the transverse direction. In comparison with single-phase jet, the coherent structure altered the particle distribution in particle-laden jets with $S_t \approx 1$ (Wicker and Eaton, 2001). The numerical results of two-phase solid-particle swirling jet with $Sw = 0.47$ indicated that the presence of particle attenuated the recirculating gas flow structure due to fewer vortices formation compare to single-phase swirling jets (Liu et al., 2010). The numerical investigation of confined particle-laden(i.e., gas-solid) swirling jet with $Sw = 0.47$ and $0.21 \leq S_t \leq 14.7$ indicated that the medium-sized particle groups (i.e., $S_t \approx 4.8$) concentrated more in the recirculation zone and this migration mostly occurred through the narrow streams surrounded by the edges of the PVC (Kazemi et al., 2018). Liu et al. (2020) investigated the dynamics of gas-particle turbulent swirling jet using glass beads of 60 μm diameter with a density of 2500 kg/m^3 and ultralight particles with a bulk density of 21.5 kg/m^3. It was found that the ultralight particle dispersion was anisotropic and the centerline axial and tangential velocities of particles and turbulence were smaller than the heavier particles. However, close to the nozzle, the velocity and turbulence in ultralight particles were larger than the heavier particles. George et al. (2009) demonstrated that not only the swirl number is a criterion for the PVC development but also, other inlet parameters such as density ratio plays an important role in the Processing Vortex Core (PVC) development in two-phase swirling jets.

The particle-particle interaction is an important phenomenon in two-phase swirling flows due to anisotropic characteristic which is different from direct jets (Gui et al., 2010). Recent laboratory experiments have shown that the swirling motion enhances the turbulent diffusion and particle-particle collision (Liu et al., 2019). Sundaram and Collins (1997) found that the inter-particle collision in two-phase gas-solid flow is a function of turbulence intensity and particle properties such as collision frequency, radial distribution, velocity and Stokes number. They also indicated for high Stokes numbers (i.e., $2 < S_t < 5$) the effects of preferential concentration and turbulent transportation dominated the flow configuration and led to higher particle collision. Gui et al. (2010) studied the particle-particle collision in gas-solid swirling jets with $0.1 \leq S_t \leq 7.93$ and $Sw = 1.42$. It was found that Stokes number plays an important role in particle-particle collision of two-phase swirling jets and for swirling jets with $S_t \geq 1$, particle-particle collision was almost independent of turbulence intensity and vortex breakdown impacts the interaction of particles for $S_t < 1$. Bluemink et al. (2010) indicated the drag coefficient increased linearly with swirling numbers (i.e., $Sw \geq 1$) in a freely rotating sphere in a solid-body rotating flow (i.e., glycerine).

The grouping effect, known as wake effect, can significantly alter the average drag coefficient, C_d, in particle-laden jets and particle clouds (Azimi et al., 2012b; Moghadaripour et al., 2017a, b; Mohammadidinani et al., 2017; Azimi, 2019; Manzouri and Azimi, 2019; Sharif and Azimi, 2020). For the slurry jets with $0.26 \leq S_t \leq 11.37$, the drag coefficients had similar values as the C_d of individual particles close to the nozzle (i.e., $x/d_o \leq 10$) whereas further downstream, the grouping effect became significant and reduced the average drag coefficient of slurry jets (Azimi et al., 2012b). Moghadaripour et al. (2017b) developed a correlation for the axial variations of drag coefficients of particle clouds with large particle sizes (i.e., $0.33 \leq S_t < 1$). They found that the grouping effect attenuated the drag coefficient significantly in comparison with the individual sand particles and a critical drag coefficient was defined when the calculated C_d became similar to the C_d of individual particles. The critical drag coefficients for $S_t = 0.22$ and 0.38 were 1.2 and 1, respectively. For relatively high aspect ratios, the drag coefficients were approximately independent of the axial distance from the nozzle (Sharif and Azimi, 2020).

Table 5.1: List of two-phase swirling jets and the controlling parameters from the literature.

Experimental study	Jet type	D_{50} (mm)	Sw	Re	d_o (mm)	d_a (mm)	ρ_s (kg/m^3)	c_o (%)
Wicker and Eaton, 2000	Solid-liquid	0.055- 0.15	0.92	13000	2	6	2500	-
Gui et al., 2010	Gas-solid	0.003 - 0.0079	1.42	3486	0.4	-	2650	5.3×10^{-5} - 1.67
Liu et al., 2010	Gas-solid	0.060	0.47	53256	32	64	2500	0.034
Kazemi et al., 2018	Gas-solid	0.01-0.1	0.47	-	19	32	2152	-
Liu et al., 2019	Gas-solid	0.060	0.1-0.47	26200	32	64	21.5-2500	0.034
Liu et al., 2020	Gas-solid	0.060	0.47	26200	32	64	21.5-2500	0.1-0.5

In Chapter 5 the results of detailed laboratory experiments of sand-water swirling jets issuing horizontally into stagnant water are discussed. Most of the previous studies have focused on the dynamics of gas-solid swirling jets (See Table 5.1). A cylinder comprised of water with spiral motion and premixed sand particles was designed to study the effects of swirling motion and particle aspect ratio on the flow properties such as mass and momentum flux, spreading rate, and velocity, and sand concentration profiles. In addition, the influence of swirling intensity on the inter-scale particle dynamics such as particle-particle collision and drag coefficients were investigated. Finally, axial and radial velocity and concentration were

formulated based on the measurements data for design and optimization of the performance of sand-water swirling jets.

This chapter is organized as follows: material and method including the experimental setup and signal processing techniques are described in section 5.2. In section 5.3, experimental results including the study of mass and momentum flux, spreading rate and mixing, axial and radial concentration and velocity measurements with limited and unlimited aspect ratios are indicated. Besides, drag reduction of group particles and power spectral density of flow coherent structure also described in this chapter. Finally, the conclusions of this study are presented in section 5.4.

5.2 Material and methods

5.2.1 *Experimental setup*

Detailed laboratory experiments were conducted in the Multiphase Flow Research Laboratory (MFRL) at Lakehead University to study the dynamics of sand-water swirling jets. A rectangular tank of 1.65 m long, 0.85 m wide, and 0.85 m deep was filled with tap water to carry out all the experiments. The homogeneity of ambient temperature and the impinged swirling flow was monitored, and the temperature was kept constant over time with a value of 20°C ± 1°C. The schematic of the experimental setup, instrumentations, and the adopted coordinate system for swirling sand-water jets are shown in Figure 5.1. A swirling cylinder was designed with an inner diameter of 32 mm surrounded by 6 inner spiral ports with 4 mm inner diameters leading water runs into the cylinder and imparting swirl flow. Sand particles added through a funnel from the upper part into the contraction cylinder to pre-mix and interact with the swirling water. The sand water mixture was discharged into the ambient water through a nozzle with a diameter of 6 mm. The geometrical configuration and assembly of the swirl cylinder and nozzle are shown in Figure 5.2. The design concept is based on air blast atomizers with the direct flow rotation (Kumar and Sahu, 2019). Due to high viscosity of water compare to gas moderate therefore, high swirling number can be achieved by six 20° degree of angle water inlets. Whilst moderate and high swirling number in air atomizer can generated by vane angles of greater that 60 degree. In order to generate maximum sand-water interaction the conical section with the dimeter of 6 mm was chosen at th outlet of the jet.

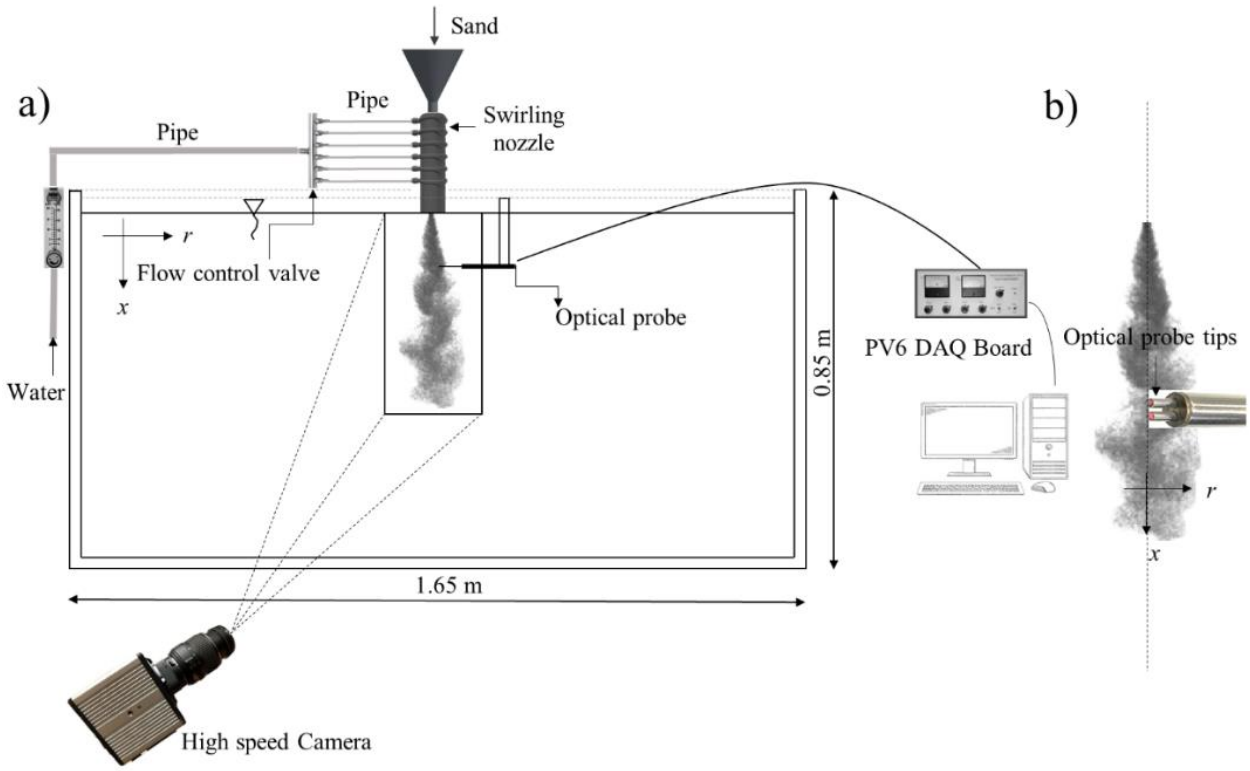

Figure 5.1: Schematics of the experimental setup, instrumentations, and the adopted coordinate system for swirling sand-water jets in stagnant water.

An accurate flow meter (LZT M-15, UXCEL, China) was used to generate different flow rates ranging between 0.5 L/min and 18 L/min which provided swirling numbers in the range of $0.45 \leq Sw \leq 0.60$. Sand particles with a median diameter of $D_{50} = 0.507$ mm and a density of $\rho_s = 2540$ kg/m^3 were used which give the Stokes number values in the range of $3.7 \leq S_t \leq 5.7$. The uniformity of particle sizes was evaluated by fitting the sand particle size distribution data with the lognormal probability curves. In addition, particle size was chosen based on probe measurement capability and initial swirling intensity. The initial sand concentration of sand-water swirling jets was approximately 60% volume/volume. Overall, 25 experiments were carried out to investigate the effects of swirling number and aspect ratio on particle dynamics of sand-water swirling jets. The effect of swirling number on particle dynamics of sand-water swirling jets was studied for two cases with unlimited sand mass (i.e., $L_o/d_o \approx \infty$) and with limited sand mass with the aspect ratio, L_o/d_o, ranging from 5.6 to 62.7. The experimental details and non-dimensional parameters are listed in Table 5.2.

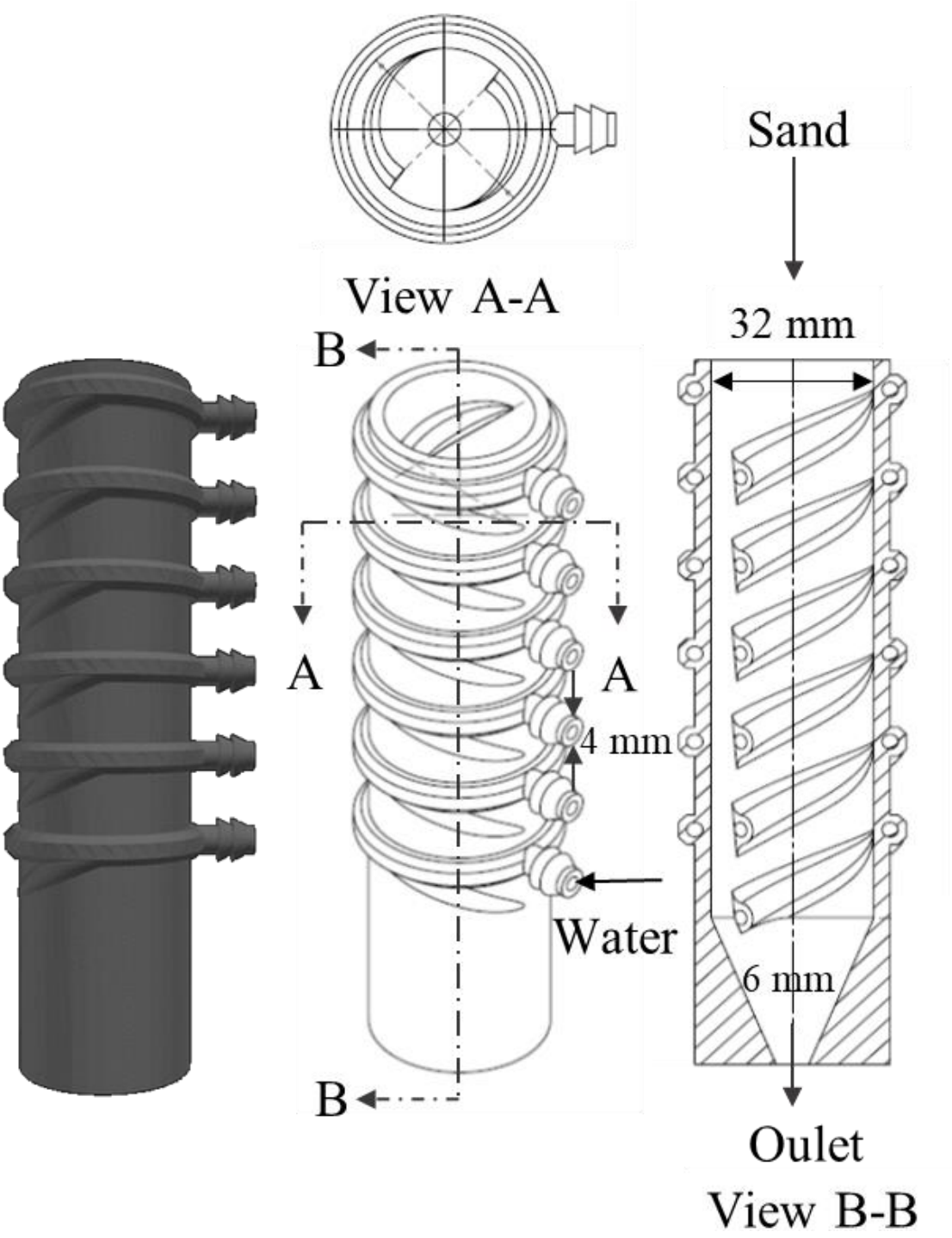

Figure 5.2: Detail schematic and three-dimensional print of the swirling cylinder and nozzle arrangement.

Table 5.2: List of experiments and the related non-dimensional numbers in the present study of sand-water swirling jets in stagnant water

No.	Test.	u_{wo} (m/s)	L_o/d_o	S_t	Sw	Re
1	A0	0	∞	3.7	0	0
2	A1	1.0	5.6	3.7	0.45	6079
3	A2	1.0	10.4	3.7	0.45	6079
4	A3	1.0	20.9	3.7	0.45	6079
5	A4	1.0	41.8	3.7	0.45	6079
6	A5	1.0	62.7	3.7	0.45	6079
7	A6	1.0	∞	3.7	0.45	6079
8	A7	1.2	5.6	4.4	0.50	7260
9	A8	1.2	10.4	4.4	0.50	7260
10	A9	1.2	20.9	4.4	0.50	7260
11	A10	1.2	41.8	4.4	0.50	7260
12	A11	1.2	62.7	4.4	0.50	7260
13	A12	1.2	∞	4.4	0.50	7260
14	A13	1.4	5.6	5	0.55	8251
15	A14	1.4	10.4	5	0.55	8251
16	A15	1.4	20.9	5	0.55	8251
17	A16	1.4	41.8	5	0.55	8251
18	A17	1.4	62.7	5	0.55	8251
19	A18	1.4	∞	5	0.55	8251
20	A19	1.6	5.6	5.7	0.60	9377
21	A20	1.6	10.4	5.7	0.60	9377
22	A21	1.6	20.9	5.7	0.60	9377
23	A22	1.6	41.8	5.7	0.60	9377
24	A23	1.6	62.7	5.7	0.60	9377
25	A24	1.6	∞	5.7	0.60	9377

To study the physical characteristics, mixing capacity, and coherent structure in sand-water swirling jets, images of the jets were recorded using a black and white high-speed camera (Photron-FASTCAM, 1024PCI-100KC) with a resolution of 1024×1024 pixels. The camera was equipped with a 15-55 mm AF-S Nikkor, 1:3.5-5.6 GII lens (Nikon, Japan) to capture images. Raw images were captured with a frame rate of between 250 and 500 frames per second and a shutter speed of 0.004 second. Figure 5.3 shows the snapshot images of sand-water swirling jets with unlimited sand mass (i.e., $L_o/d_o \approx \infty$) and different swirling numbers. As can be seen, the sand particles have more symmetrical patterns in swirling motion due to the

existence of a strong recirculation zone in sand-water swirling jets compare to the non-swirling jet.

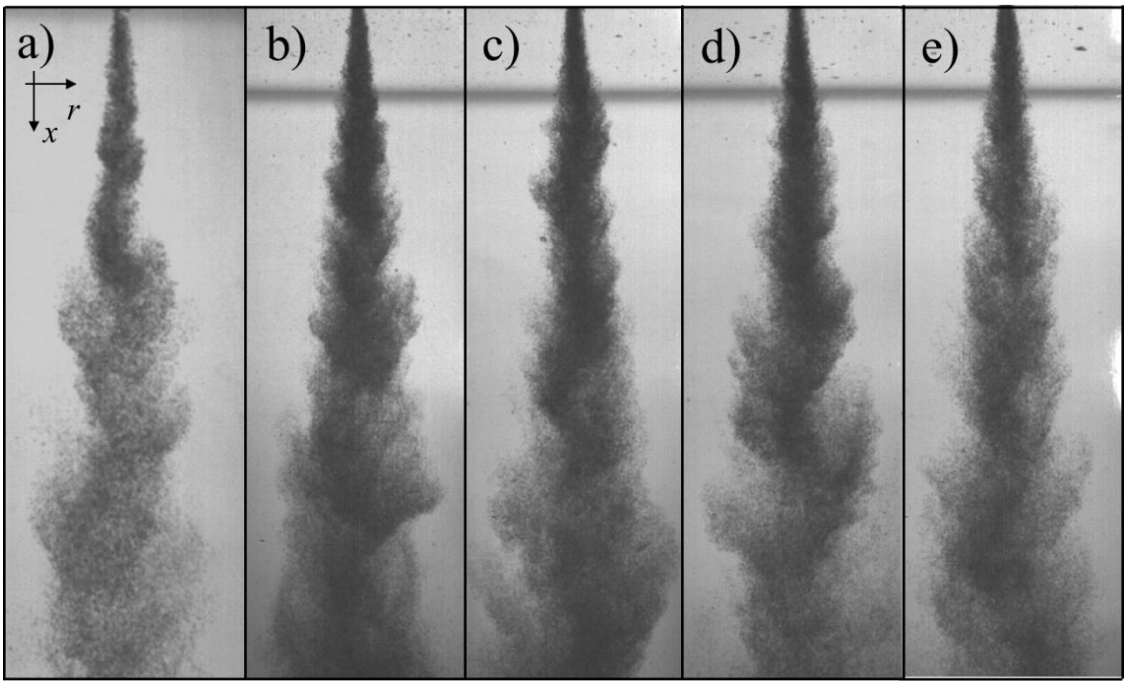

Figure 5.3: High speed images of sand-water swirling jets for different swirling numbers and $L_o/d_o \approx \infty$: a) $Sw = 0$; b) $Sw = 0.45$; c) $Sw = 0.50$; d) $Sw = 0.55$; e) $Sw = 0.60$.

The instantaneous concentration and velocity signals were captured by a light-refractive optical probe equipped with a signal transceiver and a processing unit, PV6 (Institute of Processing Engineering, Chinese Academy of Science, China). The sensing tip of the probe has a diameter of 4 mm and it contains two build-in light-refracting diodes with a diameter of 1 mm each and spaced 2.14 mm apart (see Figure. 5.1b). The fibers captured the reflection of passing solid particle signals and transferred them to an analog-to-digital data acquisition board (National Instrument, Austin, U.S.). The light refracting optical probe has shown high performance in measuring sand concentration and velocity and has been used in many experimental studies such as particle-laden jets and solid fluidization systems (Hall et al., 2010; Azimi et al., 2015; Taofeeq et al., 2018; Sharif and Azimi, 2020).

A voltage sampling rate of 61,440 Hz (Probe max gaining frequency) was selected to attain high-quality data and to have a manageable data size without aliasing. The sampling time of experiments was varied based on the aspect ratios in each test and it varied from 1.5 to 15 seconds. Based on the selected sampling frequency, each measurement contained between 92,160 and 921,600 data points. The MATLAB signal processing toolbox was implemented to process the recorded data (The MathWorks Inc., Natick, U.S.). The full MATLAB® m-file

code and an example is included in Appendix 2 and 3. The time lag, Δt, between the time series of signals in each fiber optic, was computed by cross-correlation technique. By dividing the time series of time lags by the distance between the two fiber optics (i.e., 2.14 mm), the time series of instantaneous sand velocity was calculated. Detailed information regarding the sensitivity analysis and performance of the PV6 optical probe can be found in Sharif and Azimi (2020). The sand velocity and concentration were measured along the axis of the swirling jet (x-axis) and at different transverse directions (r-axis). The time-averaged voltage signals from each probe were correlated to sand concentration by using a calibration curve. The measurement domain was selected based on signal quality and sufficient particle concentration. The centerline velocity and concentration were measured in the range of $0 < x/d_o < 60$ and the radial measurement range was $-5 < r/d_o < 5$. Beyond this domain, the measurement confidence decreased due to an insufficient number of particles passing by the probe. The swirling number was measured at $x/d_o = 5$ and the azimuthal velocity was measured at the half of the radius of the nozzle to capture both velocity components simultaneously. All experiments were repeated three times and the average of three centerline concentration and velocity measurements were used for the analysis. In addition, to test the repeatability of radial distribution of concentration and velocity profiles, data points in one profile were measured twice in each test. The variations of concentration and velocity data were ±2.1% and ±4.2%, respectively.

5.2.2 *Signal processing*

The acquired signals from turbulent flow are stochastic and oscillatory therefore, it is very important to maintain the properties of turbulent structure after denoising the raw signals. Wavelet transformation technique can be used as a powerful tool to decompose a signal into the time-frequency domain. It has been proved that the wavelet thresholding method for noise reduction works well for both uniform and transient flows (Donoho, 1991). The wavelet decomposition and denoising algorithms have been successfully employed to prepare measured voltage signals in turbulent jets and particle clouds (Weinkauff, 2015; Shojaeizadeh et al., 2018; Sharif and Azimi, 2020). Figure 5.4 shows the time series of voltage signals detected by the PV6 optical probe at the centerline of the jet and at $x/d_o = 10$. The time series of voltage signals belong to sand-water swirling jets with $Sw = 0.45$ and 0.6 and with an aspect ratio of 20.9. As can be seen, the instantaneous time history signal of $Sw = 0.45$ occurred in a shorter period in comparison with the test with $Sw = 0.6$. This indicates the influence of the central Recirculation Zone (RZ) on particle concentration for swirling jet with $Sw = 0.6$ and a uniform dissipation of concentration due to vortex formation.

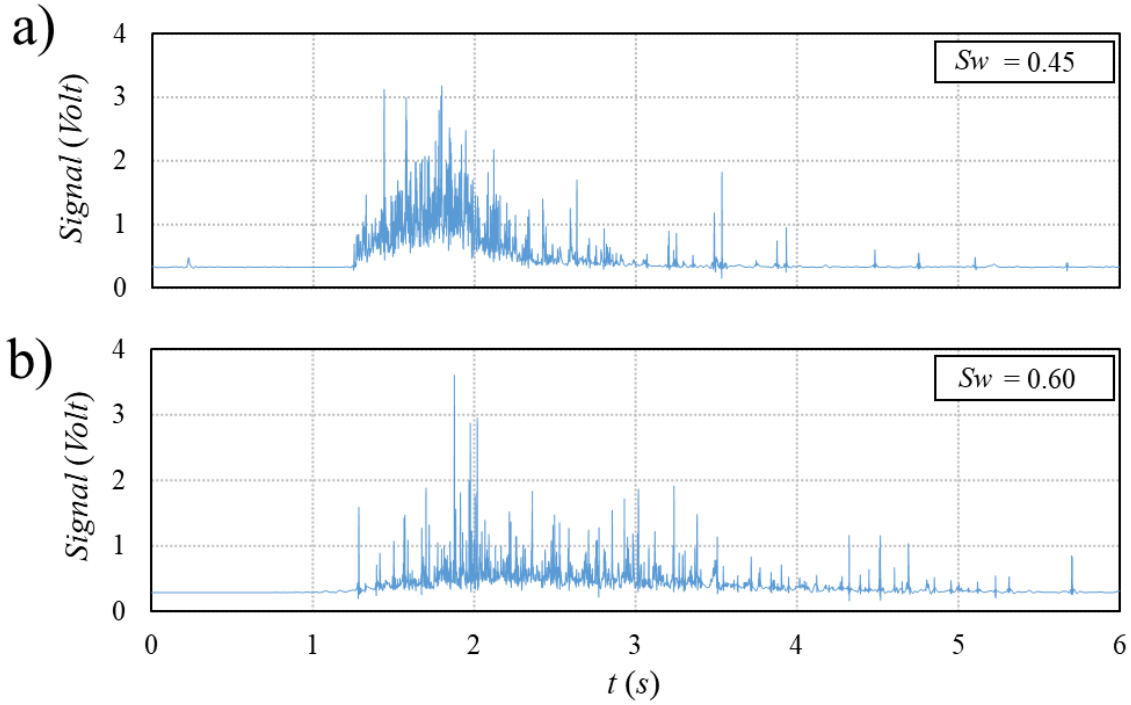

Figure 5.4: Time series of voltage signals detected by the PV6 fiber optic probe at the centerline of the jet and at x/d_o = 10. Effect of swirling number on the raw voltage signals of a sand-water swirling jet with L_o/d_o = 20.9: a) Sw = 0.45; b) Sw = 0.60.

The cross-correlation technique between the time series of voltage signals was performed to convert voltage signals to velocity data. Different data segmentation and overlapping of the time series of voltage signals were tested. A 50% overlap of the time-series segments was selected to investigate the effect of overlapping on velocity data. The overlapping technique was first employed by Welch (1967) to reduce the effect of windowing in spectral density estimation. Recently, data segmentation and overlapping technique were employed to improve the quality of signals in turbulent flows (Azimi et al., 2012a; Schmidt et al., 2017; Sharif and Azimi, 2020; Lim et al., 2020). The time histories of velocity data obtained from cross-correlations of voltage signals with different segment sizes of 512, 1,024, and 2,048 corresponding to the frequencies of 30 Hz, 60 Hz, and 120 Hz, and an overlap of 50% are shown in Figure 5.5. s. Since, the measurement signals have short-duration, the non overlapped analysis could miss the event if it occurred near the boundaries. To avoid this loss of data, the transforms are usually applied to the overlapped partition sequences. The overlap is almost always 50 or 75 percent. This overlap processing of course increases the work load to cover the total sequence length, but the rewards warrant the extra effort (Solomon; 1978; Harris, 1991). As shown in Fig. 8. The overlap is almost always 50 or 75 percent. This overlap processing of course increases the work load to cover the total sequence length, but the rewards

warrant the extra effort As can be seen, reducing the segment size increased the velocity fluctuations and spikes. It was found that the average uncertainties of velocity fluctuations for ΔL_s = 512, 1024, and 2048 were ±12%, ±8%, and ±2%, respectively. Furthermore, by applying a 50% overlap, the uncertainties of velocity fluctuations for ΔL_s = 512, 1024, and 2048 increased to ±13%, ±9%, and ±4%, respectively. The smaller window size and overlapping of data segments resulted in higher signal fluctuations and noisy data. Therefore, a segment length of ΔL_s = 2,048 with no overlapping (i.e., L_s = 0%) was selected for data preparation and analysis in this study.

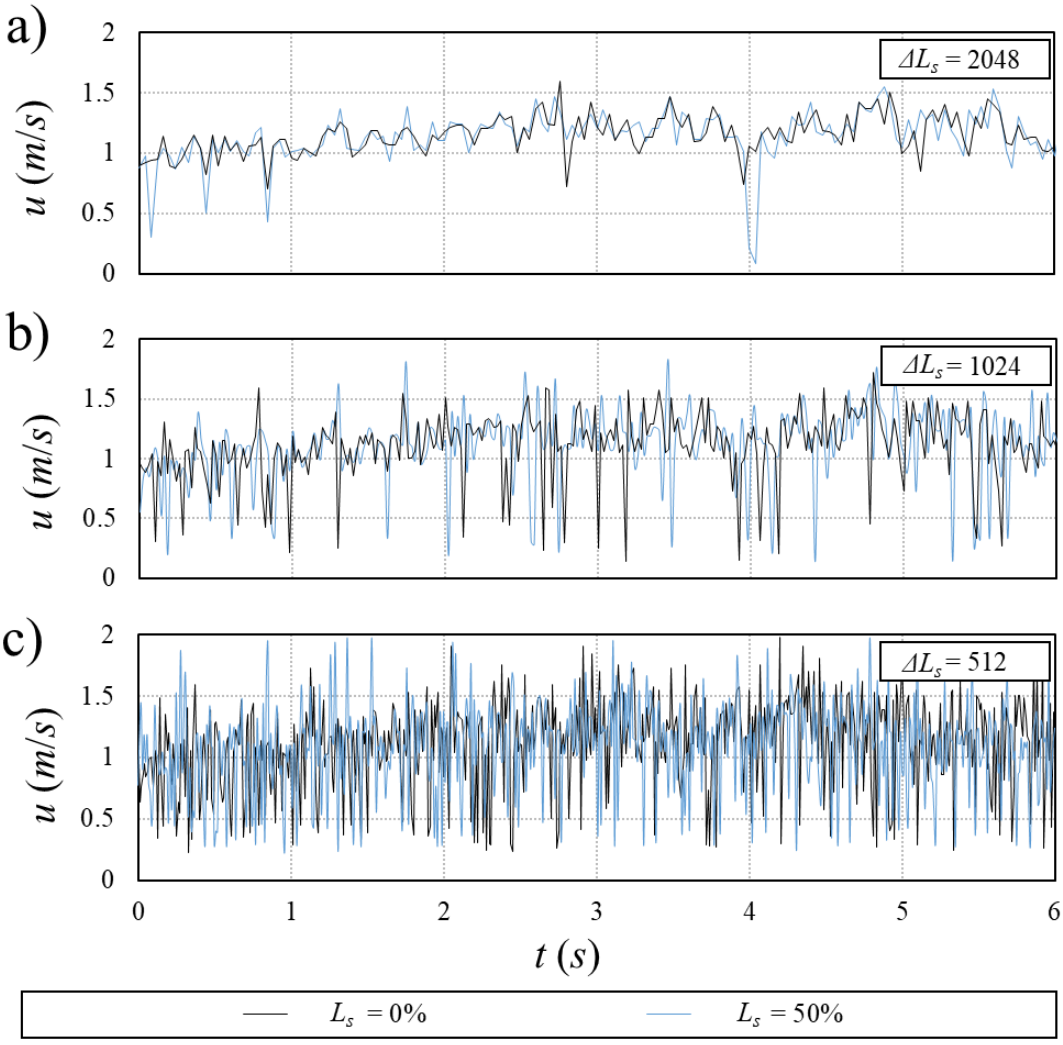

Figure 5.5: Time-history of the instantaneous sand velocity data extracted from voltage signals of the PV6 optical fiber probe. Effects of different segment overlapping, L_s = 0%, and 50% and segment lengths, ΔL_s on the centerline velocity of a swirling sand-water jet with Sw = 0.60 and $L_o/d_o \approx \infty$ at x/d_o = 10 with: a) ΔL_s = 2048; b) ΔL_s = 1024; c) ΔL_s = 512.

The effect of swirling motion on turbulent characteristics of sand-water swirling jets was investigated by comparing the time-series of turbulent intensity of sand-water swirling jets

with different swirling numbers (see Figure 5.6). The time histories of sand velocity fluctuations, u' for sand-water swirling jets with $L_o/d_o \approx \infty$ were measured at the centerline of the jet and at $x/d_o = 10$ (see Figure 5.6a). It was found that the rms of velocity for $Sw = 0$, 0.45, and 0.6 were ± 5%, ± 6%, and ± 8%, respectively. The turbulence intensity can be calculated as the ratio of the root-mean-square of sand particle velocity, u_{rms}, to the time-averaged velocity of sand particles, u_{ave}. It was found that the turbulent intensity for swirling sand-water jets with Sw = 0, 0.45, 0.6 were ± 3%, ± 4.6%, and ± 5%, respectively indicating that the turbulent intensity increased with increasing the swirling number.

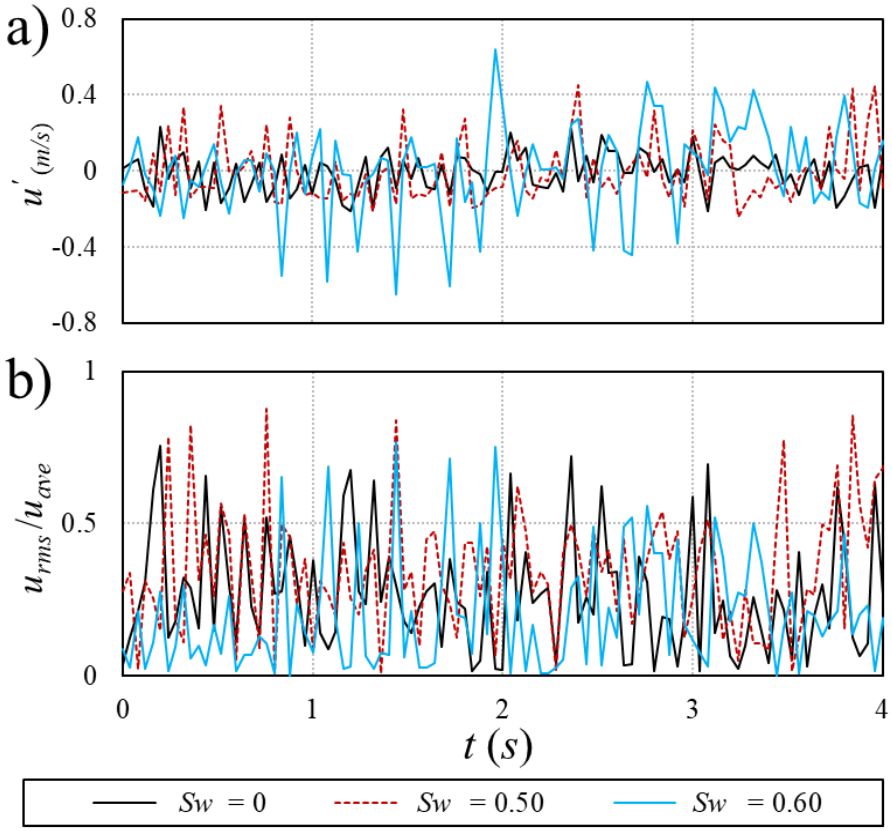

Figure 5.6: Effects of swirling number on the time history of turbulent characteristics of sand-water swirling jets with $L_o/d_o \approx \infty$. Velocity data were measured at the jet centerline and at x/d_o = 10: a) time history of velocity fluctuations, u'; b) time history of turbulence intensity, u_{rms}/u_{ave}.

5.3 Results and discussion

5.3.1 *Mass and momentum fluxes*

The variations of sand mass and momentum fluxes in different cross-sections and along the vertical axis of the jet can be used to evaluate the sensitivity of the optical probe in

measuring sand concentration and velocity. The mass conservation computations were performed by the particle mass moving across a unit area of sand-water swirling jets. The mass flux in each cross-section can be characterized as:

$$\dot{m} = \frac{dm}{dt} = 2\pi\rho_s \int_0^r cu\, r dr \tag{5.1}$$

Similarly, the sand momentum flux can be characterized in each cross-section as:

$$\dot{M} = \frac{dM}{dt} = 2\pi\rho_s \int_0^r cu^2 r dr \tag{5.2}$$

Figure 5.7 shows the variations of sand mass and momentum fluxes in sand-water swirling jets with different swirling numbers of Sw = 0.45, 0.50, 0.55, and 0.60. The integrated mass flux at each cross-section was normalized with the initial sand mass flux at the nozzle, $\dot{m}_o = \rho_s(\pi d_o^2/4)u_o c_o$. Figure 5.7a shows the variations of sand mass flux with x/d_o for sand-water swirling jets. The overbars indicate the uncertainty of measurements with the PV6 optical probe.

As can be seen in Figure 5.7a, 95% of the total sand mass was detected by the PV6 optical probe close to the nozzle. However, further downstream, the data uncertainties are spanning around 10%. Many parameters affect the conservation of mass flux such as the inefficiency of the optical probe to detect very low sand concentration and presence of multi-particle signals and high voltage spikes (Aísa et al., 2002). As a result, sand mass flux became less than unity due to particle dispersion and reduction in sand concentration particularly far from the recirculation zone. In addition, far from the nozzle, the sensitivity of probe to capture correct signals and the quality of voltage signals decreased. The variations of sand momentum flux with x/d_o for sand-water swirling jets with different swirling numbers are shown in Figure 5.7b. The sand momentum flux was normalized with the initial sand momentum flux at the nozzle, $\dot{M}_o = \rho_s(\pi d_o^2/4)u_o^2 c_o$. The computed sand momentum fluxes of slurry jets were also included for comparison (Hall et al., 2010). As can be seen, sand momentum flux significantly decreased from the nozzle until x/d_o = 20.

This indicates a significant momentum reduction in the recirculation zone due to formation of counter-rotating core. However, further downstream (i.e., $x/d_o \geq 20$), the calculated normalized momentum flux became less variant with distance from the nozzle and

decreased from $\dot{M}/\dot{M}_o = 0.20$ at $x/d_o = 20$ to $\dot{M}/\dot{M}_o = 0.1$ at $x/d_o = 60$. The counter-rotating core formation can cause radial turbulent momentum transfer outward of the jet axis and toward the Processing Vortex Core (PVC) leading to a higher axial momentum dissipation rate (Maciel et al., 2008).

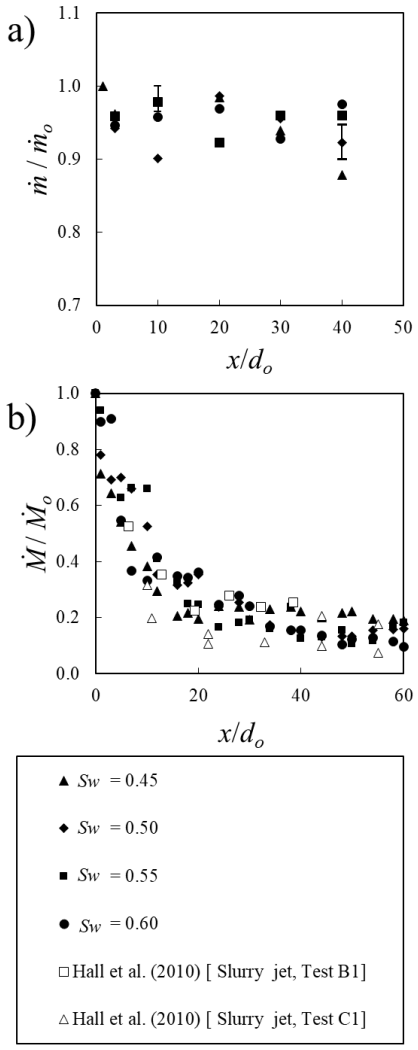

Figure 5.7: Effects of swirling number on variations of the integral quantities of sand-water coaxial jets with normalized distance from the nozzle, x/d_o for sand-water swirling jets with $L_o/d_o \approx \infty$: a) variations of the normalized sand mass flux with x/d_o; b) variations of the normalized momentum flux with x/d_o.

5.3.2 *Spreading rate and mixing*

The spreading rate in turbulent jets is known as the slope of the half-width line, $b(x)$, along the jet axis. The half-width can be estimated at a point where the velocity is 50% of the centerline velocity (Kotsovinos, 1976; Rajaratnam, 1976). Figure 5.8 shows the variations of the normalized half-width based on velocity profile, b_u, with the normalized distance from the nozzle for sand-water swirling jets with unlimited sand mass (i.e., $L_o/d_o \approx \infty$) and different

swirling numbers (i.e., $0.46 \leq Sw \leq 0.60$). The spreading rates of single-phase water jets with a value of $db(x)/dx = 0.114$ (Wygnanski and Fiedler, 1969), slurry jets, coaxial sand-water jet, and single-phase swirling jet (i.e., $db(x)/dx = 0.199$) were also added for comparison (Azimi et al., 2012b; Sharif and Azimi, 2021; Lewis et al., 2010). As can be seen, the spreading rate of swirling jets for all swirling numbers was slightly higher than the spreading rate of single-phase water, sand-water coaxial, and slurry jets. As can be seen, the spreading rate increased linearly by increasing the swirling number and became close to the spreading rate of single-phase swirling jet for $Sw = 0.6$. Overall, all exhibited swirling numbers had smaller spreading rate than single-phase swirling jets as:

$$b_u/d_o = 0.21Sw + 0.07 \tag{5.3}$$

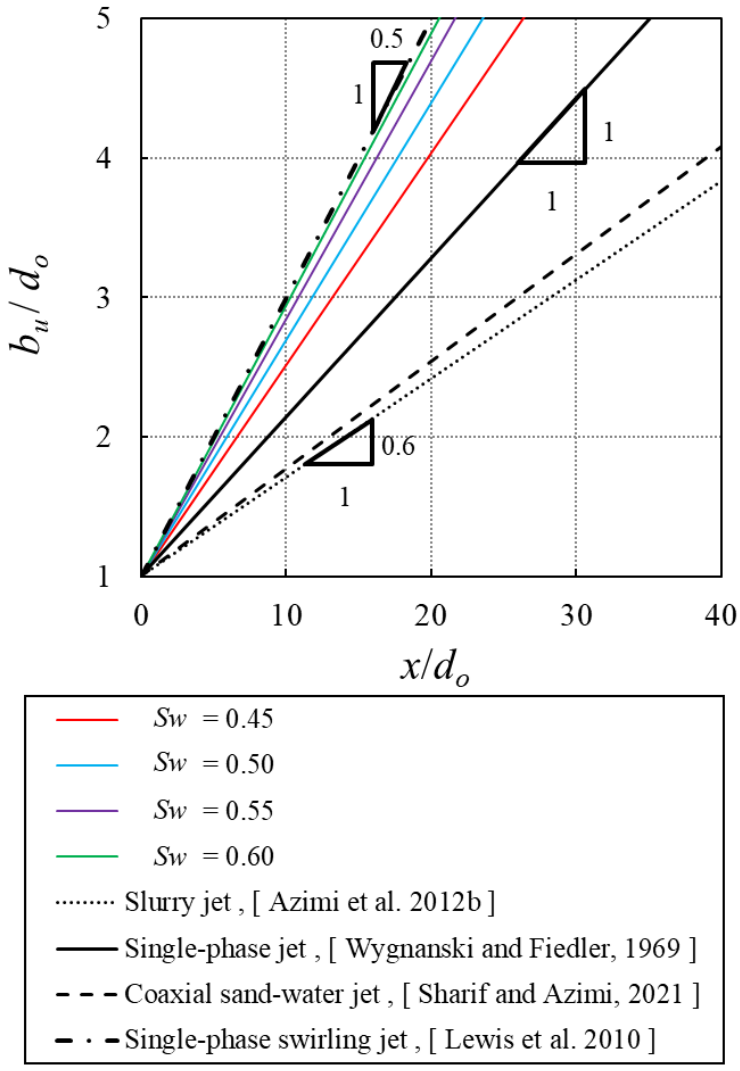

Figure 5.8: Effects of swirling number on the spreading rate of sand-water swirling jets with $L_o/d_o \approx \infty$.

5.3.3 *Swirling jets with unlimited sand mass*

The effect of swirl intensity on the axial and radial variations of sand concentration and velocity of sand-water swirling jets with unlimited sand mass (i.e., $L_o/d_o \approx \infty$) was studied. The effect of swirling number on variations of the axial mean centerline sand concentration is shown in Figure 5.9. The centerline concentration, c_m, was normalized with the initial sand concentration c_o, and the distance from the nozzle, x, was normalized with the nozzle diameter, d_o. The overbars in Figure 5.9 indicate the uncertainty of sand concentration measurements with the PV6 optical probe.

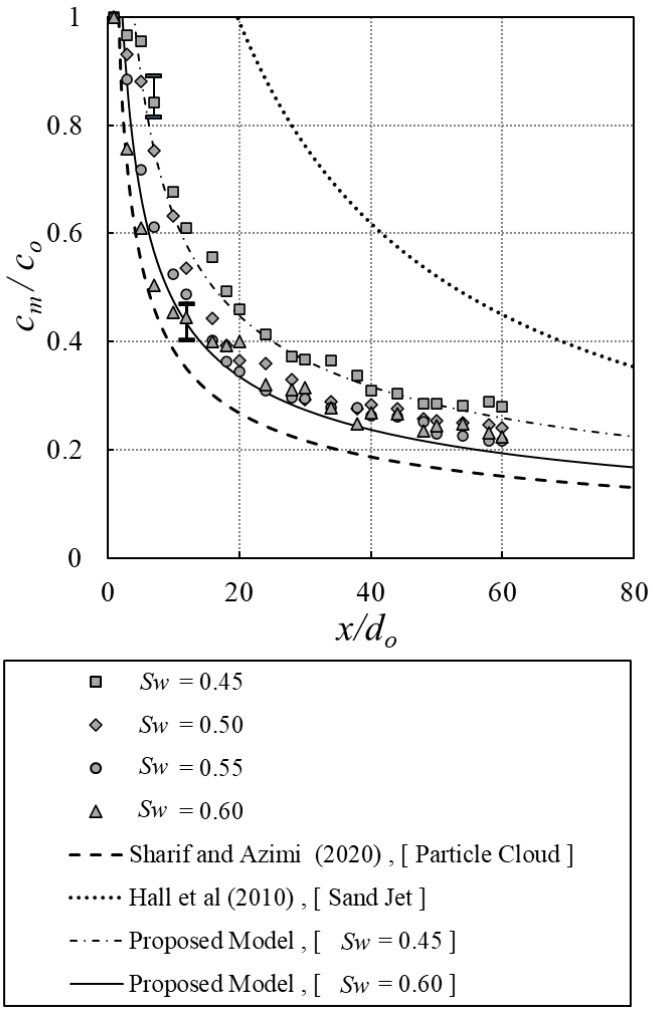

Figure 5.9: Effects of swirling number on variations of the normalized centerline sand concentration, c_m/c_o, with normalized axial distance from the nozzle, x/d_o, for sand-water swirling jets with $L_o/d_o \approx \infty$.

The maximum uncertainty of sand concentration measurements indicated a variation of ±9%. The variations of sand centerline concentration for particle cloud with an aspect ratio of

L_o/d_o = 39.2 (Sharif and Azimi, 2020) and sand jets with unlimited sand mass (Hall et al., 2010) were also included in Figure 5.9. As can be seen, the decay rate of sand concentration in sand-water swirling jets increased non-linearly with increasing swirling number. In addition, concentration decay rates are slightly higher than the concentration decay rate in slurry jets and lower than the concentration decay rate of particle clouds. A power law correlation was proposed to predict the variations of centerline sand concentration along the vertical axis in sand-water swirling jets with unlimited sand mass as:

$$\frac{c_m}{c_o} = 0.9\left(\frac{x}{d_o}\right)^{-1/2} Sw^{-1} \tag{5.4}$$

The coefficient of determination of the proposed equation R^2 is 0.97. The sensitivity of proposed model for smaller and higher swirling numbers (i.e., Sw = 0.45 and 0.60) was also included in Figure 5.9.

Figure 5.10 shows the radial variations of the normalized sand concentration, c/c_m, with the normalized transverse distance from the nozzle, r/d_o, for sand-water swirling jets with different swirling numbers (i.e., $0.45 \leq Sw \leq 0.6$) and different distances from the nozzle. As can be seen, concentration profiles in transverse direction for all exhibited swirling numbers can be fitted by a Gaussian distribution model. Using a Gaussian distribution function, the radial variations of sand concentration in sand-water swirling jets can be described as:

$$\frac{c}{c_m} = \exp\left[-0.693\left(\psi_c \frac{r}{d_o}\right)^2\right] \tag{5.5}$$

with a coefficient of determination R^2 = 0.95. The parameter ψ_c was correlated with both x/d_o and Sw and can be described as:

$$\psi_c = 3.3\left[Sw\left(\frac{x}{d_o}\right)\right]^{-1} \tag{5.6}$$

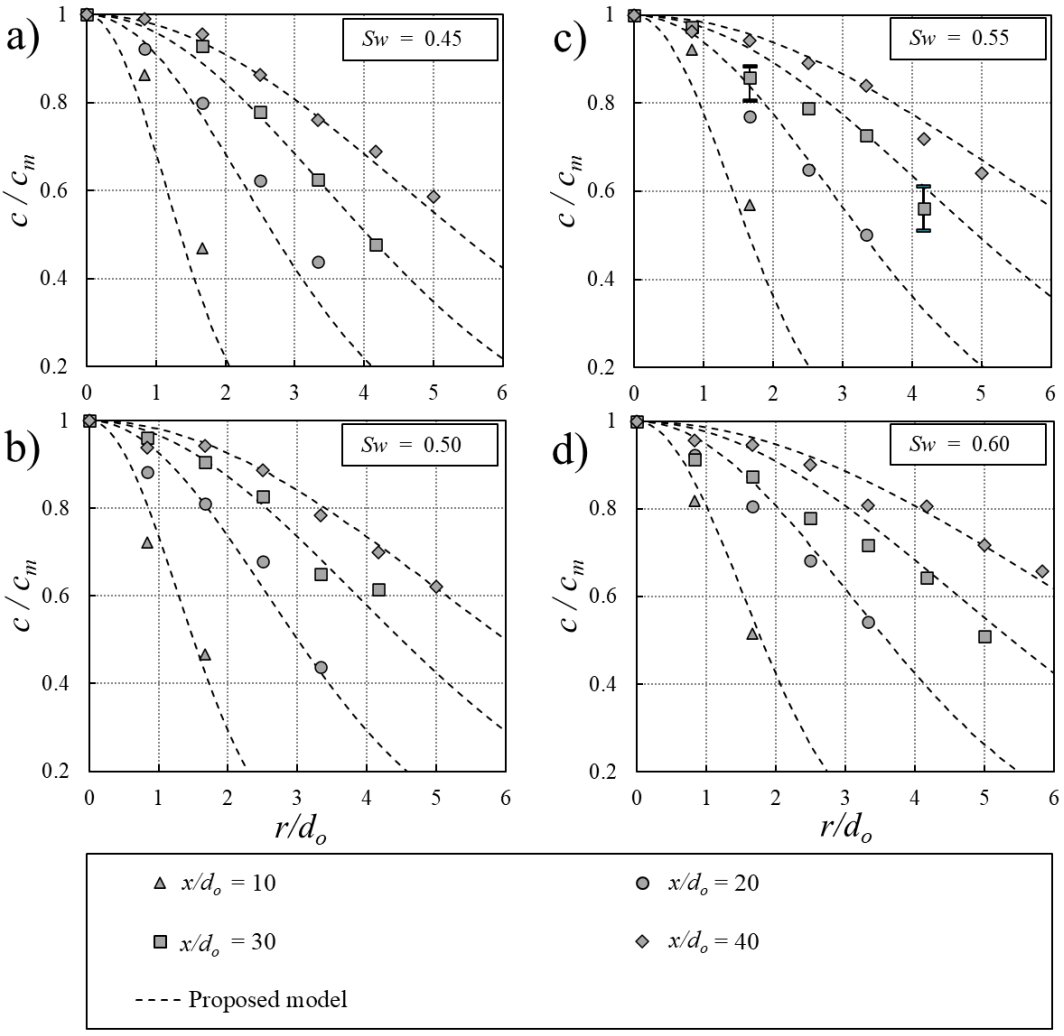

Figure. 5.10: Effects of swirling number on the radial variations of normalized sand concentration, c/c_m, with normalized distance from the nozzle, x/d_o, for sand-water swirling jet with $L_o/d_o \approx \infty$: a) $Sw = 0.45$; b) $Sw = 0.50$; c) $Sw = 0.55$; d) $Sw = 0.60$.

The maximum difference between the measurements and the model was ± 13% and it occurred at $r/d_o \geq 4$. Such high discrepancy is due to multi-particle signals and high voltage spikes at the edge of the jet and low particle concentration. The minimum deviation from the proposed model was ± 0.09%. Variations of normalized centerline velocity of sand particles with x/d_o for sand-water swirling jets with unlimited sand mass (i.e., $L_o/d_o \approx \infty$) were plotted for different swirling numbers ranging between 0.45 and 0.60 (see Figure 5.11). The centerline sand velocity, u_m, was normalized with the initial velocity of sand particles at the nozzle, u_o. The prediction model for sand centerline velocity of particle clouds with a relatively high aspect ratio (i.e., $L_o/d_o = 39.2$) from the experimental study of Sharif and Azimi (2020) and the proposed model for prediction of centerline sand velocity in slurry jets with small particle size (i.e., $0 < S_t \leq 0.1$) from study of Hall et al. (2010) were also included in Figure 5.11 for

comparison. The maximum uncertainty of sand velocity measurements was added as an overbar in Figure 5.11. As can be seen in Figure 5.11, the axial sand velocities of sand-water swirling jets non-linearly decreased with increasing x/d_o. Furthermore, the dissipation rate increased by increasing the swirling number. A mathematical model was developed to predict sand-phase centerline velocity of sand-water swirling jets with $R^2 = 0.95$ as:

$$\frac{u_m}{u_o} = 0.87\left(\frac{x}{d_o}\right)^{-1/2} Sw^{-1.13} \tag{5.7}$$

The prediction curves for smaller and higher swirling numbers were added in Figure 5.11.

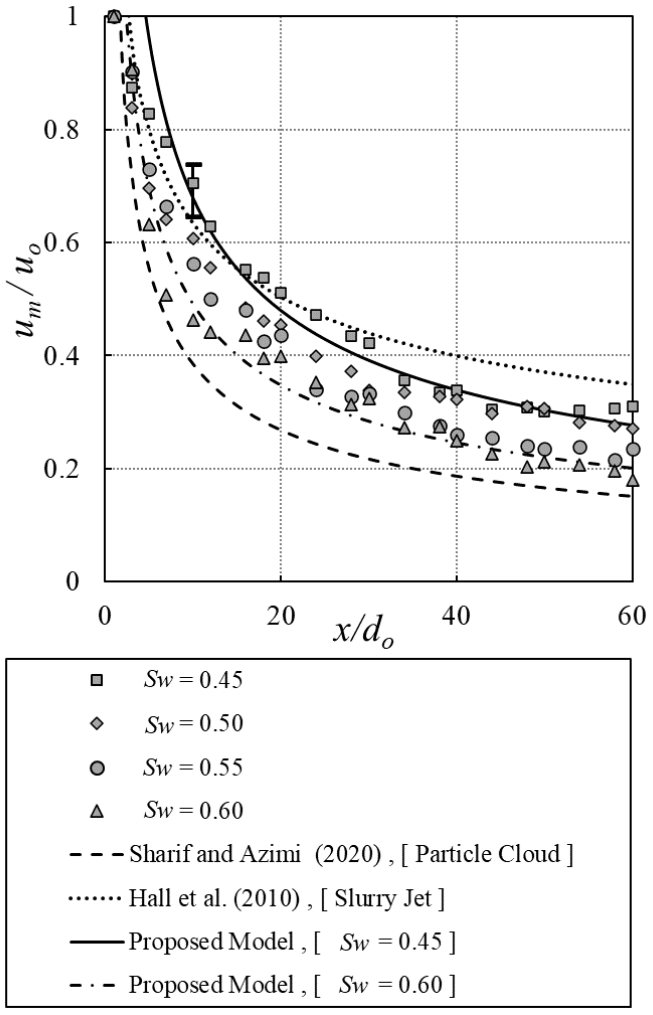

Figure 5.11: Effects of swirling number on variations of the normalized centerline sand velocity, u_m/u_o, with normalized axial distance from the nozzle, x/d_o, for sand-water swirling jets with $L_o/d_o \approx \infty$.

The effects of swirl intensity on radial distribution of sand axial velocity for sand-water swirling jets and for different normalized distances from the nozzle, x/d_o, are plotted in Figure 5.12. The axial velocities at different radial directions, u, were normalized with the centerline axial velocity, u_m, and the radial distance from the centerline, r, were normalized with the nozzle diameter, d_o. In addition, the Gaussian distribution model for the zone of flow establishment of single-phase swirling jet was also included for comparison (Lewis et al., 2010).

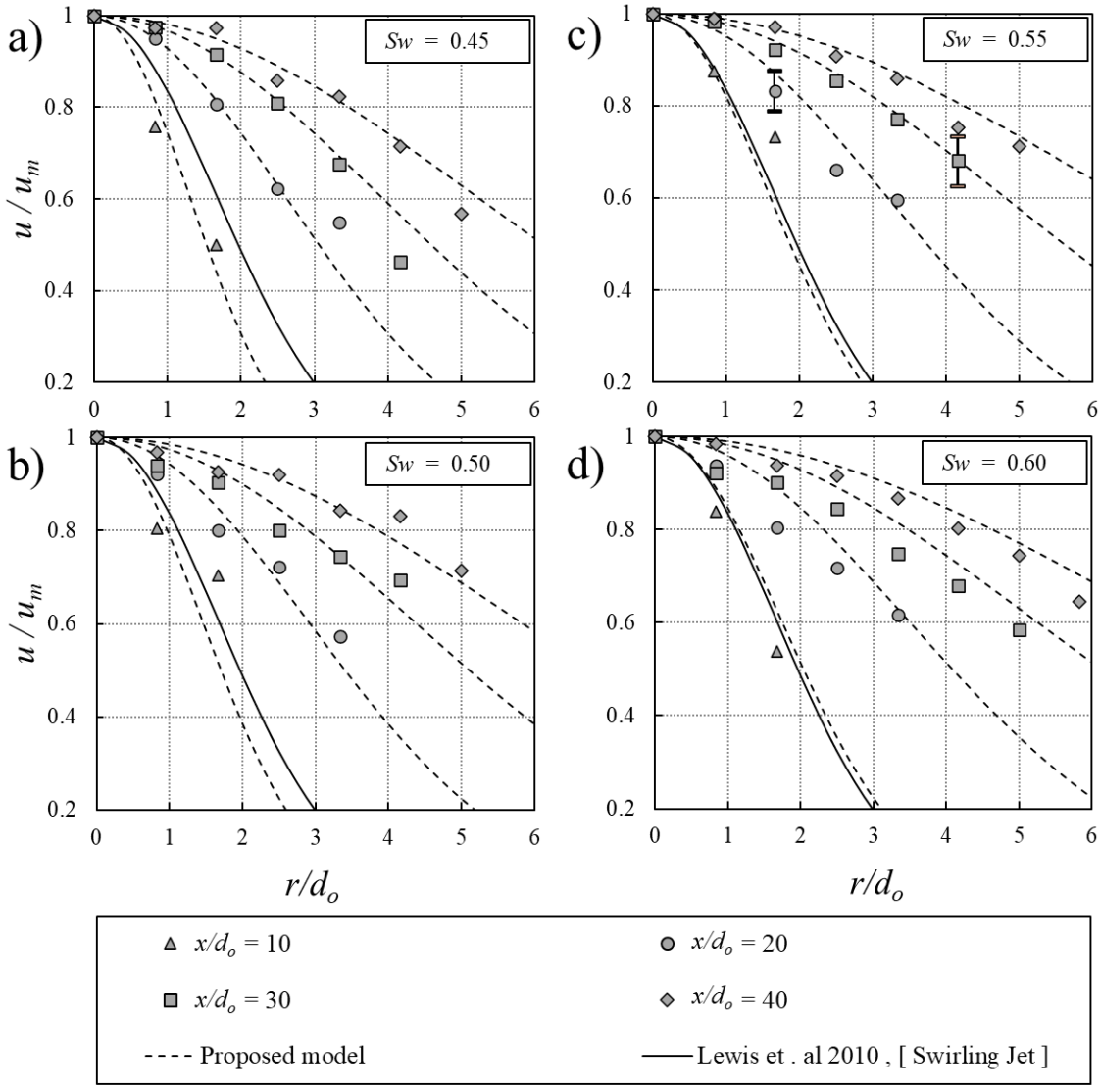

Figure 5.12: Effects of swirling number on the radial variations of normalized centerline sand velocity, u/u_m, with normalized distance from the nozzle, x/d_o, for sand-water swirling jets with $L_o/d_o \approx \infty$: a) $Sw = 0.45$; b) $Sw = 0.50$; c) $Sw = 0.55$; d) $Sw = 0.60$.

As can be seen, in sand-water swirling jets with higher swirl intensity, sand velocities were expanded in the radial direction due to formation of the Precessing Vortex Core (PVC). It can be explained that once particles impinged from the jet and placed at the recirculation

zone, the divergence from the axial direction initiates after stagnation point and the particles enter to the Processing Vortex Core due to centrifugal force, particularly in higher swirling numbers. As a result, large-scale fluctuations and dispersion occur in the transverse direction (Kazemi et al., 2018). A model based on Gaussian distribution was proposed to predict the radial distribution of sand axial velocity in sand-water swirling jets with unlimited sand mass (i.e., $L_o/d_o \approx \infty$) and with $R^2 = 0.89$ as:

$$\frac{u}{u_m} = \exp\left[-0.693\left(\psi_u \frac{r}{d_o}\right)^2\right] \tag{5.8}$$

The proposed model is applicable for $10 \leq x/d_o \leq 40$. The parameter ψ_u was found to be correlated with x/d_o and Sw as:

$$\psi_u = 2.94\left[Sw\left(\frac{x}{d_o}\right)\right]^{-1} \tag{5.9}$$

At x/d_o =10, the deviation between the proposed model decreased by increasing the swirling number in comparison with the single-phase swirling jet. This indicated the small length of the potential core in sand-water swirling jects with higher swirling numbers and the onset of Precessing Vortex Core. It was found the length of the potential core for $Sw \leq 0.55$ is five times of nozzle diameter and it was three times of the nozzle diameter for $Sw = 0.60$.

5.3.4 *Swirling jets with limited sand mass*

Sand-water swirling jets can be generated with a limited amount of sand mass which can be quantified by the aspect ratio, L_o/d_o. Figure 5.13 shows the snap-shot images of sand-water swirling jets with a wide range of aspect ratios of $5.6 < L_o/d_o < 41.8$ and with different swirl numbers ranging from $Sw = 0.45$ to 0.60. All images were taken at a non-dimensional time of $t^* = 1.4$ where $t^* = 1$ is the time when all sand particles enter to the ambient water.

As can be seen in Figure 5.13, swirling jets with small aspect ratios of $L_o/d_o = 5.6$ and 10.4 had a relatively uniform particle distribution and sand concentration decreased by increasing swirling strength (see columns (1) and (2) in Figure 5.13). Sand concentration at the jet centerline increased by increasing aspect ratio and swirling strength. As can be seen from the images, sand particles are more concentrated in the central recirculation zone (i.e., $x_o/d_o \leq$

20) and relatively uniform sand concentration distribution was found in sand-water swirling jet with Sw = 0.6 and L_o/d_o = 10.4. As the swirling strength and aspect ratio of the jet increased simultaneously, particles moved away from the vertical axis due to the effect of centrifugal force on the individual particles. Such a swirl motion forms the Precessing Vortex Core (PVC) from the stagnation point that were shown in columns (3) and (4) of Figure 5.13. Identifying the stagnation point is difficult due to high turbulence level in swirling jets. Therefore, irregular alternation of the PVC can be considered as an indicator that the flow is close to the stagnation point (Noiray and Schuermans, 2013).

The effect of swirling strength on the axial variations of normalized sand concentration of sand-water swirling jets with limited sand mass is shown in Figure 5.14. This shows the decay of sand concentration in sand-water swirling jets with aspect ratio, L_o/d_o, ranging between 5.6 and 62.7. The proposed models for prediction of sand concentration in particle clouds (i.e., u_o = 0, Sw = 0) with aspect ratios of 19.6 and 39.2 from the study of Sharif and Azimi (2020) were also added for comparison.

Figure 5.14a shows the effect of aspect ratio on variations of sand concentration for sand-water swirling jets with Sw = 0.45. The decay rate of sand concentration for sand-water swirling jets with low aspect ratio (i.e., $L_o/d_o \leq 10.4$) was found to be comparable with the decay rate of particle clouds with L_o/d_o =19.6. For Sw = 0.45 and 0.5, the decay rate of swirling jets with higher aspect ratios were similar to the proposed model for swirling jets with unlimited sand (i.e., $L_o/d_o = \infty$) and the normalized concentrations were higher than the particle clouds with L_o/d_o =39.2. Two different regimes were observed in the decay rate of sand concentration for sand-water swirling jets with Sw = 0.45 and 0.5. By increasing the swirl intensity to Sw = 0.5, swirling jets with L_o/d_o of 5.6 and 10.4 had a similar decay rate similar to particle clouds with a low aspect ratio (Figure 5.14b). For Sw = 0.55, all cases exhibited a similar decay rate and the dissipation trend was underestimated by the proposed model for sand-water swirling jet with unlimited sand particles (Figure 5.14c). On the other hand, increasing the swirling number to 0.6 the decay rate decreased considerably indicating that particles adopted the properties of carrier fluid (Figure 5.14d).

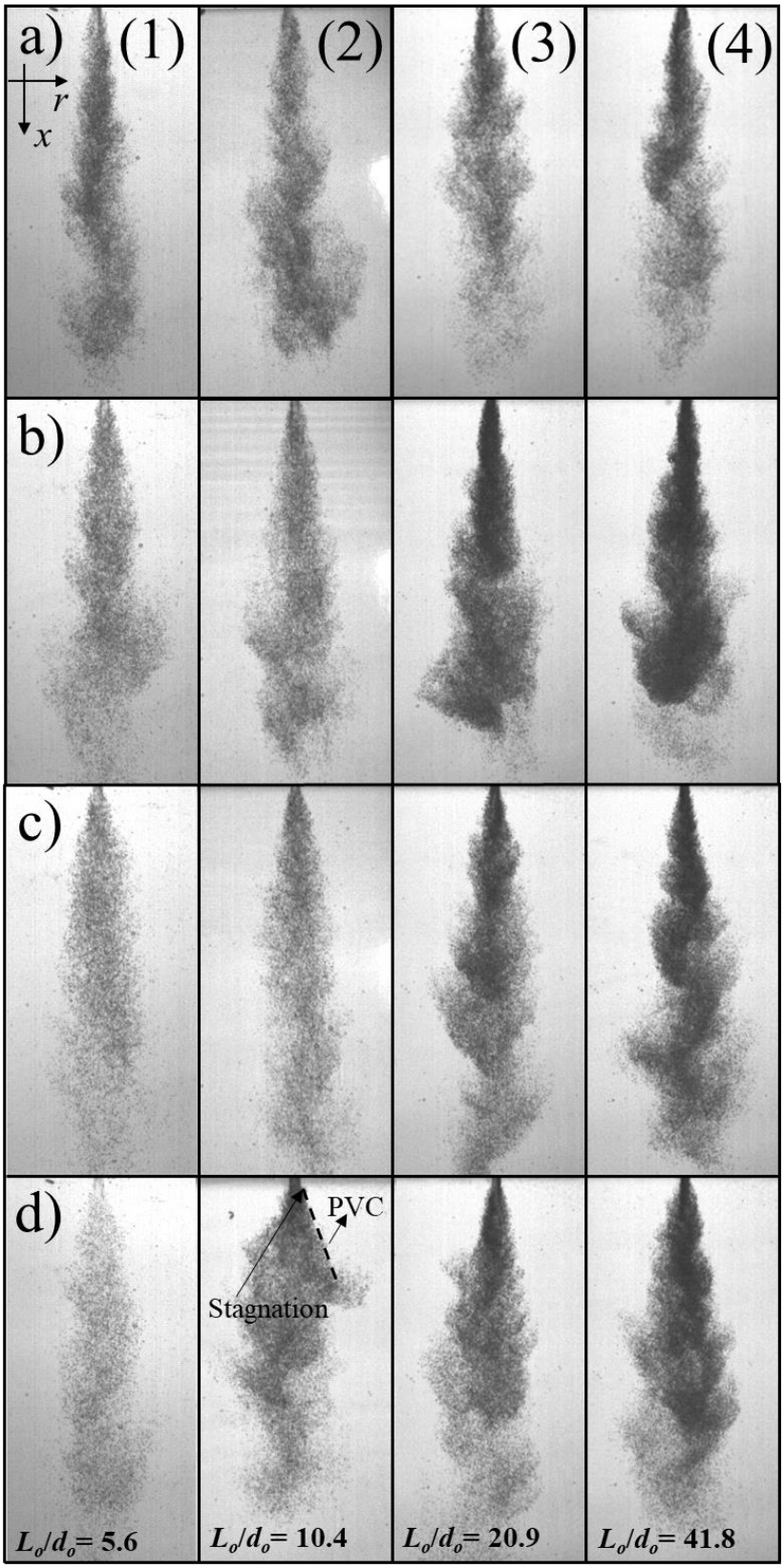

Figure 5.13: Raw images of sand-water swilring jets with different swirling number and aspect ratio at the non-dimensional time of t^* = 1.4: a) Sw = 0.45; b) Sw = 0.50; c) Sw = 0.55; d) Sw = 0.6.

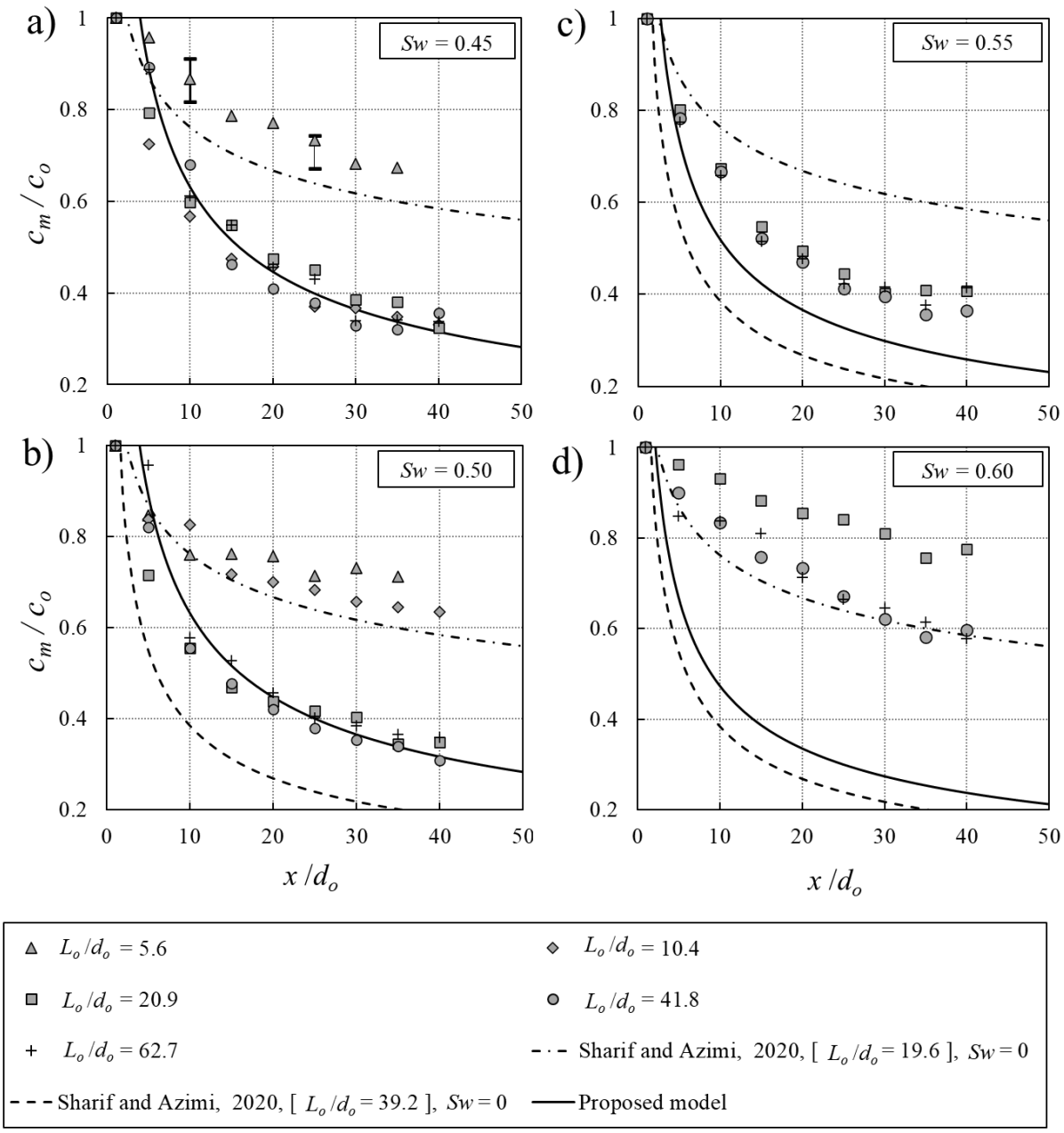

Figure 5.14: Effects of swirling number, Sw, and aspect ratio, L_o/d_o, on variations of normalized centerline sand concentration, c_m/c_o, with normalized axial distance from the nozzle, x/d_o: a) Sw = 0.45; b) Sw = 0.50; c) Sw = 0.55; d) Sw = 0.60.

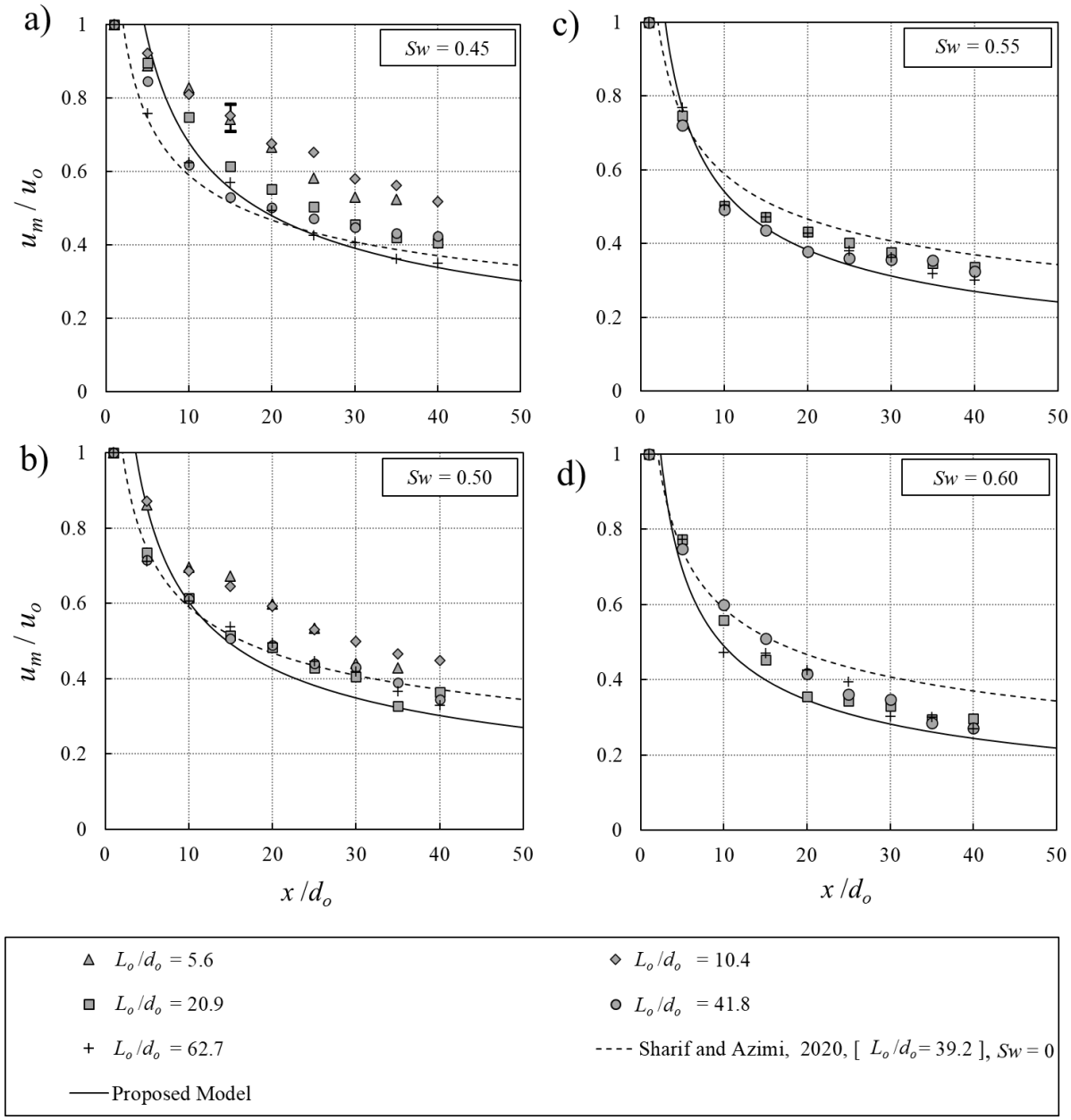

Figure 5.15: Effects of swirling number on the radial variations of normalized sand velocity, u/u_m, with normalized distance from the nozzle, x/d_o for sand-water swirling jets with $L_o/d_o \approx \infty$: a) $Sw = 0.45$; b) $Sw = 0.50$; c) $Sw = 0.55$; d) $Sw = 0.60$.

The effects of aspect ratio on the decay rate of axial velocity in sand-water swirling jets with limited sand particles (i.e., $5.6 \leq L_o/d_o \leq 62.7$) and different swirling numbers (i.e., $0.45 \leq Sw \leq 0.6$) are shown in Figure 5.15. For $Sw = 0.45$ and 0.50, the decay rate increased by increasing the aspect ratio and became close to the proposed model for unlimited sand particles (i.e., $L_o/d_o \approx \infty$) and particle clouds with no swirling motion and $L_o/d_o > 10.4$ (Figures 5.15a and 5.15b). The dissipation rate of axial sand velocity in sand-water swirling jets was approximately similar to particle clouds for all aspect ratios for $Sw = 0.55$ and 0.6 (Figures

5.15c and 5.15d). The prediction model for unlimited sand mass is suitable to predict the dissipation rates for all swirling numbers and for $L_o/d_o > 10.4$.

5.3.5 *Drag coefficient*

Parametrization of the particle motion and particle-particle interactions are important to evaluate the mixing properties in sand-water swirling jets. The radial distribution of drag coefficient, exerted by the surrounding fluid on particles, at different distances from the nozzle was calculated by employing momentum equation (see Figure 5.16). The momentum equation has been employed to compute the averaged drag coefficient on individual particles in sand/slurry and particle clouds in the literature (Azimi et al., 2012b; Moghadaripour et al., 2017; Manzouri and Azimi, 2019: Sharif and Azimi, 2020). The buoyancy force of particles can be estimated knowing the mass of sand particles, m, in each disk-shaped domain as:

$$F_{B(x)} = \frac{\pi {d_o}^2}{4} L_o \bar{c} \rho_w g \tag{5.10}$$

where $\bar{c}$ is the average concentration of sand particles occupying in a disk-shaped control volume and g is the acceleration due to gravity. Thus, by balancing the gravitational force, F_g, and buoyancy force, F_B, acting on particles with the rate of change of momentum $M_{(x)}$, the average drag force, F_D, can be computed as:

$$\left(\dot{M}_{(x)} - \dot{M}_{(x+\Delta x)}\right) = F_{D(x+\frac{\Delta x}{2})} + F_{B(x+\frac{\Delta x}{2})} - F_{g_{(x+\frac{\Delta x}{2})}} \tag{5.11}$$

The momentum flux of sand particles, $M_{(x)}$, at each cross-section can be estimated by integrating velocity and concentration profiles as:

$$\dot{M}_{(x)} = \int_0^{r_{(x)}} \rho_s c_{(x)} {u_{(x)}}^2 r_{(x)} 2\pi dr \tag{5.12}$$

On the other hand, the individual drag force acting on a single particle can be estimated by:

$$f_D = F_D / N_p \tag{5.13}$$

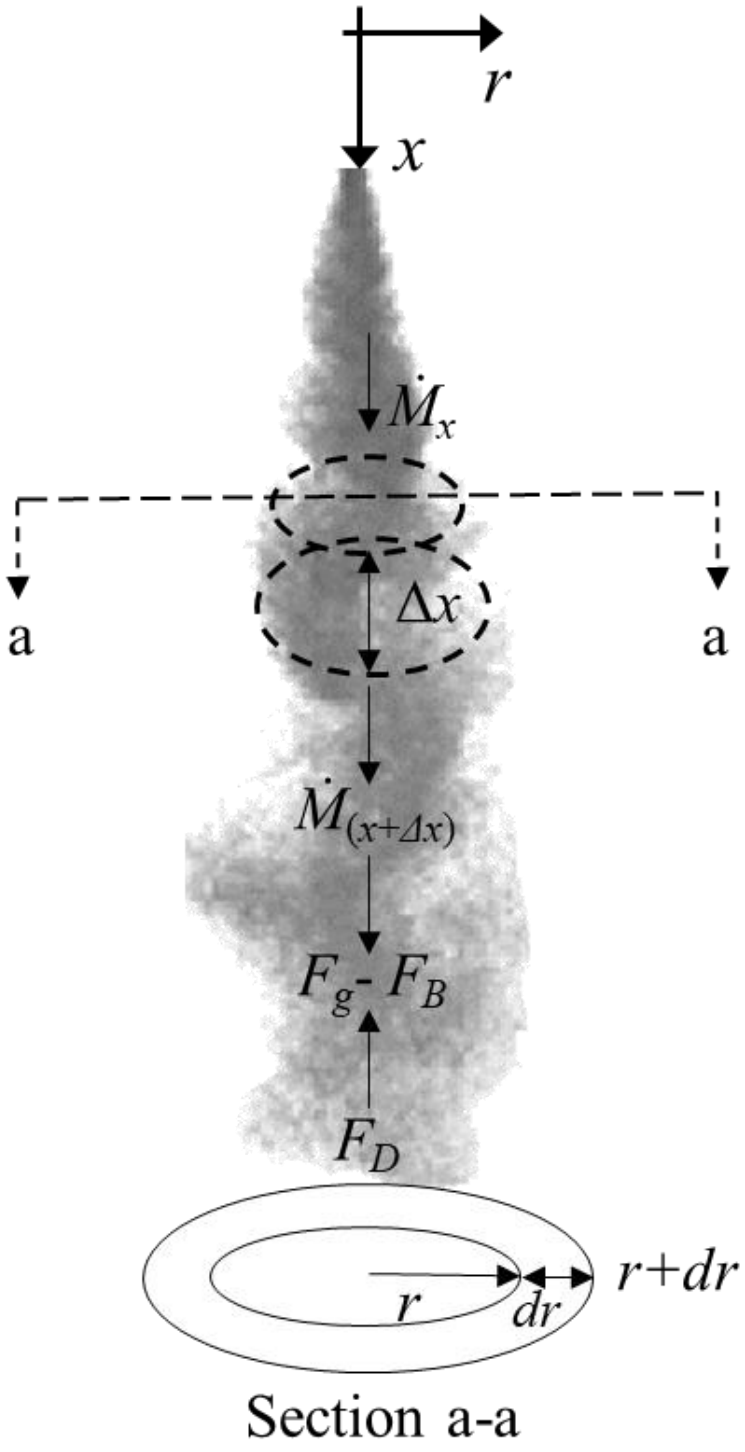

Figure 5.16: Schematic of the momentum balance in sand-water swirling jets.

where the number of particles, N_p, can be calculated as:

$$N_p = \frac{\bar{c}\, V_{disc}}{V_p} \tag{5.14}$$

where V_p is the volume of individual spherical particles (i.e; $V_p = \pi D_{50}^3/6$) and $\bar{c}\,V_{disc}$ is the product of domain control volume and average concentration which can be calculated as:

$$\bar{c}\,V_{disc} = \frac{\left(c_{(x)} + c_{(x+\Delta x)}\right)}{2}\left(\int_0^{r_{(x)}} r_{(x)}\pi dr + \int_0^{r_{(x+\Delta x)}} r_{(x+\Delta x)}\pi dr\right)\Delta x$$

(5.15)

Using the classical formulation of drag force (i.e., $f_D = 1/2\ \rho_w\ C_d\ A_p\ u^2$) where A_p is the projected frontal area of individual sand particles, (i.e., $A_p = \pi D_{50}^2/4$) to predict the drag coefficient, the individual drag coefficient acting on a particle can be calculated as:

$$C_d = \frac{8 f_D}{\rho_w A_p\ \left(u_{(x)} + u_{(x+\Delta x)}\right)^2}$$

(5.16)

The effects of swirling number (i.e., $0.45 \leq Sw \leq 0.60$) on variations of cross-sectional average drag coefficients for sand-water swirling jets with particle Reynolds number R_p in the range of $200 < R_p < 1000$ are shown in Figure 5.17. A proposed model for estimating the drag coefficient of individual sand particles as a function of sphericity ratio, φ, in the range of $0.2 \leq \varphi \leq 1$ and for $R_p \leq 5000$ was added for comparison (Chien, 1994). In addition, the classical Schiller & Neumann (Wörner, 2003) drag model for spherical particles and for $0.1 \leq R_p \leq 800$ was added in Figure 5.17. As shown in Figure 5.17, the swirling motion can significantly impact the motion of particles and the drag coefficient increased significantly in comparison to the drag coefficient of an individual particle. Furthermore, the existence of swirling motion and particle migration to the Precessing Vortex Core reduced the grouping effect far from the nozzle and as a result, the drag coefficient increased by decreasing particle Reynolds number. A formula was proposed to predict the correlation between C_d and R_p for sand-water swirling jets with a coefficient of determination of $R^2 = 0.92$ as:

$$C_d = 0.12 + 15\, e^{(-0.006 R_p)}$$

(5.17)

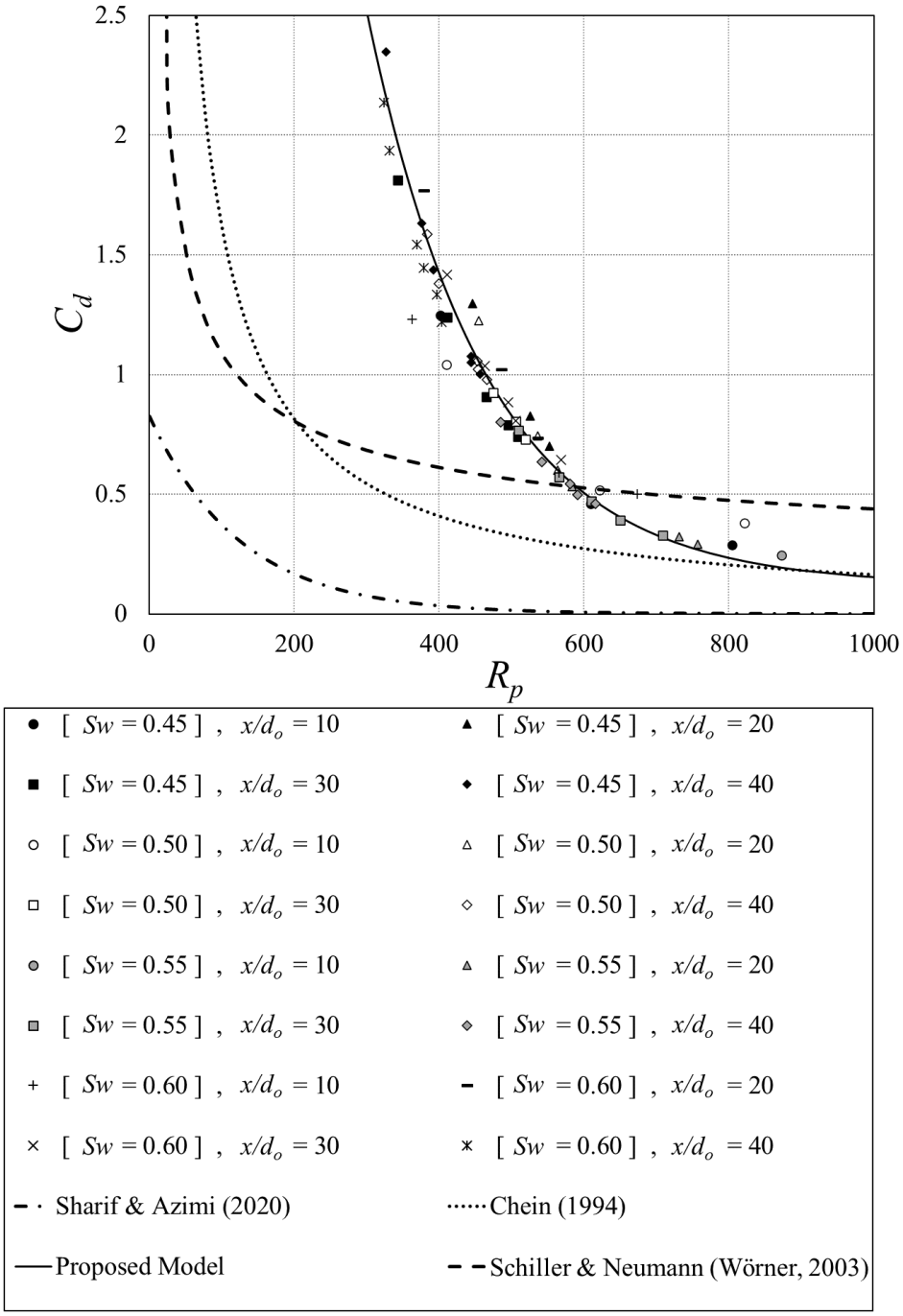

Figure 5.17: Variations of the drag coefficient of sand particles, C_d, for sand-water swirling jets with particle Reynolds number, R_p, for different normalized axial distance from the nozzle, x/d_o, and $L_o/d_o \approx \infty$.

5.3.6 *Power Spectral analysis*

The Power Spectral Density (PSD) analysis is used to investigate the motion of coherent structure and flow oscillations. The analysis of PSD was applied by Zhang and Vanierschot (2021) to obtain the dominant frequency of the Processing Vortex Core as the vortex break down occurs in stagnation point of the swirling jets. They reported a dominant

frequency range of $f \leq 22$ Hz for PVC coherent structure of single-phase swirling jet with $Sw = 0.38$. The corresponding power spectral density of voltage signals was correlated with the particle concentration fluctuations. The results of PSD analysis for $Sw = 0.45$ and 0.60 at $x/d_o = 20$ and 30 with the axial distance of $r/d_o = 2.5$ are shown in Figure 5.18. As can be seen, the Precessing Vortex Cores with different strengths were formed in different dominant frequencies. Figure 18a shows two distinct peaks with the frequencies of 2.33 Hz and 2.56 Hz for $Sw = 0.45$ and 0.60, respectively. These dominant frequencies are formed due to the higher momentum in swirling motion of sand-water swirling jet close to the nozzle (i.e., $x/d_o = 20$). Other periodic peaks correspond to low vortical motions that occurred in the frequency range of 0 Hz $< f \leq 11$ Hz. The dominant frequencies for $Sw = 0.45$ and 0.60 and at $x/d_o = 30$ decreased to 1.69 Hz and 2.43, respectively (see Figure 5.18b). The results of PSD analysis indicated that the dominant vortical frequencies decreased due to the presence of particles in comparison with single-phase swirling jets.

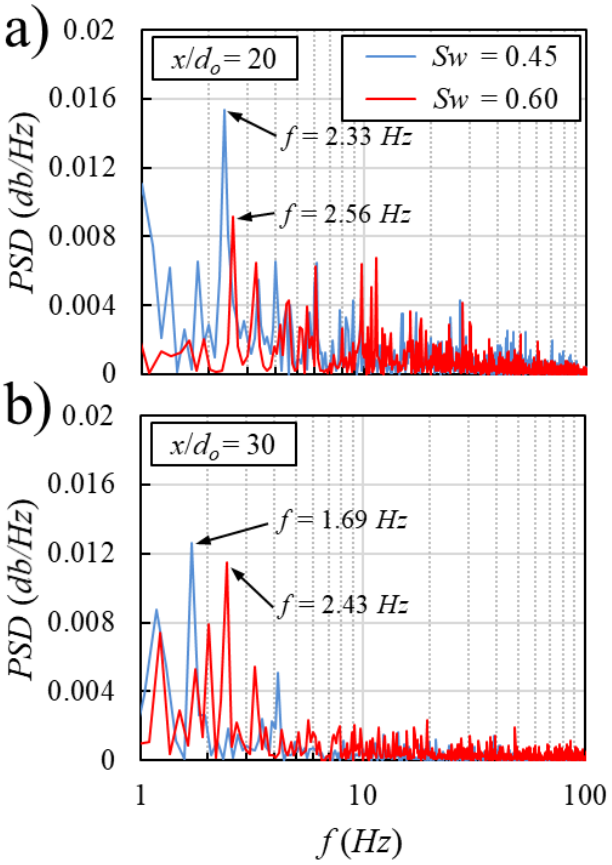

Figure 5.18: Power Spectral Density (PSD) analysis of sand concentration for sand-water swirling jets with $L_o/d_o \approx \infty$ and swirling numbers of 0.45 and 0.60: a) $x/d_o = 20$, $r/d_o = 2.5$; b) $x/d_o = 30$, $r/d_o = 2.5$.

5.4 Conclusions

A series of laboratory experiments were conducted to study the effects of swirling strength and sand mass on the dynamics of sand-water swirling jets in stagnant water. Sand concentration and velocity of sand-water swirling jets were measured in both axial and transverse directions by a light refractive optical probe (PV6). The hydrodynamics of particles in sand-water swirling jets were tested for both limited and unlimited sand masses and the availability of sand particles was quantified by the aspect ratio, L_o/d_o. The accuracy of measurements was examined by evaluating the integral quantities such as mass flux and momentum flux. Experimental observations of sand-water swirling jets indicated that the maximum uncertainty level of turbulent intensity in non-swirling and swirling jets were 3% and 5%, respectively. A sudden decay rate in momentum flux was observed along the recirculation zone due to the formation of the precessing vortex core with a distance equal to 20 times of the nozzle diameter. The effect of swirling number, *Sw*, on the spreading rate of sand-water swirling jets was evaluated and it was found that the spreading rate increased by increasing swirling number in a range of 0.15-0.2. In all swirling jets, the spreading rates were slightly higher than the single-phase jets, coaxial sand-water and slurry jets and they were smaller than the spreading rate of single-phase swirling jets.

The effect of swirling motion on the axial concentration of sand-water swirling jet indicated a direct correlation between the swirling number and decay rate for swirling jets with unlimited sand particles. The decay rates of axial concentration were slightly higher than the concentration decay rate of slurry jets and smaller than the concentration decay rate of particle clouds. It was found that for sand-water swirling jets with limited sand mass (i.e., $5.6 \leq L_o/d_o \leq 62.7$) the decay rate of sand concentration significantly altered in comparison with sand-water swirling jets with unlimited sand mass. It was found that the decay rate of axial velocity in sand-water swirling jets with $Sw = 0.45$ was similar to the velocity decay rate of slurry jets. The decay rate of sand velocity increased by increasing swirling strength. For $L_o/d_o > 10.4$, the decay rate of sand velocity was independent of swirling strength and the velocity decay can be predicted by proposed model for sand-water swirling jets with unlimited sand mass. The radial variations of sand concentration and velocity of sand-water swirling jets were also studied. The radial concentration and velocity were correlated, and their variations were modeled by Gaussian distributions. Prediction models were developed to estimate sand concentration and velocity for different flow configurations.

The average drag coefficient of sand particles in different cross-sections was calculated based on the axial and radial distributions of sand concentration and velocity. It was found that the swirling effect significantly increased the average drag coefficient in comparison to the drag coefficient of individual particles. Finally, the effect of swirling motion on the coherent structure of sand-water swirling jets was studied by employing the Power Spectrum Density analysis. In comparison with single-phase swirling jet, the dominant vortical frequencies decreased due to the presence of particles. The axial and radial elongation of the recirculation zone enhanced the mixing capability of sand-water swirling jets which can be used as an effective design parameter.

Chapter 6

General Conclusions and Recommendations for Future Research

6.1 General conclusions

In the preceding chapters, comprehensive experimental studies and analyses were presented on the dynamics of sand jets in stagnant water.

In Chapter 2, particle dynamics and mixing properties of particle cloud in stagnant water were investigated. Sand particles were released through circular nozzles with the inner diameters of d_o = 8 mm and 10 mm into a rectangular glass tank of 1.65 m long, 0.85 m wide, and 0.85 m deep. A total of 10 experiments with different masses of dry sand particles from 6 to 24 grams were carried out to develop correlations between sand mass and nozzle diameter with a relatively wide range of aspect ratios of $9.5 \leq L_o/d_o \leq 39.2$. Two particle sizes with a median diameter of D_{50} = 0.507 mm and 0.718 mm with a density of 2,540 kg/m^3 were implemented with the Stokes numbers of $0.52 \leq S_t \leq 0.93$. The axial and radial profiles of sand concentration and velocity of particle clouds were measured by an accurate and robust optical probe (PV6). Empirical formulations based on the Stokes number and aspect ratio were developed to explain the variations in sand concentration and velocity in axial and radial directions.

- The zone of jet development was found to be smaller in particle clouds than single-phase water jets and sand jets and it was between 2 d_o and 4 d_o.
- The dissipation rate of centerline sand concentration in particle clouds decreased at a slower rate than single-phase buoyant and sand jets.
- The centerline sand velocity in particle clouds decreased at a slower rate than single-phase water jets.
- It was indicated that the radial distribution of sand concentration and velocity distribution can be modeled by Gaussian distribution.
- The radial drag coefficient decreased from 0.4 to less than 0.1 in the core region due to particle grouping effect.

- A new mathematical model was developed to calculate the distribution of entrainment coefficient inside particle clouds.

- The entrainment coefficient decreased non-linearly in the radial direction and was described by a semi-empirical model.

- The aspect ratio significantly altered the radial entrainment coefficient in transverse directions.

- The coherent dominant frequency of velocity data of 1.5 Hz was observed by employing the Power Spectral Density (PSD) and followed by the Kolmogorov −5/3 scaling law.

- The inter-particle collision occurred for $x/d_o \leq 10$ for $S_t = 0.74$ and $S_t = 0.52$, and the Bagnold number values were smaller than 45 for $x/d_o \geq 20$, indicating that a micro viscous regime dominates the flow in particle cloud dynamics.

Detailed laboratory experiments were performed in Chapter 3 to study the dynamics and mixing properties of sand-water coaxial jets in stagnant water. The central nozzle diameter of funnel and the coaxial annular diameter were d_o = 12 mm and d_a = 22 mm, respectively. Sand particles with a median diameter of D_{50} = 0.507 mm and a density of ρ_s = 2,540 kg/m^3 were used in this study which had a Stokes number value of 0.57. Overall, six experiments were carried out with velocity ratios of $0 \leq Ru \leq 1.86$ and the measurement domain ranged from $1 < x/d_o < 40$ and $-5 < r/d_o < 5$. The sand mass flux was $\dot{m}_o$ = 27 g/s with a loosely packed initial sand concentration of approximately 60%. The axial and radial distributions of sand concentration and velocity were measured with the optical fiber probe (PV6), and strong correlations were developed to predict sand concentration and velocity in the axial and radial directions as a function of velocity ratios.

- The initial mixing zone was a length approximately six times the nozzle diameter and was independent of velocity ratio.

- The core stream water jet reduced the turbulent intensity of sand-water coaxial jets in a range between 3% and 7%.

- In the initial mixing zone, the axial decay rate of sand concentration increased with increasing velocity ratio and became similar to the concentration decay rate of slurry jets for higher velocity ratios (i.e., $Ru \geq 1.24$).

- The centerline sand concentration decreased at a smaller rate than single-phase buoyant jets and slurry jets for $0.62 \leq Ru \leq 1.24$ and at a higher rate than particle clouds for $0.62 \leq Ru \leq 1.86$.

- A similar decay rate close to slurry jet (i.e., $Ru \approx 1$) was observed for $Ru = 1.24$.

- The zone of the fully established flow jet was at $x/d_o \geq 32$. However, by decreasing the velocity ratio, the zone of the fully developed jet formed closer to the nozzle for $x/d_o \geq 24$.

- An adverse relationship was observed for the axial velocity decay of sand-water coaxial jets with velocity ratio.

- The spreading rate was found to be a function of velocity ratio of sand-water coaxial jets and decreased with increasing velocity ratio and reached the spreading rate of slurry jets for $Ru = 1.86$.

- Average drag coefficients were calculated using momentum balance and proposed equations for sand velocity and concentration.

- A significant drag reduction due to grouping effect was indicated in sand-water coaxial jets with lower velocity ratios.

- The axial variations of interparticle collision over the shear stress indicated that all velocity ratios experiencing the transitional regime at $x/d_o \leq 12$. However, far from the nozzle flow structure controlled by viscous fluid stresses controlled

Detailed laboratory experiments were performed to study the effects of initial water-phase Reynolds number $0 \leq Ru \leq 26{,}486$ and velocity ratio $0 \leq Ru \leq 1.86$ on the low-rank dynamics of the coaxial sand-water jet in stagnant water in Chapter 4. The flow parameters were decomposed into energy-ranked coherent modes based on the highspeed snapshot images. Spectral and Proper Orthogonal Decomposition methods were used to capture the influence of particles on the mixing, modes of coherent structures, and turbulent kinetic energy contribution

of each mode. Two different nozzle sizes with Stokes numbers of 0.4 and 0.57 were employed to provide a wide range of low (i.e., $Ru \leq 0.35$) and high-velocity ratios (i.e., $Ru \geq 0.35$).

- The POD results of flow illuminated snapshots indicated that the influence of the velocity ratio and given Reynolds number play significant roles in low-rank dynamics of sand water coaxial jets.

- The energy contributions of each POD modes were reduced by almost two times for a smaller velocity ratio (i.e., $Ru \leq 0.35$) in comparison to the higher velocity ratio (i.e., $Ru \geq 0.35$).

- The Power Spectrum Density of the POD eigenvalue coefficient indicated that the first ten-mode dominants frequency varied from 0.28 Hz to 4 Hz.

- The Spectral Proper Orthogonal Decomposition (SPOD) analysis was performed for the series speed snapshots to study the low-rank dynamic of particles and flow properties.

- The particle motion and oscillation were characterized by the Kelvin–Helmholtz (KH) type wave packets particularly in low frequencies and the first three modes associated with the annular nozzle.

- The vortex shedding and particle fluctuation were increased by increasing the velocity ratios let to larger Kelvin–Helmholtz (KH) type wave packets.

- The separation between the first and second on eigen spectral of SPOD modes demonstrated the large portion restoration of the turbulence kinetic energy and flow vortex shedding in low-frequency modes of coaxial sand-water jets with a higher velocity ratio (i.e., $Ru = 1.24$).

In Chapter 5, the effects of swirling motion (i.e., $0.45 \leq Sw \leq 0.6$) on the outflow configuration and mixing properties of sand-water swirling jets were explored by employing an advanced optical fiber probe (PV6) with an unlimited (i.e., $L_o/d_o = \infty$) and limited aspect ratio (i.e., $5.6 \leq L_o/d_o \leq 62.7$). Sand particles with a median diameter of $D_{50} = 0.507$ mm and a density of $\rho_s = 2540$ kg/m^3 were employed with the Stokes numbers of $3.7 \leq S_t \leq 5.7$. The concentration and velocity measurements were carried out in both axial and radial directions. The measured data were correlated based to obtain empirical prediction models to estimate

sand concentration and velocity of sand-water swirling jets with different initial flow parameters.

- Laboratory measurements indicated that the axial sand concentration decreased at a higher rate in comparison to non-swirling sand-water jets.
- Increasing the swirling intensity increased the dissipation rates of concentration and velocity for aspect ratio close to infinity.
- A high decay rate of momentum flux was observed along the recirculation zone at the length of approximately 20 times nozzle diameter.
- The presence of particles attenuated the spreading rates of sand water swirling jets compare to single-phase swirling jets.
- Overall, the spreading rates of sand-water swirling jets were higher than non-swirling particle laden-jets.
- It was indicated that swirling motion increased the decay rate of axial concentration in sand-water swirling jets with an unlimited amount of sand particles in comparison to non-swirling slurry jets.
- It was shown that a smaller aspect ratio (i.e., $5.6 \leq L_o/d_o \leq 62.7$) can significantly impact the dissipation rate of sand-water swirling jets compare to swirling jets with unlimited aspect ratio.
- The axial velocity decay rate of sand-water swirling jet with Sw = 0.45 was found to be close to slurry jets and increased by increasing the swirling number.
- For $L_o/d_o > 10.4$, all given swirling numbers experienced a similar dissipation rate and can be scaled by a power low model.
- Gaussian distribution models were developed to describe radial variations of concentration and velocity of sand-water swirling jets.
- It was indicated that the frequency of dominant coherent structure decreased due to the presence of particles compared to the single-phase swirling jets.

- The average radial drag coefficient was calculated based on the momentum balance and proposed models of sand velocity and concentration and it was indicated that the swirling intensity can significantly increase the drag coefficient.

6.2 Future research and studies

Several areas of research can be explored in this field for better understanding the behavior of sediment-laden jets. Since hydrodynamics of solid-liquid two-phase turbulent jets is complex, fundamental research enhances our understanding of the underlying physics and dynamics of the system. Model improvements and geometry changes can be made in the initial release configuration for better understanding the effect of carrier fluid and swirling motion. More work should be done to validate the scaling effect by comparing the results of laboratory experiments with field data.

The results of the suggested research topics can be directly employed in industrial projects. Such results can be useful for design, optimization, and monitoring of engineering projects. A list of possible applied research topics with a brief descriptions are listed below:

- *Particle cloud*

Series of experimental studies were conducted in this thesis to investigate dynamics, mixing, and particle-particle interaction of particle cloud in stagnant water (see Chapter 2). The prediction equation was developed to model axial and radial concentration and velocity distributions for particles with large Stokes numbers ($0.33 \leq S_t < 1$). One possible project is to extended the proposed models for small and mid-range Stokes numbers. According to the proposed model, the interparticle interaction and entrainment were developed to investigate inter-scale particle cloud dynamics. Since particle size and aspect ratio can significantly impact the particle cloud properties such as growth rate, progression length of particle cloud, entrainment coefficient, and particle collision, in this respect, it is recommended that extending the prediction well-posed models range leads to the quantitative link between the initial release configuration and particle cloud dynamics. Furthermore, particle clouds have three phases of motion including initial, thermal, and swarm phases. It provides detailed information about the flow and can be used to develop and define a model with broader range of variables in axial and radial directions and for different phases. Indeed, much insight can be obtained from an analysis of a broad range of models.

Besides, new types of release rather than cylinderical pipe nozzle such as hemispherical bucket as shown in Figure 6.1 can be used to investigate the effect of particle release mechanism. The axial rotation of the proposed release mechanism can be introduced to the ambient flow field which leads to a more similar open water material disposal situation and introduce asymmetry in accordance. As a result, accurate release conditions can be investigated similar to backhoe type release mechanism. A valuable contribution to the understanding of mixing and dispersion of flow field in both symmetric and axisymmetric particle clouds can be obtained by exploring such connections.

On the other hand, the particles' motion in water is a two-way coupling mechanism, therefore, numerical modeling can be employed to examine the particle-fluid interaction and the hydrodynamic impacts of particle clouds, particularly in the hemispherical bucket release condition. Thus, numerical studies can reveal further details of particle clouds in the ambient. The motion of fluid phase can be simulated based on the two-way coupling behavior of particle cloud (i.e., sand and ambient water). Therefore, the motion of fluid phase can be computed by a two-equation turbulence model for different ranges of particle size, and the numerical results can be compared and validated by experimental data. Our proposed integral models' predictions for flow entrainment and particle collision can simulate in a three-dimensional domain with symmetrical and non-symmetrical release conditions. It increases the confidence of data and the framework can readily be applied while scaling up from lab to the real field.

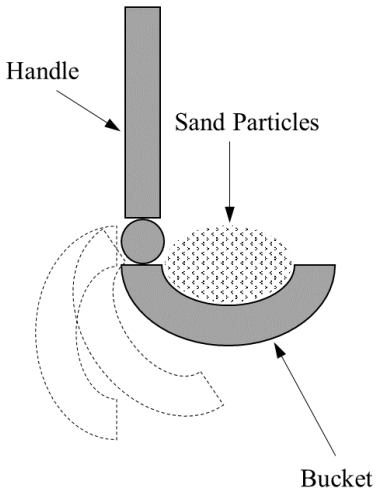

Figure 6.1: Schematic of the hemispherical bucket release mechanism.

- *Sand-water coaxial jets*

In Chapter 3, the effect of different velocity ratios on the dynamics of sand-water coaxial jet was studied without initial premixing. This fundamental study aims to understand the development and formation of particle-laden jet front injecting into the oil-sands tailing ponds or dredging pollutants with different particles density and particle shapes. Two possible options can be expanded the initial impinging set up of sand-water coaxial jets. First, a small number of particles can add up to the central water jet flow at a steady rate. Second, the water phase can be introduced to an annular section forms an annular slurry jets with low and high-velocity ratios. The particle mass flow rate can influence the entrained particle velocity and increase the complexity of the mixing system. In addition, in the case of initial geometry and particle size, the interaction between two phases (i.e., sand-water) and particle dispersion strongly depends on the Stokes number. The initial nozzle Stokes number can be changed by either increasing and decreasing the concentric nozzles and wall thickness. The effect of controlling parameters on the axial and radial profiles of velocity and concentration can significantly alter the prediction models particularly once scaling up process from the lab to the real field occurs. The effects of wall thickness on the macroscopic behaviors of sand particles can be investigated by the Spectral Proper Orthogonal Decomposition (SPOD) technique and by employing the Kelvin-Helmholtz instability method which is introduced in Chapter 4.

One possible project for future research is to investigate the effect of the annular single-phase water with dry sands impinged through the core nozzle as shown in Figure 6.2. The result of this initial configuration setup can be compared with the data obtained in Chapters 3 and 4. Furthermore, different initial flow conditions can be utilized to numerically simulate sand-water coaxial jets as two-phase coupling process by simulating the motion of water and sand phases simultaneously. In addition, the outputs of numerical model can be used to study the hydrodynamics of sand-water coaxial jet such as entrainment and mixing processes by simulating both water and particle velocities and their influences on each other. The ambient entrainment in coaxial jets can be a subject of future investigation. In Chapter 3, the guideline and framework linked to the dynamics of sand water coaxial jets and it led to develop a set of entrainment models based on numerical studies. Therefore, by linking and utilizing data from the present thesis as a benchmark, a comprehensive implication for initial flow control can be achieved. This information could provide more insight into the hydrodynamics of sand-water coaxial jets especially on the behavior of fluid-particle motion in open water disposal.

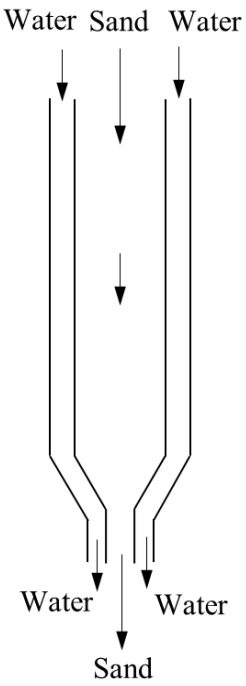

Figure 6.2: Schematic of a coaxial sand jet surrounded by an annular water jet

- *Sand-water swirling -jets*

The complexity of flow in the two-phase jets increases when the highly turbulent swirling motion is employed to enhance the mixing process. The practical swirling jets requires information about the jet initial configuration such as nozzle diameter, swirling intensity, initial mixing set up and particle size to control and optimize its operation. Therefore, in Chapter 5 the detailed investigation is carried out to understand the dynamics and mixing properties of sand-water swirling jets by considering initial premixing. A series of detailed laboratory experiments were carried out in Chapter 5 of this thesis to study the effects of initial swirling intensity with the limited and unlimited amount of sand particles. Prediction models are also considered, to help the interpretation of measurements and to evaluate different methods to analyze flow properties.

A possible project for future study is to investigate the effect of centrifugal force on sand-water swirling jets without initial pre-mixing. As depicted in Figure 6.3, a coaxial cylinder can be designed to separate the solid phase from the liquid phase. The water enters the core nozzle through the injector and spiral ports surrounding the mainstream. The solid-phase impinges through an annular nozzle and mixes with swirling phases at the end of the nozzle. Therefore, the impact of non-premixing initial flow configuration on the recirculation zone,

processing vortex core, the vortex structure, turbulence, and other flow characteristics such as velocity and concentration can be compared with the results presented in Chapter 5 to have a better understanding of mixing and dynamics of sand-water swirling jets. The combination of axial and tangential velocity and high concentration flow field amplifies instability particularly in the Recirculation Zone (RZ) and forms a Precessing Vortex Core (PVC). Obtaining a connection between these two parameters is crucial to have a comprehensive understanding on the dynamics, mixing, and entrainment of two-phase swirling jets. Due to the existence of azimuthal and axial velocity, Particle Image Velocimetry (PIV) technique can be utilized as rigorous method for velocity field measurements. This measuring equipment can provide an instantaneous two-dimensional velocity field, especially in RZ and PVC zones. Therefore, the coherent vortex structure, turbulence kinetic energy, and other flow characteristics can be extracted from the PIV measurements. Ideally, linking and comparing the PIV data with the Spectral Proper Orthogonal (SPOD) results can describe the coherent features of flow dynamical and transport processes which can be a subject of future research. The extracted temporal and special modes of stability can be used to describe the underlying physics in sand-water swirling jets. Leading to identify and characterize the stagnation point and formation of PVC.

On the other hand, numerical modeling can also be applied to simulate both water and sand phases simultaneously to validate the experimental results and to offer insight in the mechanisms governing the evolution of particle clouds. Stochastic numerical models under the non-stationary conditions can applied to describe the dispersion of tracer particles and simulate the particle paths. In exploring such connections, it can be obtained that whether shear-flow dispersion has a steady-state counterpart and in what respects the physics of the two phases are fundamentally different. In the present research, the swirling intensity was in the range of $0.45 \leq Sw \leq 0.60$. This study can be extended for higher swirling numbers $Sw > 0.60$ along with different Stokes numbers and comparing flow metrics with a limited and unlimited amount of sand particles. Finally, the work on the ambient current threshold between weak, transitional, and strong currents can be investigated to understand the hydrodynamics of swirling and non-swirling jets. Since open-water disposal is important in many engineering applications, the accuracy of scaling up from the lab to the real field can increase by the proposed future projects.

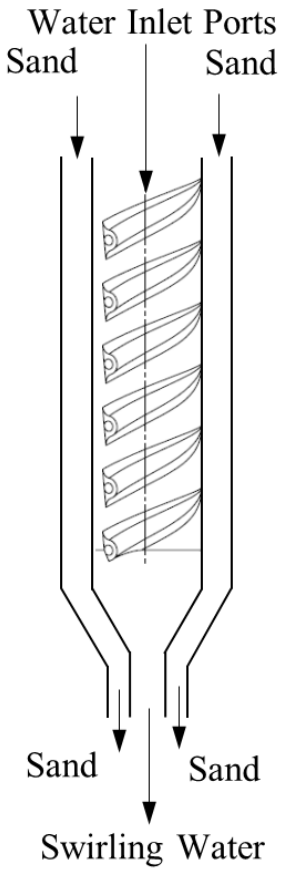

Figure 6.3: Schematic of the swirling coaxial without initial premix mechanism.

Appendix 1

Experimental study of Sand-Water Coaxial Jets with Low-Velocity Ratio

Abstract

A series of detailed laboratory experiments were conducted to investigate particle dynamics in vertically discharged sand-water coaxial jets in stagnant water. The central and the coaxial annular nozzle diameters were d_o = 6 mm and d_a = 12 mm, respectively. The annular jet contained sand with a median diameter of 0.389 mm with an initial sand concentration of 60% by volume. Different core water discharges were tested providing a Reynolds number range between 6,622 and 11,919. The axial and radial distributions of sand concentration and velocity were measured by an advanced optical fiber probe (PV6). The effects of velocity ratio (Ru) between the annular and the core nozzles on the dynamics of particles and momentum transfer were studied for $Ru < 0.5$. The experimental results demonstrated that the decay rate of axial velocity and concentration of sand particles in the initial region, a distance less than 5 times of nozzle diameter, were independent of the velocity ratio. Beyond the initial region, the velocity decay rate of coaxial sand-water jets was higher than particle clouds and similar to single-phase water jets. It was found that the decay rate of sand concentration is lower than particle clouds and similar to slurry jets. The role of sand particles in turbulence augmentation and inter-scale coherent structures of the jet was also investigated using the Spectral Proper Orthogonal Decomposition method (SPOD). The SPOD method is used to decompose the flow into energy-ranked coherent structures and extract the energy spectra. It was found that a considerable portion of the turbulence kinetic energy is stored in low-frequency modes for velocity ratios smaller than 0.16. The Kelvin–Helmholtz (KH) type wave packets were observed in low frequencies and the first ten modes were found to be associated with the annular nozzle.

A paper based on the content of this appendix has been accepted in the 48th, *CSCE 2021 Annual Conference, May* 2021as Sharif, F., Azimi, A. H., 2021. Experimental study of Sand-water Coaxial Jets with Low-Velocity Ratio.

1. Introduction

Sand-water turbulent jets are commonly used in many engineering applications such as waste disposals and industrial processes and they have been a topic of interest (Bühler and Papantoniou, 2001; Balarac et al., 2007; Azimi 2012a, 2012b; Manzouri and Azimi, 2019a, 2019b; Sharif and Azimi, 2020).

A single-phase turbulent jet occurs when a moving fluid enters a quiescent body of the same fluid causing a velocity shear and decelerates until its mean momentum is dissipated. (Abramovich, 1963; Rajaratnam, 1976; Lee and Chu, 2003). By introducing solid particles as the second phase in water jets particle-laden or slurry jets are formed. A coaxial jet is compromised of two inner and outer annular concentric jets employing as a method to enhance mixing capabilities of different outlet streams in combustion chambers, industrial burners, air blast atomizers (Balarac et al., 2007; Safer and Beghidja, 2019).

Several research studies have been performed to study the dynamics of particles in two-phase turbulent jets (Brush, 1962; Fan et al., 1990; Mazurek et al., 2002; Mohammadidinani, et al., 2017; Hall et al., 2010; Azimi et al., 2012a, 2012b; Azimi et al., 2011; Azimi et al., 2014; Manzouri and Azimi, 2019a; Azimi, 2019). The inclusion of solid particles with different mean particle size D_{50}, initial particle concentration c_o, and nozzle diameter d_o into the ambient fluid can impact the governing flow dynamic configuration. The effects of particle size on the dynamics of particle-laden jets can be described by Stokes number, S_t. The Stokes number can be defined as the ratio of the particle momentum response time, $\tau_p = \rho_s D_{50}^2/18\mu$, and the time scale of the flow, $\tau_f = d_o/u_o$, where ρ_s is the density of solid particles, μ is the dynamic viscosity of the ambient fluid, and u_o is the jet initial velocity. For $S_t << 1$, the particles follow the fluid motion, for $S_t \approx 1$, particles are propelled of the vortex core, and for $S_t >> 1$ particles adopt limited properties of the carrier fluid (Crowe et al., 1985). Moghadaripour et al. (2017a) classified the particle size in particle clouds based on the Stokes number as: small particles ($0 < S_t \leq 0.1$), medium particles ($0.1 < S_t < 0.33$), and large particles ($0.33 \leq S_t < 1$). The Stokes number can affect mixing parameters of particle-laden jets such as entrainment, particle collision, spreading rate, and depth progression (Bühler and Papantoniou, 2001; Azimi et al., 2012a; Moghadaripour et al., 2017b; Pakzad and Azimi, 2017; Manzouri and Azimi, 2019b).

Many research studies have investigated the dynamics and mixing capabilities of single-phase coaxial jets based on the velocity ratio of annular to central streams, *Ru.* (Dahm et al., 1992; Wicker and Eaton, 1994; Villermaux and Rehab, 2000; Balarac et al., 2007). Ko

and Kwan (1976) indicated that the flow structure in single coaxial jets can be classified into three different regions: the initial merging zone (i.e., potential core), the intermediate merging zone, and the fully developed zone. The evolution of the mixing process of coaxial jets occurs by the formation of two different shear layers between the surrounded fluid and the annular jet and the second shear layer is created between the annular and the core jet (Balarac et al., 2007). The potential core defines as a region in which the dynamic properties such as velocity are the similar initial configuration at the nozzle (Akaike and Nemoto, 1988). Champagne and Wygnanski (1971) indicated that the velocity ratio had a significant impact on the mixing capability in the potential core or the initial merging zone of coaxial jets. An axisymmetric alternation was reported in single-phase coaxial jets with $Ru > 0.71$ (Dahm et al., 1992). Wicker and Eaton (1994) found that in coaxial jets the velocity ratio (i.e., $Ru > 1$) had less influence on the initial vortex formation.

Introducing solid phase to the single-phase coaxial jets can alter the dynamics and mixing properties of solid-liquid jets (Mostafa et al., 1990; Fan et al., 1996; Sadr and Klewicki, 2005; Kannaiyan and Sadr, 2013). For two-phase solid particle coaxial jets with $Ru = 1.5$, the potential core was found to be symmetric for $x/d_o \leq 4$ and for Reynolds number of $Re = 8400$, where Re can be defined as $Re = \rho_w u_{ow} d_o/\mu$ and u_{ow} is the initial water velocity at the nozzle and ρ_w is water density (Pedel et al., 2014). Mostafa et al. (1990) found that a discrete particle diameter of 0.105 mm reduced the turbulence intensity and increased the energy dissipation rate. The experimental results of Sadr and Klewicki (2005) demonstrated a small and moderate enhancement in the axial turbulent intensity of less than 10%. Kannaiyan and Sadr (2013) found the decay of mean flow velocity in the axial direction was similar in both single-phase and two-phase coaxial jets with a velocity ratio of $Ru = 1.11$.

Several statistical methods can be used to capture the influence of particles on the mixing and inter-scale coherent structures in turbulent flow fields. The most widely used statistical method to resolve turbulent data is the Proper Orthogonal Decomposition (POD) technique (Lumley, 1967). The POD technique decomposes the time-history data into its lower-ranked special components modes and the frequency-ranked dynamic modes. The Proper Orthogonal Decomposition (POD) technique has been extensively used to identify dominant structures in the flow fields (Butcher and Spencer, 2019). This method was first proposed by Pearson (1901) for the superlative description of multi-component data sequences. Most recently, Schmidt et al. (2017) proposed an empirical method to extract coherent structures or modes in both space and time known as Spectral Proper Orthogonal

Decomposition (SPOD) based on the POD method. Since coherent motions could occur at different scales of special, frequencies, and energy levels, the traditional phase averaging methods (i.e., POD and DMD) are not capable of obtaining coherent structures in both space-frequency. Therefore, SPOD can extract the energy content and frequency by combining POD and DMD capabilities. Schmidt et al. (2017) indicated that the temporal coefficients of the orthogonal modes of turbulent jets can be characterized by Kelvin-Helmholtz (KH) type wave packets. Kadu et al. (2020) employed the SPOD method to annotate the physical structures or modes in a coaxial jet. They found that the pairs of counter-rotating vortical structures can be identified by the first two modes in the inner mixing layer. Zhang et al. (2021) indicated that the different detected orthogonal modes and their frequencies can be connected to the coherent structures in the near-field region of turbulent jets.

Most of the previous studies have focused on the dynamics of two-phase coaxial jets that the particles as the second phase pre-mixed with a carrier fluid and impinged through the coaxial outlet nozzle with almost high-velocity ratios (Mostafa et al., 1990; Fan et al., 1996; Sadr and Klewicki, 2005; Kannaiyan and Sadr, 2013; Pedel et al., 2014). A series of experiments on particle-laden coaxial jets were performed by a new coaxial jet set-up consists of two concentric nozzles to generate a central water jet surrounded by an annular sand jet. The main objective of this research study part is to examine the effects of velocity ratio on variations of the jet's characteristics such as axial and radial sand velocities and concentration profiles. The secondary objective is to study the low-ranked coherent flow configuration of the coaxial sand-water jet using the Spectral Proper Orthogonal Decomposition technique. The SPOD coefficients provide insight into the time scale associated with the spatial modes.

2. Experimental setup

Laboratory experiments were carried out in the Multiphase Flow Research Laboratory (MFRL) at Lakehead University to study the dynamics of coaxial sand-water jets. All experiments were carried out in a rectangular tank of 1.65 m long, 0.85 m wide, and 0.85 m deep. The tank was filled with tap water and the ambient temperature was kept constant over time with a value of 20 °C ± 1 °C. An assembly consists of a funnel with a core nozzle outlet surrounded by an annular nozzle was designed to model the coaxial jets. The core nozzle diameter of the funnel and the concentric annular diameter were d_o = 6 mm and d_a = 12 mm, respectively with an annular gap thickness of 2.5 mm. The water was discharged through the core nozzle and sand was released through the funnel and discharged in the water with no initial

pre-mixing with water. An accurate flow meter (LZT M-15, UXCEL, China) was implemented to generate different initial flow rates ranging between 0.5 L/min and 18 L/min which provided velocity ratios in the range of $0 \leq Ru \leq 0.33$ and Reynolds numbers between 6,622 to 11,919. Sand particles with a median diameter of D_{50} = 0.386 mm and a density of ρ_s = 2540 kg/m^3 were used in this study. The sand mass flux was $\dot{m}_o$ = 10 g/s with a loosely packed initial sand concentration of approximately 60% by volume. Overall, 4 experiments were tested in this study to investigate particle dynamics of sand-water coaxial jets. The Stokes number, S_t, was calculated based on particle size and annular nozzle and it was 0.7. Based on Moghadaripour's (2017a) classification (i.e., $0.33 \leq S_t < 1$) sand particles are classified as large particles in this study. Experimental details and non-dimensional parameters are listed in Table A1.

Table A1: Experimental details of sand-water coaxial jets and non-dimensional parameters.

No.	Test No.	D_{50} (mm)	d_o (mm)	d_a (mm)	$\dot{m}_o$ (g/s)	u_{wo} (m/s)	*Re*	*Ru*	S_t
1	C1	0.386	6	12	10	0	0	0	0.7
2	C2	0.386	6	12	10	0.75	6622	0.33	0.7
3	C3	0.386	6	12	10	1.16	9270	0.21	0.7
4	C4	0.386	6	12	10	1.49	11919	0.16	0.7

The axial and radial distributions of sand concentration and velocity were measured by an advanced optical fiber probe (PV6, Institute of Processing Engineering, Chinese Academy of Science, China). The probe is capable of measuring simultaneous time-series of sand concentration and velocity. The full MATLAB® m-file code and an example is included in Appendix 2 and 3. The probe tip has a diameter of 4 mm and contains two light sources and two light-refracting optical sensors with a diameter of 1 mm each. The fiber optics are 2.14 mm apart and they receive the emitted light from the two light sources in the sensor's tip. A high-resolution data acquisition board (National Instrument, Austin, U.S.) was used for analog to digital voltage conversion by taking raw signals from the PV6 processing unit. The fiber optic probe and the PV6 signal processing unit have been successfully utilized and validated in many two-phase turbulent flow experiments such as gas-solid fluidization systems (Taofeeq et al., 2018), particle-laden jets (Hall et al., 2010; Azimi et al., 2015), and particle clouds (Sharif and Azimi, 2020). To investigate the flow properties such as mixing and periodic motions

higher frame rate snapshots were recorded using a high-speed camera (Photron-FASTCAM, 1024PCI-100KC) with a resolution of 1024×1024 pixels. The camera was equipped with a 15-55 mm AF-S Nikkor, 1:3.5-5.6 GII (Nikon, Japan) lens to capture images. Raw images were captured with a frame rate of 250-500 frames per second and a shutter speed of 0.004 sec.

3. Signal processing

The wavelet transforms noise reduction toolbox (The MathWorks Inc., Natick, U.S.) was employed to enhance the quality of voltage signals. The wavelet denoising technique does not need any prior knowledge of signals to compare to other methods such as frequency analysis (Welch, 1967; Wu et al., 2001). This noise removal technique has been successfully employed in turbulent wall jets and particle clouds studies (Azimi et al., 2015; Sharif and Azimi, 2020). To obtain accurate signal velocity data, the cross-correlation technique was implemented based on different segment sizes of voltage signals. The effects of segment sizes, ΔL_s (i.e., $\Delta L_s = 2^9 = 512$, $2^{10} = 1024$ and $2^{11} = 2048$) and segment overlap (i.e., $L_s = 50\%$) on instantaneous velocity data was studied and the results are shown in Figure A1. The segment sizes correspond to sampling frequencies of 120 Hz, 60 Hz, and 30 Hz. The overlapping technique was first employed by Welch (1967) to reduce the effect of windowing in spectral density estimation.

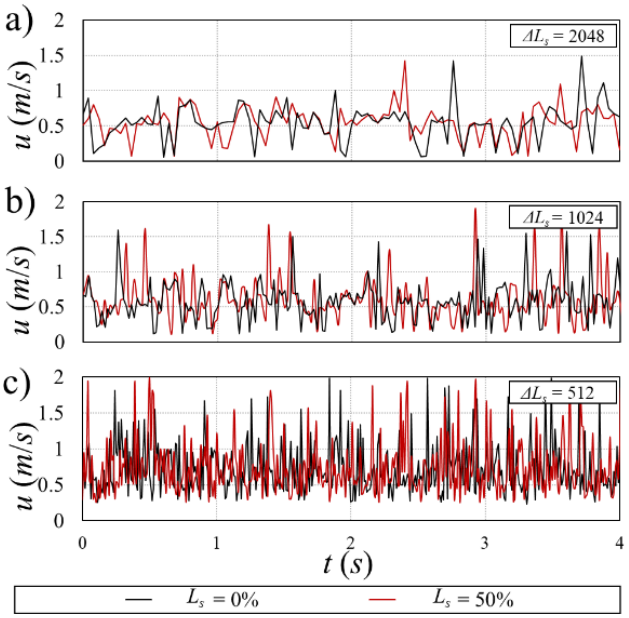

Figure A1: Typical instantaneous sand velocity data extracted from voltage signals and using different segment overlapping $L_s = 0\%$ (i.e., no overlap), and 50% and segment lengths ΔL_s for $Ru = 0.16$, $x/d_o = 20$ a) $\Delta L_s = 2048$; b) $\Delta L_s = 1024$; c) $\Delta L_s = 512$.

As depicted in Figure A1 the cross-correlations of voltage signals with a lower segment size increased the velocity fluctuations. It was found that the data uncertainty associated with 2048, 1024, and 512 were ±4%, ±9%, and ±13%, respectively. It was also found that the maximum data uncertainty of velocity between 0% and 50% overlap was ±1.5%. Therefore, a segment length of 2048 with 0% overlap (i.e., no overlap) was selected for all data in this study.

Each individual captured time-averaged voltage signals by the probe's tips can be converted to sand concentration at the point of measurement using a calibration curve concentration (Hall et al., 2010). The acquired velocity and concentration data accuracy were examined by the integrated mass flux(i.e., the mass of a substance which passes per unit of time) at different cross-sections along with the sand-water coaxial jet as:

$$\dot{m} = \frac{dm}{dt} = 2\pi\rho_s \int_0^r cu\, r dr \tag{1}$$

where u is the particle velocity and r is the horizontal distance from the jet axis. The integration results demonstrated the mass conservation of above 90%.

4. Spectral Proper Orthogonal Decomposition SPOD

The Spectral POD method is conceptually and algorithmically (i.e., eigenvectors of a matrix) similar to the POD method. The main algorithm of SPOD is based on Welch's decomposition method (Schmidt et al., 2017, 2020). The full MATLAB® m-file code is included in Appendix 4. Welch (1967) proposed an averaging technique to the converting time history data set from the time domain to the frequency domain knows as the Power Spectrum Density (PSD). Therefore, temporal coefficients of the orthogonal modes can be explained as an increasing range of frequency spectrum. The initial step to perform the SPOD method is by adjusting a time series of snapshots to construct a single data matrix P using N_p snapshots and M_p pixels. The matrix P first needs to be segmented into N_b blocks that overlap by N_o snapshots. The size of the N_b block can be obtained as $N_b=(N_p-N_o)/(N_f-N_o)$ where N_f is the length of segmentation (i.e., 64, 128, 256…) corresponding to an overlap of 50%. However, by choosing larger block sizes and overlap them, the variance of data is increased accordingly. The Welch periodogram method was employed to constructs an ensemble of realizations of the temporal Fourier transform of the data from a single time series consisting of N_p snapshots by breaking it into N_b then, reordering it by frequency in each block. The POD of an ensemble of frequency-based blocks P_B leads to the extraction of the spatial modes such that any image of each block

can be expressed as a linear weighted sum of the modes and can be described by (Sirovich, 1987):

$$P_{B_i}(x_a, t_a) = \sum_{j=1}^{r_p} \alpha_{ij} \varphi_j(x) \tag{2}$$

where x_a and t_a are the independent variables denoting space and time, respectively, $i = 1$ to N_b, $j = 1$ to $r_p < N_b$. Besides, the coefficient $\alpha_{ij}(t)$ can be defined as:

$$\alpha_{ij}(t) = \beta_{ij}(t)\ \lambda_j^{0.5} \tag{3}$$

where β_{ij} is the temporal coefficients and λ_j is called the eigenvalue. The orthogonal eigenvectors or spatial modes, $\phi_j(x)$, represent the ensemble-averaged spatial features of the whole ensemble. The eigenvalues are arranged in decreasing order ($\lambda_1 > \lambda_2 > \lambda_3 \cdots$) yields the SPOD of each block. Therefore, SPOD modes are the eigenvectors of a cross-spectral density tensor at each frequency corresponding to the modal kinetic energy.

5. Results

Figure A2a shows the effect of velocity ratio (i.e., $0.16 \leq Ru \leq 0.33$) on the variations of the axial mean centerline sand concentration of coaxial sand-water jets. The centerline concentration, c_m, was normalized with the initial sand concentration, c_o, and the distance from the nozzle, x, was normalized with the nozzle diameter, d_o. The overbar indicates the uncertainty of sand phase concentration measurements. The data uncertainty of concentration measurement was found to be ±9%. The variations of sand centerline concentration for slurry jet and particle cloud were also included in Figure A2a (Hall et al., 2010; Sharif and Azimi, 2020). As can be seen, all given velocity ratios experiencing a similar non-linear dissipation rate for $x/d_o \leq 16$ and the results are independent of Ru. Such correlations can be attributed to the intermediate mixing zone. However, for $x/d_o > 16$, the sand water coaxial jets with $Ru = 0.33$ had a smaller decay rate in comparison with $Ru = 0.16$ and 0.21 which decay at a faster rate close to the slurry jet model. For all cases, sand concentration in coaxial sand-water jets dissipated lower than particle clouds indicating the dissipation rate as a function of the velocity ratio further downstream of jets. The potential core (i.e., $c_m/c_o \approx 1$) of the sand-water coaxial jet was found to be five times the nozzle diameter. The zone of jet development is six times that of the nozzle diameter for single-phase jets and between $3.7d_o$ and $5.8d_o$ for slurry jets (Hall et al., 2010).

Variations of the normalized sand centerline velocity with x/d_o and different velocity ratios (i.e., $0.16 \leq Ru \leq 0.33$) are shown in Figure A2b. The centerline sand velocity, u_m, was normalized with the initial velocity of sand particles at the nozzle, u_o. The predictions of sand centerline velocity of particle cloud (Sharif and Azimi, 2020) and water jet (Lee and Chu, 2003) were also included in Figure A2b. The maximum uncertainty of sand velocity measurements was found to be approximately ±11 %. As shown in Figure A2b the axial velocities of the sand phase are independent velocity ratio for $x/d_o \leq 16$ and decreased non-linearly. However, for $x/d_o > 16$ decreasing the velocity ratio (i.e, $Ru = 0.16$) caused a higher decay rate similar to the water jet and adopting the water phase flow velocity. However, coaxial jets with the velocity ratio of 0.33 and 0.21 had higher dissipation in comparison with particle clouds and the dissipation rate was smaller than slurry jets. Figure A3 shows the transverse profiles of the normalized sand concentration, c/c_m, with the normalized transverse distance from the nozzle, r/d_o, for sand-water coaxial jets with the velocity ratio of $Ru = 0.16$ and 0.21. As can be seen, all velocity ratios and the radial concentration exhibited a near-field hump at $r/d_o = 1.25$ indicating the migration and mixing of particles jet towards the jet's axis and reduction in the intensity of hump further downstream in the flow development zone. It was found that by increasing the velocity ratio particle distribution in the radial direction was increased (see Figure A3b).

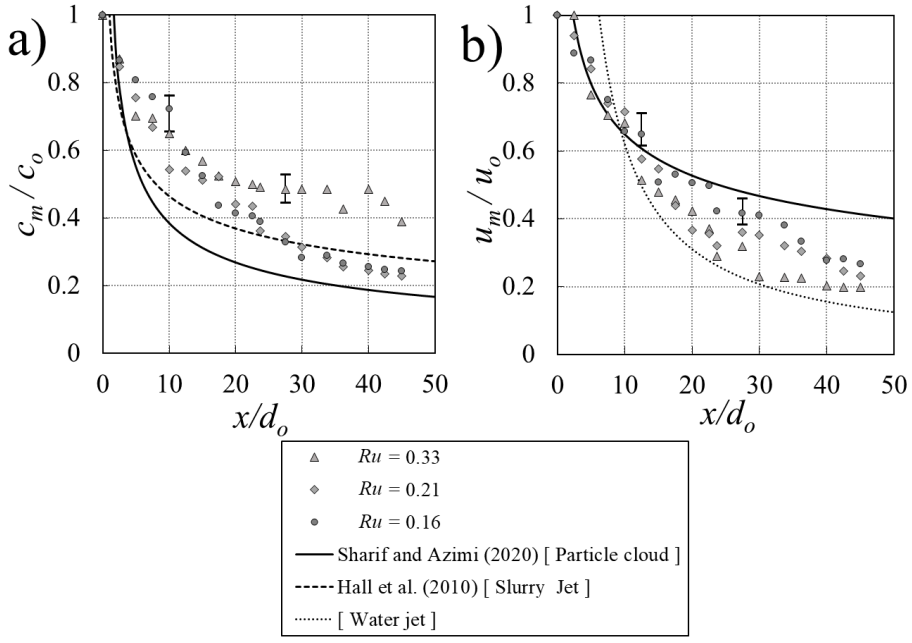

Figure A2: a) Effects of velocity ratio on variations of the normalized sand concentration, c_m/c_o, with normalized axial distance from the nozzle, x/d_o; b) Effects of velocity ratio on

variations of the normalized sand velocity, u_m/u_o, with normalized axial distance from the nozzle, x/d_o.

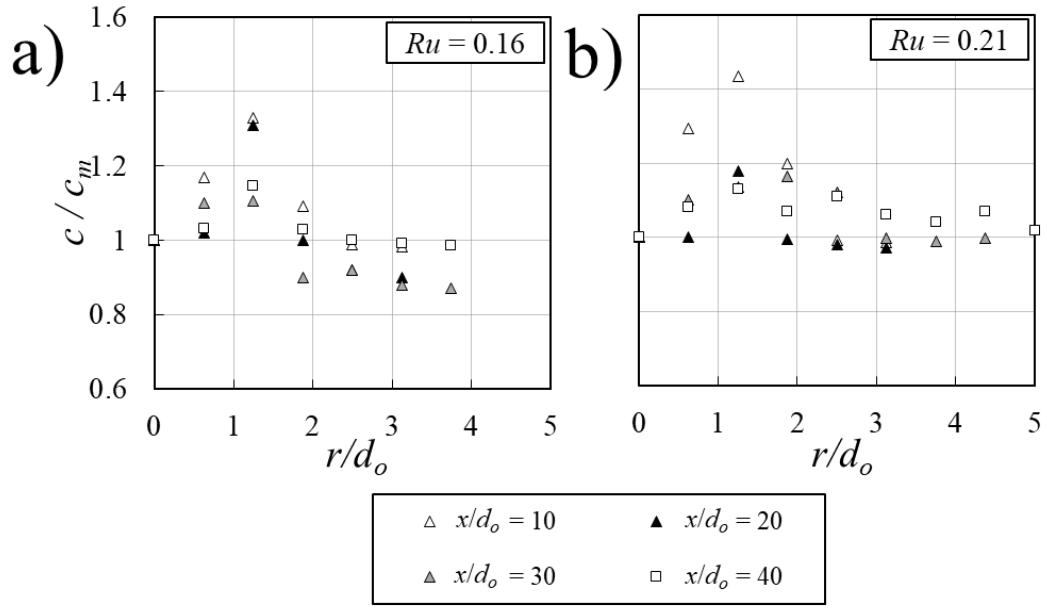

Figure A3. Effect of velocity ratio on the radial distribution of sand particles concentration: a) $Ru = 0.16$; b) $Ru = 0.21$.

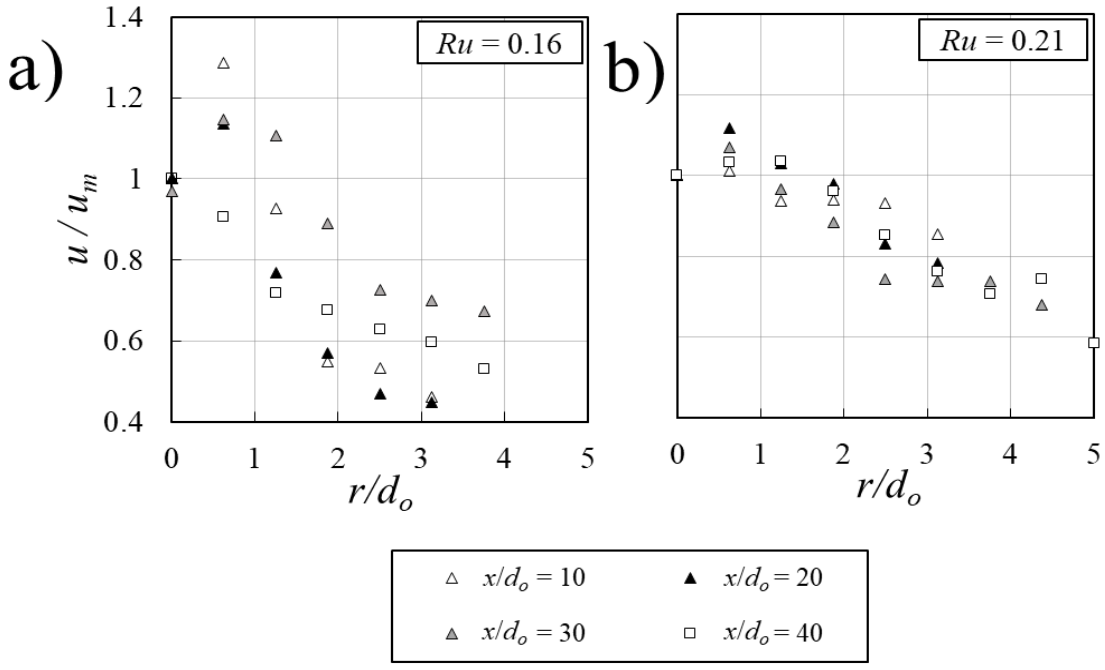

Figure A4: Effect of velocity ratio on the radial distribution of sand particles velocity: a) $Ru = 0.16$; b) $Ru = 0.21$.

Figure A4 shows the axial velocities of sand particles at different radial directions. The axial velocity, u, was normalized with the centerline axial velocity, u_m, and the radial distance from the centerline, r, was normalized with the nozzle diameter, d_o. As can be seen in Figure A4a, the hump similar to the radial distribution of sand concentration exists at $r/d_o = 1.25$ and for $x/d_o \leq 30$. The normalized distance of $x/d_o \leq 30$ corresponds to the flow development zone. The intensity of the peak axial velocity decreased by decreasing the velocity ratio indicating a faster particle-flow mixing velocity ratio decreased (see Figure A4b).

The high-speed images of sand water-coaxial jets with various velocity ratios (i.e., $0 < Ru < 0.33$) are shown in Figure A5. As shown in Figure A5a and Figure A5b particle and flow oscillation was high for $Ru = 0$ and 0.33. However, by increasing the initial water phase Reynolds number (leading to smaller velocity ratios) more uniform flow and particle distribution were observed (see Figure A5c and Figure A5d).

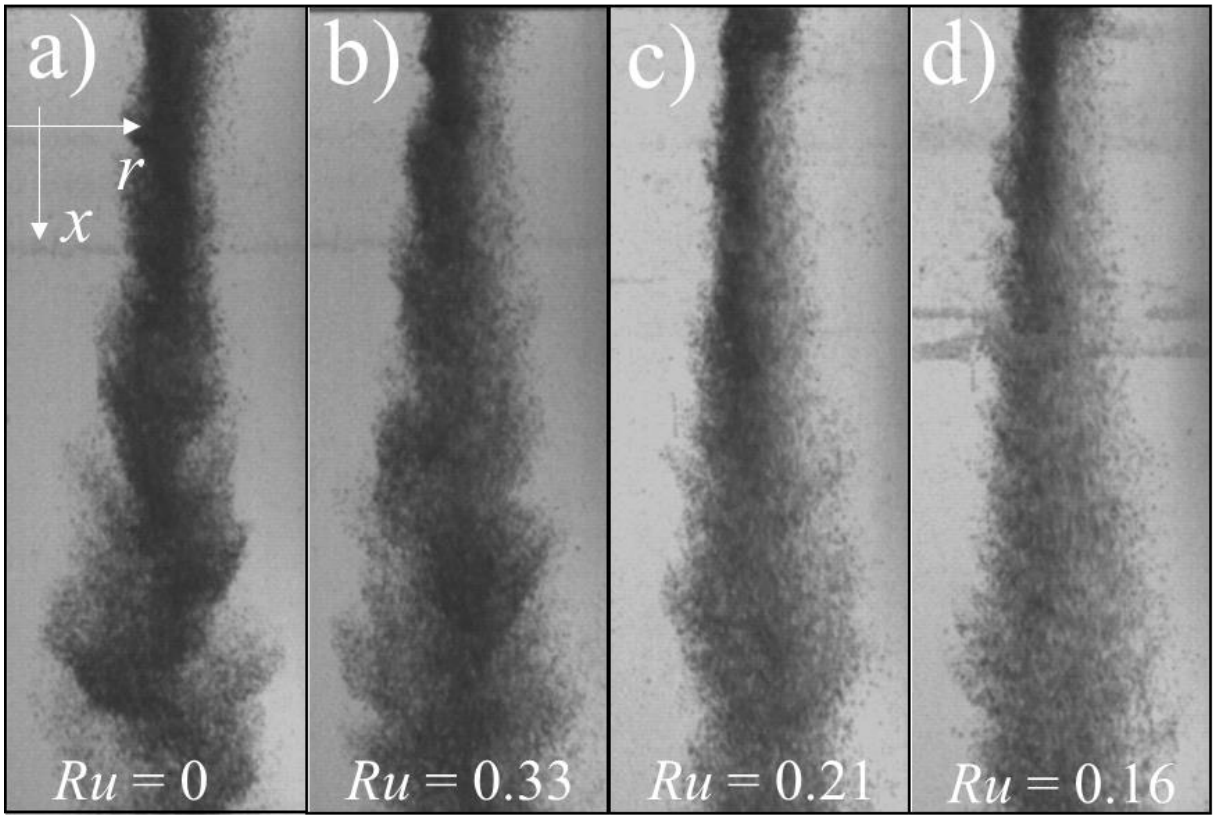

Figure A5: High speed images of sand-water coaxial jets for different velocity ratios: a) $Ru = 0$; b) $Ru = 0.33$; c) $Ru = 0.21$; d) $Ru = 0.16$.

The SPOD analysis was performed for the series of 1500 high-speed snapshots to investigate the low-rank dynamic of particles and flow properties. The block size was chosen

as 256 data with a 50% overlap. The first SPOD mode visualization for the frequencies of 0, 3.91, and 7.81 Hz for the velocity ratio of 0, 0.16, and 0.33 are shown in Figure A6. The Kelvin–Helmholtz (KH) type wave packs can be distinguished in all exhibited velocity ratios. The large size in wave packs for the velocity ratio of 0 and 0.33 with the frequency of 0 and 3.91 Hz can be distinguished at the downstream section for the frequency of zero (see Figure A6a and Figure A6d). Such wave packs indicate particle oscillation and shedding which was already shown in instantaneous high-speed images (See Figure A5a and Figure A5b). However, by increasing the Reynolds number of water and decreasing the velocity ratio (i.e., Ru = 0.16) wave packs turned to an axially elongated shape. Comparing the modal shape represented in Figure 6g with the high seed images demonstrated an almost uniform flow and particle pattern along the jet axis (see Figure A5c and Figure A5d). In all three cases of Ru for the frequencies of 3.91 and7.81 Hz, the a-wave train dominant mode can be observed and localized further downstream.

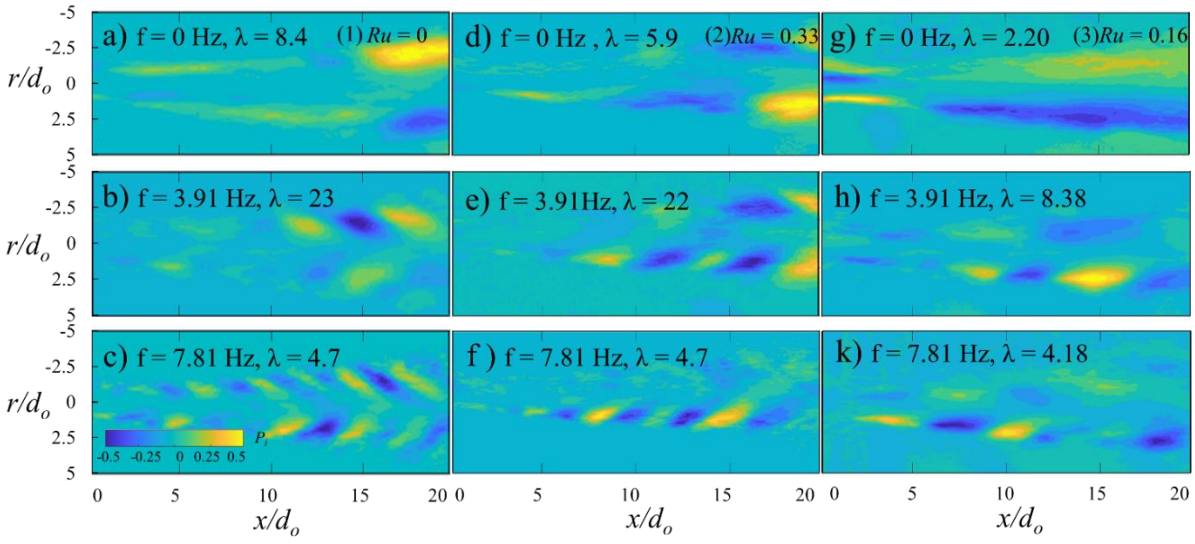

Figure A6: Visualization of the SPOD mode number one for frequencies of 0, 3.91 and 7.81 Hz for the velocity ratios of Ru = 0, 0.33 and 0.16.

Besides, the SPOD energy spectrum or eigenvalues, λ, the turbulent kinetic energy decreased by a reduction in the velocity ratio from 0.33 to 0.16. The SPOD energy spectrum, λ, for the first seven modes with the velocity ratio of 0.16 and 0.33 are displayed in Figure A7. Large separation between the eigenvalues is a good indicator of dominant mode and energy contribution. As shown in Figure A7a the first two modes had a larger separation due to higher energy levels. The separation between eigen spectra of the modes implies that vortex shedding dominated the dynamics of the connected modes (Nidhan et al., 2020). However, by decreasing

the velocity ratio, the separation distance decreased accordingly due to less vortex shedding intensity (see Figure A7b). It was found that most of the turbulence kinetic energy was stored in the first ten modes especially for smaller velocity ratios (i.e., $Ru = 0.16$) in sand-water coaxial jets.

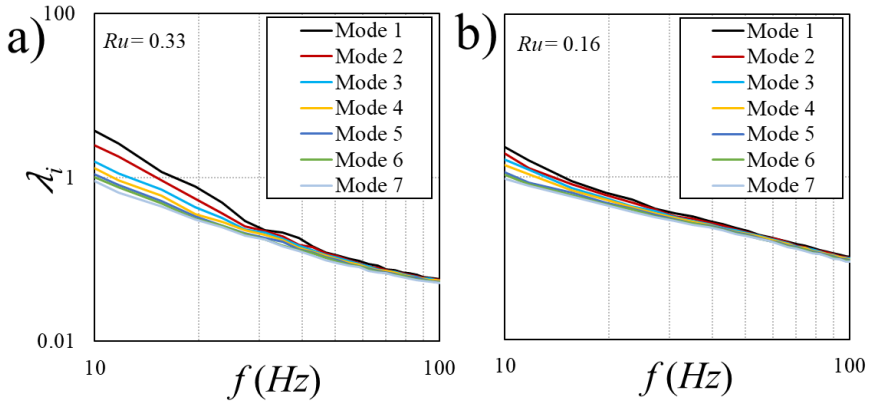

Figure A7: The SPOD eigenvalue spectra of the first seven modes: a) $Ru = 0.33$; b) $Ru = 0.16$.

6. Conclusion

A series of laboratory experiments were carried out to investigate the effects of low-velocity ratio ($Ru < 0.5$) on the dynamics of sand-water coaxial jets in stagnant water. A novel light refractive optical probe was utilized to measure sand concentration and velocity of sand-water coaxial jets in axial and transverse directions. The probe accuracy and data measurements consistency were examined by conservation of mass in different cross-sections with an uncertainty level of 10%. The initial mixing zone was found to be around 5 times the nozzle diameter and the zone of intermediate flow establishment was found to occur at $x/d_o \leq 16$. The axial variations of velocity and concentration were found to be independent of the velocity ratio in the intermediate zone of flow establishment. However, by decreasing the velocity ratio in the zone of flow development (i.e., $x/d_o > 16$), the decay rate increased accordingly and became similar to single-phase water jets. The concentration decay rate was found to be smaller than the decay rates of particle clouds and slurry jets, particularly for the high-velocity ratio ($Ru = 0.33$). The radial distributions of concentration and velocity profiles were also investigated. A near-field hump was observed at $r/d_o = 1.25$ for all cases in concentration and velocity profiles due to migration and mixing of particles with the central water jet. The presence of a SPOD eigenvalue spectra gap indicated that a significant portion of the turbulence kinetic energy and flow vortex shedding is stored in low-frequency modes of coaxial sand-water jets with a higher velocity ratio (i.e., $Ru = 0.33$). Furthermore, for velocity ratios smaller than 0.16, most of the

energy distribution occurred in the first ten modes. The Kelvin–Helmholtz (KH) type wave packets were observed in low frequencies and the first ten modes associated with the annular nozzle.

Appendix 2

A MATLAB® Signal Processing

A light-refractive fiber optic probe contained two light sources and two light-refracting optical sensors with signal amplification and processing unit (PV6) was employed to measure instantaneous time-series sand velocities and concentrations (Institute of Processing Engineering, Chinese Academy of Science, China). To capture and convert the analog voltage signals from a PV6, a high-resolution data acquisition board (National Instrument, Austin, U.S.) was utilized. The probe tip had a diameter of 4 mm, and contained two light sources with a diameter of 1 mm each and set 2.14 mm apart (see Figure 2.1). The reflected light emitted from the optical fiber bundles can capture by two sensors. More information and measuring principle of the system was described by Liu et al. (2003a). The time lag between these two series of data is obtained using the cross-correlation function of the MATLAB signal processing toolbox. The sample cross-correlation of two time-delayed recorded signals was shown in Figure A8.

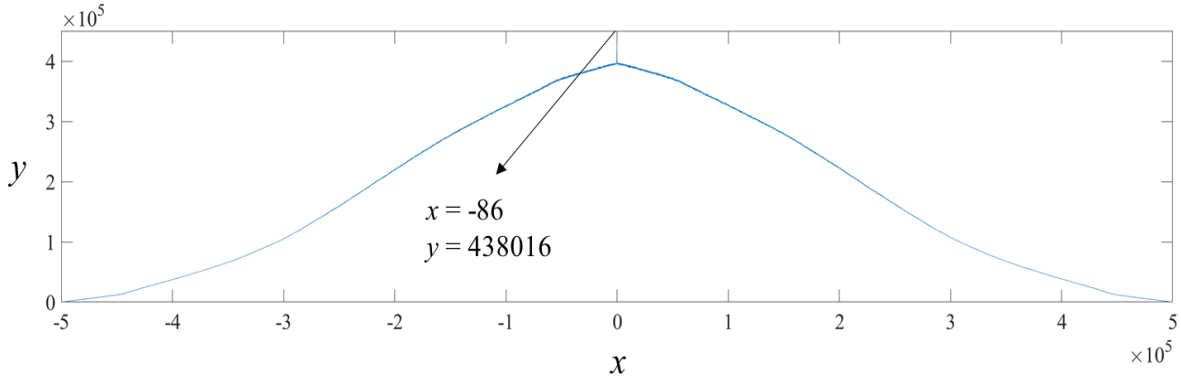

Figure A8: Plot of sample result of the cross-correlation function.

The sample rate of the probe is 61440 Hz. Therefore, the time lag between two signals can found by dividing the cross-correlation absolute value of the lag difference to signal frequency. Finally, the distance between two optical bundles (2.14 mm) can be divided by the obtained time lag to calculate velocity. The velocity between two sensors would be:

2.14/(86/61440) = 15.28 cm/sec

Appendix 3

A MATLAB® Velocity Cross-Correlation

```
clear

load a.txt;         %Load file name for analysis
load b.txt;

fsample=50000;      % Frequency of measurement (Hz)
d=0.00214;          % Distance between diodes  (m)


Fs=50000;

s22 = b(:,2);
s11 = a(:,2);

s22(s22 > 100) = s22(s22 > 100)/1000;
s11(s11 > 100) = s11(s11 > 100)/1000;

x1=s11;
x2=s22;

lev = 10;
xd1 = wden(x1,'rigrsure','s','one',lev,'sym8');
t1 = (0:length(xd1)-1)/50000;
subplot(2,1,1)
plot(t1,xd1)
title('xd1')
saveas(gcf,'xd1');
xd2 = wden(x2,'rigrsure','s','one',lev,'sym8');
t1 = (0:length(xd2)-1)/50000;
subplot(2,1,2)
plot(t1,xd2)
title('xd2')
saveas(gcf,'xd2');

z2=xd2(1:299995);
z1=xd1(1:299995);
x=z2-mean(z2);
y=z1-mean(z1);

for k=1:p           % k = Number of data chunk
    ch=2048;        % ch= Length of data chunk
    G=[x y];
L=G(k*ch:(k+1)*ch,:);
E2=L(:,1);
E1=L(:,2);

[acor,lag] = xcorr(E2,E1);
[~,I] = max(abs(acor));
lagDiff = abs(lag(I))
timeDiff = abs(lagDiff/Fs)


dlmwrite('timeDiff.txt',timeDiff);
u(k,1)= lagDiff/Fs; % Time      (sec)
u(k,2)=d/timeDiff;  % Velocity (m/sec)
```

```
u(u >= Inf) = 0;

                    %bar(u);
                    %title('instantaneous velocity');
                    %saveas(gcf,'instantaneous velocity');

end


dlmwrite('u.txt',u);
u( ~any(u,2), : ) = [];
u( :, ~any(u,1) ) = [];
u1 = u(:,2);
u1( ~any(u1,2), : ) = [];
dlmwrite('u1.txt',u1);
Vmean_col = sum(u, 1)./sum(u~=0, 1);
dlmwrite('Vmean_col.txt',Vmean_col);

Cm=mean(z1);
dlmwrite('Cm.txt',Cm);

[pks,locs]=findpeaks(z1);
Cp=mean(pks);
dlmwrite('Cp.txt',Cp);
load u1.txt;
dpikeVelocity = medfilt1(u1,3);
dlmwrite('dpikeVelocity.txt',dpikeVelocity);


R=(dpikeVelocity/0.5);              %Power spectrum density
Fsv=fv;                             %Fv = velosity frequency

N = length(R);
xdft = fft(R);
xdft = xdft(1:N/2+1);
psdx = (1/(Fsv*N)) * abs(xdft).^2;
psdx(2:end-1) = 2*psdx(2:end-1);
freq = 0:Fsv/length(R):Fsv/2;

loglog(log10(freq),log10(psdx))
saveas(gcf,'SPC log Log')
grid on
title('Periodogram Using FFT')
xlabel('Frequency (Hz)')
ylabel('Power/Frequency (dB/Hz)')
frequency=freq';
dlmwrite('frequency.txt',frequency);
dlmwrite('psdx.txt',psdx);
um=mean(dpikeVelocity);
utf=dpikeVelocity-um;
dlmwrite('utf.txt',utf);
MEANDSPVELOCITY=mean(dpikeVelocity);
dlmwrite('MEANDSPVELOCITY.txt',MEANDSPVELOCITY);
```

Appendix 4

A MATLAB® Spectral and Proper Orthogonal Decomposition

```
clc
clear all
miFolder='Image directory';

filePatron = fullfile(miFolder, '*.jpg');
jpegFil = dir(filePatron);
Resultados= Image directory to save';
mkdir(Resultados);
for k = 1:p
                % k = Number of data chunk
baseFN = jpegFil(k).name;
fullFN = fullfile(miFolder, baseFN);
I=imread(fullFN);
I2=imcrop(I);
%[J, rect] = imcrop(I);
imwrite(I2, fullfile(Resultados, ['c', num2str(k), '.jpg']));
image_gray=rgb2gray(I2);
image_gray_double = im2double(image_gray);
imshow (image_gray_double);
imwrite(image_gray_double, fullfile(Resultados, ['cg', num2str(k),
'.jpg']));
B=reshape(image_gray_double,1,[]);
mat(k,:)=B;
X=mat;          %Matrix of sequence snapshots to apply for SVD OR POD;


 mat(k,:,:)=image_gray_double;
 p=mat;
                %3D Matrix of sequence snapshots to apply for SPOD;

   end

dims=size(X);

%Removes mean. Note: Not removing the mean biases the modes as the
%data points centroid is shifted. If one wants to capture only the
%oscillations around the mean, the mean MUST be removed.
X1=X-repmat(mean(X,1),[dims(1) ones(1,length(dims)-1)]);

%Reshapes X
X2=reshape(X1,dims(1),prod(dims(2:end)));
%Performs SVD
[U, S, V]=svd(X2,'econ');
To preform SPOD (Schmidt and Colonius, 2018):

https://www.mathworks.com/matlabcentral/fileexchange/65683-spectral-proper-
orthogonaldecompositionspod#:~:text=SPOD()%20is%20a%20Matlab,proper%20ortho
gonal
%20decomposition%20(SPOD).
```

References

Abramovich, G. N., (1963). The theory of turbulent jets. MIT Press, 671.

Adrian, R. J., (1986a). Image shifting technique to resolve directional ambiguity in double-pulsed velocimetry. Appl. Opt. 25, 3855–3858.

Aísa, L., Garcia, J. A., (2002). Particle concentration and local mass flux measurements in two-phase flows with PDA: application to a study on the dispersion of spherical particles in a turbulent air jet. Int. J. Multiph. Flow. 28, 301–324.

Akaike, S., Nemoto, M., (1988). Potential core of a submerged laminar jet. J. Fluids Eng. 110, 392–398.Azimi, A. H., Zhu, D. Z., Rajaratnam, N., 2011. Effect of particle size on the characteristics of sand jet in water. ASCE, J. Eng. Mech. 137, 1–13.

Alberta Energy and Utilities Board, (2005). Alberta's reserves 2004 and supply/demand outlook 2005-2014. Report No. ST98-2005. Alberta Energy and Utilities Board, Calgary, AB.

Arienti., M., Soteriou., M. C., (2009). Time-resolved proper orthogonal decomposition of liquid jet dynamics. Phys. Fluids. 21, 112104.

Arote, A., Bade, M., Banerjee, J., (2020). On coherent structures of spatially oscillating planar liquid jet developing in a quiescent atmosphere. Phys. Fluids. 32, 082111.

Azimi, A. H., Zhu, D. Z., Rajaratnam, N., (2012a). Experimental study of sand jet front in water. Int. J. Multiph. Flow. 40, 19–37.

Azimi, A. H., Zhu, D. Z., Rajaratnam, N., (2012b). Computational investigation of vertical slurry jets in water. Int. J. Multiph. Flow. 47, 94–114.

Azimi, A. H., Zhu, D. Z., Rajaratnam, N., (2014). Experimental study of subaqueous sand deposition from slurry wall jets. ASCE, J. Eng. Mech. 140, 296–314.

Azimi, A. H., Zhu, D. Z., Rajaratnam, N., (2015). An experimental study of circular sand–water wall jets. Int. J. Multiph. Flow. 74, 34–44.

Azimi, A.H., (2019). Experimental investigation on the motion of particle cloud in viscous fluids. ASME J. Fluids. Eng. 141, 031202.

Bagnold, R.A., (1954). Experiments on a gravity-free dispersion of large solid spheres in a Newtonian fluid under shear. Proc. R. Soc. Lond A 225, 49–63.

Balarac, G., Métais, O., (2005). The near field of coaxial jets: A numerical study. Phys. Fluids 17, 065102.

Balarac, G., Métais, O., Lesieur, M., (2007). Mixing enhancement in coaxial jets through inflow forcing: A numerical study. Phys. Fluids. 19, 075102.

Batchelor, G.K., (1954). Heat convection and buoyancy effects in fluids. Q. J. R. Mete- orol. Soc. 80 (345), 339–358.

Becker, H .A., Massaro, T.A., (1968). Vortex evolution in a round jet. J. Fluid. Mech. 31, 435–448.

Benjamin, T. B., (1962). Theory of vortex breakdown phenomenon. J. Fluid. Mech. 14, 593–629.

Berkooz, G., Holmes, P., Lumley, J. L., (1993). The proper orthogonal decomposition in the analysis of turbulent flows. Annu. Rev. Fluid. Mech. 25, 539–575.

Billant, P., Chomaz, J. M., Huerre, P., (1998). Experimental study of vortex breakdown in

swirling jets. J. Fluid. Mech. 376, 183–219.

Bluemink, J. J., Lohse, D., Prosperetti, A. Van Wijngaarden, L., (2010). Drag and lift forces on particles in a rotating flow. J. Fluid. Mech. 643, 1–31.

Bond, D., Johari, H., (2005). Effect of initial geometry on the development of thermals. Exp. Fluids 39, 589–599.

Bühler, J., and Papantoniou, D.A., (1991). Swarms of coarse particles falling through a fluid. J. Environ. Hydraul, Lee and Cheung, eds., Balkema, 196–201.

Bühler, J., Papantoniou, D., (2001). On the motion of suspension thermals and particle swarms. J. Hydraul. Res. 39, 643–653.

Buresti, G., Petagna, P., Talamelli, A., (1998). Experimental investigation on the turbulent near-field of coaxial jets. Exp. Therm. Fluid Sci. 17, 18–26.

Bush, J.W.M., Thurber, B.A., Blanchette, F., (2003). Particle clouds in homogeneous and stratified environments. J. Fluid Mech. 489, 29–54.

Butcher, D., Spencer, A., (2019). Cross-correlation of POD spatial modes for the separation of stochastic turbulence and coherent structures. Fluids. 4, 134.

Brush, L.M.J., (1962). Exploratory study of sediment diffusion. J. Geophys. Res. 67, 1427–1433.

Canton, J., Auteri, F., Carini, M., (2017). Linear global stability of two incompressible coaxial jets. J. Fluid. Mech. 824, 886–911.

Ceglia, G., Discetti, S., Ianiro, A., Michaelis, D., Astarita, T., Tomographic., (2013). PIV measurements of the flow at the exit of an aero engine swirling injector with radial entry, 10th International Symposium on Particle Image Velocimetry.

Casciola, C., Gualtieri, P., Picano, F., Sardina, G., Troiani, G., (2010). Dynamics of inertial particles in free jets. Physica Scripta. T142.

Champagne, F. H., Wygnanski, I. J., (1971). An experimental investigation of coaxial turbulent jets. Int. J. Heat. Mass. Transf. 14, 1445–1464.

Charalampous, G., Hardalupas, Y., (2014). Application of proper orthogonal decomposition to the morphological analysis of confined co-axial jets of immiscible liquids with comparable densities. Phys. Fluids. 26, 113301.

Charalampous, G., Hadjiyiannis, C., Hardalupas, Y., (2019). Proper orthogonal decomposition of primary breakup and spray in coaxial air blast atomizers. Phys. Fluids. 31, 043304.

Chan, W. T., Ko, N. W. M., (1978). Coherent structures in the outer mixing region of annular jets. J. Fluid. Mech. 89, 515–533.

Chien, S.F., (1994). Settling velocity of irregularly shaped particles. SPE Drill Completion 9, 281–289.

Clift, R., Grace, J. R., Weber, M. E., (1978). Bubbles, Drops, and Particles. Academic Press, New York, 380.

Crow, S. C., Champagne, F. H., (1971). Orderly structure in jet turbulence. J. Fluid. Mech. 48, 547–591.

Crowe, C. T., Gore, R. A., Troutt, T. R., (1985). Particle dispersion by coherent structures in free shear flows, Particulate Sci and Tech, Int. J. 3, 149–158.

Dahm, W. J. A., Clifford, E. F., Tryggvanson, G., (1992). Vortex structure and dynamics in the near field of a coaxial jet. J. Fluid Mech. 241, 371–402.

Davies, T. W., Béer, J. M., (1971). Flow in the wake of bluff-body flame stabilizers. Symp.Int. Combust. 13, 631–638.

Donoho, D. L., (1991). Denoising by soft thresholding, IEEE Transaction on Information Theory. 41, 613–627.

Eaton, J. K., Fessler, J. R., (1994). Preferential concentration of particles by turbulence, Int. J. Multiph. Flow. 20, 169–209.

Engelund, F., Hansen, E., (1967). A Monograph on Sediment Transport in Alluvial Streams. K: Technical University of Denmark, Copenhagen, 0stervoldgade 10.

Fan, J., Zhang, L., Zhao, H., Cen, K., (1990). Particle concentration and particle size measurements in a particle-laden turbulent free jet. J. Exp. Fluids 9, 320–322.

Fan, J., Zhao. H., Jin, J., (1996). Two-phase velocity measurement in particle-laden coaxial jets. Chem. Eng. J. 63, 11–17.

Fan, J., Zhang, X., Chen, L., Cen, K., (1997). New stochastic particle dispersion modeling of a Turbulent Particle-Laden Round Jet, Chem. Eng. J. 66, 207–215.

Fischer, H. B., List, E. J., Koh, R. C. Y., Imberger, J., Brooks, N. H., (1979). Mixing in inland and coastal waters. Academic press, San Diego, California, USA. 483.

Flora, J. J., Goldschmidt, V. W., (1969). Virtual origin of a free plane turbulent jet. AIAA. J. 7, 2344–2446.

Hall, N., Elenany, M., Zhu, D.Z., Rajaratnam, N., (2010). Experimental study of sand and slurry jets in water. J. Hydraul. Eng. ASCE. 136, 727–738.

Harris, F. J., (1978). On the use of windows for harmonic analysis with the discrete Fourier transform. IEEE, 66., 51–83.

He, Z., Zhang, W., Houshuo, H., Zhao, L., Han, X., (2018). Experimental study of sand and slurry jets in water. J. Hydraul. Eng. ASCE, (144), 04018072, 15.

Higham, J.E., Brevis, W., Keylock, C.J., (2018). Implications of the selection of a particular modal decomposition technique for the analysis of shallow flows. J. Hydraul. Res. 56, 796-805.

Holmes, P., Lumley, J., Berkooz, G. (1996). Turbulence coherent structures, dynamical systems and symmetry. Cambridge University Press, Cambridge.

Huai, W., Xue, W., Qian., Z., (2013). Numerical simulation of slurry jets using mixture model. Water Sci and Eng. 6, 78–90.

Hua, J., Gunaratne, G., Talley, D., Gord, J., Roy, S., (2016). Dynamic-mode decomposition based analysis of shear coaxial jets with and without transverse acoustic driving. J. Fluid. Mech, 790, 5–32.

Hunt, M. L., R. Zenit, C. S. Campbell, and C. E. Brennen., (2002). Revisiting the 1954 suspension experiments of R. A. Bagnold. J. Fluid. Mech, 452, 1–24.

Gai, G., Hadjadj, A., Kudriakov, S., Thomine, O., (2020). Particles-induced turbulence: A critical review of physical concepts, numerical modelings and experimental investigations, Theoretical and Applied Mechanics Letters. 10., 241–248.

García-Villalba, J., Fröhlich, Rodi, W., (2006). Identification and analysis of coherent structures in the near field of a turbulent unconfined annular swirling jet using large eddy simulation. Phys. Fluids 18, 055103.

George, A. S., Xi, J., Luiz, C. W., (2009). Dynamics of annular gas–liquid two-phase swirling jets. Int. J. Multiph. Flow. 35, 450–467.

Gensheimer III, R. J., (2010), Dynamics of particle clouds in ambient currents with application to open-water sediment disposal. MSc. Thesis, Dept. of Civil and Environmental Engineering, MIT, Cambridge, MA, 260.

Gomes, M. S. P., Vincent, J. H., (2002). The effect of inertia on the dispersion of particles in the flow around a two-dimensional flat plate. Chem. Eng. Sci. 57, 1319–1329.

Gore, R.A., Crowe, C.T., (1989). Effect of particle size on modulating turbulent intensity. Int. J. Multiph. Flow. 15, 279–285.

Gutmark, E., Ho, C.M., (1983). Preferred modes and the spreading rates of jets. Phys. Fluids. 26, 2932‑2938.

Grinstein, F. F., DeVore, C.R., (1996). Dynamics of coherent structures and transition to turbulence in free square jets. Phys. Fluids.8, 1237–1251.

Gui, N., Fan, J.R., Chen, S., (2010). Numerical study of particle–particle collision in swirling jets: a DEM–DNS coupling simulation. Chem. Eng. Sci. 65, 3268–3278.

Gupta, A. K., Lilley, D. G., Syred, N., (1984). Swirl flows. Abacus Press, Tunbridge Wells, 488.

Gutmark, E., Ho, C. M., (1983). Preferred modes and the spreading rates of jets. Phys. Fluids 26, 2932–2938.

Janati, M., Azimi, A. H., (2021). Mixing of Twin Particle Clouds in Stagnant Water, ASCE J. Eng. Mech., 147,04021022.

Jiang, J. S., Law, A. W. K., and Cheng, N. S., (2005). Two-phase analysis of vertical sediment-laden jets. J. Eng. Mech. 131, 308–318.

Jufar S.R., Le M.D., Hsu C.M., (2020). Spreading characteristics of swirling double-concentric jets excited at resonance Strouhal number.Exp. Therm. Fluid. Sci.110–109922.

Kadu, A., Sakai, Y., Ito, Y., Iwano, K., Sugino, M., Katagiri, T., Hayase, T., Nagata, K., (2020). Application of spectral proper orthogonal decomposition to velocity and passive scalar fields in a swirling coaxial jet. Phys. Fluids 32, 015106.

Kannaiyan, K., and Sadr, R., (2013). Numerical Simulation of Particle-Laden Coaxial Turbulent Jets. Int. J. Comput. Methods Eng. Sci. Mech. 14, 61–73.

Karhunen, K., (1946). Zur spektral theorie stochastischer prozesse. Annales Academiæ Scientiarum Fennicæ. A1, 34.

Karami, S., Soria, J., (2018). Analysis of coherent structures in an under-expanded supersonic impinging jet using spectral proper orthogonal decomposition (SPOD). Aerospace. 5, 1–16.

Kazemi, S., Adib, M., Amani, e., (2018). Numerical study of advanced dispersion models in particle-laden swirling flows, Int. J. Multiph. Flow 101, 167–185.

Ko, N.W.M., and Kwan, A.S.H., (1976). The initial region of subsonic coaxial turbulent jets. J. Fluid. Mech.73, 305–332.

Koschmieder, E. L., (1993). Benard cells and Ttaylor vortices. Cambridge University Press.

Kotsovinos, N., (1976). A note on the spreading rate and virtual origin of a plane turbulent jet. J. Fluid. Mech. 77, 305–311.

Krieger, I. M., (1972). Rheology of monodisperse lattices. Adv. Colloid Interface Sci. 3, 111–136.

Kumar, A., Sahu, S., (2018). Optical visualization and measurement of liquid jet core in a coaxial atomizer with annular swirling air. J. Flow Vis. Image. Process. 25, 229–244.

Lau, T., Nathan, G., (2014). Influence of Stokes number on the velocity and concentration distributions in particle-laden jets. J. Fluid. Mech. 757, 432–457.

Lai A. C. H., Zhao B, Law AWK, Adams EE., (2013). Two-phase modeling of sediment clouds. J. Environ Fluid Mech. 13, 435–463.

Lai A. C. H., Zhao B, Law AWK, Adams EE., (2015). A numerical and analytical study of the effect of aspect ratio on the behavior of a round thermal. J. Environ. Fluid. Mech. 15, 85–108.

Lai, A. C. H., Chan, S. N., Law, A. W. K., and Adams, E. E., (2016). Spreading hypothesis of a particle plume. ASCE, J. Hydraulic. Eng., 12, 04016065.

Lambourne, N. C., Bryer, D. W., (1961). The bursting of leading-edge vortices: some observations and discussion of the phenomenon. Aeronautical Research Council R. & M 3282, 1–36.

Lee, J.H.W., Chu, V.H., (2003). Turbulent Jets and Plumes; A Lagrangian Approach. Kluwer Academic Publishers Group, The Netherlands. 390.

Lewis, D. M., Lambert, M. F., Burch, M. D., Brookes, J. D., (2010). Fields measurements of mean velocity characteristics of a large-diameter swirling jet. ASCE J. Hydraul. Eng, 136, 642–650.

Liang, H., Maxworthy, T., (2005). An experimental investigation of swirling jets. J. Fluid Mech. 525, 115–159.

Lim, H. D., Ding, J., Shi, S., New, T. H., (2020). Proper orthogonal decomposition analysis of near-field coherent structures associated with V-notched nozzle jets. Int. J. Heat Mass Transf. 112, 894–1777.

Liu, S., Masliyah, J. H., (1996). Rheology of Suspensions (ed. L. L. Schramm). Washington, DC: American Chemical Society. 3, 107–176.

Liu, J., Grace, J. R., and Bi, X. (2003a) Novel multifunctional optical-fibre probe: I. development and validation. AIChE. J. 49, 1405–1420.

Liu, Y., Zhou, L.X., Xu, C.X., (2010). Numerical simulation of instantaneous flow structure of swirling and non-swirling coaxial-jet particle-laden turbulence flows. Phys. A. 389, 5380–5389.

Liu, Y, Zhang, L, Zhou, L. (2019)., Effects of swirling flow on ultralight particle dispersion characteristics in coaxial jet combustor. Energy Sci Eng. 7, 3220–3233.

Liu, Y., Zhang, L., Chen, Z., Zhou, L., (2020). Numerical investigation on mixture particle dispersion characteristics in swirling particle-laden combustion chamber. Int Communications in Heat and Mass Transfer. 117, 104720.

Loève, M., 1945. Functions aleatoire de second ordre. Comptes Rendus de l'Académie des Sciences, 220.

Loiseleux, T., Chomaz, J.M., (2003). Breaking of rotational symmetry in a swirling jet experiment. Phys. Fluids 15, 511–523.

Lou, Y., He, Z., Houshuo, J., Han, X., (2019). Numerical simulation of two coalescing turbulent forced plumes in linearly stratified fluids. Phys. Fluids. 31, 037111.

Lumley, J. L., (1967). The structure of inhomogeneous turbulence. In Atmospheric Turbulence and Wave Propagation, ed. A. M. Yaglom, V. I. Tatarski.166-78.

Lumley, J., Holmes, P., Berkooz, G., (1996). Turbulence, coherent structures, dynamical systems and symmetry. Cambridge Monographs on Mechanics. doi:10.1017/CBO9780511622700.

Mallat, S., Hwang., W. L., (1992). Singularity Detection and Processing with Wavelets. IEEE Trans. Infor. Theory. 38, 617-643.

Maciel, Y., Facciolo, L., Duwig, C., Fuchs, L., Alfredsson, P.H., (2008). Near-field dynamics of a turbulent round jet with moderate swirl. Int. J. Heat. Fluid. Flow. 2, 675–686.

Manoharan, K., Frederick, M., Clees, S., O'Connor, J., Hemchandra, S., (2020). A weakly nonlinear analysis of the precessing vortex core oscillation in a variable swirl turbulent round jet. J. Fluid. Mech. 884, A29.

Manzouri, M., and Azimi, A. H. (2019a). A study of mound formation by discharging sand particles through oblique pipes in stagnant water. Int. J. Sediment Res, https://doi.org/10.1016/j.ijsrc.2019.05.003.

Manzouri, M., and Azimi, A. H. (2019b). Effects on oily sand jet evolution from impact momentum and channelization of particles through an immiscible interface. Int. J. Multiph. Flow.121, 103124.

Martinelli, F., Olivani, A., Coghe, A., (2007). Experimental analysis of the precessing vortex core in a free swirling jet. J. Expe in Fluids. 42, 827–839.

Mazurek, K.A., Christison, K., Rajaratnam, N., (2002). Turbulent sand jet in water. J. Hydraul. Res. 40, 527–53.

MATLAB [Computer software]. MathWorks, Natick, MA.

Meliga, P., Gallaire, F. & Chomaz, J. M., (2012). A weakly nonlinear mechanism for modeselection in swirling jets. J. Fluid. Mech. 699, 216–262.

Mcllwain, S., Pollard, A., (2002). Large eddy simulation of the effects of mild swirl on the near field of a round free jet. Phys. Fluids. 14, 653–66.

Michalke, A., 1965. On spatially growing disturbances in an inviscid shear layer. J. Fluid. Mech. 23, 521–544.

Moghadaripour, M., Azimi, A. H., Elyasi, S., (2017a). Experimental study of particle clouds in stagnant water, ASCE J. Eng. Mech., 143, 04017082.

Moghadaripour, M., Azimi, A. H., Elyasi, S., (2017b). Experimental study of oblique particle clouds in water. Int. J. Multiph. Flow. 91, 101–119.

Mohammadidinani, N., Azimi, A.H., Elyasi, S., (2017). Experimental investigation of sand jets passing through immiscible fluids. ASME, J. Fluids Eng. 139, 13 051303.

Montgomery, R. L., Engler, R. M., (1986). Fate of dredged material during open-water disposal. Environmental Effects of Dredging Technical Notes, Technical Report EEDP-01-2, U.S. Army Engineer Waterways Experiment Station, Vicksburg, MS.

Morel, T., (1975). Comprehensive design of axisymmetric wind tunnel contractions. ASME, J. Fluids Eng, Trans. 97, 225–233.

Morel, T., (1977). Design of two-dimensional wind tunnel contractions, ASME, J. Fluids. Eng, Trans.99, 371–378.

Morton, B.R., Geoffrey Taylor, Turner, J.S., (1956). Turbulent gravitational convection from maintained and instantaneous sources. Proc. R. Soc. Lond. A Math. Phys. Eng. Sci. 234 (1196), 1–23.

Mostafa, A.A., Mongia, H.C., Mcdonell, V.G., Samuelsen, G.S, (1990). An experimental and numerical study of particle-laden coaxial jet flows. Int. J. of Heat and Fluid Flow. 11, 90–97.

Murugan, S., Huang, R. F, Hsu., C. M., (2020). Effect of annular flow pulsation on flow and mixing characteristics of double concentric jets at low central jet Reynolds number. Int. J. Mech. Sci. 186, 105907.

Noiray, N., Schuermans, B., (2013). Deterministic quantities characterizing noise-driven Hopf bifurcations in gas turbine combustors. Intl. J. Non-Linear Mech. 50, 152–163.

Noh, Y., Fernando, H.J.S., (1993). The transition in the sedimentation pattern of a particle cloud. Phys. Fluids. 5, 3049–3055.

Nidhan, S., Chongsiripinyo, K., Schmidt, O., Sarkar, S., (2020). Spectral POD analysis of the turbulent wake of a disk at Re = 50, 000. Phys. Rev. Fluids. 5, 124606.

Oberleithner, C. O., Paschereit, R. S., Wygnanski, I., (2012). Formation of turbulent vortex breakdown: Intermittency, criticality, and global instability. AIAA J. 50, 1437–1452.

Ogus, G., Baelmans, M., Vanierschot, M., (2016). On the flow structures and hysteresis of laminar swirling jets. Phys. Fluids. 28, 123604.

Pakzad, L. and Azimi, A. H. (2017). Investigations on the Dynamics of Particle Clouds in Stagnant Water Using Response Surface Methodology. Canadian J. Civil. Eng, CSCE. 44, 117-128.

Papanicolaou, P. N., and List, E. J., (1988). Investigations of round vertical turbulent buoyant jets. J. Fluid. Mech., 195, 341–391.

Parthasarathy, R.N., Faeth, G.M., (1987). Structure of particle-laden turbulent waterjets in still water. Int. J. Multiph. Flow 13, 699–716.

Park, C. J., and Chen, L. D., (1989). Experimental investigation of confined turbulent jets, Part I: Single-phase data. AIAA J., 27, 1506–1510.

Pearson, K., (1901). On lines and planes of closest fit to systems of points in space. Philos. Mag. 2, 559–572

Pedel, J., Thornock, J. N., Smith, S. T., Smith, P. J., (2014). Large eddy simulation of polydisperse particles in turbulent coaxial jets using the direct quadrature method of moments. Int. J. Multiph. Flow. 63, 23–38.

Prevost, F. , Boree, J. , Nuglisch, H.J. , Charnay, G. , (1996). Measurements of fluid/particle correlated motion in the far field of an axisymmetric jet. Int. J. Multiph. Flow., Flow 22, 685–701.

Rahimipour, H., Wilkinson, D., (1992). Dynamic behavior of particle clouds. In: Proceedings of the Eleventh Australasian Fluid Mechanics Conference, 1 and 2. University of Tasmania, Hobart, Australia, 743–746.

Rajaratnam, N., (1976). Turbulent Jets. Elsevier, Netherlands, 304 p.

Richardson, J. F., and Zaki, W. N., (1954). Sedimentation and Fluidization—Part I. Trans. Inst. Chem. Eng., 32, 35–53.

Sadr, R., and Klewicki, J. C, (2003). An experimental investigation of the near-field flow development in coaxial jets. Phys. Fluids.,15. 1233–1246.

Sadr, R., and Klewicki, J. C., (2005). Flow field characteristics in the near field region of particle-laden coaxial jets. Exp. Fluids., 39. 885–894.

Safer, D., Beghidja., A., (2019). Mixing in turbulent coaxial jet. J. Mech. Eng. Res. Dev. 42, 110-119.

Schetz, J. A., (1980). Injection and mixing in turbulent flow. AIAA, New York, USA.

Schlichting, H., (1955). Boundary-Layer Theory. McGraw-Hill, New York, 83-89.

Schmid, P. J., Meyer, K. E., Pust, O., (2009). Dynamic mode decomposition and proper orthogonal decomposition of flow in a lid-driven cylindrical cavity. In the 8th international symposium on particle image velocimetry-PIV09, Monash University. 3, 1–4.

Schmidt, O., Towne, A., Colonius, T., Cavalieri, A., Jordan, P., Brès, G., (2017). Wavepackets and trapped acoustic modes in a turbulent jet: Coherent structure eduction and global stability. J. Fluid. Mech, 825, 1153–1181.

Schmidt, O., Towne, A., Rigas, G., Colonius, T., Brès, G., (2018). Spectral analysis of jet turbulence. J. Fluid. Mech. 855, 953-982.

Schmidt, O., Colonius, T., (2020). Guide to Spectral Proper Orthogonal Decomposition. AIAA J. 58. 1-11.

Schultz, E. F., Wilde, R. H., Albertson, M.L., (1954). Influence of Shape on Fall Velocity of Sedimentary Particles, Report for the Missouri River Div., Corps of Engineers, U.S. Army, through Colorado Research Foundation, Fort Collins CO. 178.

Semeraro, O., Bellani, G., Lundell, F., (2012). Analysis of time-resolved PIV measurements of a confined turbulent jet using POD and Koopman modes. Exp. Fluids. 53**,** 1203–1220.

Sieber, M., Paschereit, C., Oberleithner, K., (2016). Spectral proper orthogonal decomposition. J. Fluid. Mech. 792, 798-828.

Sirovich, L., (1987). Turbulence and the dynamics of coherent structures. I. Coherent structures. Q. Appl. Math. 45, 561–571.

Siegel, S., Cohen, K., Seigel, J., McLaughlin, T., (2006). Proper orthogonal decomposition snapshot selection for state estimation of feedback controlled flows. AIAA Aerospace Sciences Meeting and Exhibit, Reno/NV. Paper 1400.

Sharif, F., Azimi, A. H., (2020). Particle cloud dynamics in stagnant water. Int. J. Multiph. Flow. 125, 101–119.

Sharif, F., Azimi, A. H., (2021). Effects of velocity ratio on dynamics of sand-water coaxial jets. Int. J. Multiph. Flow. 140, 103643.

Shen, Y., Gulam., M., Zhang, K., Gutmark, E., Duwing., C., (2020). Vortex breakdown of the swirling flow in a Lean Direct Injection burner. Phys. Fluids. 32, 125118.

Shojaeizadeh, A., Safaei, M., Alrashed, A., Ghodsian, M., Geza, M., Abbassi, M., (2018). Bed roughness effects on characteristics of turbulent confined wall jets. Measurement 122, 325–338.

Solomon, Jr. O. M., (1991). PSD computations using Welch's method. [Power Spectral Density (PSD)]. United States: N. p. doi:10.2172/5688766.

Sundaram, S., Collins, L.R., (1997). Collision statistics in an isotropic particle-laden turbulent suspension. Part 1. Direct numerical simulations. J. Fluid. Mech. 335, 75–109.

Syred, N., 2006. A review of oscillation mechanisms and the role of the precessing vortex core (PVC) in swirl combustion systems. Prog. Energy. Combust. Sci. 32, 93-161.

Swamee, P.K., Ojha, C.S.P., (1991). Drag coefficient and fall velocity of non-spherical particles. ASCE. J. Hydraul. Eng. 117, 660–667.

Tamburello, D., Amitay, M., (2008). Active manipulation of a particle-laden jet. Int. J. Multiph. Flow. 34, 829–851.

Taofeeq, H., Aradhya, Sh., Shao, J., Al-Dahhan, M., (2018). Advance Optical Fiber Probe for Simultaneous Measurements of Solids Holdup and Particles Velocity Using Simple Calibration Methods for Gas-Solid Fluidization Systems. Flow. Meas. Instrum. 63, 18–32.

Teshome, S., (2012). Droplet Combustion and Non-Reactive Shear-Coaxial Jets with Transverse Acoustic Excitation Department of Mechanical and Aerospace Engineering. PhD thesis, University of California Los Angeles. 282.

Turner, J. S., (1964). The flow into an expanding spherical vortex. J. Fluid. Mech. 18, 195–208.

Turner, J.S., (1969). Buoyant plumes and thermals. Annu. Rev. Fluid. Mech. 1, 29–44.

Truitt, C. L., 1988. Dredged Material Behavior During Open-Water Disposal. J. Coast. Res. 4, 489-497.

Vanierschot, M., Ogus, G., (2019). Experimental investigation of the precessing vortex core in annular swirling jet flows in the transitional regime. Exp. Therm. Fluid. Sci. 106, 148–158.

Villermaux, E., Rehab, H., (2000). Mixing in coaxial jets. J. Fluid. Mech. 425, 161–185.

Virdung, T., Rasmuson, A., (2007). Hydrodynamic properties of a turbulent confined solid-liquid jet evaluated using PIV and CFD. Chem. Eng. Sci. 62, 5963–5979.

Wang, H., Law, A. W. K., (2002). Second-order integral model for a round turbulent buoyant jet. J. Fluid. Mech. 459, 397–428.

Wang, R., Wing-Keung Law, A., Adams, E.E., (2014). Large-eddy simulation (LES) of settling particle cloud dynamics. Int. J. Multiph. Flow. 67, 65–75.

Wang, Y., Yang, V., (2018). Central recirculation zones and instability waves in internal swirling flows with an annular entry. Phys. Fluids, 30, 013602.

Warda, H. A., Kassab, S. Z., Elshorbagy, K. A., Elsaadawy, E. A., (1999). An experimental investigation of the near-field region of free turbulent coaxial jet using LDA. J. Flow Meas. Instrum. 10, 15–26.

Weisbrot, I., Einav, S., and Wygnanski, I., (1982). The nonunique rate of spread in the two-dimensional mixing layer. Phys. Fluids. 25, 1691–1693.

Weinkauff, J., Trunk, P., Frank, J. H., Dunn, M.J., Dreizler, A., Bohm, B., (2015). Investigation of flame propagation in a partially premixed jet by high-speed-stereo-PIV and acetone-PLIF. Proc. Combust. Inst. 35, 3773–3781.

Welch, P. D., (1967). The use of fast Fourier transform for the estimation of power spectra; A method based on time averaging over short, modified periodograms, IEEE Trans. Audio. Electroacoust. 15, 70–73.

Weeks, M. (2010). Signal Processing Using MATLAB & Wavelets. Jones and Bartlett Publishers, Inc., 500.

Wegener, J. L., (2014). Multi-phase Combustion and Transport Processes Under the Influence of Acoustic Excitation. PhD Thesis, UCLA University, LA, United States.

Wen, F. & Nacamuli, A., (1996). The effect of the Rayleigh number on a particle cloud. In Hydrodynamics: Theory and Applications vol. 1 and 2, 1275–1280.

Wicker, R. B., Eaton, J. K., (1994). Near field of a coaxial jet with and without axial excitation. AIAA J. 32, 542-546.

Wicker, R. B., and Eaton, J. K. (1999). Effect of Injected Longitudinal Vorticity on Particle Dispersion in a Swirling, Coaxial Jet. ASME. J. Fluids. Eng. 121, 766–772.

Wicker, R.B., Eaton, J.K., (2001). Structure of a swirling, recirculating coaxial free jet and its effect on particle motion. Int. J. Multiph. Flow 27, 949–970.

Wildemuth, C. R., Williams, M. C., (1984). Viscosity of suspensions modeled with a shear-dependent maximum packing fraction. Rheological. Acta. 23, 675–635.

Willert CE, Gharib M., (1991). Digital particle image velocimetry. Exp. in Fluids. 10:181e93.

Winant, C. D., Browand, F.K., 1974. Vortex pairing: the mechanism of turbulent mixing layer growth at moderate Reynolds number. J. Fluid. Mech. 63, 237–255.

Wörner, M., (2003). A compact introduction to the numerical modeling of multiphase flows. Forschungszentrum, Karlsruhe, 38.

Wu, H.J., Zhou, F.D., Wu, Y.Y., (2001). Intelligent identification system of flow regime of oil–gas–water multiphase flow. Int. J. Multiph. Flow. 27, 459–475.

Wygnanski, I., Fiedler, H., (1969). Some measurements in the self-preserving jet. J. Fluid. Mech. 38, 577–612.

Zang, B, T.H., (2015). New, On the wake-like vortical arrangement and behaviour associated

with twin jets in close proximity. Exp. Therm. Fluid. Sci. 69, 127‑140.

Zhang, L., Zhong, D., Guan, J., (2018). Drift velocity in sediment-laden downward jets. Environ. Fluid. Mech., 746, 193–213.

Zhang, Y., Vanierschot., M., (2021). Determination of single and double helical structures in a swirling jet by spectral proper orthogonal decomposition. Phys. Fluids. 33, 015115.

Zhao, B., Law, A. W. K., Adams, E. E., Shao, D., and Huang, Z., (2012). Effect of Air Release Height on the Formation of Sediment Thermals in Water. J. Hydraul. Res., 50, 532–540.

Zhao, B., Law, A. W. K., Adams, E. E., and Er, J. W., (2014). Formation of Particle Clouds. J. Fluid. Mech., 746, 193–213.